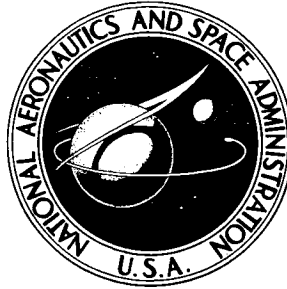


NASA TECHNICAL NOTE



NASA TN D-2798

NASA TN D-2798

FACILITY FORM 602	N65 29550 (ACCESSION NUMBER)	N65-29562 (THRU)
	179 (PAGES)	1 (CODE)
	 (NASA CR OR TMX OR AD NUMBER)	13 (CATEGORY)

GPO PRICE \$ _____

CFSTI PRICE(S) \$ 3.00

Hard copy (HC) _____

Microfiche (MF) 1.00

ff 653 July 65

GODDARD SPACE FLIGHT CENTER CONTRIBUTIONS TO THE COSPAR MEETING - MAY 1964

*Goddard Space Flight Center
Greenbelt, Md.*

GODDARD SPACE FLIGHT CENTER
CONTRIBUTIONS TO THE COSPAR MEETING - MAY 1964

Goddard Space Flight Center
Greenbelt, Md.

NATIONAL AERONAUTICS AND SPACE ADMINISTRATION

For sale by the Clearinghouse for Federal Scientific and Technical Information
Springfield, Virginia 22151 - Price \$5.00

GODDARD SPACE FLIGHT CENTER
CONTRIBUTIONS TO THE COSPAR MEETING

MAY 1964

FOREWORD

The Committee on Space Research (COSPAR) held its fifth International Space Sciences Symposium in May 1964 in Florence, Italy. This volume presents a collection of papers co-authored or presented at the meeting by personnel of NASA's Goddard Space Flight Center, Greenbelt, Maryland.

There has been no attempt to arrange the papers in any particular sequence. Their publication within a single NASA Technical Note, rather than as separate ones, was prompted by recognition of the growing need for more inter-disciplinary communication. It is to be hoped, therefore, that the readers of any of these papers will find material of interest in all of them.

Technical Information Division
Goddard Space Flight Center
Greenbelt, Maryland

CONTENTS

Foreword	i
"Inferences of Stratospheric and Mesospheric Circulation Systems from Rocket Experiments" G. Warnecke and W. Nordberg	1 ✓
"Stratospheric Temperature Patterns based on Radiometric Measurements from the Tiros VII Satellite" W. Nordberg, W. R. Bandeen, G. Warnecke, and V. Kunde	13 ✓
"New Knowledge of the Earth's Atmosphere from the Aeronomy Satellite (Explorer XVII)" N. W. Spencer, G. P. Newton, C. A. Reber, L. H. Brace, and R. Horowitz	37 ✓
"The Temperature of Charged Particles in the Upper Atmosphere" R. E. Bourdeau	51 ✓
"On the Diurnal Variation of the Upper Atmosphere" I. Harris and W. Priester	63 ✓
"Results from the IMP I Retarding Potential Analyzer" G. P. Serbu	77 ✓
"Initial Results of the IMP I Magnetic Field Experiment" N. F. Ness, C. S. Searce, and J. B. Seek	87 ✓
"Theoretical Studies of Protons in the Outer Radiation Belt" M. P. Nakada, J. W. Dungey, and W. N. Hess	143 ✓
"Solar Cycle Changes in Inner Zone Protons" R. C. Blanchard and W. N. Hess	149 ✓
"Solar X-Ray Bursts in the 20 to 100 Kev Range Observed by OSO-I" K. J. Frost	163 ✓
"Detection of Interplanetary 3- to 12-Mev Electrons" T. L. Cline, G. H. Ludwig, and F. B. McDonald	169 ✓
"Measurement of Low Energy Primary Cosmic Ray Protons on IMP 1 Satellite" F. B. McDonald and G. H. Ludwig	175 ✓

N65-29551

INFERENCES OF STRATOSPHERIC AND MESOSPHERIC CIRCULATION SYSTEMS FROM ROCKET EXPERIMENTS*

by

G. Warnecke† and W. Nordberg
Goddard Space Flight Center

SUMMARY

29551

Synoptic rocket grenade experiments and meteorological rocket network soundings performed during the winter seasons 1962/63 and 1963/64 were interpreted to show the existence and movement of conventional circulation systems throughout the upper stratosphere and in the mesosphere. Pressure maps for North America were derived from the rocket measurements at various altitudes up to 70 km. Considerable disturbances were found in the zonal pressure distribution at all altitudes. These disturbances were observed to persist several days and some moved considerable distances during that period. Although these disturbances exhibit depths of 10 to 20 km, no clear cut relationship between such systems in the stratosphere and mesosphere could be found. Evidence of such moving pressure systems exists only up to 70 km where the nature of the circulation changes abruptly. The regular wind pattern primarily determined by the circumpolar pressure distribution disappears at altitudes above 70 km, and rocket wind measurements indicate that other forces, probably tidal in nature, become exceedingly predominant above 70 km. At these altitudes, we may only conclude that the nature of the circulation is radically different from lower altitudes, but because of the rapid variation in the wind patterns, we were unable to show the existence of pressure systems such as we found below 70 km.

Warnecke

INTRODUCTION

Since the early rocket grenade experiments more than ten years ago and the successful firings during IGY, the experiments have been continued by NASA at Wallops Island. Thus numerous soundings are available which provide a climatological survey on the gross features of the winds and the thermal structure in the upper stratosphere and in the mesosphere (References 1 and 2). Experiments have also been performed in Australia, Japan, Sweden, Italy, and France and the United States program will be extended to include simultaneous launchings at Churchill, Wallops Island, and Ascension Island (Reference 3). The number of rocket stations reporting data above the normal Meteorological Rocket Network (MRN) levels is gradually increasing and promises improving global data coverage for the levels between 50 and 90 km during the forthcoming International

*Scheduled, but not presented.

†NAS-NRC Research associate; on leave from Institut für Meteorologie and Geophysik der Freien Universität Berlin.

Geophysical Year (IQSY). In this report, interesting features are derived from the first simultaneous rocket grenade experiments performed at Churchill, Manitoba, and Wallops Island, Virginia, and from simultaneous Meteorological rockets launched at the various MRN sites over North America. While the earlier sporadic experiments enabled a study of gross climatological features of the mesospheric circulation, these simultaneous observations have encouraged the investigation of the dynamic structure of the mesosphere on a smaller scale by means of synoptic presentation of flow patterns for selected days over the North American continent. At the higher altitudes, the acoustic temperature and wind measurements were supplemented by other sounding techniques such as wind measurements by means of sodium vapor release.

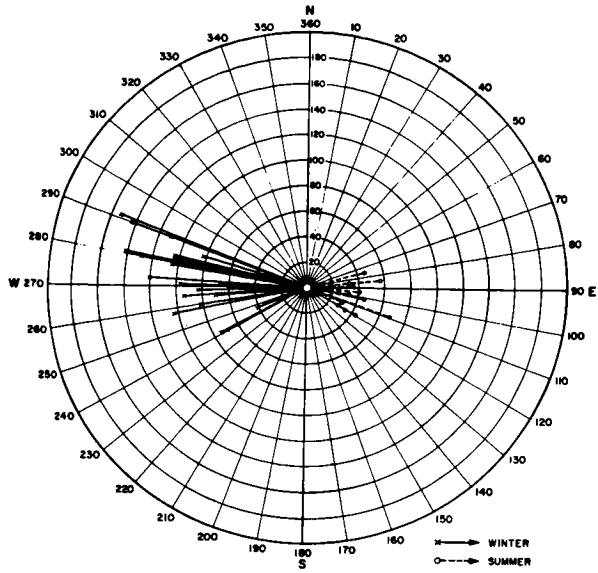
THE VERTICAL CHANGE IN STRATOSPHERIC AND MESOSPHERIC WIND STRUCTURE

Considering the seasonal variations of stratospheric and mesospheric winds as measured at Wallops Island over a period of 3 years, we find a remarkable change in the behavior of mesospheric winds around the height of 70 km. Below this level, the wind follows a consistent and predictable seasonal pattern while above 70 km the wind structure becomes very irregular and does not show the well-known regular features observed at levels up to 70 km (Reference 2).

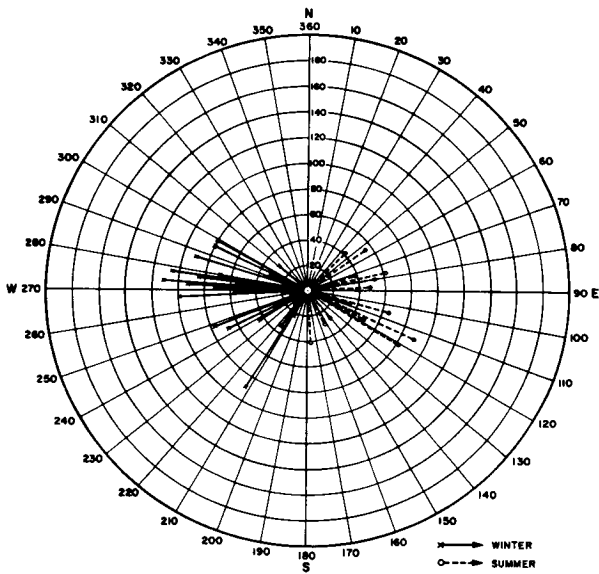
This irregularity is apparent in Figure 1, where all rocket grenade winds for the years 1960 through 1963 are presented in polar diagrams for the lower, middle, and upper mesosphere. The winds in the 45-55 km layer show the same general features as in the stratosphere: strong and relatively steady westerly winds with maximum deviations of $\pm 25^\circ$ about an average direction of 265° and light but equally steady easterly winds in summer. During the transitions between winter and summer seasons, there is a large variability in wind strength and direction; however, this variability is still part of a consistent seasonal pattern which has been the subject of several previous analyses (Reference 4). In the middle mesosphere (60-70 km) we find qualitatively the same behavior, although variations in the wind directions are somewhat larger. In the upper mesosphere (80-90 km), however, the picture changes completely. The winds both in winter and summer are blowing from all directions and in highly variable strengths. The same characteristics are shown by the results of recent sodium vapor release experiments at Wallops Island (Reference 5). Wind direction profiles from five experiments reaching below 70 km are reproduced, in Figure 2 and the drastic change in wind structure between 70 and 80 km is apparent.

From these rocket observations with both the grenade and sodium release methods, we may conclude that above a transition layer between 70 and 80 km the dynamic behavior of the mesosphere becomes so complex that synoptic representations of the flow patterns on a day to day basis will be meaningless. The motions above this layer appear to be highly "disorganized" from the standpoint of conventional synoptic meteorology. Therefore, such an abrupt change in the wind structure may very well be due to the increasing importance of tidal motions and possibly in the fact that the atmospheric structure as a whole undergoes basic and major changes at the 80 km level.

(a) 45-55 km.



(b) 60-70 km.



(c) 80-90 km.

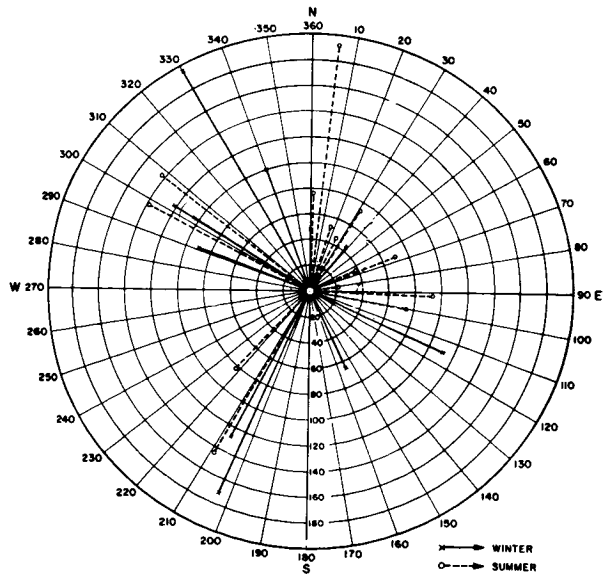


Figure 1—Winds (m/sec) measured by rocket grenade experiments at Wallops Island, 1960-1963.

Nevertheless, up to this level the mesospheric motions are still organized in the usual meteorological sense, and synoptic presentations are quite justified and well representative of the stream patterns over periods of several days.

INFERRED MESOSPHERIC SYNOPTIC CIRCULATION SYSTEMS UP TO 70 KILOMETERS

Several investigators have already extended presentation of synoptic weather maps up to 0.5 or 0.4 mb level (about 55 km) by using Meteorological Rocket Network data (References 6, 7, 8, and 9). Herein, an attempt is made to construct synoptic maps up to the 0.05 mb level (68 km) for a few special days by making use of recent grenade and MRN data.

Data from the first simultaneous rocket grenade soundings at Churchill and Wallops Island, in early December 1962 (Reference 10) were analyzed in addition to Meteorological Rocket Network data (Reference 11) also available for that time period. Variation of flow and pressure patterns for various upper stratospheric and mesospheric levels over the American continent were investigated by constructing synoptic maps for December 4 and December 6, 1962. In these maps, the pressure fields at constant heights are presented. Using the geostrophic approximation, the isobars were spaced such that each pressure field is in accordance with the observed winds. The pressure values of the isobars were determined by the observed pressures over the discrete points of observation.

The circulation in the lower stratosphere (100 mb or 16 km) around December 5, 1962 was characterized by the displacement of the cold polar vortex to Siberia, the entire North American continent being under a rather uniform westerly stratospheric flow with a slowly developing trough moving gradually eastward over the United States (Figure 3 and Reference 12). The middle stratosphere (30 mb or 23 km) shows a quite different stream pattern over the entire western hemisphere (Figure 4 and Reference 13) with a weak but, nevertheless, unusual quasi-stationary anticyclone over Canada and a zonally oriented trough over the United States along the 40° latitude. In the upper stratosphere (10 mb or 30 km) the same contour pattern appears with greater intensity: the easterly wind at the southern flank of the Canadian anticyclone exceeds 25 m/sec (50 knots), whereas a stratospheric jet stream with winds up to 50 m/sec (100 knots) is located over the Gulf coast (Figure 5). There are no significant changes of the circulation pattern at 30 km within the period December 4-6, 1962, so that Figure 5 applies to this interval. The North American high pressure

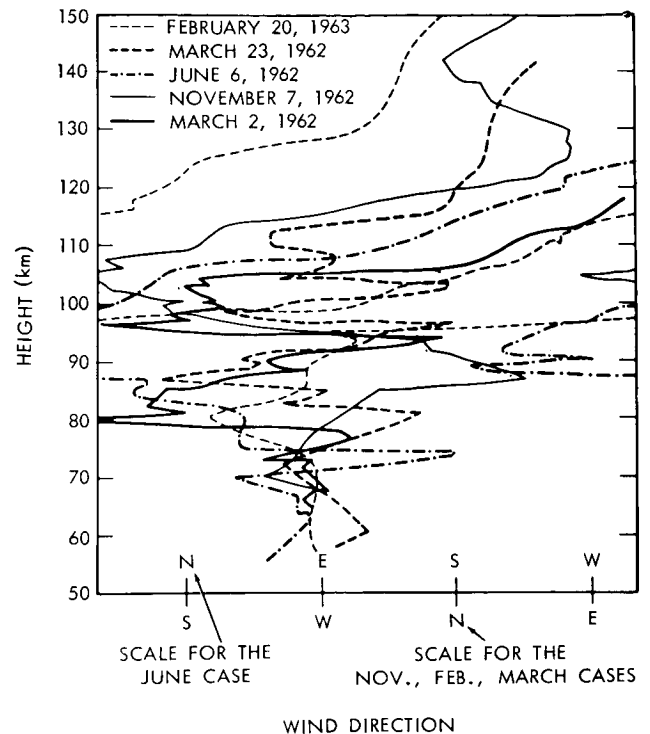
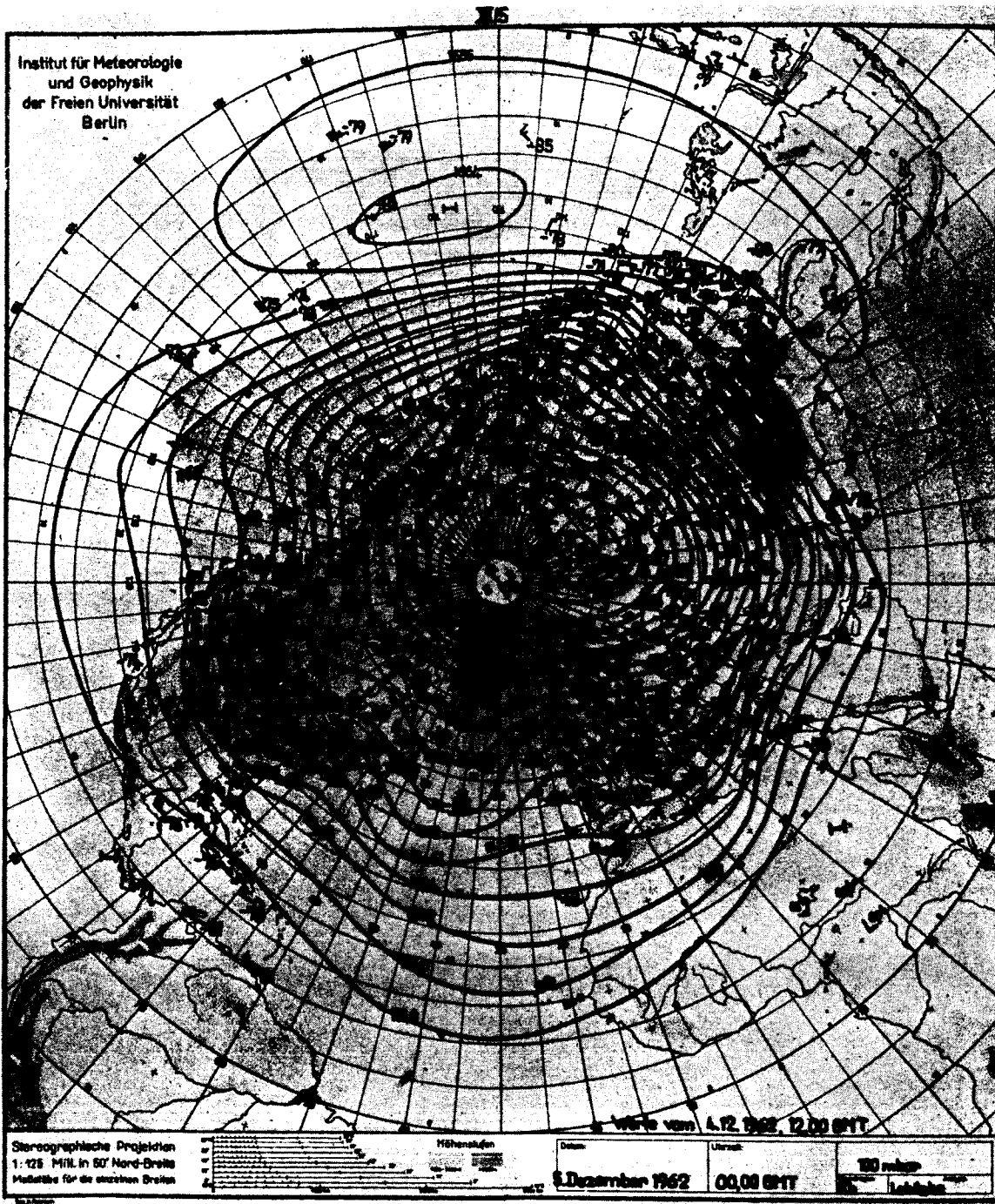


Figure 2—Wind direction profiles from five sodium vapor trail experiments extending below 70 km.



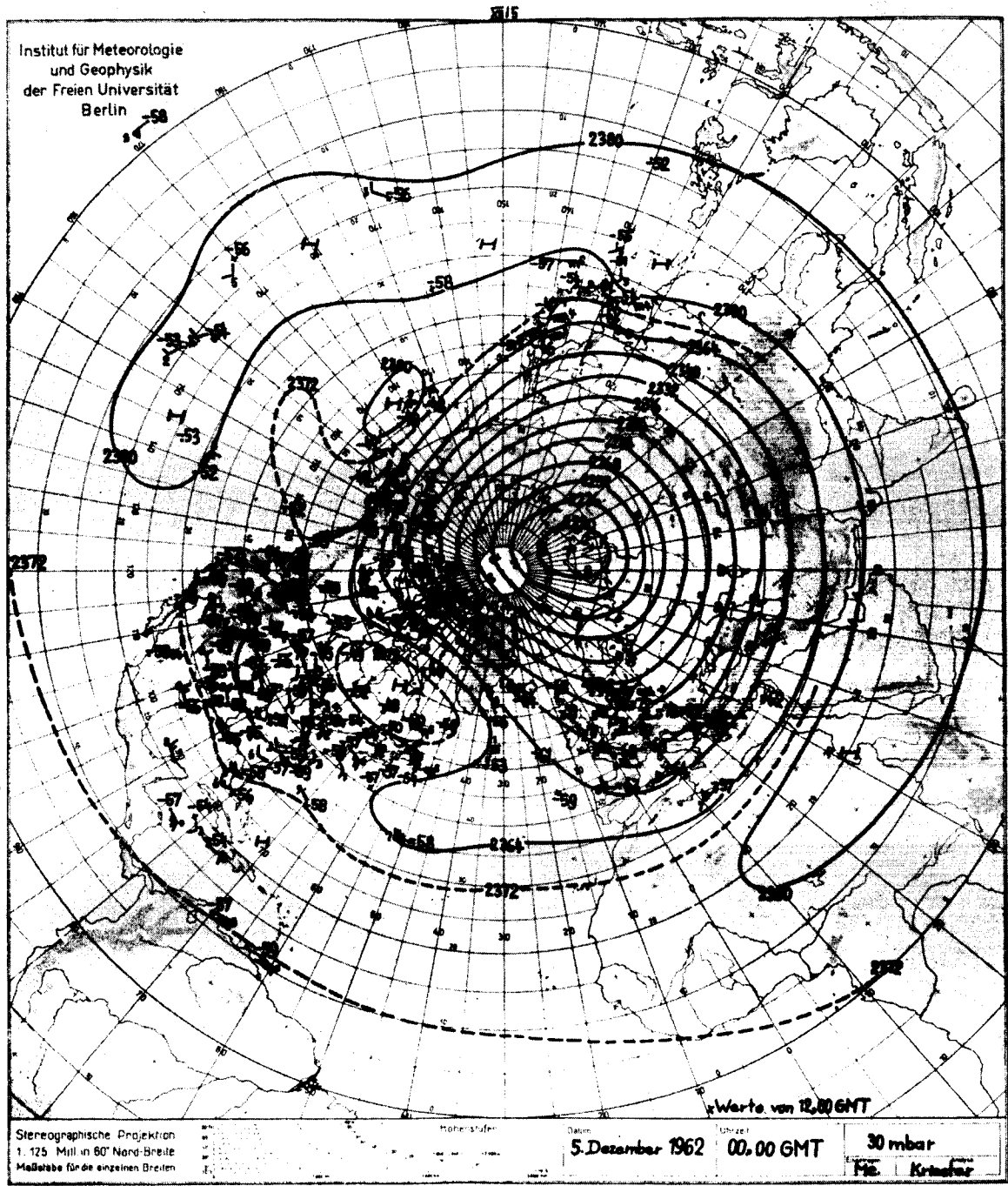


Figure 4—Stratospheric circulation (23 km) of the northern hemisphere, December 5, 1962 (Reference 13).

XII/4

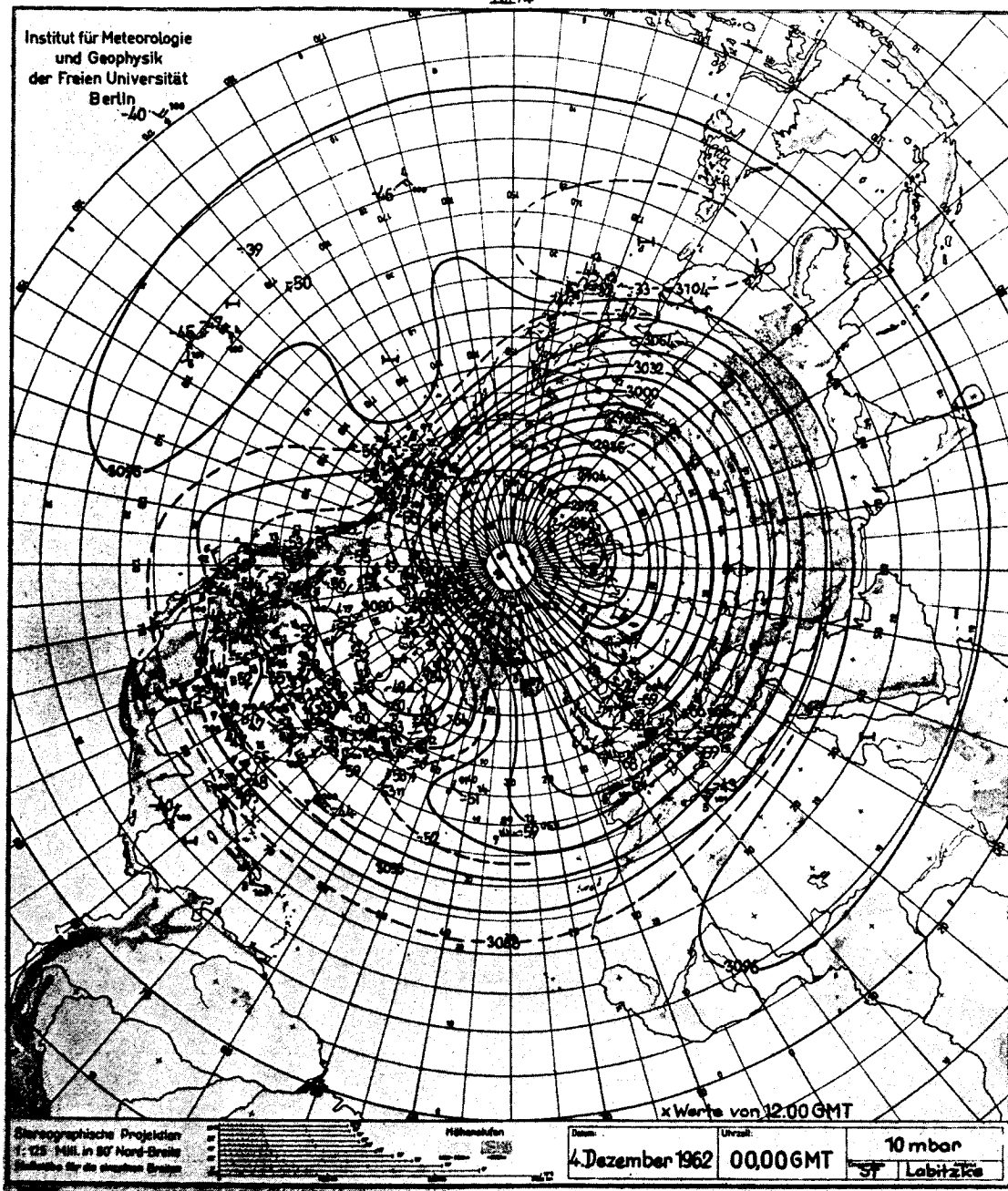


Figure 5—Stratospheric circulation (30 km), of the northern hemisphere, December 4, 1962 (Reference 13).

systems represent an eastwardly displaced Aleutian anticyclone that governed the Northern hemispheric circulation throughout November (Reference 14) and is still apparent at the 5 mb surface, which was constructed for December 5, 1962 (Figure 6). The 40 km pressure maps (Figure 7) show the pronounced trough over the Great Lakes area moving slowly southward, whereas the existence of the Canadian anticyclone is not necessarily indicated at this level. Its center may well have shifted to the Pacific region, Alaska and Canada being in the regime of the polar vortex. The anticyclone can still be observed ten kilometers higher (Figure 8), and here there is a definite indication that its center has shifted northward, causing a nearly northerly wind over Churchill on December 4th and a southwesterly wind over Alaska. Although the stream pattern remains essentially

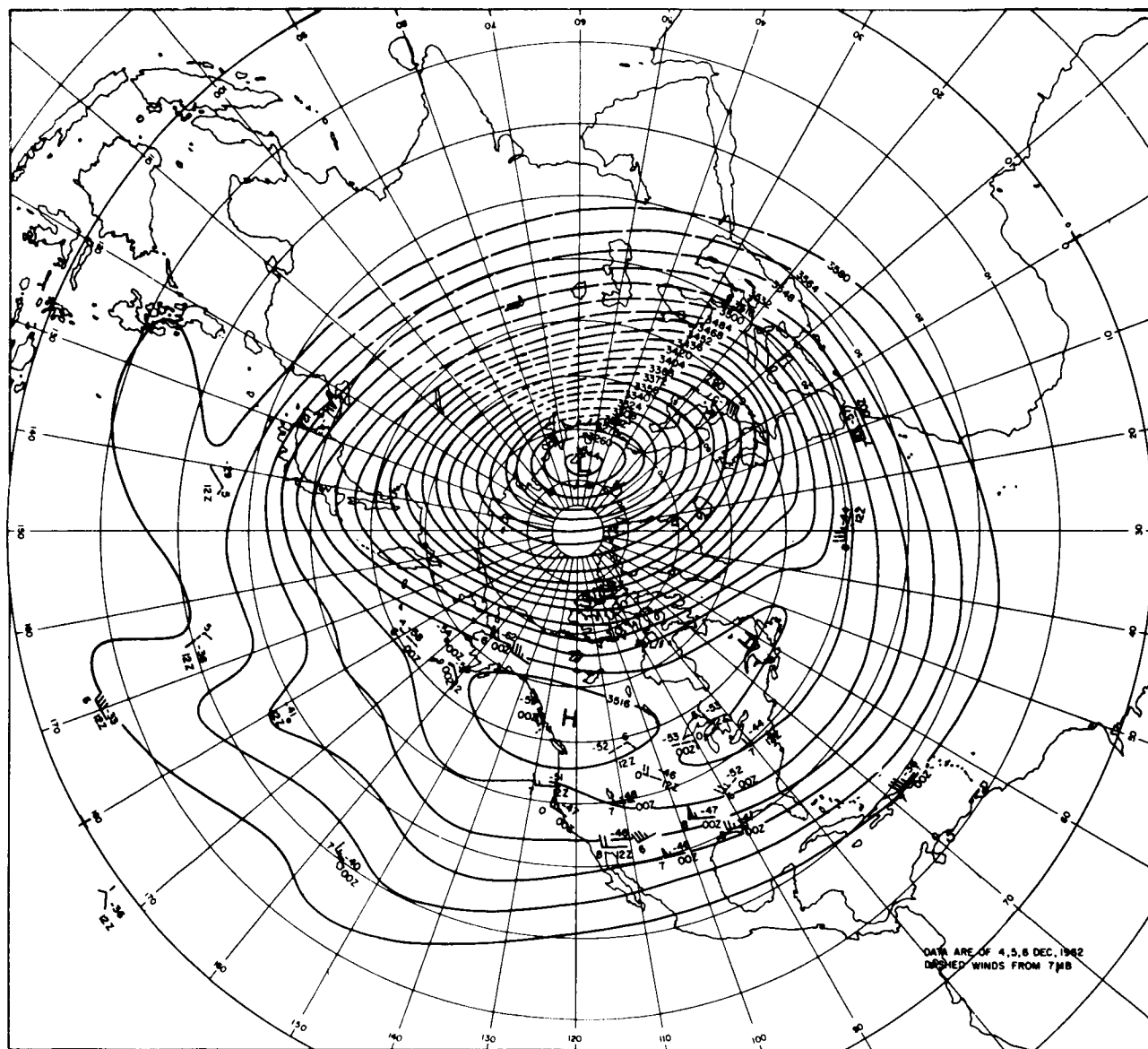
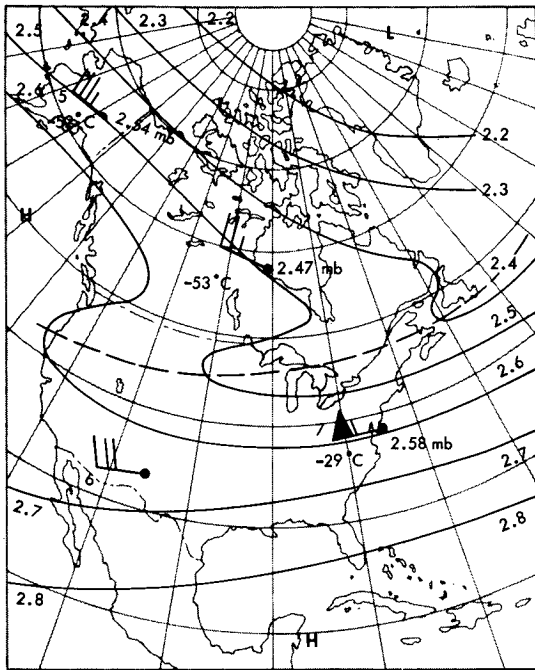
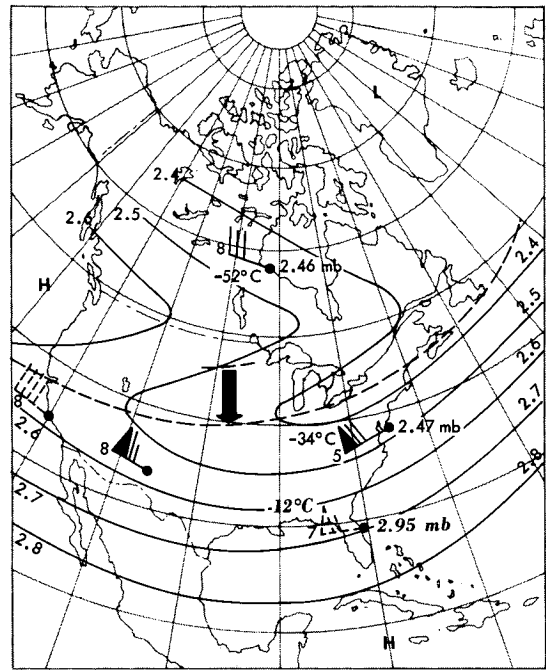


Figure 6—Stratospheric circulation (35 km) of the northern hemisphere, December 4-6.

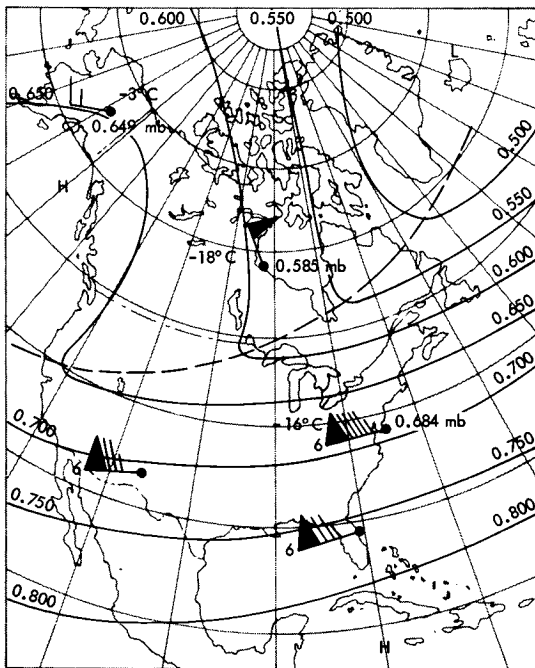


(a) 40 km, December 4, 1962 (Wallops Island data, December 1, 1962).

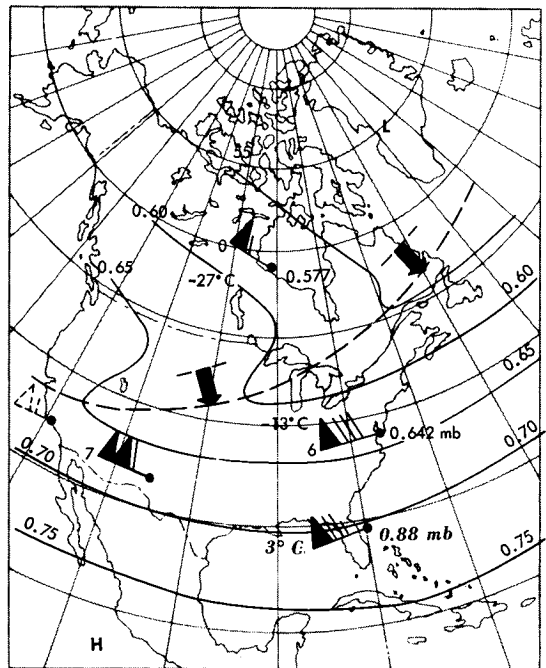


(b) 40 km, December 6, 1962 (Italics and dashed lines indicate data obtained on December 7, 1962).

Figure 7—Rocket measurements of wind (m/sec) and temperature (°C) over North America.



(a) 50 km, December 4, 1962.



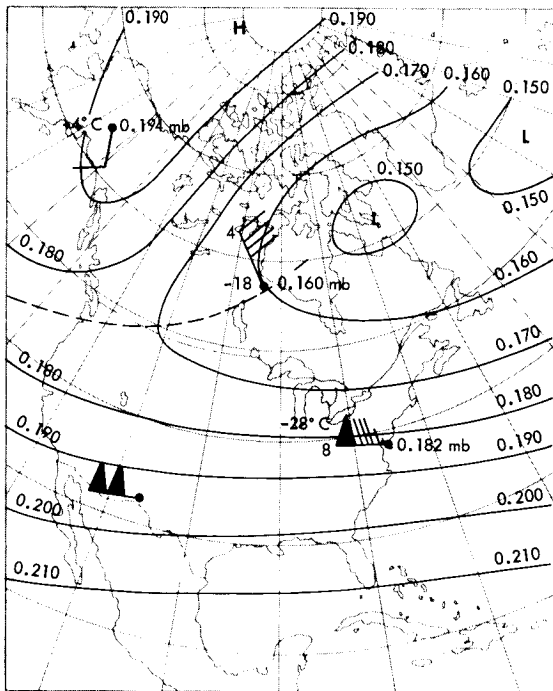
(b) 50 km, December 6, 1962 (Italics and dashed lines indicate data obtained on December 7, 1962).

Figure 8—Rocket measurements of wind (m/sec) and temperature (°C) over North America, showing trough.

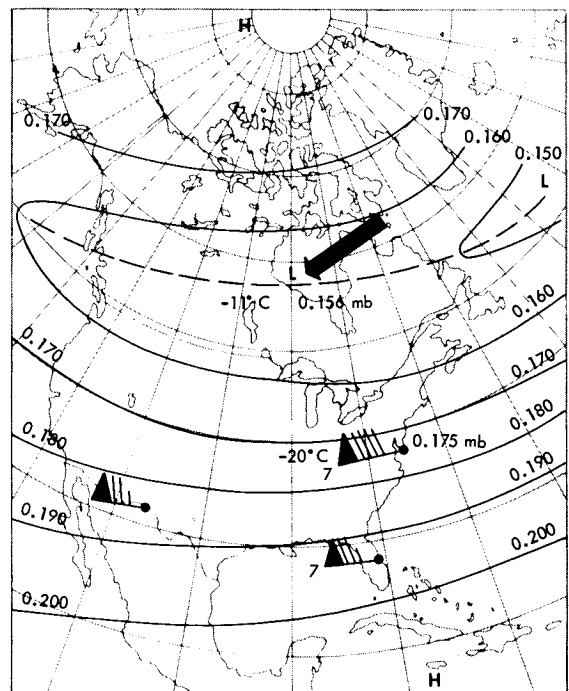
the same at 60 km (Figure 9), there is a distinct further shift in the position of the center of the anticyclone. It is apparently displaced toward the Arctic, as indicated by the southeasterly wind over Alaska. The pronounced trough, which has persisted at all altitude levels from 23 km up, is still located over southern Canada; and there is some indication that its vertical axis is slightly inclined to the north, such that at 60 km the trough has taken the position of the ridge in the stratosphere (20 to 35 km).

At 68 km (Figure 10) data are very sparse and are mainly based on grenade soundings at Churchill and Wallops Island. There is evidence that the zonally oriented trough over North America still exists, as indicated by strong winds from the west southwest over the United States and very light northwesterly wind inside the trough over Churchill on December 4, 1962. In general, it is interesting to note the alternation between low and high pressure systems on a vertical scale between the 30 and 60 km levels as shown in Figures 5 through 10. This seems to confirm the theoretical expectation of such alternations as previously expressed by Paetzold (Reference 15).

Differences in the flow and pressure patterns between December 4 and 6 were found to be insignificant at 40, 50, and 60 km. This is not surprising because the patterns in the stratosphere also remained nearly unchanged. At 68 km, however, a significant change seems to have taken place between December 4 and 6 over Churchill and between December 1 and 6 over Wallops Island.



(a) 60 km, December 4, 1962 (Wallops Island data, December 1, 1962).



(b) 60 km, December 6, 1962.

Figure 9—Rocket measurements of wind (m/sec) and temperature (°C) over North America.

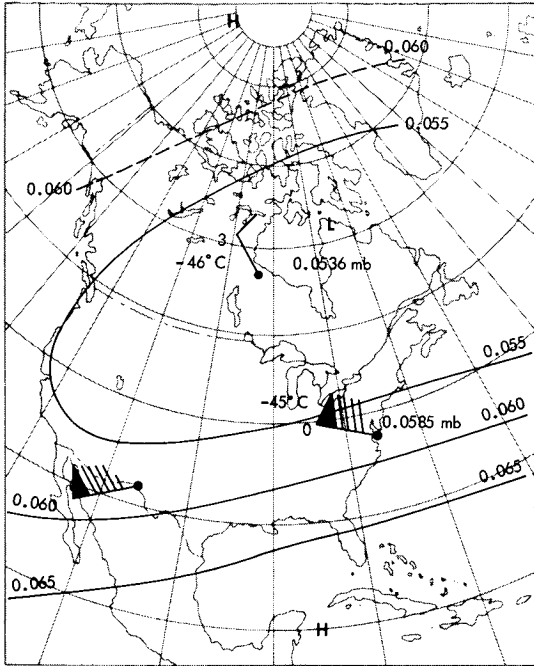


Figure 10a—Winds (m/sec) and temperature (°C) measured by rocket experiments at White Sands (66 km; December 4, 1962), Fort Churchill (70 km, December 4), and Wallops Island (68 km, December 1, 1962).

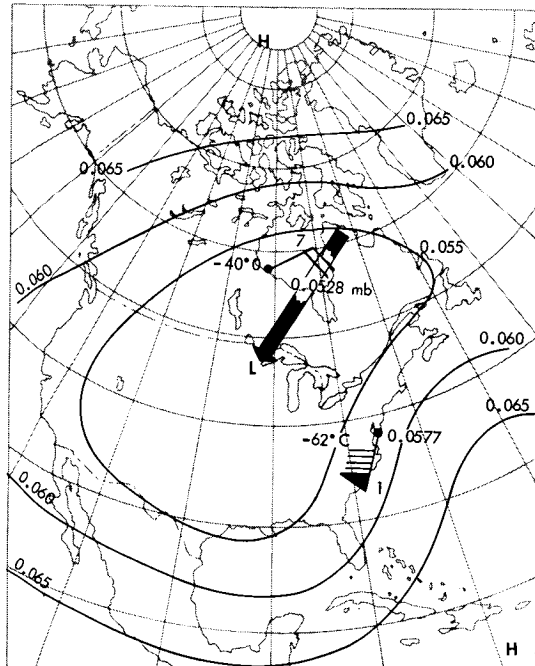


Figure 10b—Winds (m/sec) and temperature (°C) measured by rocket experiments at Wallops Island and Fort Churchill (68 km, December 6, 1962).

There is a 90° rotation of the wind vectors at both stations, but at Churchill this rotation is clockwise, while at Wallops Island it is counter clockwise. This may be interpreted as a southwestward motion of the low pressure system (Figures 10a and 10b).

Of course the sparsity of data permits only a very crude analysis even in this case, which could be considered well documented by rocket sounding standards. Nevertheless, this case shows that significant nonuniformities exist in the slopes of the constant pressure surfaces which are generally inclined downward toward the winter pole. If in the past such uniformity was assumed, it was only because the available data were not sufficient to observe any detail. It is to be expected that systematic rocket observations of the mesosphere extended over the hemisphere and spaced over distances in the order of 1000 km will reveal up to about 70 km circulation systems of similar variability and variety as observed at lower altitudes.

REFERENCES

1. Stroud, W. G., and Nordberg, W., "Seasonal, Latitudinal and Diurnal Variations in the Upper Atmosphere", NASA Technical Note D-703, April 1961.
2. Nordberg, W., and Smith, W., "Rocket Measurements of the Structure of the Upper Stratosphere and Mesosphere", *Meteorologische Abhandlungen* 36:391-397, 1963.

3. Nordberg, W., "Rocket Soundings in the Mesosphere", *Astronautics* 2(5):48-58, May 1964.
4. Miers, B. T., "Zonal Wind Reversal between 30 and 80 km over the Southwestern United States", *J. Atmos. Sci.* 20(2):87-93, March 1963.
5. Manring, M., et al., "An Experimentally Determined Model for the Periodic Character of Winds from 85 to 135 km", Geophysics Corporation of America Technical Rept. no. 63-27-N (Contract No. NAS W-712), November 1963.
6. Scherhag, R., "Eine erste synoptische Höhenwetterkarte der 0.5 mbar-Fläche", *Berliner Wetterkarte*, Beilage 33, May 1961.
7. Warnecke, G., "Eine synoptische Höhenwetterkarte für das 0.5 mbar-Niveau vom Sommer 1960", *Berliner Wetterkarte*, Beilage 37, May 1961.
8. Keegan, T. J., "Synoptic Patterns at 100,000 to 200,000 Feet," In: *Proceedings of the National Symposium on Winds for Aerospace Vehicle Design*, Air Force Cambridge Research Labs., Geophysics Research Directorate, Vol. II: 195-210, AFCRL-22-273, II; Also AF Surveys in Geophysics No. 140, March 1962.
9. Finger, F. G., and Teweles, S., "Synoptic Charts Based on Rocketsonde Data", *Meteorologische Abhandlungen*, 36:379-390, 1963.
10. Smith, W., Katchen, L., Sacher, P., Swartz, P., Theon, J., "Temperature, Pressure, Density and Wind Measurements with the Rocket Grenade Experiment, 1960-1963", Goddard Space Flight Center Document X-651-64-106, May 1964.
11. "Data Reports of the Meteorological Rocket Network", Finngs: Winter 1961-62-Finngs, Vol X ed. by Meteorological Rocket Network Committee, White Sands Missile Range, New Mexico; Inter-Range Instrumentation Group document 109-62, February 1962, December 1962.
12. Scherhag, R. et al., "Tägliche Höhenkarten der 100 mbar Fläche sowie monatliche Mittelkarten für das Jahr 1962", *Meteorologische Abhandlungen*, 23(4): X/1-X/31, October-December 1962.
13. Scherhag, R. et al., "Preliminary Daily Northern Hemisphere 30 mbar Synoptic Weather Maps of the Year 1962", *Meteorologische Abhandlungen*, 25(4): X/1-X11/31, October-December 1962.
14. Scherhag, R. et al., "Preliminary Daily Northern Hemisphere 10 mbar Synoptic Weather Maps of the year 1962", *Meteorologische Abhandlungen*, 26(4).
15. Paetzold, H. K., "On the Problem of Solar Activity Effects on the Lower Terrestrial Atmosphere", *Meteorologische Abhandlungen*, 36 353-363, 1963.

N65-29552

STRATOSPHERIC TEMPERATURE PATTERNS BASED ON RADIOMETRIC MEASUREMENTS FROM THE TIROS VII SATELLITE

by

W. Nordberg, W. R. Bandeen,

G. Warnecke*, V. Kunde

Goddard Space Flight Center

SUMMARY

29552

The TIROS VII meteorological satellite carried a sensor to map the emitted terrestrial radiation in the 15μ carbon dioxide band. The spectral response of the sensor ranged from 14.8 to 15.5μ . The radiation observed by the satellite is a function of the temperatures of the atmosphere varying along the optical path. Atmospheric layers at various altitudes contribute to the observed radiation in varying amounts. More than 96 percent of this contribution stems from altitudes above 10 km and more than 60 percent from a layer ranging in altitude from 18 to 35 km; thus, the radiation measurements were interpreted in terms of average temperatures of a major portion of the stratosphere.

Temperature patterns were analyzed from June 1963 to March 1964. The measurements demonstrate on a global scale the varying patterns of stratospheric temperatures and circulation. Smooth temperature gradients were found to coincide closely with latitudinal circles on both summer hemispheres. Temperatures increased at high latitudes toward the summer pole (250°K) and rapidly decreased toward the winter pole (200°K).

A fairly uniform region with temperatures generally around 230°K extended between 25° latitude of the summer hemisphere and 40° latitude of the winter hemisphere during solstices. During both equinoxes, the large latitudinal temperature gradients at high latitudes disappeared and differences of about $10\text{--}15^{\circ}\text{K}$ existed with latitudes as well as with longitude. Winter temperature patterns in both hemispheres exhibited strong temperature gradients between the pole and 40° , but a completely uniform pattern never existed in either winter hemisphere. A warm area over the Indian Ocean, though initially small, seemed to play a similar role in the southern winter as the Aleutian warm center during the northern winter. The morphology of a stratospheric warming which occurred over southwestern Asia and penetrated to Europe immediately after the tropical belt had cooled by about 10°K was observed.

Auth

*NAS-NRC Research Associate; on leave from Institut für Meteorologie und Geophysik der Freien Universität Berlin, Berlin, Germany.

INTRODUCTION

A radiometer aboard the Tiros VII satellite measured infrared radiation, emitted mainly by carbon dioxide, in the earth's atmosphere at wavelengths ranging from 14.8 to 15.5 μ . The instrument used in these measurements was very similar to the 5-channel radiometers flown on previous Tiros satellites and described by Bandeen, et al. (Reference 1) except that one of the optical channels was modified to have a spectral response as shown in Figure 1a. The initial objective of radiation measurements in this region of the spectrum was to study the characteristics of the earth's

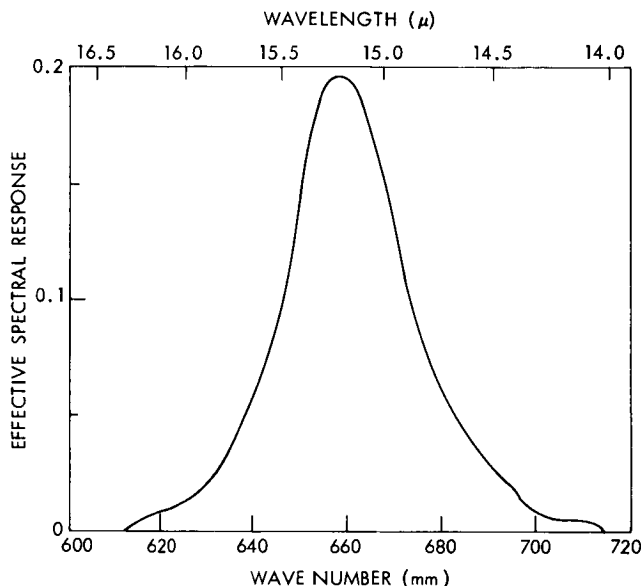


Figure 1a—Effective spectral response of the Tiros VII 15 μ channel as a function of wavelength.

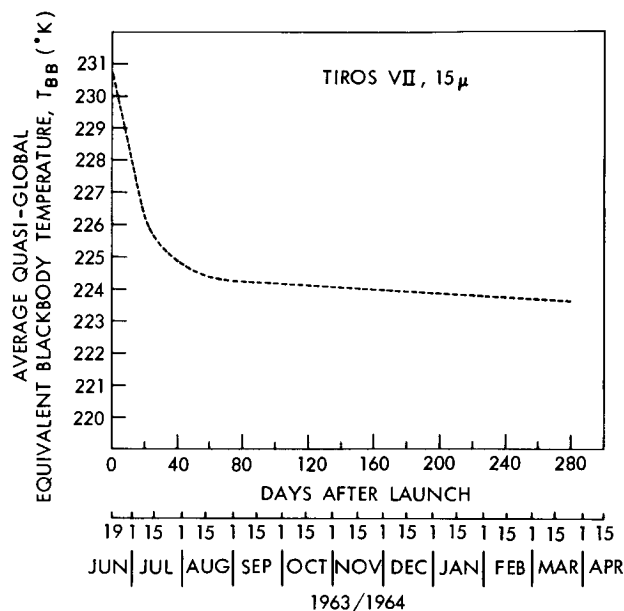


Figure 1b—Average quasi-global equivalent blackbody temperatures versus time. The heavy dashed curve indicates the derived apparent degradation in the instrumental response.

horizon as described by Hanel, et al. (Reference 2) and later reported by Bandeen, et al. (Reference 3). Now with continuous observations over a period of more than six months, daily covering the global zone from 65°N to 65°S, it is possible to use the radiation measurements to describe a number of interesting features of the atmosphere. It will be shown that most of the radiation reaching the satellite in this spectral region is emitted within a defined altitude interval in the stratosphere whose average temperature can be derived from the observed radiation intensities. Quasi-global maps of these average temperatures for different seasons not only reflect the expected variations in the mean stratospheric temperatures, but also reveal the development and behavior of major synoptic systems in that region of the atmosphere. A complete description of the 5-channel radiation experiment on Tiros VII as well as a critique and summary of all data resulting from this experiment will be contained in the Tiros VII Radiation Data Catalog and Users' Manual (Reference 4).

RELATION BETWEEN RADIATION AND STRATOSPHERIC TEMPERATURES

The spectral response of the instrument was chosen to coincide as closely as possible with the 15μ absorption band of carbon dioxide. The radiance \bar{N} from the earth and atmosphere measured by the radiometer, whose spectral response function $\phi(\lambda)$ is shown in Figure 1a, can be expressed as:

$$\bar{N} = \frac{1}{\pi} \int_{s=0}^{\infty} \int_{\lambda=\lambda_1}^{\lambda_2} \phi(\lambda) B(\lambda, T) \frac{\partial \tau}{\partial s} (\rho, p, T, \lambda) d\lambda ds, \quad (1)$$

where ρ is the carbon dioxide density, B the Planck function, s the distance along radiation path, λ_1 and λ_2 the wavelengths between which $\phi \neq 0$, p the atmospheric pressure, T the atmospheric temperature, and τ the atmospheric beam transmissivity. It is reasonable to assume that a constant ratio, $r = 0.000471$, exists between the densities ρ (for carbon dioxide) and ρ_{air} for air: $\rho = r \rho_{air}$. Furthermore, a number of typical distributions of temperature with height h for surface pressures of 1013.25 mb were chosen so that ρ_{air} , p , and T could be expressed as functions of h , where ρ_{air} and p were computed as a function of h from T by the hydrostatic equation. A relationship between s and h , $s = s(h)$ was established through the choice of several angles at which the satellite viewed the earth from approximately 635 km. The integration of Equation 1 over λ was then performed for seven nadir angles: 0° , 29.2° , 39.7° , 46.7° , 51.7° , 55.3° , and 58° . The function $\tau(\lambda, h)$ was then determined using, in principle, the method described by Hanel, et al. (Reference 2). That method is based on the general treatment by Elsasser (Reference 5) of the absorption within the 15μ CO_2 band. Thus

$$\int_{\lambda_1}^{\lambda_2} \phi(\lambda) B(h, \lambda) \frac{\partial \tau}{\partial s} (h, \lambda) \frac{\partial s}{\partial h} d\lambda = \psi(h). \quad (2)$$

Hence

$$\bar{N} = \frac{1}{\pi} \int_0^{\infty} \psi(h) dh. \quad (3)$$

N was then computed from Equation 3 for each of the assumed temperature profiles and for each nadir angle. The assumed temperature distributions with height and the resulting distribution functions $\psi(h)$ are shown in Figure 2. In accordance with previous practices of reporting Tiros radiation measurements (References 6, 7, and 8), \bar{N} may be expressed by the temperature T_{BB} of a blackbody whose radiant emittance \bar{W} is given by

$$\bar{W} = \int_{\lambda_1}^{\lambda_2} \phi(\lambda) B(T_{BB}, \lambda) d\lambda = \pi \bar{N}. \quad (4)$$

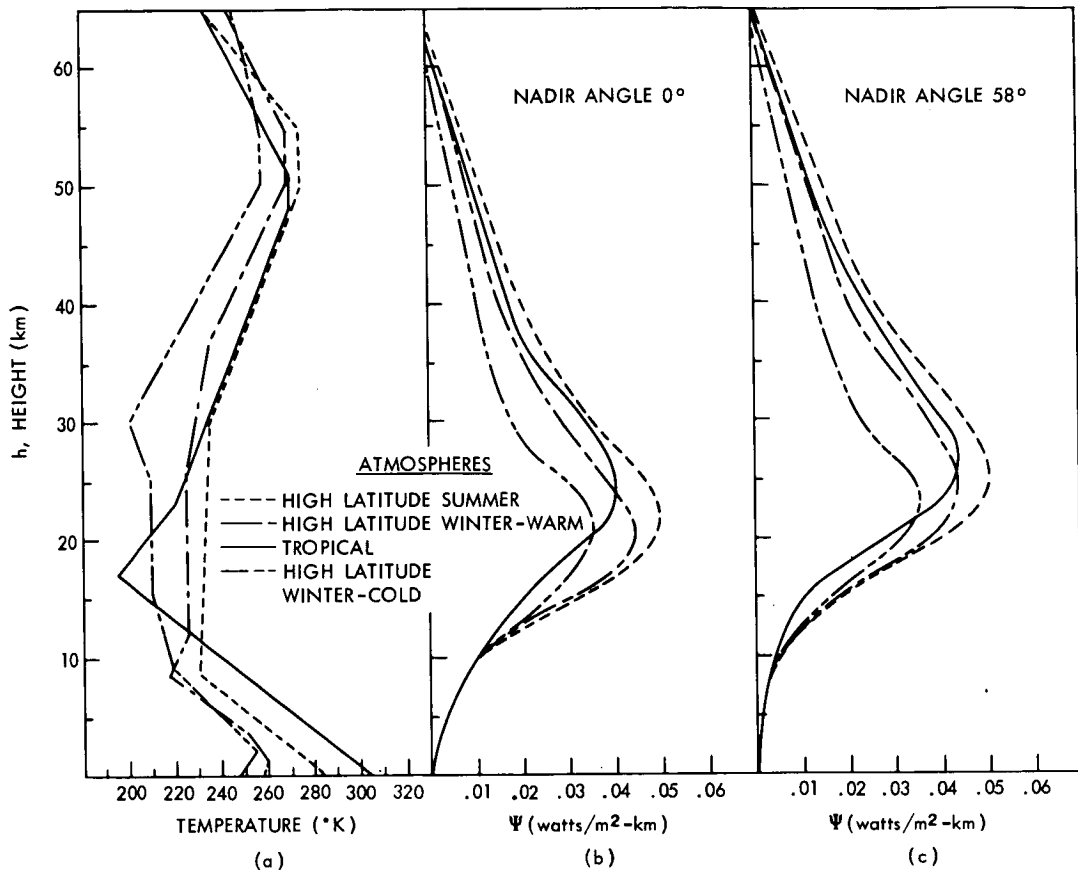


Figure 2—(a) Typical temperature profiles based on proposed supplements to the "U. S. Standard Atmosphere 1962" for 60° North summer, 60° North winter (warm and cold) and 15° North. The "warm" and "cold" temperature profiles for 60°N ("high latitude winter") can be considered typical at these latitudes depending on the state of the stratosphere in these regions. The supplements to the U. S. Standard Atmosphere 1962 are in the process of preparation by the U. S. Committee for Extension of the Standard Atmosphere and were summarized by Cole in Reference 16. (b) Weighting functions $\psi(h)$, applying to the measured outgoing radiance \bar{N} ; nadir angle = 0°. (c) Weighting functions, $\psi(h)$, applying to the measured outgoing radiance \bar{N} ; nadir angle = 58°.

Indeed, since the radiometers were calibrated using blackbodies at various temperatures, the measurement of T_{BB} may be considered as the primary quantity while \bar{N} is derived from Equation 4. The values of T_{BB} corresponding to the temperature profiles of Figure 2a are summarized in Table 1 (page 26).

The radiation measurement expressed by T_{BB} thus represents a mean temperature of the atmosphere in which the vertical temperature distribution is open to choice and where the temperature at each altitude must be given a different weight with regard to its contribution to the measured mean. The weighting function is given by $\psi(h)$ (Figures 2b and 2c), and although $\psi(h)$ depends to a certain degree on the assumed vertical temperature profile, it may be seen that for most realistic temperature profiles at a nadir angle $\eta = 0$; temperatures between 20 and 25 km are weighed most heavily with about 65 percent of the weight being concentrated in the region

from 15 to 35 km and more than 96 percent of the weight lying at altitudes above 10 km, (Figure 2b). It may also be seen from Figure 2c that the maximum weight shifts to somewhat higher altitudes with increasing nadir angle. But, since this shift amounts to less than 5 km from $\eta = 0$ to $\eta = 58^\circ$, it is not possible to make a precise quantitative determination of the variation of temperature with altitude from measurements of T_{BB} at various nadir angles. However, we shall show that we may infer qualitatively from such measurements whether the temperature is increasing, decreasing, or constant with height over the altitude range where the ψ functions reach their maxima. Furthermore, with a prudent and realistic choice of assumed vertical temperature profiles, such as shown in Figures 2a, we can easily determine from the T_{BB} measurements which profile represents the best fit qualitatively to actual conditions at a certain location on the globe; and, more important, we may determine from continuous observations how the choices of such "best fits" vary with time. Thus, the maps of T_{BB} measurements plotted for the "quasi-global" (65°N to 65°S) zone for different times of the year (presented in Figures 3-12), enable the synoptic analysis of phenomena related to the temperature structure in the stratosphere between about 15 and 35 km. The occurrence of such events as explosive warmings, the establishment of the Aleutian anticyclone in winter, the onset of the seasonal circulation reversals and similar events may be categorized as such phenomena. Although the Tiros VII radiometer views the entire global zone from 65°N to 65°S during the course of 12 hours, data from only about 60 percent of the orbits during any one day can be acquired because only stations within the United States are capable of receiving the data which are stored aboard the satellite for no longer than one orbital period. This causes two significant gaps in the data displayed in the maps, Figures 3-12. One such gap exists at 90°W just off the west coast of South America, the other is at 90°E over the central Soviet Union.

As will be stated in the Tiros VII Radiation Data Catalog and Users' Manual (Reference 4) the precision of each individual measurement is probably not much better than $\pm 3^\circ\text{K}$. However, we may assume that the physical properties of the stratosphere remain generally constant for several days and are uniform over distances of less than 500 km. Since the field of view of the radiometer is about 5 degrees, covering an area of about 50×50 km on the surface of the earth for small nadir angles, and since in general measurements for the entire quasi-globe are obtained at least once every 24 hours up to about 1000 measurements may result within one week over an area of about 500×500 km. Therefore, a precision of better than 1°K can be estimated for the temperature values shown in the maps (Figures 3 through 9, 11 and 12) which were obtained by averaging measurements within each grid element (ranging from 5° latitude \times 5° longitude at the equator to 2.5° latitude \times 5° longitude at 60° latitude) over the period of one week.

Although the precision of the temperature measurement is greatly enhanced by reducing the random error in the averaging process, there are a number of systematic errors which must be considered. Attempts have been made to reduce these errors by applying the appropriate corrections, but uncertainties still remain and, cause the overall accuracy to be considerably poorer than the fraction of 1°K stated for the precision. Aside from correcting for an instrumental degradation which will be discussed later, a correction was applied to the data for an as yet unexplained deviation from the original preflight calibration. The radiometer, which alternately views the earth through one of two viewing ports showed that a consistently lower response on one

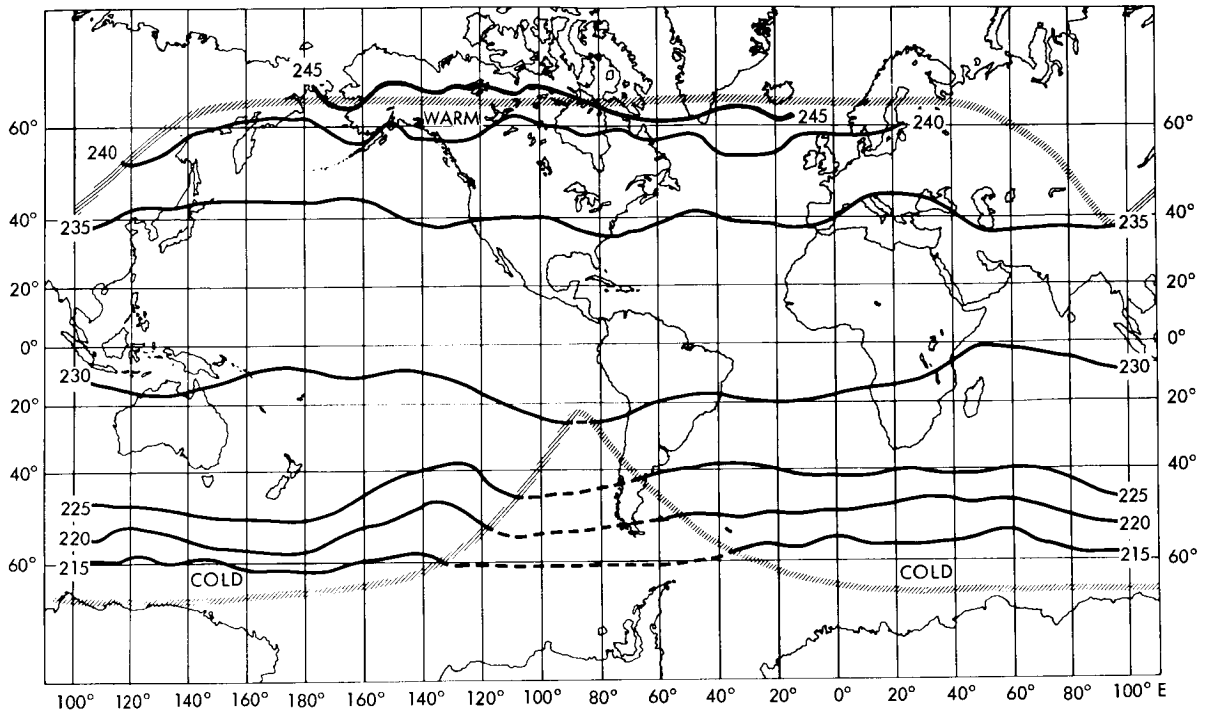


Figure 3a—Quasi-global map of 15 μ equivalent blackbody temperatures averaged over the week 19-25 June 1963; nadir angle 0°-40°.

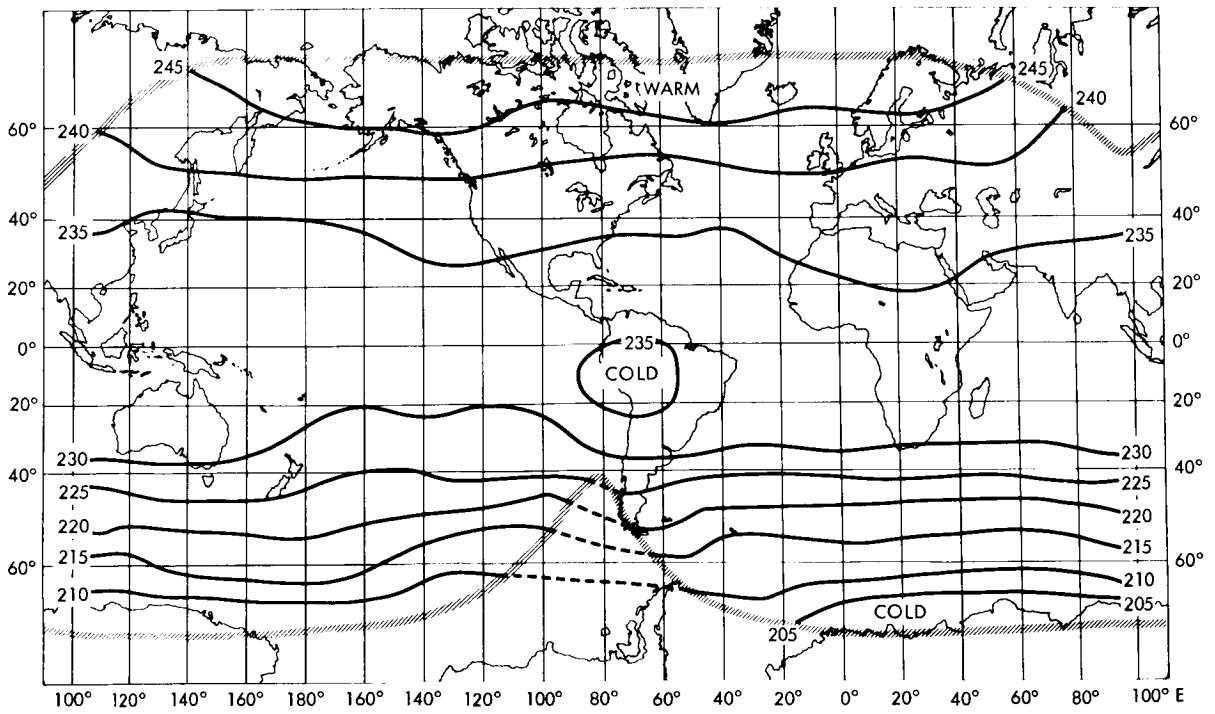


Figure 3b—Quasi-global map of 15 μ equivalent blackbody temperatures averaged over the week 19-25 June 1963; nadir angle 52°-58°.

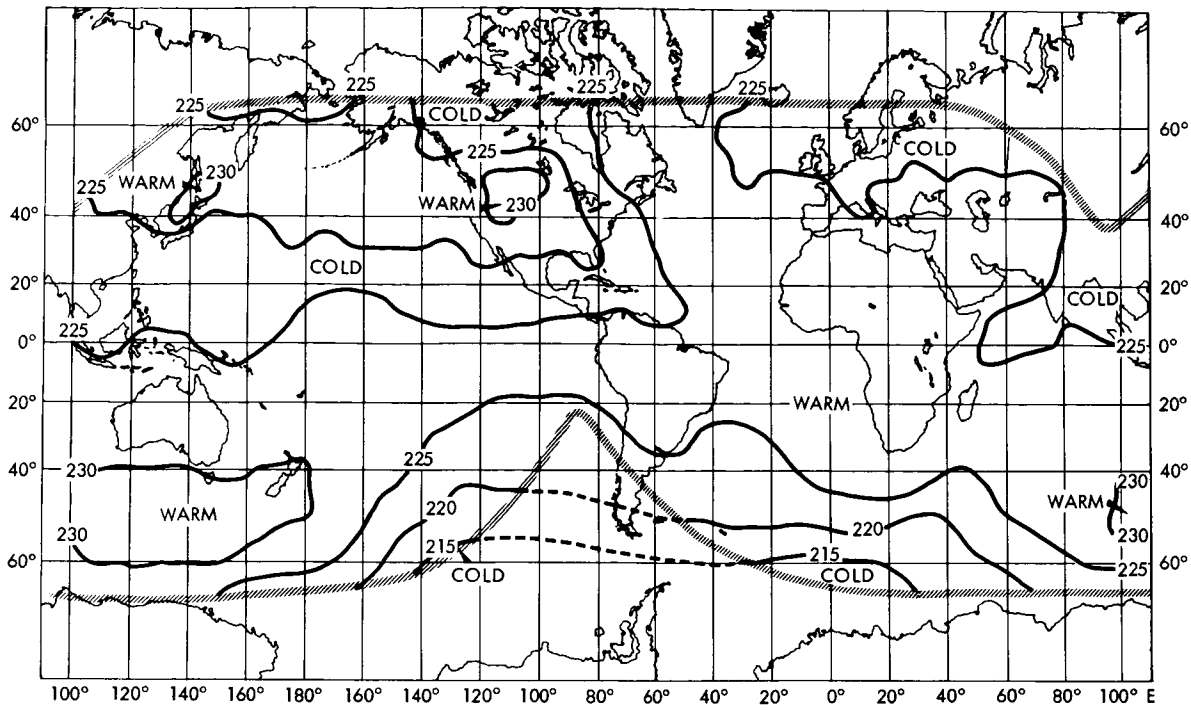


Figure 4—Quasi-global map of 15μ equivalent blackbody temperatures averaged over the week 11-18 September 1963; nadir angle 0°-40° .

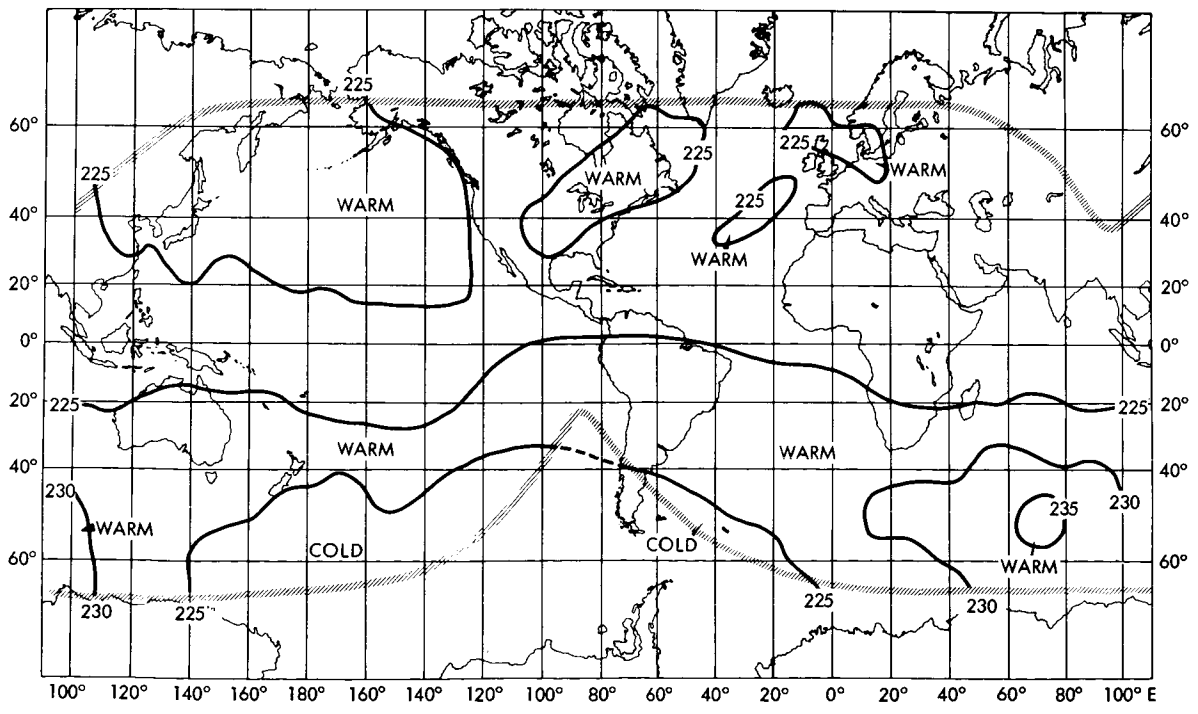


Figure 5—Quasi-global map of 15μ equivalent blackbody temperatures averaged over the week 25 September - 1 October 1963; nadir angle 0°-40° .

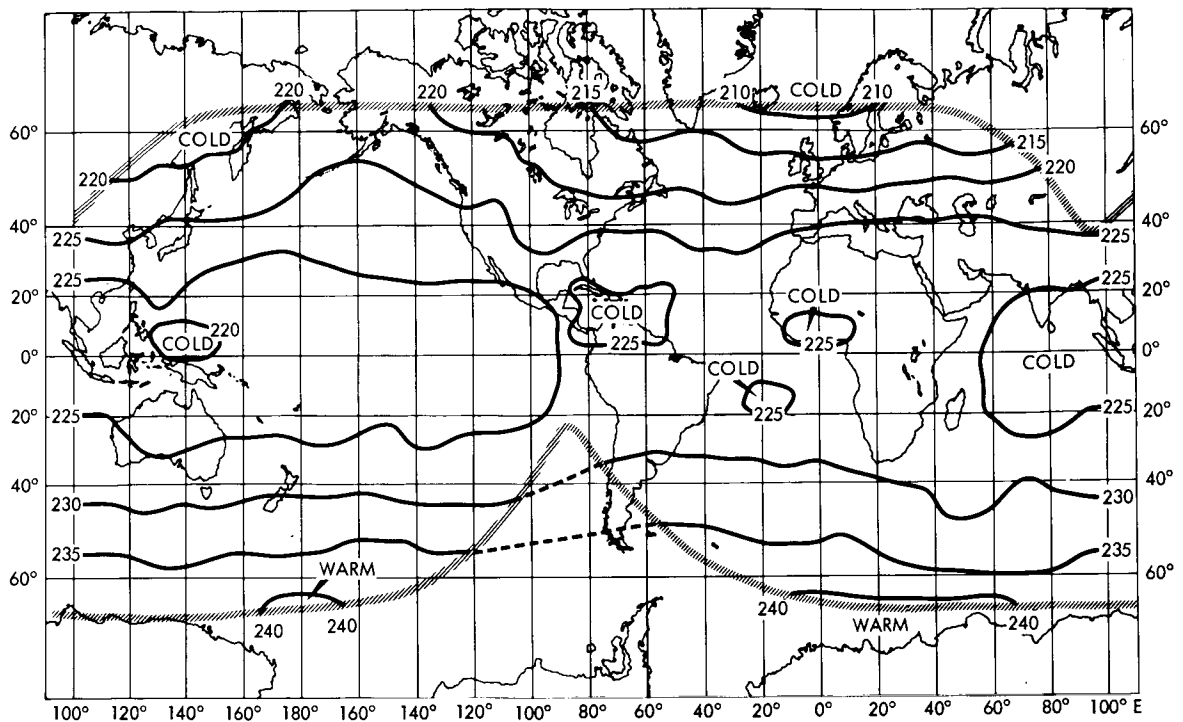


Figure 6—Quasi-global map of 15μ equivalent blackbody temperatures averaged over the week 20-26 November 1963; nadir angle 0° - 40° .

of these viewing ports with respect to the other was apparently causing half of the measured temperatures to be too low and half to be too high. According to the preflight calibration, there should be no such difference. For lack of a better correction procedure, the difference between the temperatures measured through the two viewing ports over the same area at the same time were determined for all cases shown in the maps. (Figures 3 through 12). Temperatures for the lower side were then corrected upward by half this difference, while those for the higher side were corrected downward by the same amount. Total differences were generally 5° to 8°K , so that the corrections were in the order of 2.5° to 4°K .

The maps were prepared from the magnetic tapes (FMRT's) containing all the Tiros VII radiation data (Reference 4) by an IBM 7094 computer and contour lines were drawn manually. This mapping procedure was the same as the one used on similar maps published previously (Reference 9).

ANALYSIS OF STRATOSPHERIC TEMPERATURES, JUNE 1963 TO MARCH 1964

Solstice - June 1963

A typical temperature pattern at the start of the northern hemisphere summer and southern hemisphere winter for the quasi-globe is shown in Figure 3a. Stratospheric mean temperatures

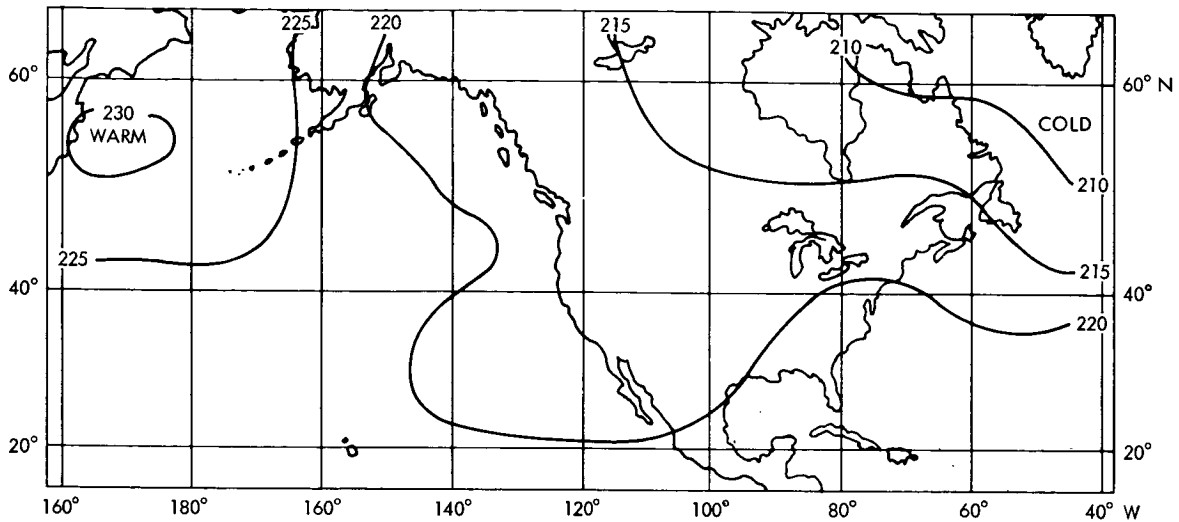


Figure 7a—Map from the North Pacific to the North Atlantic of 15μ equivalent blackbody temperatures averaged over the week 12-15 December 1963; nadir angle 0° - 40° .

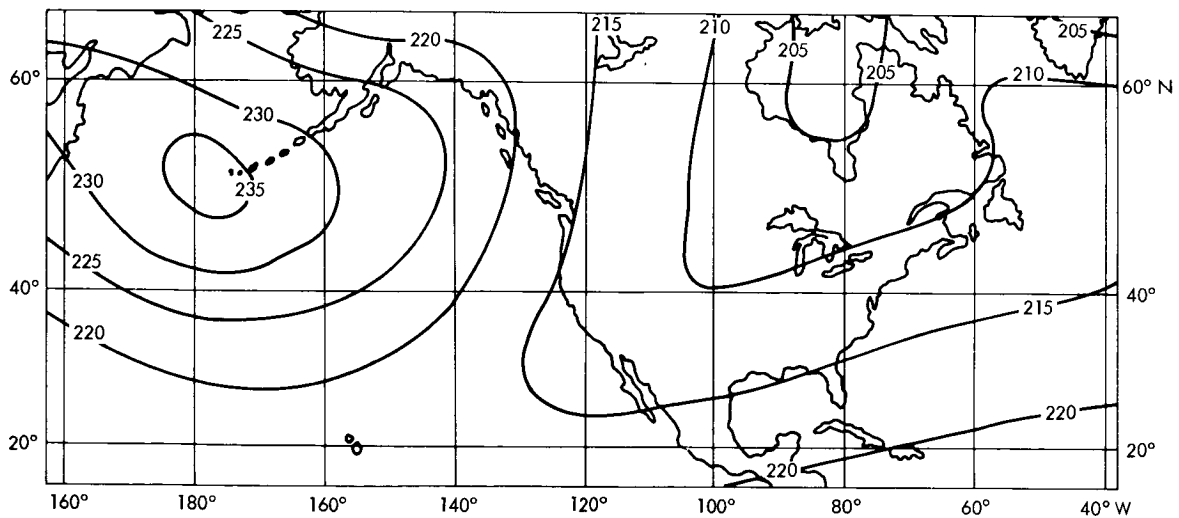


Figure 7b—Map from the North Pacific to the North Atlantic of 30 mb air temperatures measured by radiosonde balloons averaged over the week 5-12 December 1963 (data from stratospheric analysis charts, Institut für Meteorologie und Geophysik, der Freien Universität Berlin).

were averaged over nadir angles between 0° and 40° and averaged over the week from 19 June to 25 June, the first week's operation of Tiros VII, and range from 240°K near 60°N to 215°K near 60°S . The generally zonal structure of the temperature pattern, with isotherms running practically parallel to latitude circles, confirmed the established knowledge of the physics of the lower stratosphere; namely, the existence of a very strong cyclonic circulation system around a low pressure core centered near the winter pole. This low pressure was caused by the intense cooling of the

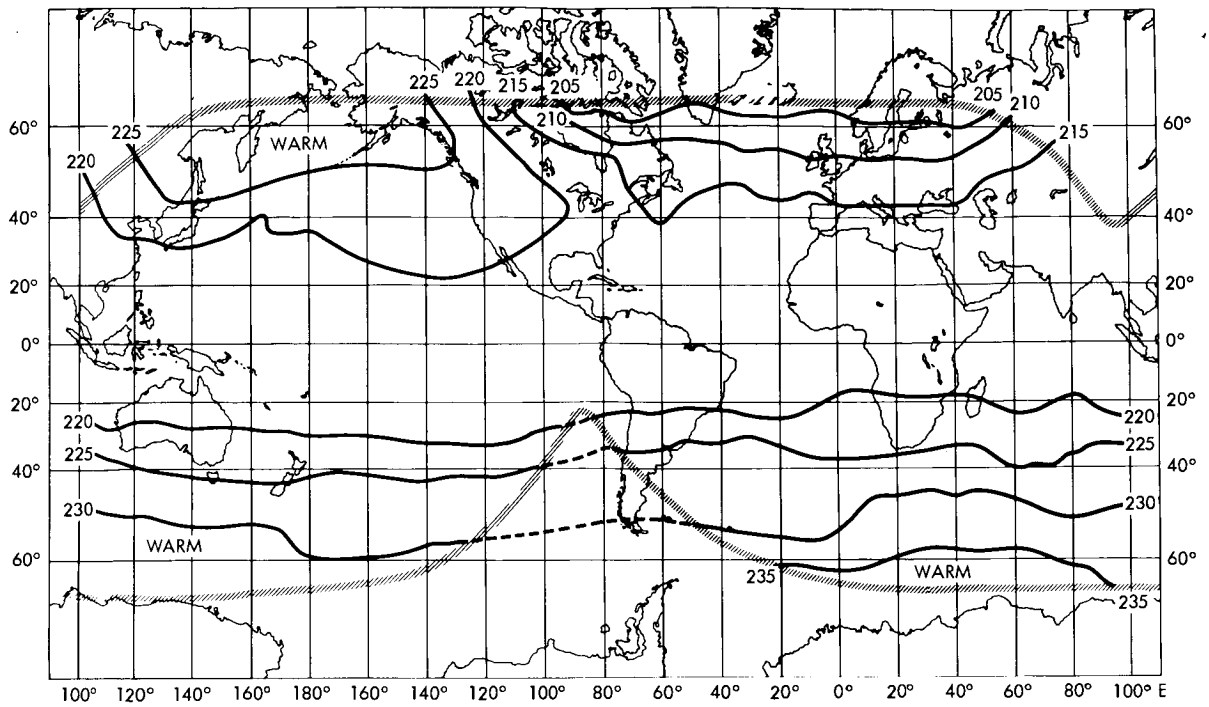


Figure 8a—Quasi-global map of 15μ equivalent blackbody temperatures averaged over the week of 15-22 January 1964; nadir angle $0-40^\circ$.

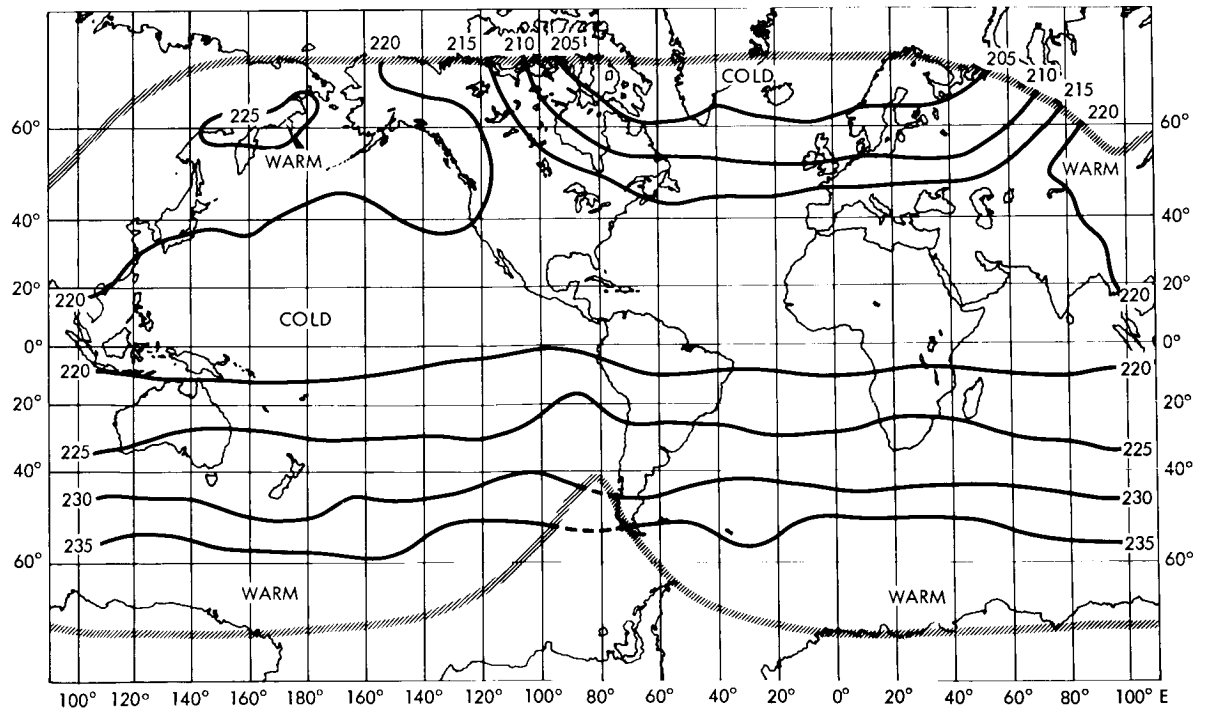


Figure 8b—Quasi-global map of 15μ equivalent blackbody temperatures averaged over the week 15-22 January, 1964; nadir angle $52-58^\circ$.

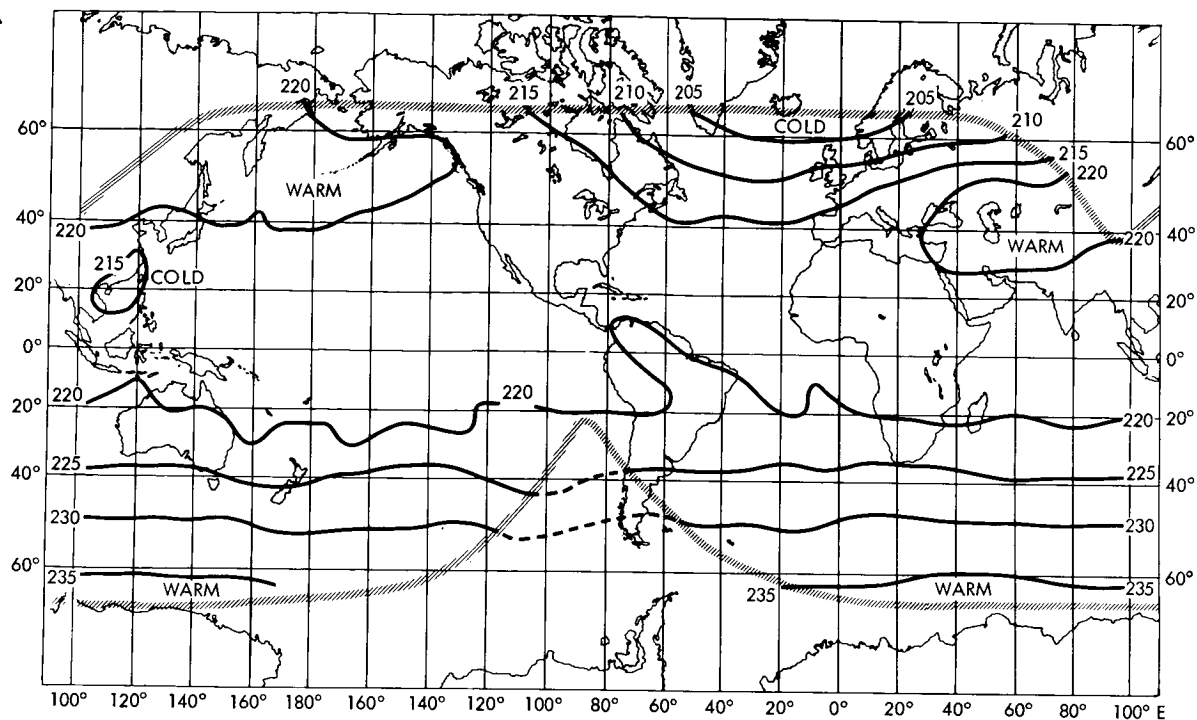


Figure 9a—Quasi-global map of 15μ equivalent blackbody temperatures averaged over the week 22-29 January, 1964; nadir angle 0° - 40° .

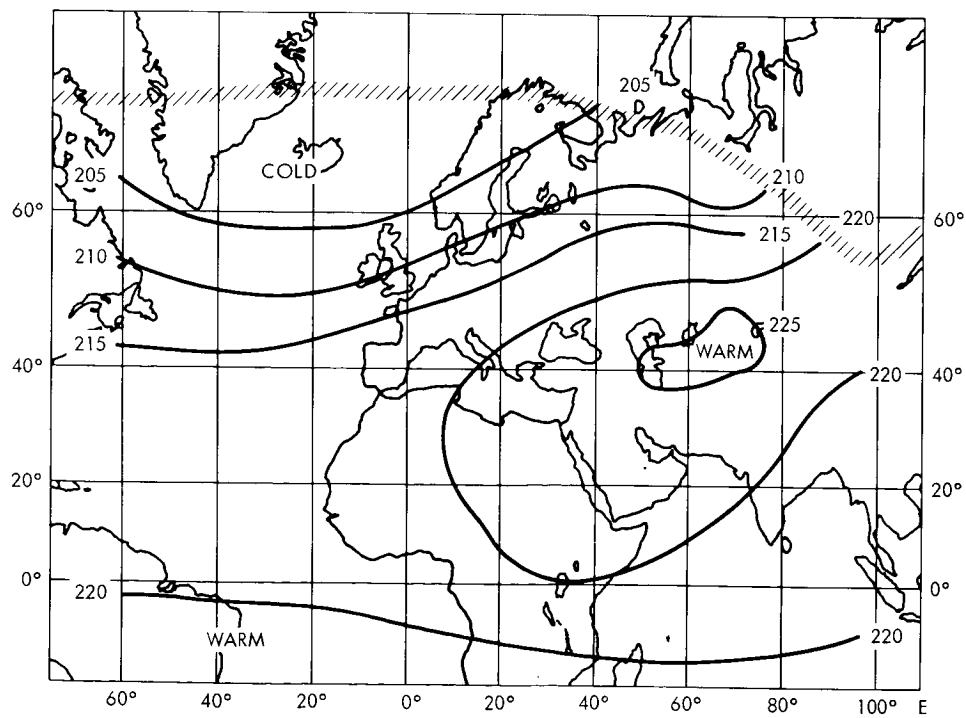


Figure 9b—Regional map of 15μ equivalent blackbody temperatures averaged over the week 22-29 January 1964; nadir angle 52° - 58° . The effects of a stratospheric warming over Eastern Europe are illustrated. No essential change in the temperatures occurred in other areas of the quasi-globe relative to Figure 8b.

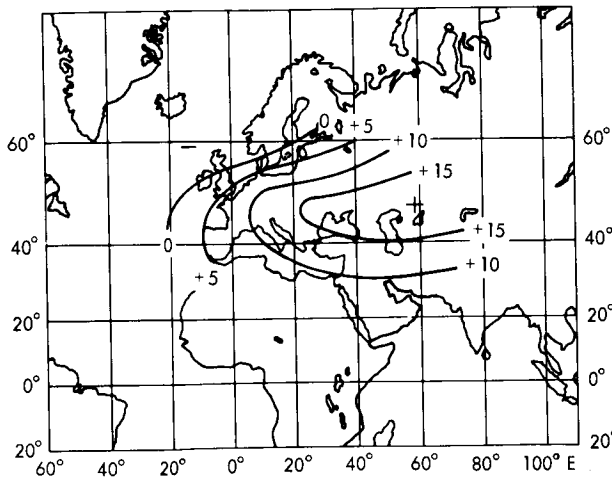


Figure 10—Regional map of the differences between the 15μ equivalent blackbody temperatures measured on 27 January 1964 and those averaged over the week 9-15 January; nadir angle 0° - 40° . The effects of a stratospheric warming over Eastern Europe are illustrated.

to a latitude of about 15° N. From there to the summer pole, the temperature increased gradually, and the gradients were not as steep as over the winter hemisphere. This confirmed the expectation that the winter cyclone is considerably stronger than the summer anticyclone. The measured mean temperatures of 215° K near 60° S and of 240° K near 60° N agree reasonably well with the computed values of 213° K and 238° K, respectively (Table 1), for the temperature profiles for the high latitude cold winter and summer shown in Figure 2a. The measured temperatures of 230° K within the belt 40° S to 25° N are 3° K higher than those computed (Table 1) for the tropical temperature profile shown in Figure 2a. This disagreement with the computation seems to be consistent with the cases at 60° N and 60° S where the measured temperatures were 2° K too high. The reason for this consistent discrepancy could be due to a number of assumptions contained in the radiative transfer calculations, which could have resulted in computed values of T_{BB} (Table 1) being several degrees too low.

A course picture of the temperature gradient with altitude can be obtained by comparing Figures 3a and 3b. In Figure 3b, temperatures measured at nadir angles between 52° and 58° were plotted. The weighting functions in Figures 2b and 2c show that all measurements shown in Figure 3b reflect temperatures at altitudes approximately 3-4 km higher than the temperatures shown in Figure 3a. Thus, by comparing Figures 3a and 3b, we may distinguish three categories in the temperature profiles:

1. Increasing temperatures with altitude between 15 and 35 km where the measured temperature differences are positive
2. Decreasing temperatures with altitude between 15 and 35 km where negative differences are measured; and
3. Isothermal regions between 15 and 35 km if the differences are close to zero.

stratosphere over the winter pole. Conversely, anticyclonic circulation prevailed over the summer pole where solar heating caused the warm stratosphere resulting in a high pressure system. The predominantly zonal isotherms at high northern latitudes (summer) suggest that solar heating was primarily responsible for this pattern. At high southern latitudes (winter) however, there are slight but apparently significant disturbances in this zonal pattern. Isotherms over the South Pacific between 30° S and 60° S deviated from a perfect zonal course, and showed a definite slope from southwest to northeast. Temperatures increased rapidly from the winter pole toward the equator causing very steep temperature gradients with latitude in the winter hemisphere. A temperature of about 230° K was reached near 20° S. This temperature prevails over the tropical region

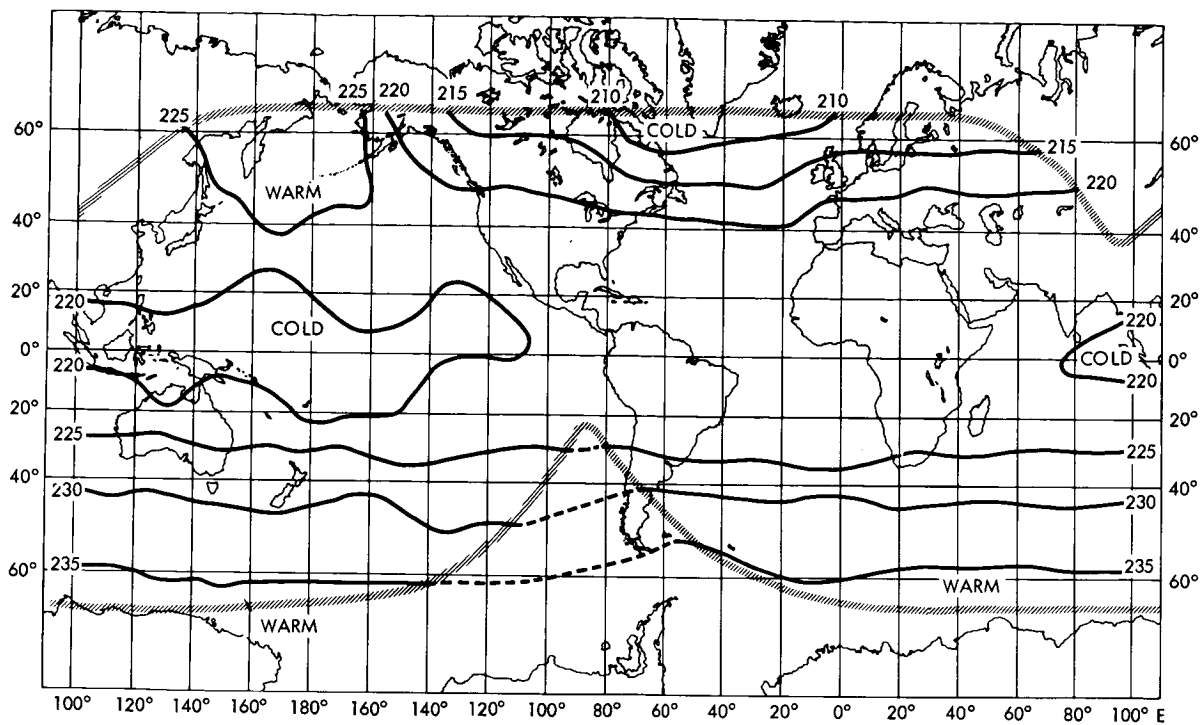


Figure 11a—Quasi-global map of 15 μ equivalent blackbody temperatures averaged over the week 31 January - 8 February 1964; nadir angle 0°-40°.

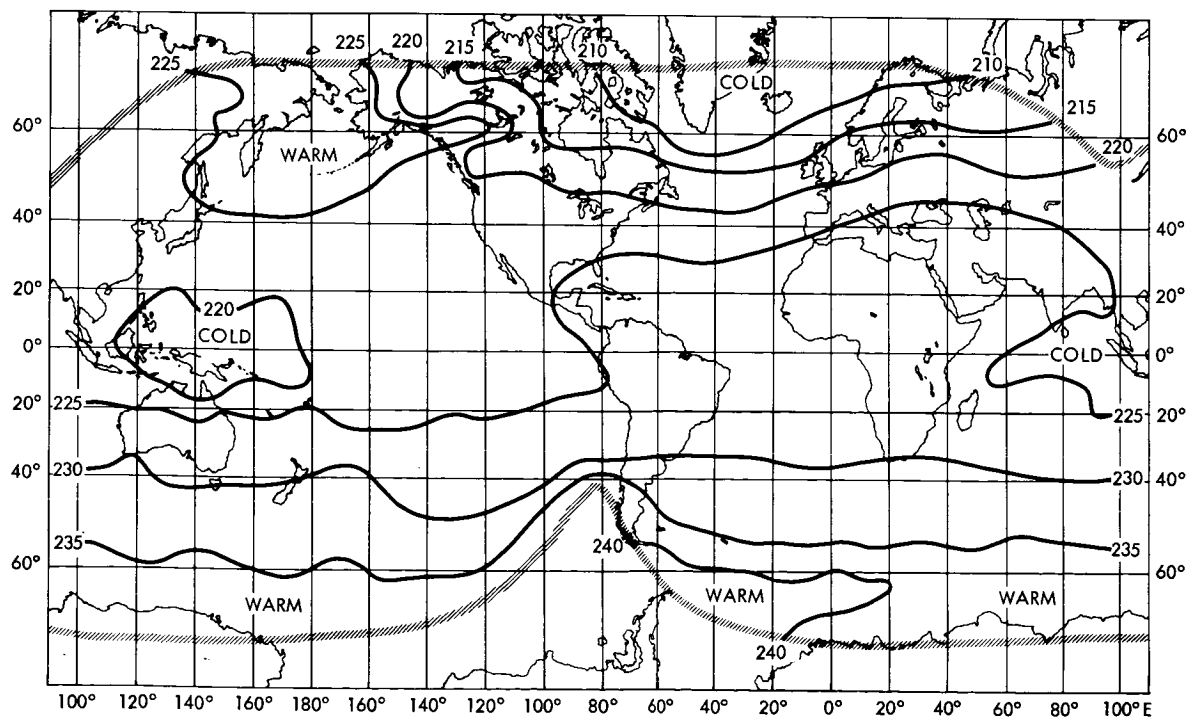


Figure 11b—Quasi-global map of 15 μ equivalent blackbody temperatures averaged over the week 31 January - 8 February 1964; nadir angle 52°-58°.

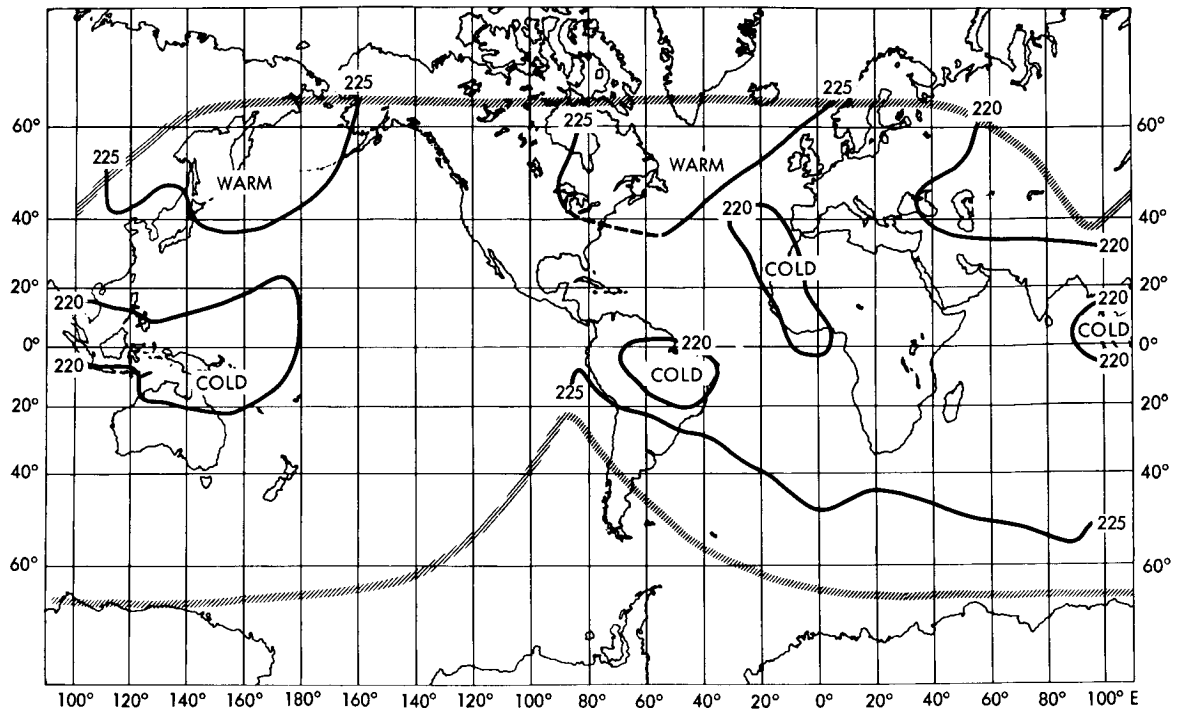


Figure 12—Quasi-global map of 15μ equivalent blackbody temperatures averaged over the week 18-25 March, 1964; nadir angle 0° - 40° .

Table 1

Computed Mean Temperatures (T_{BB}) Expected to be Observed by 15μ Radiometer for Temperature Profiles Shown in Figures 2a at Nadir Angles of 0 and 58 Degrees.

Nadir Angle (degrees)	Computed Mean Temperatures ($^{\circ}$ K)			
	Tropical	High Latitude Summer	High Latitude Cold Winter	High Latitude Warm Winter
0	227	238	213	229
58	231	240	214	231

It can be seen that differences of about $+2^{\circ}$ K occur in the topics where strongly positive temperature gradients with altitude prevail. This difference agrees with the values calculated for a tropical profile (Table 1). Over the higher northern latitudes (summer) and over the high southern latitudes (winter) moderately increasing temperatures with altitude and isothermal profiles are suggested. This is in fair agreement with the calculations (Table 1).

Seasonal Reversal, September - October 1963

As the solar illumination gradually became symmetrical with respect to northern and southern hemispheres, as during September 1963, temperature patterns at high latitudes markedly reflected the resulting change in solar heat input. In some areas, this change took place rapidly while other regions underwent a much slower transition. During the first two months following the solstice, there were practically no temperature gradients along any given latitude circle in the northern hemisphere; but strong longitudinal temperature patterns began to develop during the transitional season, especially after the September equinox. During July and August, the temperature patterns remained essentially the same as those during 19-25 June (Figure 3a). There was one important change, however, which exhibited the same characteristics as similar changes observed on measurements in other spectral regions in previous Tiros satellites (References 7 and 8). All measured temperatures over the entire world seemed to decline during the first three weeks of observation. It is extremely probable that a gradual degradation in the response of the radiometer was responsible for this decline. By mid-July 1963 the magnitude of this sensitivity decrease was about 7°K . After that the degradation seemed to level off and continued at a much lesser rate. An approximate time history of this instrumental degradation based on the preliminary information available at this time is given in Figure 1b. A more complete version will be given in the *Tiros VII Radiation Data Catalog and Data Users' Manual*. An appropriate correction based on Figure 1b should, therefore, be added to all temperature measurements quoted thereafter and shown in the maps (Figures 4 through 12). Although this degradation leaves some uncertainties in the exact absolute magnitudes of the temperature measurements, it does not appreciably affect the ability to assign the appropriate temperature profile (Figure 2a) to a measurement at a given location or the implications drawn from the distribution of relative temperature patterns.

The first indication of any significant change in the post solstice temperature pattern occurred during the week 28 August to 3 September; the temperatures at high northern latitudes decreased by about 5°K to a temperature of about 228°K ($+7^{\circ}$ correction) at 60°N . At northern mid-latitudes (20° - 50°N) there also was a slight temperature decrease from the summer (19-25 June) conditions. However, here this decrease did not take place uniformly at all longitudes. There were pocket-like regions where warmer temperatures seemed to persist longer than over other regions, thereby causing some inhomogeneities in contrast to the quite uniform zonal pattern observed in June. Going southward, temperatures in general decreased very gradually from about $228 + 7^{\circ}\text{K}$ at 60°N to about $223 + 7^{\circ}\text{K}$ at 40°S with the latter temperatures prevailing over most of the zone from about 25°N to 40°S . From there southward temperatures decreased rapidly with latitude. Thus, the remainder of the southern hemisphere remained essentially unchanged, still reflecting typical winter conditions ($205 + 7^{\circ}\text{K}$ at 60°S) except for a warm region of $225 + 7^{\circ}\text{K}$, which developed during late winter over the Indian Ocean between 40° to 50°S . The disturbance noted during June at these latitudes over the western South Pacific had grown throughout July and early August, and a warm region now extended over the entire Indian Ocean showing a definite longitudinal pattern. For example, temperatures over the southern Indian Ocean at 60°S were about $216^{\circ} + 7^{\circ}\text{K}$. At the same latitude over the Atlantic and central South Pacific, temperatures were $213 + 7^{\circ}\text{K}$ and $203 + 7^{\circ}\text{K}$ respectively.

During September, the European and West Asian portions of the northern hemisphere and parts of North America began to cool rapidly. There temperatures at 60°N had cooled to about $223 + 7^{\circ}\text{K}$ while over the northwest Atlantic and North Pacific somewhat warmer temperatures still prevailed ($228 + 7^{\circ}\text{K}$) during the week of 11-18 September (Figure 4). At the same time, the breakdown of the winter over the southern hemisphere was gaining impetus. The same, even intensified, longitudinal patterns as observed in August were apparent. Temperatures in the Indian Ocean warm area were about $234 + 7^{\circ}\text{K}$. This area had spread out between the longitudes of 95° to 180°E along the 50th parallel, yet temperatures at this latitude over the South Atlantic and the eastern South Pacific still remained relatively cold ($220 + 7^{\circ}\text{K}$). Temperatures at low and mid-latitudes, in general, ranged around $225 + 7^{\circ}\text{K}$ (Figure 4).

The week following the equinox (25 September - 1 October) showed that the temperature gradients between the two hemispheres (Figure 5) had reached their minimum during this transition period. With the exception of the very warm region of $50\text{-}55^{\circ}\text{S}$ over the Indian Ocean reaching maximum temperatures of $236 + 7^{\circ}\text{K}$ at 70°E and some cold pockets over the west Asia, temperatures over the entire quasi-globe were nearly constant at $225 + 7^{\circ}\text{K}$. It is significant to note that the temperature gradient within a given latitude belt could now be much greater than gradients between 60°N and 60°S at most longitudes: temperatures along 50°S vary from $236 + 7^{\circ}\text{K}$ at 70°E to $223 + 7^{\circ}\text{K}$ near 170°W , while along the 180th meridian, for instance, temperatures at 60°S are about $222 + 7^{\circ}\text{K}$, at 60°N about $228 + 7^{\circ}\text{K}$ and at the equator about $223 + 7^{\circ}\text{K}$. This was a total variation of 6°K along the meridian compared to a variation of 13°K along the 50°S parallel (Figure 5). The phenomenon of very pronounced temperature differences between the Indian and Pacific Oceans at all latitudes between 45°S and 65°S persisted during the entire transition period from winter to summer. The maximum temperature difference was about 15°K throughout this time, with the Indian Ocean area showing the warmest and the eastern South Pacific showing the coldest temperatures (Figure 5). The phenomenon first appeared on a large scale during the middle of August and lasted until about October 20th. During early and middle October, the eastern portion of the southern hemisphere (40°W to 120°E) was relatively warm ($230 + 7^{\circ}\text{K}$ at 60°S) with the warm center of $234 + 7^{\circ}\text{K}$ at 80°E , while the western portion remained relatively cold with the cold center of $220 + 7^{\circ}\text{K}$ at 170°E . During late October (the week of 23rd to 29th) the entire southern hemisphere finally achieved a typical summer temperature pattern, with wide and uniform latitudinal temperature belts ranging from about $230 + 7^{\circ}\text{K}$ at 60°S to about $225 + 7^{\circ}\text{K}$ at 30°S . There was a uniform belt with temperatures of almost exactly $225 + 7^{\circ}\text{K}$ between 30°S and 30°N . Over the Atlantic, Europe, and Western Asia, temperatures dropped rapidly from $225 + 7^{\circ}\text{K}$ at 30°N to $215 + 7^{\circ}\text{K}$ at 60°N , while over the Pacific they remained at $225 + 7^{\circ}\text{K}$ up to 60°N .

During the entire fall transition period, the north Pacific area had not cooled off as rapidly as the rest of the northern hemisphere and in general remained warmer throughout much of the winter. During the course of October, this pattern intensified whereby temperatures in all northern regions except over the north Pacific and eastern Asia continued to decline. Finally, at the end of October, as previously stated, the northern hemisphere showed a typical winter pattern with the same tight gradients with latitude as observed three months previously in the southern hemisphere.

At 60°N, temperatures were uniformly cold ($215 + 7^{\circ}\text{K}$) over Eurasia, the North Atlantic, and North America, but warm over Alaska and the Bering Sea ($225 + 7^{\circ}\text{K}$). The global picture did not change appreciably between the end of October and the week 20-26 November shown in Figure 6. Although the warm area ($224 + 7^{\circ}\text{K}$) over the North Pacific had somewhat diminished in size compared to the end of October, and it was now located over the Gulf of Alaska, the isotherms over that area still showed a very definite departure from a zonal pattern and ran northwest to southeast over North America and northeast to southwest over east Asia. While temperatures were still uniform with latitude over the Atlantic and Eurasian continent and ranged from $213 + 7^{\circ}\text{K}$ at 60°N to $225 + 7^{\circ}\text{K}$ at 40°N, the summer temperature pattern in the southern hemisphere was perfectly uniform with latitude and temperature, ranging from $235 + 7^{\circ}\text{K}$ at 60°S to $225 + 7^{\circ}\text{K}$ at 25°S (Figure 6). This pattern is identical to the temperature pattern during June, however, with northern and southern latitudes reversed.

The "Aleutian Anticyclone," December 1963

An unexpectedly warm stratosphere occurring as a regular climatological feature during winter in the general area of the Aleutian Island chain had long been recognized as the cause of a strong anticyclonic stratospheric circulation system in that area (Reference 10). Such circulation is unusual because in winter we would expect a very cold stratosphere resulting in a cyclonic circulation symmetric around the winter pole. Indeed, this cyclone exists, but in the northern hemisphere during mid-winter it is strongly disturbed and displaced by the Aleutian anticyclone. The morphology of this stratospheric warming over the North Pacific has received much attention in the past and numerous attempts have been made to explain its origin on the basis of dynamic processes (Reference 11). Satellite temperature measurements made it possible to follow the variation of mean temperatures in the lower stratosphere over this entire region throughout the winter of 1963. Figure 7a shows the averaged temperature measured by the satellite between 40°, 160°W and 20°N to 65°N for the week 5-12 December. Globally, there is practically no change from the patterns shown in Figure 6, except that the warm North Pacific region, which had previously remained at higher temperatures because it simply cooled more slowly than the other areas, has actually warmed between the end of November and early December. It was centered at the end of the Aleutian Island chain and stood out clearly with temperatures of $232 + 7^{\circ}\text{K}$. An analysis of temperatures at the 30 mb level from conventional radiosonde observations analyzed and obtained from the Freien Universität Berlin for the same area and time is shown in Figure 7b for comparison. The excellent agreement in the patterns between the two maps can serve as a measure of the validity of the satellite data. As can be seen from Figures 8, 9, 11, and 12, the Aleutian warm region was a permanent feature of the entire winter after the week of 5-12 December. However, although temperatures within the warm center had not shown an actual *increase* until 5-12 December, a warm area in one form or another had been present since the end of summer over the North Pacific as described previously (Figures 4, 5, and 6). This meant that the winter anomaly over the Pacific though variable in extent during early winter, grew directly out of the summer conditions without ever reaching as low temperatures as other portions of the northern hemisphere do. Although, during early December, the system took on a more permanent form and location and intensified somewhat, it had originated not because of a sudden heating phenomenon

during winter, but simply because it had refused to cool off at the end of summer. Naturally, there must be a mechanism to maintain the higher temperature during winter, while other regions at equal latitudes cool rapidly. It should be noted that those dynamic mechanisms which would have to depend on the existence of the complete winter cyclone could not explain the warm regions which already exist even before the cyclone is fully established. It might be interesting to investigate mechanisms by which the warm regions can be maintained throughout the winter by absorption of infrared radiation.

The satellite measurements showed that the situation in the northern hemisphere actually did not differ vastly from that of the southern hemisphere where a warm region over the southeastern Indian Ocean—though not quite as intense as the Aleutian one—had persisted throughout the winter and then had spread to make one half of the hemisphere almost 15°K warmer than the other. In the northern winter, almost a mirror image of this process occurs; the Pacific is warm and the Atlantic and Eurasia are cold, while in the south the Pacific is cold and the Atlantic and Indian Ocean areas are warm. In the north, the temperature gradients between warm and cold regions are somewhat greater (about 20°K between 180° and 40°W at 60°N). However, satellite data thus far only exist for the seasonal cycle 1963/64, and the observations described here must be tested by experiments in future years.

Solstice, December 1963

Between November 1963 and the middle of January 1964, there was very little change from the temperature patterns shown in Figure 6. The aforementioned Aleutian warm center became somewhat stronger and quite stationary during early December and, in contrast, the Atlantic and Eurasian cold regimes had remained unchanged with very tight latitudinal temperature gradients and isotherms perfectly aligned with latitude during the week 15-22 January 1964 (Figure 8a). It is interesting to note that the temperature difference of about 15°K between 60°N and the tropical belt over the eastern portion of the northern hemisphere is less than the longitudinal temperature difference between the Aleutian warm center and the North Atlantic at 60°N . A similar situation existed in the southern hemisphere at the end of winter (Figure 5); but during the solstice, the Australian warm area did not extend to such high latitudes as the Aleutian area does. As shown in Figure 8a, the mid-latitude and tropical regions had cooled considerably; and the temperature between 25°S and 40°N was now about $218 + 7^{\circ}\text{K}$, while earlier temperatures in the same zone ranged near $225 + 7^{\circ}\text{K}$. This remarkable cooling over so wide an area was particularly significant since it preceded by about one week the occurrence of a stratospheric warming over western Asia. Instrumental degradation cannot be responsible for such a temperature decrease, since Figure 12 did indicate higher temperatures again in March. Also, ever since November temperatures at high southern latitudes had remained unchanged. Relatively moderate and very uniform temperature zonal temperature gradients existed at all longitudes. Temperatures at 60°S are $235 + 7^{\circ}\text{K}$.

Temperatures of $231 + 7^{\circ}\text{K}$ at 50°S and of $206 + 7^{\circ}\text{K}$ at 60°N (eastern portion only) are compatible with the computed temperatures of 238 and 213°K respectively for the "summer" and

"cold winter" profiles (Table 1). Temperatures calculated for the "tropical" profile (227°K Table 1) are about 2°K higher than those measured in the now cold mid-latitude belt ($218 + 7^{\circ}\text{K}$). Mean temperatures of $232 + 7^{\circ}\text{K}$ in the center of the Aleutian warm region measured during December suggest that the average temperature of the stratosphere in the 15 to 35 km region was about 12°K higher than that shown in the "warm winter" profile of Figure 2, which yields a mean temperature of only 229°K (Table 1). Of course, such a temperature profile in this particular altitude region is merely postulated since, for example, a low average stratospheric temperature of 205°K in the altitude region from 15 to 35 km (such as shown in the "cold winter" profile, Figure 2a) could be balanced by an extraordinarily high average temperature of 300°K in the region from 35 to 60 km to produce the measured radiation temperature of 239°K . But, such a temperature profile is much less probable than the one postulated. The validity of an assumed average stratosphere temperature increase of 12°K between 15 and 35 km is also suggested by comparing the satellite measurements at low nadir angles ($0-40^{\circ}$, Figure 8a) to those at high nadir angles ($52-58^{\circ}$, Figure 8b). Temperatures over the Aleutian warm area are practically the same at both nadir angle ranges indicating a nearly isothermal or at least a very slowly varying temperature gradient with altitude in the region where the weighting functions $\psi(h)$ are at their maximum (15-35 km, Figures 2b and 2c). A temperature profile such as the aforementioned one with a mean temperature of 205°K between 15 and 35 km and 300°K between 35 and 60 km would produce a difference of 9°K between the radiation temperatures measured at 0° and 58° nadir angle. Figures 8a and 8b, however, indicate no temperature differences over the Aleutian warm center. Thus, we find that the difference in the mean temperatures between 15 to 35 km level and the 35 to 50 km level cannot be excessively large, and with that restriction, a temperature increase of 10°K for the standard "warm winter" profile from 15 to 35 km follows for the North Pacific area. Similarly, we find that there is no temperature difference for the two nadir angles over the North Atlantic and Northern Europe (Figures 8a and 8b) which agrees well with the calculated difference of 1°K for the "cold winter" profile. The larger temperature differences over the tropics—the 220°K isotherm is about 10° further north in Figure 8b than in Figure 8a—indicate the rapid temperature increase with altitude above 15 km and agree well with the computed difference of 4°K for the "tropical" profile (Table 1); while the calculated values of 238 and 240°K for "high latitude summer" (Table 1) agree well with the observed temperatures ($+7^{\circ}$ correction) and temperature differences between 50 and 55°S .

This picture has changed considerably during late January (Figures 11a and 11b) where temperature differences at mid-latitudes and in the tropics over the entire eastern hemisphere are as high as or exceed the differences observed previously within the tropics. Such large differences exceeding 5°K extend particularly into North Africa, the eastern Mediterranean, and the Near East (Figures 11a and 11b). This indicates that neither the "tropical" nor the "summer" temperature profiles (Figure 2a) apply in this case. In that area, temperatures at 15 km must be somewhat higher than those given by the "tropical" profile; and there must be a pronounced increase of temperature with altitude resulting in a very warm upper stratosphere (i.e., a very strong vertical temperature gradient between the lower and upper stratosphere). It is significant that this change occurred over the area into which the sudden warming, described below, moved in its decaying stages.

Sudden Warming, January 1964

The type of temperature measurement obtained with the satellite described herein was expected to be most useful for the detection of the occurrence and the observation of the behavior of stratospheric warmings. These warmings were first observed over Berlin by Scherhag (Reference 12) and since then have been the subject of intensive observation and analysis (Reference 13). The sudden warmings have now been observed almost every year during the northern hemisphere winter and, during their occurrence, the lower stratosphere over a limited area may be heated by as much as 30°K within a few days. Causes for such warmings have thus far not been explained. In contrast to the Aleutian warm center described above, the sudden warmings show no regularity in their time and location of occurrence. In order to be detectable by the Tiros radiometer, the warming must occur at altitudes between 15 and 35 km or, if it occurs at other levels, it must be unproportionally intense. Calculations based on the "warm winter" temperature profile of Figure 2a show that a uniform temperature increase of 12°K between 15 and 35 km will increase the radiation temperature by 10°K , while a similar change of the temperature profile between 34 and 44 km will cause a rise in the radiation temperature of less than 1°K .

A number of small and weak warmings occurred over America and Europe during December 1963 and January 1964, but those did not penetrate to altitudes below 30 km (Reference 14). Therefore, they could not be detected by the satellite. During the week 22-29 January, however, a warming of apparently moderate intensity occurred over the region of the Caspian Sea, extending between the Himalayan Mountains and the Black Sea (Figure 9a). Radiation temperatures over that area have increased by about 8°K over the previous week (Figure 8a). During that week (15-22 January), there was practically no indication of any disturbance in the perfect latitudinal temperature structure over that region, except perhaps for a very small area over Iran where a temperature increase of about 2-3 degrees could be observed; but in the high nadir angle measurements, there is an indication of increased temperatures over South Central Asia (Figure 8b) inferring that the subsequent warming might have originated in the upper stratosphere (above 30 km) in that area. Unfortunately, the warming developed in an area where no conventional meteorological data are available at these altitudes, and the satellite observations provide the only method of analyzing the event. Furthermore, even the satellite observations are limited in coverage, since this area is located near the data gap over the central Soviet Union which exists because of the particular geometry of the data readout stations for Tiros. The satellite data were, therefore, analyzed for individual days of 22, 24, 25, 26, 27, and 29 January. These daily analyses showed that the temperatures within the warm center were as high as $230 + 7^{\circ}\text{K}$ on 29 January, but because they extended only over very small regions and because of the motion of the center from day to day, these high temperatures became obscured in the weekly averages (Figure 9a). The first definite indication of the warming occurred on 22 January, where a small and relatively weak warm center of $225 + 7^{\circ}\text{K}$ appeared over Pakistan, Afghanistan, and Eastern Iran. This is already a few degrees higher than the average temperature over the same area for the preceding week of 14-22 January (Figure 8a). Two days later on 24 January, the warm region had spread out somewhat to the north, and the center had also moved in that direction but had not intensified significantly. On 25 January, temperatures of $225 + 7^{\circ}\text{K}$ ranged over the entire middle East extending as far

eastward as central China. The center was now just east of the Caspian Sea and had just barely reached a temperature of $230 + 7^{\circ}\text{K}$. On 26 January, the same situation prevailed with the center becoming slightly warmer and larger. On 27 January, the center had grown considerably larger and temperatures of $230 + 7^{\circ}\text{K}$ extend over an area of at least 30° longitude and 10° latitude north-east of the Caspian Sea. The $225 + 7^{\circ}\text{K}$ isotherm had advanced to a latitude of 50°N , causing a tremendously tight temperature gradient over northern Europe where temperatures increased by more than 20°K from southern Norway to the Black Sea. Due to the warming, isotherms have been tilted to follow a course from southeast to northwest instead of the perfect eastwesterly direction still prevailing on 22 January. Finally, on 29 January a warm center, extending over the 10° great circle arc with temperatures of $230 + 7^{\circ}\text{K}$, stretched from the Black Sea eastward to China. One 225° isotherm now ran east-west along the 40th parallel between 40°E and 80°E . The other ran southwest to northeast from the Black Sea to about 50°E and 55°N . The center was located near 65°E and 50°N . This situation was summarized in Figure 10 which shows that on 27 January the radiation temperatures had increased by 15°K over the averages for the week 9-15 January near the center and that the periphery of the warming extended as far west as the North Sea, and the Atlantic and as far south as North Africa and Arabia. Figure 11a shows that during the week 31 January to 8 February the warming had passed its climax. Rather homogeneous temperature patterns with latitude returned over northern Europe and eastern Asia, but south of 40°N a broad warm area of about $223 + 7^{\circ}\text{K}$ now covered the entire region between about 40°N and 25°S latitude and 110°W and 80°E longitude (Figure 11a). This meant that the mid-latitude belt which had cooled so drastically before the warming had been restored close to its normal temperature of about $223 + 7^{\circ}\text{K}$ between 25°S and 40°N . Figures 8, 9, and 11 show that the Aleutian warm center had remained undisturbed during the entire period of the warming. On 30 January, the warming was detected by a radiosonde ascent over Berlin—the only one available for this analysis (Stratospheric Analysis Charts, Freien Universität Berlin, Reference 15). This radiosonde temperature profile, when compared to a prewarming profile shows that the warming over Berlin occurred primarily over 30 km. For the week of 22-29 January, temperatures at high nadir angles were about 5°K higher than at low nadir angles not only over the warm center, but also extended far beyond the center, particularly along the southern and western periphery of the warming (Figure 9a and 9b). This means that over the center temperatures have increased not only in the lower stratosphere but more so in the upper stratosphere. The much greater extent of the warming in the high nadir angle temperature patterns compared to the low nadir angle patterns suggested that along the western and southern periphery the warming occurred only in the upper stratosphere. This also confirms the above mentioned radiosonde observation over Berlin. Since the much larger warming (13°K) in the center would require an unreasonably large temperature if the warming were confined to altitudes above 30 km, and since such a strong vertical temperature gradient would be clearly noticeable as a much greater temperature increase at the larger nadir angles, it must be concluded that the warming near the center penetrated to much lower altitudes where the ψ functions are at maximum. If the warming occurred uniformly at altitudes from 15 to 35 km, a temperature increase of about 15°K would satisfy the radiation measurements. Such an increase is quite commensurate with a moderate stratospheric warming.

Equinox, March 1964

The global temperature structure undergoes a major change during the period from early February (Figure 11a) to the week of 18-25 March (Figure 12). The steep zonal winter time temperature gradients at high northern latitudes, particularly over the eastern hemisphere, as well as the zonal summer pattern in the southern hemisphere had disappeared. The southern hemisphere had cooled considerably, and parts of the northern hemisphere had warmed. This results again—as during the September equinox—in an almost constant temperature over the entire quasi-globe. In fact, temperature gradients, longitudinally or latitudinally are even shallower than during September. Over the eastern Pacific, there was no temperature gradient at all between 60°S and 60°N , with temperatures of about $223 + 7^{\circ}\text{K}$ prevailing at all latitudes. As the southern hemisphere cooled, a temperature gradient along 60°S seemed to develop similarly as during the previous winter. The South Indian and Atlantic Oceans were now about 5°K warmer than the South Pacific. In the northern hemisphere near 60° the North Atlantic and northeast North America had warmed rapidly by about 20°K since February, while the region east of the Black Sea, where the sudden warming occurred in January, had returned to its prewarming winter temperatures of $217 + 7^{\circ}\text{K}$. Temperatures in the Aleutian region had remained practically constant throughout the winter and were still at about $228 + 7^{\circ}\text{K}$. This produced temperature differences of about 10°K between the Atlantic and Pacific warm regions and central Asia at 50°N , which was the largest temperature difference found during this equinox (Figure 12). Since these data have been reduced only very recently, there has not yet been adequate opportunity to analyze the January to March transition as thoroughly as the June to October period. Such an analysis will be made in the future.

CONCLUDING REMARKS

Satellite measurements of emitted radiation in the 15μ carbon dioxide band have demonstrated that mean temperatures in the lower stratosphere can be mapped on a global scale. By comparing measurements at high and low nadir angles, a qualitative inference can be made about the vertical temperature gradient between the lower to upper stratosphere. Analysis of global temperature patterns from June 1963 to March 1964 revealed that temperature patterns in both hemispheres remain relatively undisturbed during summer. These patterns are oriented very precisely along latitude circles with the temperature maximum occurring at the summer pole. Near maximum temperatures are reached in the southern summer about one month after the equinox. After that, temperatures increase only slightly through the solstice and remain high until the next equinox.

The northern summer could only be analyzed through its peak and declining phases, June to September 1963. Temperatures decline very slowly during the first two months following the solstice. Then, a rapid decline occurs just before the equinox. During both equinoxes, temperatures were relatively uniform and differences of about $10\text{-}15^{\circ}\text{K}$ may exist both with latitude and longitude. Winter temperature patterns in both hemispheres exhibit strong temperature gradients between the pole and 40° , but a completely uniform pattern never exists in either winter hemisphere. A fairly uniform region with temperatures generally around 230°K extends between 15° latitude

* of the summer hemisphere and 40° latitude of the winter hemisphere during solstice. The satellite measurements not only permitted for the first time a continuous analysis of the southern hemisphere from June 1963 to March 1964 up to a latitude of 65°S, but also demonstrated the usefulness of uniform and continuous data coverage over the entire quasi-globe. A warm area over the Indian Ocean, though initially small, seems to play a role in the southern winter similar to the Aleutian warm center during the northern winter. During winter 1963, this warm region grew out of a disturbance in the isotherms during June and finally divided the entire stratosphere of the winter hemisphere into a "warm" and "cold" portion with the warm portion located between Africa and Australia. Temperature differences between these warm and cold areas amounted to about 15°K and disappear with the warming of the South Pacific area during late October, giving way to the homogeneous summer pattern. Similarly, there is no homogeneous winter pattern in the northern hemisphere. A large region over the North Pacific does not cool off as rapidly after the equinox as the rest of the stratosphere. Just before the solstice, this region becomes well established and intensifies in the area where the Aleutian anticyclone is usually found.

The morphology of a stratospheric warming over southwestern Asia and its penetration to Europe was observed by the satellite indicating that heating (of possibly 20°K) penetrated down to at least 20 km over the center of the warming, but at the periphery warming of perhaps somewhat greater magnitude remained at altitudes above 30 km. The persistent climatological inhomogeneities of warm cells over both winter hemispheres lead to the speculation that during winter the stratospheric temperatures may be influenced by radiation from underlying surfaces, while during summer solar heating is dominant.

A study was also made of the effect of high altitude clouds on the measured temperatures, since the weighting functions (Figure 2b) are not negligible at 10 km. The result indicated that very large and high cloud systems such as hurricanes do decrease the measured temperatures by as much as 10°K if the clouds reach above 10 km and by less than 4°K if the clouds, filling the field of view are at 6 km; but it was shown that such effects are only isolated and are averaged out by the weekly analyses which formed the basis for this investigation.

ACKNOWLEDGMENTS

Experiments resulting in findings such as the ones herein always require the efforts of many hundreds of dedicated individuals. We gratefully acknowledge the contributions of those who have contributed to the success of the Tiros VII experiments. We are particularly indebted to Mr. Robert Hite and his team for the computational efforts in reducing the vast amount of radiation measurements to the maps presented here.

REFERENCES

1. Bandeen, W. R., Hanel, R. A., Licht, J., Stampfl, R. A. and Stroud, W. G., "Infrared and Reflected Solar Radiation Measurements from the Tiros II Meteorological Satellite," *J. Geophys. Res.* 66(10):3169-3185, October 1961.

2. Hanel, R. A., Bandeen, W. R., and Conrath, B. J.: "The Infrared Horizon of the Planet Earth," *J. of Atmos. Sciences*, 20, 73-86, March 1963.
3. Bandeen, W. R., Conrath, B. J., and Hanel, R. A., "Experimental Confirmation from the Tiros 7 Meteorological Satellite of the Theoretically Calculated Radiance of the Earth within the 15 Micron Band of Carbon Dioxide," *J. of Atmos. Sciences*, 20, 609-614, November 1963.
4. "TIROS VII Radiation Data Catalog and Users' Manual," Goddard Space Flight Center, Greenbelt, Maryland (to be published).
5. Elsasser, W. M., with Margaret F. Culbertson: "Atmospheric Radiation Tables," *Meteorological Monographs*, 4, 23, August 1960, American Meteorological Society.
6. "TIROS II Radiation Data Users' Manual," Goddard Space Flight Center, Greenbelt, Maryland, August 15, 1961.
7. "TIROS III Radiation Data Users' Manual Supplement," Goddard Space Flight Center, Greenbelt, Maryland, December 1, 1963.
8. "TIROS IV Radiation Data Catalog and Users' Manual," Goddard Space Flight Center, Greenbelt, Maryland, December 15, 1963.
9. Bandeen, W. R., Kunde, V., Nordberg, W., and Thompson, H. P.: "A Radiation View of Hurricane Anna from the TIROS III Meteorological Satellite," Goddard Space Flight Center, Greenbelt, Maryland (to be published in *Tellus*, 1964).
10. Wege, K.: Druck-, Temperatur- und Strömungsverhältnisse in der Stratosphäre über der Nordhalbkugel, *Meteorol. Abhandl. d. Freien Universität Berlin*, Bd. V, Heft 4(1957).
11. Boville, B. W.: "What are the Causes of the Aleutian Anticyclone?" *Proceedings of the International Symposium on Stratospheric and Mesospheric Circulation 20 to 31 August, 1962, Berlin, Meteorologische Abhandlungen*, 36:107-119, 1963.
12. Scherhag, R. A.: "Die Explosionsartigen Stratosphärenenerwanmungen des Spätwinters 1951/52." *Berichte des Deutschen Wetterdienst in der U. S. Zone*, 38, 51-63, 1952.
13. Reed, R. J.: "On the Cause of the Stratospheric Sudden Warming Phenomenon." *Proceedings of the International Symposium on Stratospheric and Mesospheric Circulation 20 to 31 August, 1962, Berlin, Meteorologische Abhandlungen*, 36:315-334, 1963.
14. Teweles, S.: "Stratowarm Alerts 1964," *IQSY Stratowarm Agency, Stratosphere Analysis Project*, U. S. Weather Bureau, Washington.
15. Stratospheric Analysis Chart for 1963-1964, Institut für Meteorologie und Geophysik der Freien Universität Berlin, *Meteorologische Abhandlungen*.
16. Cole, Allen E., Kantor, A. J., and Court, A., "Supplemental Atmospheres," *Interim Notes on Atmospheric Properties - 32 (Rev.)*, June 6, 1963, Air Force Cambridge Research Laboratories, Office of Aerospace Research, Bedford, Massachusetts.

N65-29553

NEW KNOWLEDGE OF THE EARTH'S ATMOSPHERE FROM THE AERONOMY SATELLITE (EXPLORER XVII)

by

N. W. Spencer, G. P. Newton, C. A. Reber,
L. H. Brace and R. Horowitz
Goddard Space Flight Center

SUMMARY

29553

The Explorer XVII satellite performed direct, very localized measurements of the total neutral particle density, the concentration of neutral particle masses 4, 14, 16, 28, and 32 and the temperature and concentration of thermal electrons, between the altitudes of 258 and 920 km over those regions of the earth where the satellite was accessible to the Minitrack network—in particular between $\pm 58^\circ$ latitude. Pressure gages on the satellite showed that the total density at 280 km was about 50 percent lower than is given by the appropriate atmospheric models based on satellite drag measurements. Daily variations in total density are more strongly dependent on a_p (the magnetic index) than had been believed previously. Neutral mass spectrometers showed that He is the predominant neutral constituent above 600 km, O is predominant between 250 and 600 km, and N_2 is predominant below 250 km. The scale heights of the various constituents agree in general with the corresponding model atmospheric scale heights. Langmuir probe results confirmed the global extent of thermal non-equilibrium ($T_e > T_g$) and provided high resolution of the diurnal variation of electron temperature and density at several stations. For example, the electron temperatures near the F_2 maximum over Blossom Point show a nighttime value of about 1100°K, followed by a mid-morning maximum of 2800°K and an afternoon plateau of 2200°K. A consistent and strong latitude effect, evident particularly at Blossom Point, caused a significant positive gradient in electron temperature (the order of 25°K/degree of latitude) and an inverse gradient in electron density in a manner approximately in accord with recent theories of Hanson and Dalgarno.

INTRODUCTION

The Explorer XVII (1963-9A) satellite (Figure 1) was designed to provide direct measurements of aeronomic parameters as a basis for new studies of the physics of the earth's upper atmosphere. Thus instruments were selected for the satellite which would provide both total and relative concentration of the neutral particles and high resolution measurements of the electron temperature and density, both of which are of considerable significance in studies of the physical processes controlling the upper atmosphere. These data would help also to (1) clarify and define

the structural properties of the atmosphere, previously established primarily through inferences from satellite drag measurements; and (2) investigate the variability and dependence of the atmosphere on solar conditions.

The technological advance of measurement techniques was also an objective of the project, as part of a continuing effort to improve experimental capability. The application of laboratory-developed techniques required engineering as well as measurement technique refinements and adaptation to new environments. The atmospheric data to be obtained, if it were to be of maximum benefit consistent with its timeliness, required computer usage for processing the large quantity of data (of the order of 2×10^9 bits of information).

EXPERIMENTS

The choice of experiments to obtain the desired data was based mainly upon laboratory vacuum technique experience; thus both thermionic and cold-cathode pressure gages (obtained from proven laboratory sensors) were selected for the measurements of the total neutral particle density. Double-focusing magnetic mass spectrometers were chosen for the measurements of neutral particle concentrations. Two Langmuir probe experiments were employed for measurements of the electron temperature and ion density.

It is of special significance from the point of view of determining local values of the ambient concentrations of constituents that proven laboratory vacuum system techniques were employed in constructing the satellite. For example, to minimize potential sources of contaminating gases, nearly all external surfaces were constructed of stainless steel, and all satellite joints were either welded or utilized copper shear gaskets for vacuum sealing. A significant effort was thus devoted to making the satellite-sensor system a true "inside-out" ultrahigh vacuum system so that the experimenter could be confident that the atmospheric samples measured were not contaminated by materials carried aloft by the satellite.

The Pressure Gages

The density measurements made by the Explorer XVII ionization gages extended to satellite usage the technique employed in rocket manometer experiments (References 1 and 2) to measure

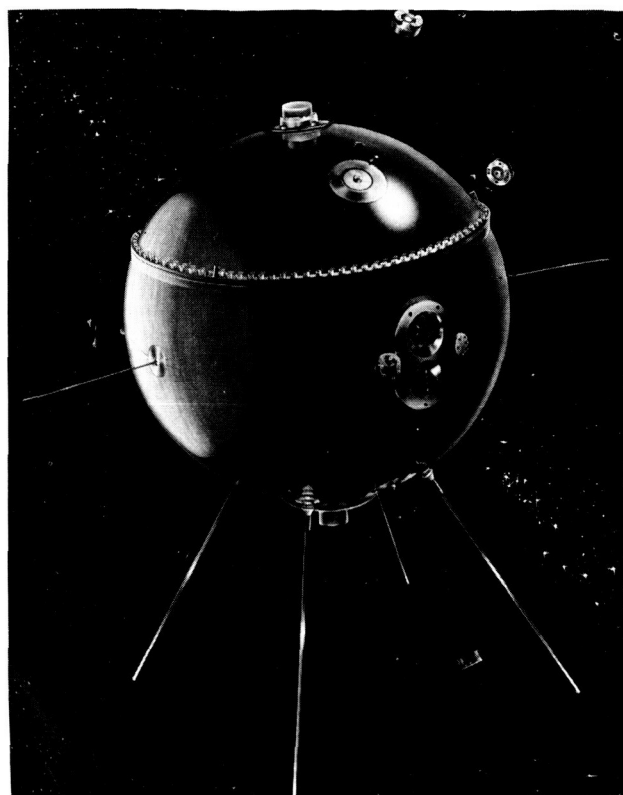


Figure 1—Artist's conception of Explorer XVII in orbit.

the total atmospheric density. The description of the instrumentation, the calibration technique, and the flight response of the Explorer XVII sensors have been reported (Reference 3).

Four independent pressure gage experiments were employed: two Bayard-Alpert type (thermionic cathode) ionization gages and two Redhead type (cold-cathode, magnetic) gages. Each sensor was equipped with a special vacuum-sealed orifice that could be opened after the satellite was in orbit. Thus the sensor, properly cleaned, calibrated, and sealed under vacuum, was to be opened on command to the space environment. This procedure, whose validity was previously established through rocket experience, assured the necessary high degree of vacuum cleanliness for the sensors.

The use of both cold and thermionic cathode gages was considered essential because of uncertainties in (1) the response of a hot cathode gage in a sometimes predominately atomic oxygen environment (not subject to adequate laboratory calibration) and, (2) the general applicability of ionization gages to the high-velocity satellite environment. At the same time, a desirable redundancy was accomplished and valuable studies of the usefulness of the two fundamentally different sensors were made possible. Each pressure gage was provided with an appropriate electrometer amplifier and other electronic support devices which enabled conversion of the sensor output current to a voltage suitable for telemetry. The electronic systems also included provision for in-orbit current calibration of the amplifiers once during each operating cycle of the gages.

Neutral Particle Mass Spectrometers

Two identical double focusing magnetic mass spectrometers were employed for the determination of the local concentrations of atmospheric helium (mass 4), atomic nitrogen (mass 14), atomic oxygen (mass 16), molecular nitrogen (mass 28) and molecular oxygen (mass 32). Although detailed descriptions of the spectrometers are provided elsewhere (References 4, 5, 6, and 7), their significant features are summarized herein. The external ion source, designed to reduce the interactions of the sampled particles with the sensor, was followed by an electrostatic ion lens which focused the relatively high energy ions on the entrance slit of the analyzer. In this way, it was possible for the instrument to accept particles from a 2π steradian solid angle, and up to 12 ev kinetic energy. In the magnetic analyzer the beam of ions was separated according to mass, a given mass falling on the appropriate collector electrode in spectrograph fashion.

Each of the spectrometers was provided with a sensitive electrometer and logarithmic amplifier for conversion of the collected ion current to the proper telemetry voltages. Electronic logic circuitry accomplished the required changes in sensitivity and mass-number selection. As with the pressure gages, a vacuum-seal arrangement was adopted which permitted exposure of the spectrometer ion source to the atmosphere after the satellite was in orbit.

The primary task of the data analysis was to determine the relationship of the measured ion currents to the ambient neutral particle densities. Particles could enter the region of ionization in one of three ways: (1) directly with no collisions; (2) after suffering one or more collisions with surfaces in the source region; (3) by entering the spectrometer analyzer, becoming

thermalized, and subsequently being re-emitted. The relationships between the measured ion currents and the ambient atmosphere were computed on the basis of these three mechanisms and the laboratory gas calibrations. The validity of these calculations is demonstrated by the fact that the total mass-density measured by the spectrometer is in satisfactory agreement with that obtained independently by the companion pressure gage experiments described above.

Langmuir Probes

Two independent Langmuir probe systems, based on established techniques and previous rocket usage (References 8, 9, and 10) were employed to provide measurements of the ion concentration (N_i), and the electron temperature (T_e) of the ionosphere. Each probe system used a cylindrical electrode (projecting into the plasma) whose potential was varied with respect to the satellite shell. The resulting current to the probe was converted to a voltage suitable for telemetry.

By using the following equation, the temperature was derived from the electron current to the probe as it was swept from the satellite potential to the plasma potential:

$$\frac{d \log_e i_e}{dV} = \frac{e}{kT_e} \quad (1)$$

To localize the T_e measurement, the electron temperature probe was swept at a rate of 10 sweeps per second; and to maximize the resolution, the voltage was swept in two ranges, 0 to +3/4 v and 0 to 1 1/2 v, respectively. As a result, each temperature measurement was completed in less than 400 meters of the satellite path—and to that extent represents a point measurement. The telemetry sampling rate was sufficiently high to permit determination of temperature values as low as 400°K (although the lowest temperatures actually recorded were about 900°K).

The ion density probe was swept from -3 to +2 volts in a 2-second period, which was long compared with the satellite spin period of 0.7 seconds. N_i was derived from the ion current maxima which occurred each time the probe axis was perpendicular to the velocity vector.

Sensor Location

As noted above, the capability to provide measurements of the constituents of the space environment required close adherence to established laboratory vacuum techniques. Thus, in addition to providing a sealed housing which would not itself contaminate the local atmosphere, the eight sensors were located so as to provide maximum separation from each other.

Consideration of sensor orientation with respect to the direction of motion required that the mass spectrometers be located at the two ends of the spin axis to minimize changes in orientation during each mass-sampling sequence. The four pressure gages were distributed uniformly about the spherical satellite to insure that at least one gage would always experience pressure variations due to satellite spin, regardless of the spin axis orientation. One pressure gage of each

type was located on the satellite equator to enable a comparison of the gage responses under identical conditions. The two Langmuir probes were also located on the equator at points nearly diametrically opposite each other.

SUPPORTING SYSTEM

The interpretation of data from various sensors required detailed knowledge of the instantaneous angle between any sensor and the satellite's direction of motion. This information was provided through the use of a multiple optical sensor arrangement, which enabled sensing the direction of the sun and/or moon and the instants of passage, during spin, of the Earth's horizons.

Direct measurement sensors like those employed on Explorer XVII provide time rates-of-change of data requiring high telemetry sampling rates. For example, the spectrometers and pressure gages required 60 samples per second and the "high speed" Langmuir probe required 180 samples per second. To meet these needs a pulse code modulated (PCM) telemetry system capable of 1000 samples per second was selected. This system had the additional advantage of providing a digital format which facilitated computer data processing.

The satellite was powered exclusively by silver-zinc cells, since solar cells presented the possibility of local contamination of the atmosphere. The 150 pounds of cells employed provided adequate energy to operate the entire satellite system for a total of 75 hours. A command-and-control system permitted the experiments to be turned on for four-minute periods, each of which was terminated by an internal programmer. Because a tape recorder was not employed, responses were confined to geographic regions of approximately 4000 kilometers diameter about each minitrack command station. Figure 2 illustrates the geographic coverage attained by showing the path of the satellite during each data-producing response. Some of the pertinent statistics of the satellite are summarized in Table 1.

EXPERIMENTAL RESULTS

The Pressure Gage Experiment

As noted above, four independent gage systems were employed on the satellite, and all gages operated in orbit. Three of the gages gave useful and meaningful data during the active life-time of the satellite. The fourth gage, however, experienced an apparent decrease in sensitivity after opening in orbit and no atmospheric structure data from this gage are available at present. Some of the results from the other three gages for five northern midlatitude stations, representing approximately 25 percent of the total available data are presented here.

Figure 3 shows the measured atmospheric density over Grand Forks, Minnesota during a pass at 2000 hours local time and demonstrates typical resolution of the density gage data. It may be seen that the total altitude change was only 5 km for this pass, and at the average altitude of

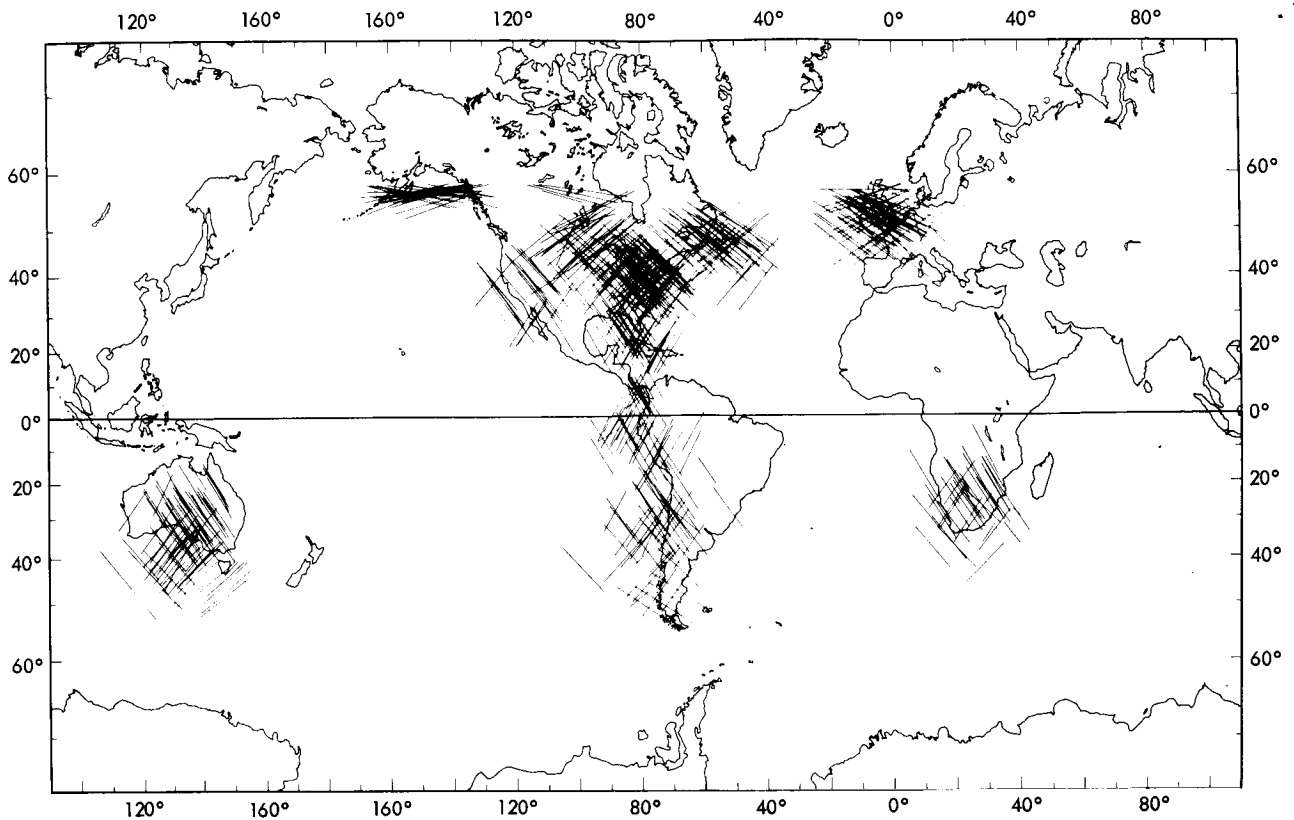


Figure 2—Explorer XVII geographic coverage.

Table 1
Explorer XVII Statistics

Launch Date	April 3, 1963
Inclination	58°
Perigee	258 km
Apogee Range	920-870 km
Useful lifetime	100 days
Perigee motion	+39° to +58° to -18°
Data responses	650 on command
Telemetry	PCM - 8640 bits/sec
Spin rate	90 rpm
Power supply	Chemical
Size and shape	1 meter diameter sphere
Weight	410 pounds

265 km, the atmospheric density was 2×10^{-14} gm/cm³. Each point shown is the average of the three independent density measurements. The resolution of the density data from each gage is such that the density was measured every 700 milliseconds or once every six kilometers along the satellite orbit. The observed small scatter of the density data makes quantitative density scale height determination possible for passes possessing significant altitude changes. The magnitude of the error in the absolute value of the density is ± 25 percent for this pass and can be attributed

primarily to uncertainty in the absolute calibration of the sensors in the laboratory. At an altitude of 600 km, the error in the absolute value of the measured density is ± 55 percent for some passes. Generally, the precision of the density measurements is better than ± 20 percent.

Figure 4 (Reference 11) provides a comparison of the atmospheric densities directly measured by the gages in the altitude range 258 to 300 kilometers, to the density obtained from drag

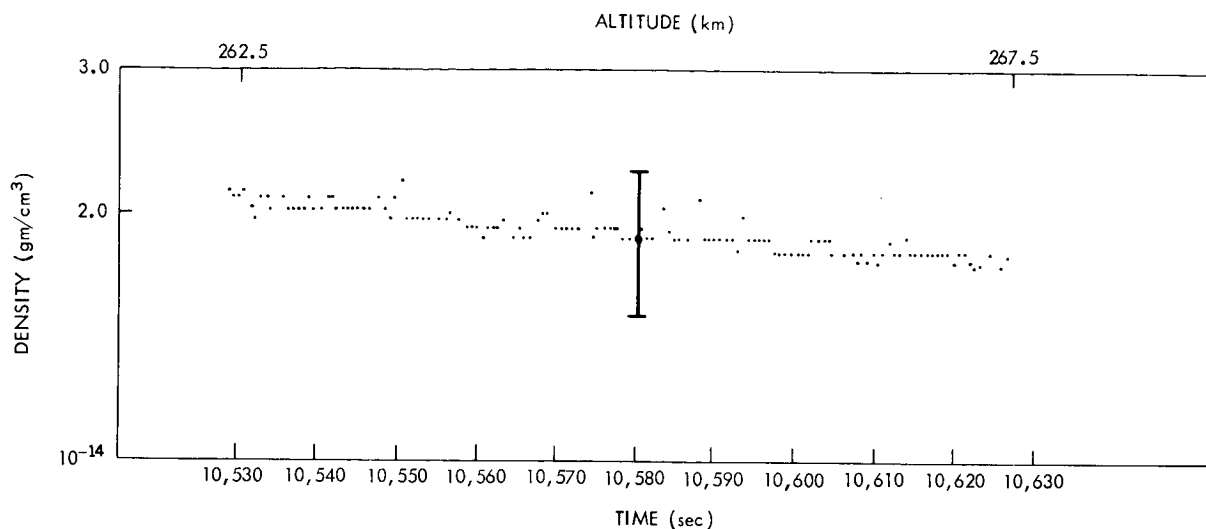


Figure 3—Density data derived from a single pass over Grand Forks, Minnesota demonstrating the resolution of the pressure gage data.

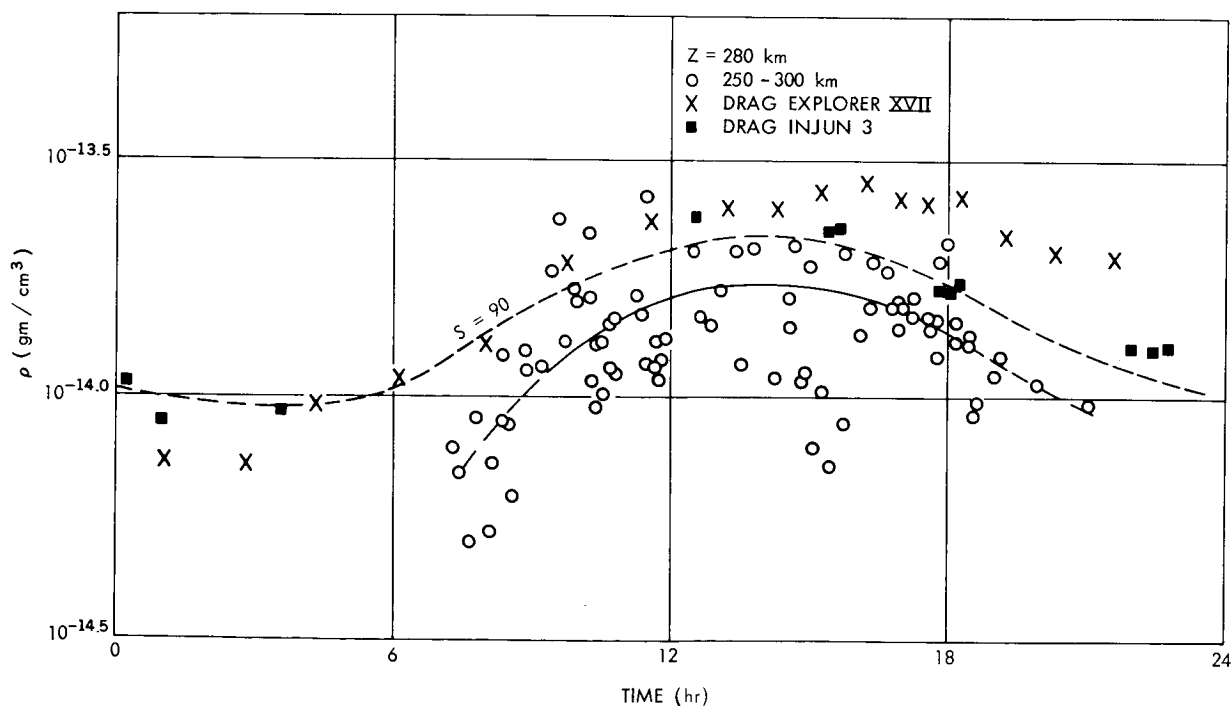


Figure 4—Comparison of directly-measured and drag-derived atmospheric densities.

observations of Explorer XVII (Reference 12) and Injun 3 (Reference 13). All data are normalized to a height of 280 kilometers for comparison purposes, by using density gradients obtained from the Harris and Priester model with $S = 90$.

The Injun 3 data (indicated by squares) were selected for quiet geomagnetic conditions ($A_p = 2$) for the time interval of February 18 through June 30, 1963. During this period, the latitude

of the satellite perigee varied between -40° and $+60^\circ$. The drag data from Explorer XVII (indicated by crosses) correspond to the time interval from April 3 to July 6, 1963, when the latitude of the satellite perigee was between $+58^\circ$ and -20° . All Explorer XVII data in the figure have been reduced to quiet conditions ($A_p = 0$) by using the preliminary linear reduction relation:

$$\log \rho = 0.006 A_p$$

Further analysis of the gage data indicates, however, that the correlation between density and geomagnetic activity should be a steeper, nonlinear relation with the steepest portion applicable for A_p (Reference 11). Application of the modified relation is expected to (1) remove some of the scatter from the gage data (which reflects real atmospheric variations), and (2) lower the average value of the directly measured densities by a small amount.

It is observed that the densities determined from drag are systematically 40 to 50 percent greater than the normalized densities measured by the gages, and that this separation is just outside the combined, stated uncertainties of the two sets of data. This difference is significant but at this time is not considered serious, since it could be accounted for by modest changes in the altitude to which the drag data are assigned, the drag coefficient, or the gage calibration constants.

Figure 5 shows measured atmospheric density-versus-altitude for the altitude range 258 to 600 km. These data result from approximately 60 passes for an A_p between 0 and 10, $F_{10.7}$

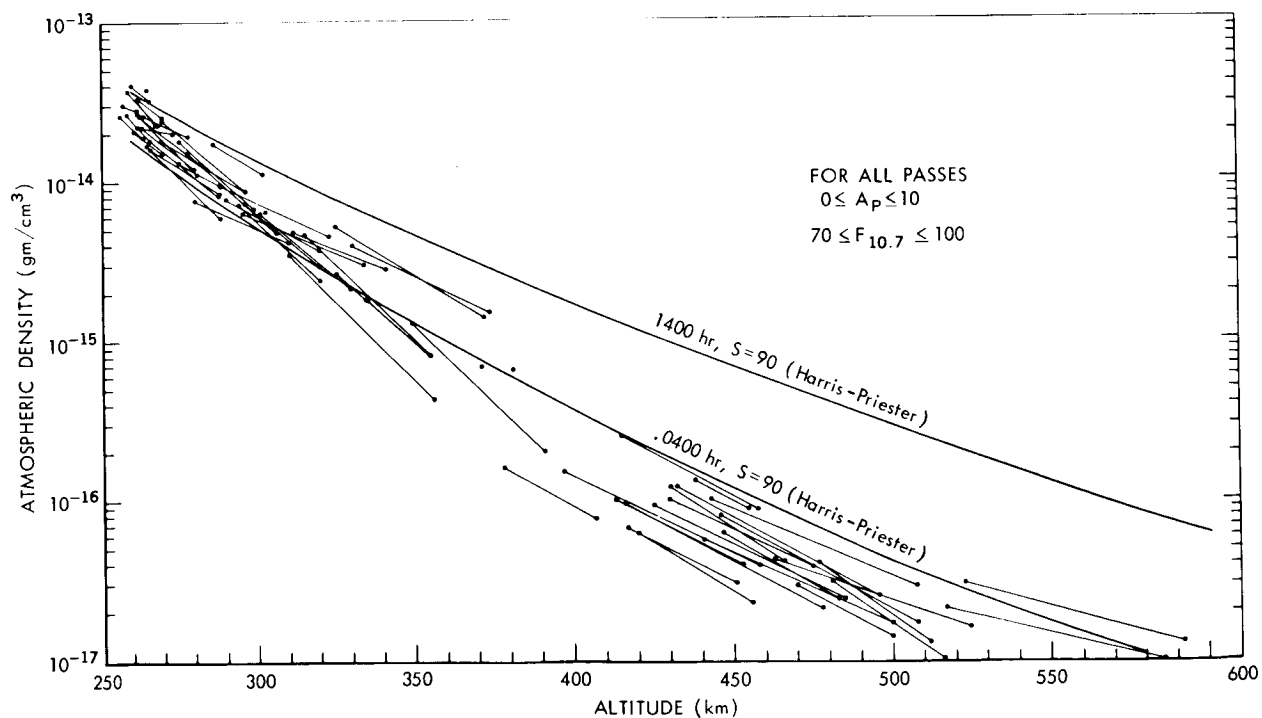


Figure 5—Atmospheric density versus altitude measured by the pressure gage experiment.

between 70 and 100, and most local times. It is seen that considerable variation in the atmospheric density occurs, resulting primarily from the differences in local time, a factor of 5 diurnal variation at 360 km being observed. The Harris and Priester model densities ($S = 90$) for 0400 and 1400 hours are shown for comparison purposes.

Continued analysis of the Explorer XVII data are currently underway to further define: (1) The quiet atmosphere and its variation with local time; (2) The variations from the quiet atmosphere resulting from solar and geomagnetic disturbances; and (3) Other effects not now apparent.

Mass Spectrometer Experiment Data

Concentrations as a function of altitude are shown in Figure 6 (Reference 14) where Nicolet's* model is included for reference. The data points shown are measured values converted to ambient number densities. Measurements of each mass taken on the same satellite interrogation are made approximately one minute apart and in the figure are joined by straight lines. The numbers refer to orbit numbers. Table 2 lists pertinent information for the passes shown in Figure 6.

*M. Nicolet, Private communication.

Table 2

Tabulated Mass Spectrometer Data (The Local Sun Time, Angle of Attack, Geographic Latitude and Longitude are Averaged Over the Four Minute Pass.)

Pass and station*	Date	Local Time (hr)	Angle α of attack (degrees)	Geographic Latitude (degrees)	Geographic Longitude (degrees)
15 BP	4/4/63	21.15	6	38.5	-75.0
50 COL	4/6/63	0.65	16	57.0	-149.0
80 COL	4/8/63	0.99	9	55.0	-147.0
80 FTM	4/8/63	4.89	63	18.0	-92.0
118 BP	4/10/63	18.81	70	37.0	-72.0
120 GF	4/11/63	20.32	51	51.0	-98.5
138 BP	4/12/63	2.51	12	37.0	-84.0
152 BP	4/13/63	2.01	14	39.5	-68.5
167 BP	4/14/63	1.65	20	39.5	-75.0
182 BP	4/15/63	1.54	25	37.0	-78.0
183 QUI	4/15/63	3.26	23	4.5	-79.0
197 BP	4/16/63	1.43	27	34.0	-81.5
211 BP	4/17/63	0.53	45	41.5	-71.5
226 BP	4/18/63	0.48	53	38.5	-74.0
241 BP	4/19/63	24.19	62	38.0	-79.5
242 MOJ	4/19/63	0.64	54	31.0	-121.5
254 NFL	4/20/63	22.75	82	49.0	-53.0
270 BP	4/21/63	23.30	80	41.5	-71.5
271 GF	4/21/63	22.88	85	45.0	-101.0
708 NFL	5/20/63	7.18	39	49.5	-49.5
795 OOM	5/26/63	15.81	63	-34.0	137.5
800 JOB	5/26/63	15.90	65	-37.5	19.0
888 JOB	6/1/63	13.24	33	-27.0	25.0

*The stations involved are: BP - Blossom Point, Md.; COL - College, Alaska; FTM - Fort Myers, Fla.; GF - Grand Forks, Minn.; QUI - Quito, Equador; MOJ - Mojave, Calif.; NFL - Newfoundland; OOM - Woomeera, Australia; JOB - Johannesburg, South Africa.

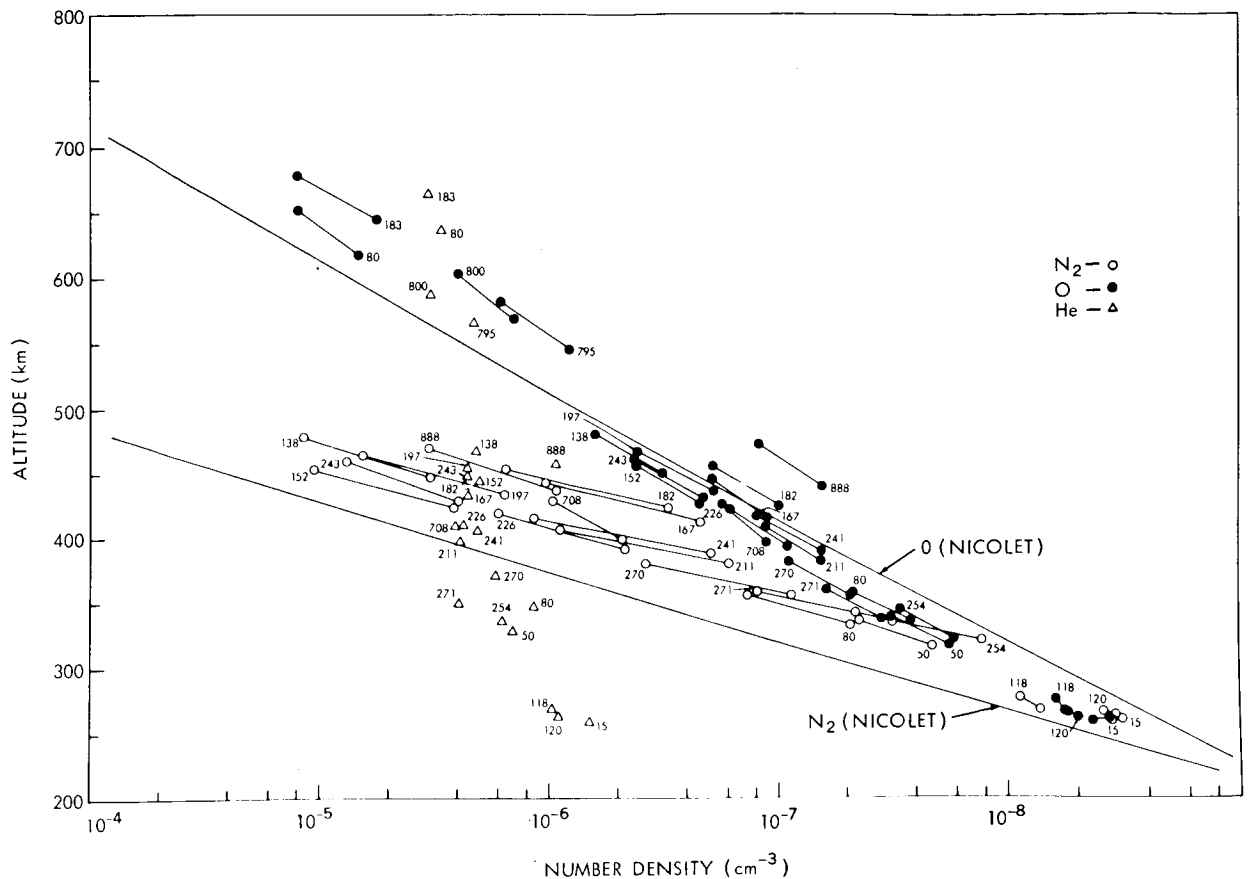


Figure 6—Average daytime and nighttime concentrations of He, O, and N₂ from Explorer XVII mass spectrometer experiment.

Of particular interest are the helium concentration versus altitude, and the altitude regions where helium, atomic oxygen and molecular nitrogen are predominant. It is seen that helium is the major constituent above 600 km, molecular nitrogen is predominant below 250 km, and atomic oxygen is predominant between these levels. It should be noted that the scale heights of the constituents at higher altitudes correspond to temperatures of about 700° at night.

A possible deviation of the nighttime N₂ distribution from a diffusive equilibrium condition at altitudes less than 400 km is also suggested by this figure. One possible explanation is that the diffusion time in this altitude region is the same order of magnitude as the diurnal variation period. It should also be kept in mind, however, that these data represent a variety of times and geographic locations and thus do not accurately present an instantaneous vertical profile.

Figure 7 shows the variation of mean mass with altitude. The mean mass was computed using the major constituents, N₂, O and He. Hydrogen, which the instrument was not designed to measure, could significantly reduce the value of the mean mass at higher altitudes.

The variation of concentration ratios of helium-to-oxygen and atomic oxygen-to-molecular nitrogen with altitude is shown in Figure 8. The solid lines drawn through the points are average

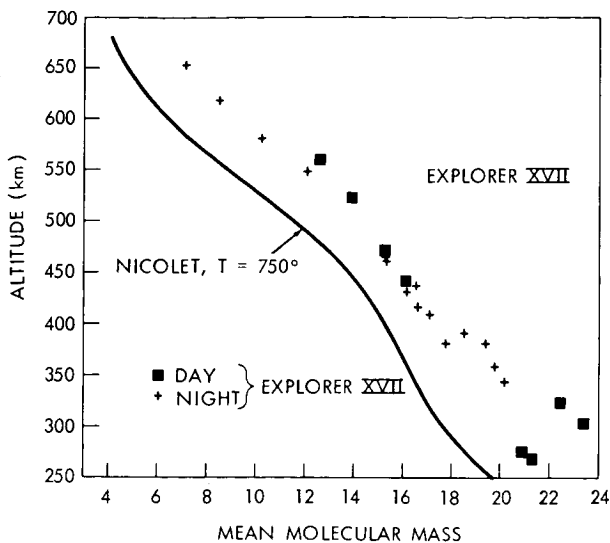


Figure 7—Mean molecular mass versus altitude from mass spectrometer.

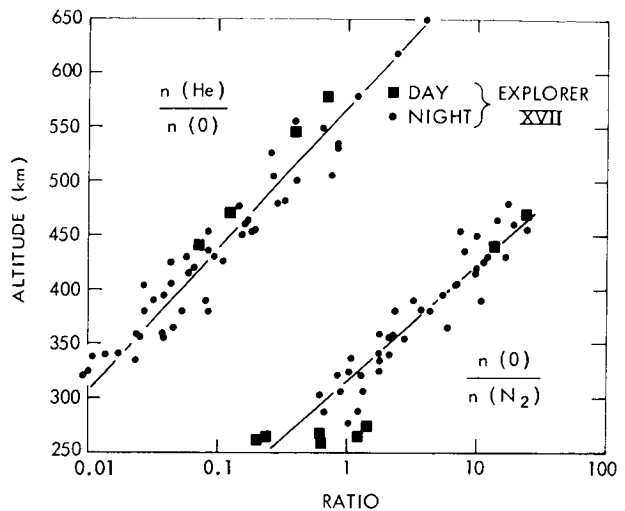


Figure 8—Ratios of $n(\text{He})/n(\text{O})$ and $n(\text{O})/n(\text{N}_2)$ versus altitude from mass spectrometer experiment.

values; as in all the data presented, the points are measured values and are not averaged, nor do they reflect any smoothing. It can be seen here again that helium is the dominant component above 600 km and that molecular nitrogen is predominant below about 250 km.

Langmuir Probe Experiment Results

Figure 9 shows the detailed variation of τ_e and N_i , measured during a series of near perigee passes near the F_2 maximum over Blossom Point, Maryland. These data were obtained over the three month satellite lifetime during which the rotation of the orbit plane caused a complete diurnal variation to occur. The data are shown as points or pairs of points, the latter corresponding to the measured values at the beginning and at the end of individual satellite passes.

At first glance one is struck by the lack of correlation between the gross diurnal variations (smoothed curves) and the changes during the individual passes, especially in the afternoon. Since perigee passes such as these can exhibit very little altitude change, this in-pass variation must be largely latitude dependent (10° change in latitude within average pass). The average in-pass change in τ_e implies a latitude gradient near Blossom Point of approximately 25°K per degree of latitude, corresponding to about a 10 percent change in τ_e within a pass. With few exceptions the changes in τ_e within a pass are accompanied by an inverse change in N_i which is even greater than 10 percent.

Plots similar to Figure 9 have been prepared from τ_e and N_i measurements at two other latitudes (10°N at Quito, 60°N at College), and the resulting gross diurnal variation curves at all three latitudes are shown in Figure 10. These data also correspond to the region of the F_2 maximum (below 400 km).

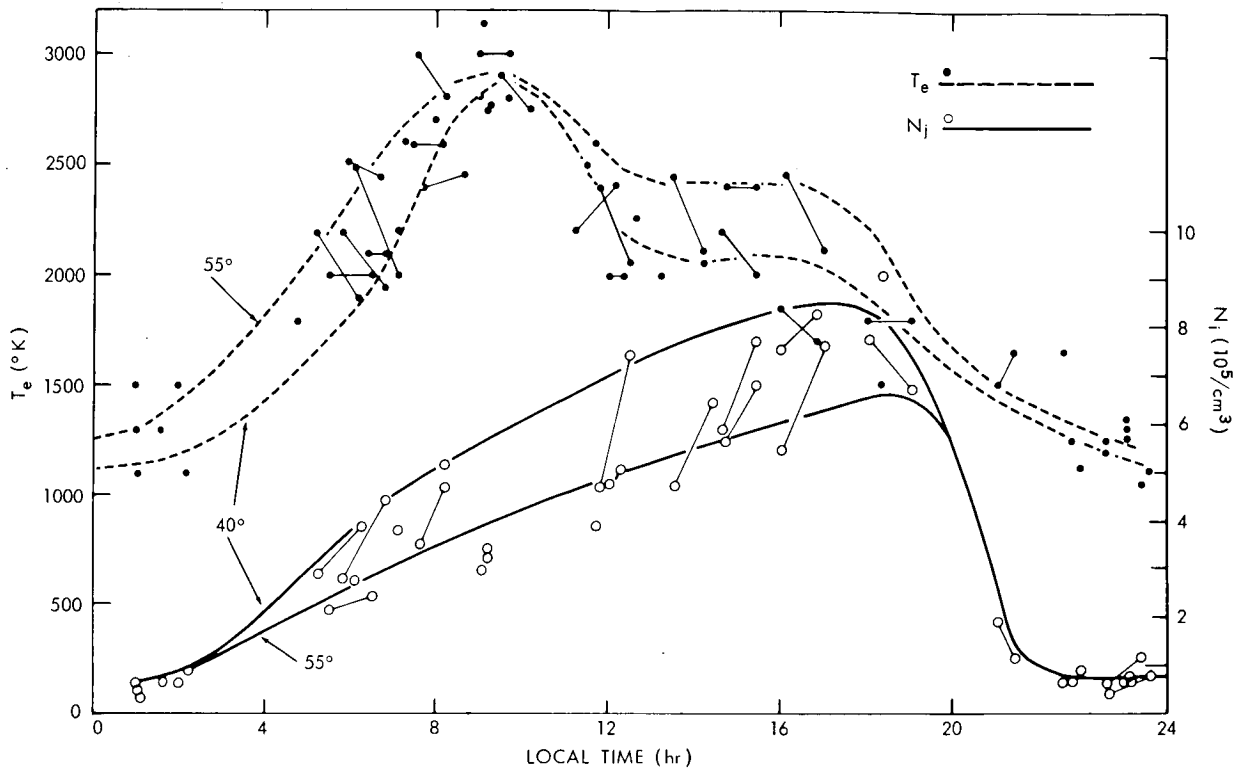


Figure 9—Diurnal variation of T_e and N_i for magnetic latitudes 40–55°N and altitudes 258 to 350 km, from the Langmuir probes.

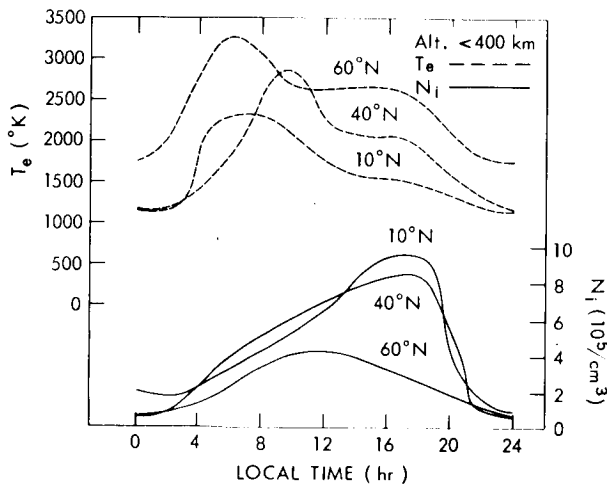


Figure 10—Averaged T_e and N_i showing the diurnal variation above three selected stations; Quito (10°N), Blossom Point (40°N) and College (60°N).

The T_e variation at the F_2 maximum at all latitudes shown is characterized by a steep morning rise, a mid-morning maximum, and afternoon plateau, and a gradual decrease near sunset. The nighttime values of T_e are somewhat variable but are always significantly above the neutral particle temperature (Reference 15), particularly at College, Alaska where the summer night at F_2 altitudes is short or non-existent.

The values of N_i rose gradually throughout the day, reaching a maximum density in the late afternoon, except at College where the maximum occurred in the early afternoon.

It should be noted that the curves in Figure 10 represent direct "in situ" measurements above specific geographic locations during the late spring and summer of 1963, and therefore should not be considered models of the diurnal variation at other altitudes, longitudes, and seasons. However, the analysis of higher altitude data from these sites, as well as data from other sites is now

in progress, and it is hoped that these data will help provide a better understanding of the global structure of the ionosphere.

In conclusion, it is clear from the simultaneous measurements that T_e and N_i are related in a generally inverse manner which agrees reasonably well with the inverse square relationship predicted by Hanson (Reference 16) and Dalgarno, et al. (Reference 17). The elevated nighttime values of T_e show that there is a heat source for the electrons at night, although its energy content is only a few percent of that required to cause the electron temperatures observed in the daytime (Reference 18).

ACKNOWLEDGMENTS

The success of a satellite laboratory such as discussed above results, clearly, from the efforts of many individuals. The authors gratefully and sincerely wish to acknowledge these efforts and specifically mention the major contributors: Messrs. J. S. Albus, J. P. Corrigan, J. L. Cooley, P. C. Donnelly, D. F. Fitzpatrick, W. D. Hoggard, R. E. Kidwell, J. N. Libby, C. C. Stephanides, and V. Zanner.

REFERENCES

1. Schultz, F. V., Spencer, N. W., and Reifman, A., "Upper Air Research Program, Progress Report No. 2," Contract W-33-038 ac-14050, Engineering Research Institute, University of Michigan, July 1, 1948, pp 129-137.
2. Horowitz, R., and Kleitman, D., "Upper Atmosphere Research Report XVIII: A Method for Determining Density in the Upper Atmosphere during Rocket Flight," U. S. Naval Research Laboratory Rept. NRL R 4246; PB 114748, October 1953.
3. Newton, G. P., Pelz, D. T., Miller, G. E., and Horowitz, R., "Response of Modified Redhead Magnetron and Bayard-Alpert Vacuum Gages Aboard Explorer XVII," NASA Technical Note D-2146, February 1964.
4. Meadows, E. B., "Design Requirements of a Mass Spectrometer for Satellite Use," presented at the 8th Annual Meeting of ASTM Committee E-14 on Mass Spectroscopy Atlantic City, N. J., June 1960.
5. Hall, L. G., P. F. Howden and T. F. Iwasaki, "Design of a Mass Spectrometer for Use in a Satellite," presented at the 8th Annual Meeting of the ASTM Committee E-14 on Mass Spectroscopy.
6. Spencer, N. W., and Reber, C. A., "A Mass Spectrometer for an Aeronomy Satellite," in: *Space Research III: Proceedings 3rd International Space Sciences Symposium*: 1151-1155, New York: Interscience, 1963.
7. Reber, C. A., and L. G. Hall, The Explorer XVII Mass Spectrometer, (in preparation).

8. Spencer, N. W., Brace, L. H., and Carignan, G. R., "Electron Temperature Evidence for Nonthermal Equilibrium in the Ionosphere," *J. Geophys. Res.* 67(1):157-175, January 1962.
9. Brace, L. H., Spencer, N. W., and Carignan, G. R., "Ionosphere Electron Temperature Measurements and Their Implications," *J. Geophys. Res.* 68(19):5397-5412, October 1, 1963.
10. Nagy, A. F., Brace, L. H., Carignan, G. R., and Kanal, M., "Direct Measurements Bearing on the Extent of Thermal Nonequilibrium in the Ionosphere," *J. Geophys. Res.* 68(24):6401-6412, December 15, 1963.
11. Newton, G. P., Horowitz, R. Priester, W., "Pressure Gage Experimental Data and Interpretation," AGU Presentation of Aeronomy Results from the Explorer XVII Satellite, 45th Annual Meeting, Washington, D. C., April 23, 1964.
12. Bryant, R., "Densities Obtained from Drag on the Explorer 17 Satellite," *J. Geophys. Res.* 69(7):1423-1425, April 1, 1964.
13. Jacchia, L. G., and Slowey, J., "Atmospheric Heating in the Auroral Zones: A Preliminary Analysis of the Atmospheric Drag of the Injun 3 Satellite," *J. Geophys. Res.* 69(5):905-910, March 1, 1964.
14. Reber, C. A., and Nicolet, M., "Mass Spectrometer Data and Interpretation," AGU Presentation of Aeronomy Results from the Explorer 17 Satellite, AGU 45th Annual Meeting, April 21-24, 1964.
15. Harris, I., and Priester, W., "Theoretical Models for the Solar-Cycle Variation of the Upper Atmosphere," *J. Geophys. Res.* 67(12):4585-4592, November 1962.
16. Hanson, W. B., "Electron Temperatures in the Upper Atmosphere," in: *Space Research III: Proceedings 3rd International Space Sciences Symposium*: 282-302, New York: Interscience, 1963.
17. Dalgarno, A., McElroy, M. B., and Moffett, R. J., "Electron Temperatures in the Ionosphere," *Planet. Space Sci.* 11(5):463-484, May 1963.

N65-29554

THE TEMPERATURE OF CHARGED PARTICLES IN THE UPPER ATMOSPHERE

by

R. E. Bourdeau

Goddard Space Flight Center

SUMMARY

29554

Three general methods of investigating charged particle temperatures in the upper atmosphere have been used: direct measurements from rockets and satellites; indirect determination using electron scale heights measured from rockets and satellites; ground-based radar incoherent backscatter experiments. The latitude, altitude, and temporal trends of these results are reviewed and the implications discussed.

Observations by all three methods are consistent in showing that the electron temperature increases with latitude for both daytime and nighttime conditions. Moderate differences between the daytime electron and neutral gas temperatures are indicated to altitudes well above the F2 peak for a winter mid-latitude ionosphere at an epoch between solar maximum and solar minimum conditions. Much larger daytime differences are observed for summer months and for solar minimum conditions. All of these trends reflect corresponding changes in the electron density.

The daytime observations are consistent with ultraviolet radiation as the predominant heat source if the possibility of photoelectrons diffusing along magnetic field lines and depositing their excess energy elsewhere is included. A nighttime heat source (small compared to the daytime ultraviolet effect) is required to explain the observations.

Author

INTRODUCTION

At the first COSPAR meeting, in Florence, early direct measurements of electron temperature T_e were reported from rockets (Reference 1) and from the Explorer VIII Satellite (Reference 2). The Japanese rocket results suggested temperature equilibrium between electrons and neutral constituents in the E region of the daytime ionosphere. Low values of T_e in the daytime E region subsequently were confirmed by rocket experiments (Reference 3). However, other rocket electron temperature measurements (References 4, 5, and 6) showed that significant departures from temperature equilibrium are more often observed than not in the E region even at night. The results of Spencer, et al. (Reference 3) showed that departures from temperature equilibrium extended well into the daytime F region.

Early measurements of charged particle temperatures applicable to the region considerably above the F2 peak at mid-latitudes for solar conditions when the 10.7 cm flux index ($S_{10.7}$) was $150/\text{wm}^2$ cps were reviewed by Bauer and Bourdeau (Reference 7) and Bourdeau (Reference 8). Implications of temperature equilibrium at high altitudes (which they optimistically derived from the data) critically depended on the assumed neutral gas temperature T_g . When these early direct measurements of T_e and of the average electron-ion temperature $(T_e + T_i)/2$ obtained from electron density profiles are compared with more recent reference atmospheres, moderate values of T_e/T_g of the indicated level of solar activity of about 1.3 are indicated at midday even to altitudes above 1000 km. These observations are in approximate agreement with the theoretical model of Hanson (Reference 9) who assumed electron density values close to these particular observational conditions.

More extensive charged particle temperature observations for different epochs of the solar cycle now have been made by use of ground-based radar incoherent backscatter experiments, by additional direct measurements from rockets and satellites, and indirectly from electron density profiles obtained from rockets and the Alouette Topside Sounder Satellite (1962 $\beta\gamma 1$). In general, the trend is toward much larger departures from temperature equilibrium than indicated in the theoretical models and in the earlier observations especially at the higher altitudes.

It is timely then, as done herein, to compare these trends with the introduction of latitude and temporal electron density variations in the early theoretical models.

FACTORS CONTROLLING THE ELECTRON TEMPERATURE

The principal factors controlling T_e are:

Heat Input

I. Solar Ultraviolet Radiation

1. Locally-deposited energy
2. Diffusing photoelectrons ($Z > 300$ km)

II. Corpuscular Radiation

Heat Loss

I. Inelastic collisions with neutral constituents ($Z < 250$ km)

II. Elastic collisions with ions ($Z > 250$ km)

1. Ion temperature controlled only by neutral constituents
2. Ion temperature also controlled by electrons ($Z > 600$ km)

III. Coulomb collisions of photoelectrons with ambient electrons

Thermal conductivity in the electron gas ($Z > 600$ km)

Theoretical charged particle temperature models based on solar ultraviolet heating alone have been developed by Hanson and Johnson (Reference 10), Hanson (Reference 11), and Dalgarno, et al. (Reference 12). Of these, Hanson's model is the most complete in that he introduced the possibility of (1.) photoelectrons diffusing along magnetic field lines and depositing their energy elsewhere, (2.) the loss of ion temperature control by the neutral constituents and (3.) the importance of thermal conductivity in the electron gas at high altitudes. The indicated altitudes where these factors are important represent Hanson's estimates based on his assumed model atmosphere and electron density profile.

The models of Hanson and of Dalgarno, et al. each used a single electron density profile and both depended on rocket measurements of ultraviolet radiation intensity (Reference 13) to estimate the heat input, Q . The EUV intensity used applies to a level of solar activity corresponding to $S_{10.7} \approx 100$. The heat input is the product of the EUV intensity, the ionization cross-sections, and the density of the ionizable constituents and of the heating efficiency. Both theoretical charged particle temperature models exhibit approximately the same altitude behavior wherein low values of T_e/T_g are indicated in the E region, with the ratio reaching a maximum of about 2.0 to 2.5 at 200 km and decreasing in the upper F region. A principal and important difference is that the model of Dalgarno, et al. has $T_e - T_g$ essentially vanishing above 300 km whereas Hanson's model permits constant values for T_e/T_g of about 1.2 at extremely high altitudes.

Because the observational evidence is most heavily weighted for altitudes above the F2 peak, the most important effect to examine is the efficiency of cooling to positive ions. On the assumption that cooling occurs only by elastic collisions to atomic oxygen ions, the electron temperature is given by (Reference 9):

$$\frac{T_e - T_i}{T_e^{3/2}} \approx \frac{2.1 \times 10^6 Q}{N_e^2}, \quad (1)$$

where Q is the heat input to the electrons expressed in $\text{ev}/\text{cm}^3 \text{ sec}$ and N_e is the electron density. For values of Q greater than a critical value Q_c ,

$$Q_c \approx 2 \times 10^{-7} N_e^2 T_i^{-1/2}, \quad (2)$$

there is no solution to Equation 1 and T_e is not limited by energy transfer to positive ions (Reference 10). If $Q = Q_c$, $T_e > 2T_i$ and if $Q \gg Q_c$, very large "runaway" values of T_e will result and heat conduction in the electron gas is an important effect.

SOLAR CYCLE VARIATIONS OF T_e

In Figure 1 are illustrated daytime mid-latitude electron density profiles typical of December 1960 and 1962, respectively. The principal differences to note are the much higher values of N_{max} and h_{max} for the 1960 period, and the constant electron scale height for the 1960 case in contrast to the continually varying scale height for the 1962 profile. The monthly mean of the solar 10.7 cm flux during December 1960 was $150/wm^2$ -cps.

In Figure 2 is presented the mid-latitude diurnal electron temperature variation directly measured during November-December 1960 (Reference 14) from the Explorer VIII Satellite for magnetically-quiet days assuming T_e is constant with altitude. Depending on which of the current reference atmospheres for the pertinent level of solar activity is used, the average midday T_e value of $1600^\circ K$ taken at midday and at altitudes above 1000 km corresponds to an estimated value for T_e/T_g of about 1.15 to 1.33.

It is seen from Equation 1 that the ratio of the heat input to the square of the electron density, Q/N_e^2 , controls the electron temperature at high altitudes. The Q/N_e^2 computed at 400 km from the December 1960 N_e profile in Figure 1 closely corresponds to the value used by Hanson as an upper limit in his model. We have taken into account that the heat input Q would be larger than in Hanson's case by assuming a linear change of EUV intensity with the decimetric flux index, $S_{10.7}$, and a corresponding change in the density of the ionizable constituent, $n(0)$. The higher heat input is compensated for largely by the higher electron density than that used by Hanson. Thus we should and do estimate similar values for T_e .

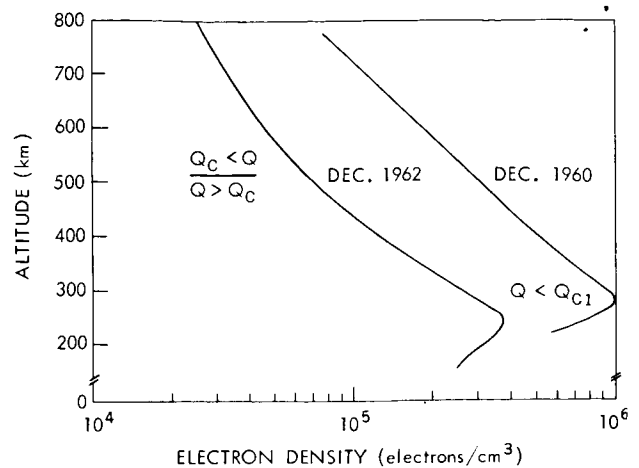


Figure 1—Typical winter mid-latitude electron density profiles.

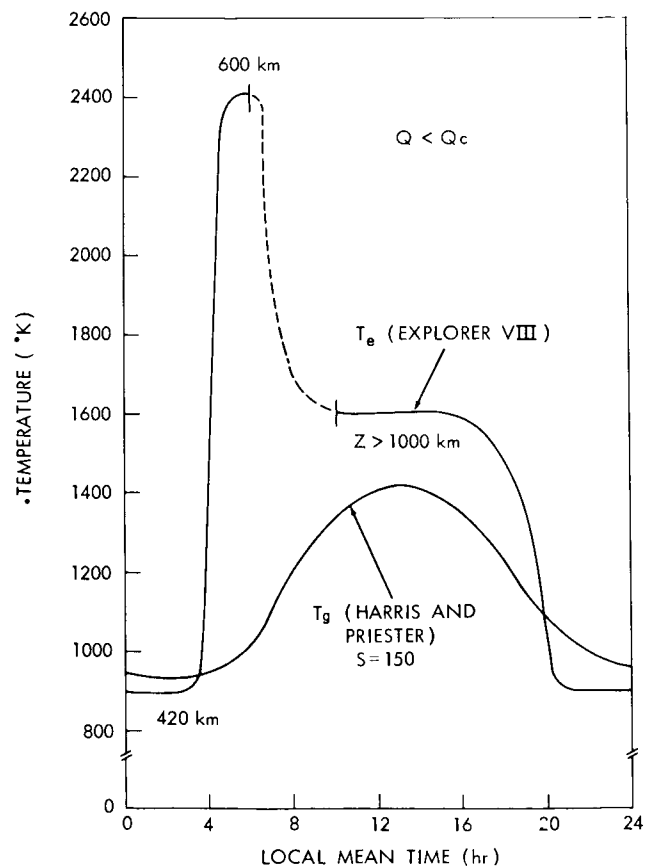


Figure 2—Diurnal electron temperature variation measured during November 1960 from Explorer VIII for magnetically-quiet days at mid-latitudes assuming T_e is constant with altitude (425-2400 km).

as did Hanson. Consequently, we find excellent agreement between the observed T_e/T_g of 1.15 to 1.33 and Hanson's theoretical upper limit of about 1.15.

In Figure 3, the Explorer VIII data are included with measurements of $(T_e + T_i)/2$ computed from early rocket N_e profiles on the assumption of diffusive equilibrium. Of particular interest is the ion density profile obtained by Hale (Reference 15) at midday and at about the same time as the Explorer VIII observations. Here a value for $(T_e + T_i)/2$ of 1600°K (Reference 11) is derived for the region above 1000 km. The data are too sparse for a firm conclusion but there is a suggestion by the inter-comparison that for winter midday mid-solar cycle conditions $T_e \approx T_i$ at altitudes above 1000 km but that both the electron and ion temperatures are moderately higher than the neutral gas temperature. This would be consistent with Hanson's arguments that above 600 km: (1) thermal conductivity of the electron gas could support differences between T_e and T_g which are constant with altitude and furthermore; and that (2) the electrons rather than the neutral constituents could control the ion temperature so that $T_i > T_g$.

Low midday values of T_e/T_g at high altitudes also can be implied from the measurement in December 1961 of a value for $(T_e + T_i)/2$ of 1235°K (Reference 16) from a rocket flight for which an equivalent ion temperature has been inferred (Reference 17). However, we emphasize here Equation 1 and the extreme sensitivity of T_e to the electron density. We further emphasize that in the actual case, ratios of Q/N_e^2 which permit only moderate rather than large midday departures from temperature equilibrium as is indicated for December 1960 at high altitudes perhaps represent the exception rather than the rule at middle and high latitudes.

Now we shall consider the drastic changes in charged particle temperature characteristics as we approach solar minimum conditions. The average value for the index S of solar activity corresponding to the December 1962 profile illustrated in Figure 1 was 85. Taking into account a linear decrease in EUV intensity from the time of the rocket EUV measurements (Reference 13) and a corresponding decrease in the density of the ionizable constituents and computing Q_c directly from the observed N_e profile, the estimated ratio Q/Q_c is larger than 2. Because of the uncertainties in our knowledge of ionization cross-sections and model atmospheres, the computation of Q/Q_c is suggestive rather than quantitative. Within these uncertainties, it does appear that the EUV effect for low electron densities is sufficient to cause very large electron and possibly runaway electron temperatures.

Figure 4 is a mid-latitude diurnal variation of electron scale heights calculated for an altitude of 500 km from electron density profiles obtained from Alouette satellite during the period October-December 1962 (Reference 17). It is seen that on the assumption of diffusive equilibrium and O^+ as the principal ionic constituent, values for $(T_e + T_i)/2$ of 1500°K are indicated at midday. Assuming $T_i = T_g$, a value for T_e/T_g of about 2.0 is indicated (Reference 18), which is much in excess of the December 1960 value. This should not be surprising because of the large increase in the ratio Q/N_e^2 at 400 km and above from December 1960 to December 1962.

If the assumed model atmosphere and ionization cross-sections on which the computation of Q/Q_c depends are correct, the fact that runaway electron temperatures are not observed suggests

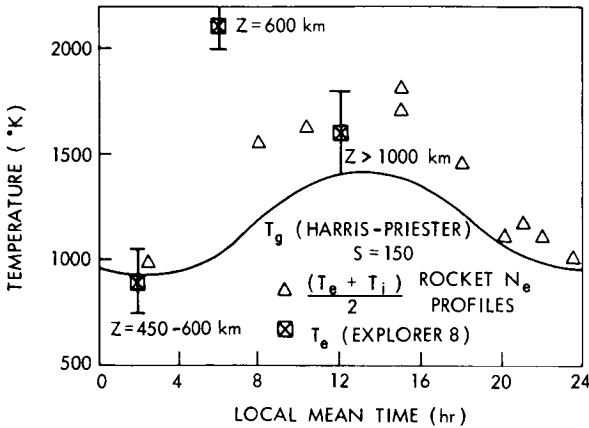


Figure 3—Early charged particle temperature measurements in the upper ionosphere.

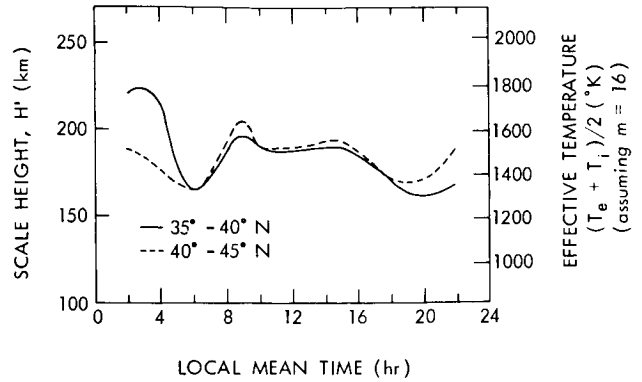


Figure 4—Scale heights at 500 km from Alouette data (Reference 18).

that much of the heat input is not deposited locally. Also it should be emphasized that the ratio of 2.0 for T_e/T_g must be considered an upper limit since it assumes that at 500 km the ion and neutral gas temperatures are the same. Evans (Reference 19) with radar-back-scatter experiments observes at similar latitudes and under similar conditions that $T_i > T_g$ even as low as 400 km. Thus the values for T_e implied from Figure 4 may indeed be somewhat overestimated. That the electron temperature begins to control the ion temperature at an altitude lower than that estimated by Hanson is explainable on the basis that the scale heights illustrated in Figure 4 were measured for a different model atmosphere and electron density profile than that assumed by Hanson.

In summary, the observational evidence shows, as expected, a large increase in T_e/T_g between December 1960 and December 1962 which corresponds to a change in the ratio of the heat input to the square of the electron density. In the 1962 case, there still appears to be a sufficient EUV flux to explain the high daytime electron temperatures observed at 500 km during periods of low electron density. There is indirect evidence that some of the energy is not locally deposited and direct evidence from Evans' results that the ion as well as the electron temperature is raised above the neutral gas temperature.

SEASONAL VARIATION OF T_e

Ionosonde data have shown that the electron density is much higher at the F2 peak in winter than it is in summer. For example, N_{max} measured at Washington, D. C., was on the average more than a factor of two larger in the summer than in the winter of 1962. Corresponding changes in $S_{10.7}$, which reflect changes in heat input, are not observed. These factors contribute to making the ratio Q/N_e^2 much higher in the summer than in the winter months. Consequently, it is possible that, at least for mid-latitudes in the Northern Hemisphere, high ratios of T_e/T_g will persist high into the upper F region throughout a solar cycle. This could explain why some of the early rocket results taken between solar maximum and solar minimum conditions (Reference 3) show different electron temperature behavior.

DIURNAL VARIATION OF ELECTRON TEMPERATURE

As illustrated in Figure 2, the Explorer VIII satellite results suggest a significant increase in T_e during the early morning hours. High values of T_e in the early morning at the F2 peak are also indicated in ground-based backscatter observations (Reference 20) and, at higher altitudes, by Evans (Reference 19).

Early morning maxima in electron temperature have been confirmed by use of the Explorer XVII satellite from which the maximum value of T_e is placed near 9h local time (Reference 21). The electron scale height results from Figure 4 also suggest a maximum T_e at approximately the same local time (Reference 18). Here the high scale heights for night-time conditions reflect the importance of light ionic constituents. However, for daytime conditions it would be expected that m_i is relatively constant and thus that the early morning maximum represents a true T_e maximum. It should be pointed out that the nature and existence of an early morning peak in T_e has not been emphasized in the Ariel (1962 01) satellite results (Reference 22).

It is possible to show—from ionosonde data and Equation 1 on the assumption of no EUV absorption above 300 km—that the ratio Q/N_e^2 which controls T_e near the F2 peak maximizes at dawn. However, at high solar zenith angles there could be enough absorption above 300 km to shift the T_e maximum to later in the morning. This reasoning would insert a latitude and altitude dependence on the time of the diurnal T_e maximum. It would be expected that the effect becomes more diffuse at higher altitudes because here the diurnal amplitude of the ionizable constituent has increased relative to the amplitude of the diurnal N_e variation (Reference 14).

LATITUDE VARIATION OF ELECTRON TEMPERATURE

Early ionosonde data showed that the daytime electron density at the F2 maximum increases drastically as we go from mid-latitudes toward the geomagnetic equator. More recently, results from the Alouette satellite have extended the observation that the geomagnetic field plays an important role in governing the electron density distribution to altitudes well above the F2 peak. In Figure 5 an idealized representation of the latitudinal behavior of N_e prepared by Jackson* is presented by combining topside sounder (Reference 23), and ionosonde (Reference 24) results. Other Alouette data (Reference 25) show that the equatorial anomaly builds up earlier in the day at the eastern longitudes. It should be clear from the illustration and Equation 1, that in the daytime T_e should increase with increasing latitude on the basis of the electron density behavior alone, if we assume no EUV absorption above 300 km and no latitude dependence of the neutral gas characteristics. An increase of daytime electron temperatures with latitude is indicated by all three methods of charged particle temperature investigation for altitudes below about 800 km. Alouette satellite data suggest constant electron scale heights above 800 km (Reference 25).

The ground-based incoherent backscatter results at the geomagnetic equator (Reference 26) show that in the region 200-350 km T_e/T_i is close to 2 during the daytime hours, maximizing at about 275 km. Above about 400 km in the daytime the results show that T_e/T_i is unity. Daytime ion temperatures† for March 1964, in the vicinity of 1000°K are observed. Depending on the

*J. E. Jackson, Private communication.

†K. Bowles, Private communication.

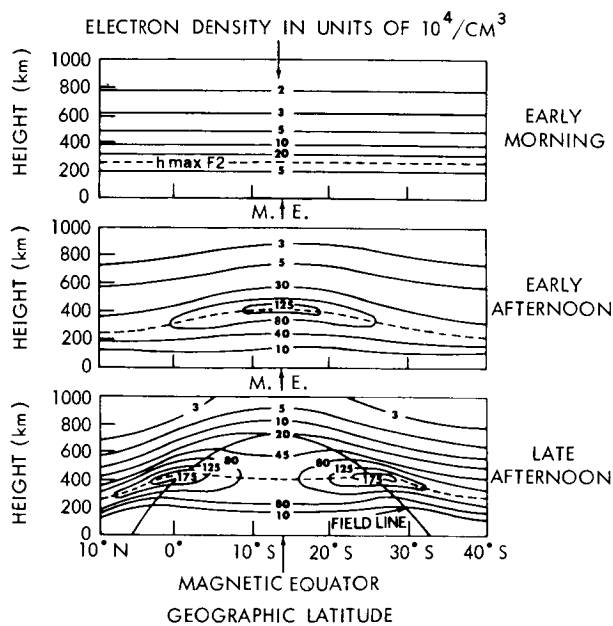


Figure 5—Idealized representation of equatorial anomaly along 75 W meridian based upon data by Lockwood and Nelms (Topside) and J. W. Wright (Bottomside).

in the 300-400 km and that T_e increases with altitude up to 700 km (Reference 27). In more recent results taken during July 1963, Evans (Reference 19) offers two possible interpretations for his daytime data obtained for altitudes up to 700 km: (1) if the ionic constituent is all O^+ , T_e and T_i continually increase with altitude to values of 2320°K and 2040°K at approximately 700 km; or (2) by assuming a mixture of 80 percent O^+ and 20 percent He^+ at 700 km, T_e maximizes at about 450 km then decreases to 1960°K at 700 km while T_i increases to a value of 1410°K at 700 km. The trend of ion composition results (References 9, 16, 28, 29, and 30) would imply that the latter alternative is the more likely. If so, it would be consistent with high values of Q/N_e^2 permitting high values of T_e especially below 450 km, and the possibility that cooling to light ionic constituents is becoming effective above 450 km. It should be noted that Equation 1 applies only for O^+ and that the cooling efficiency to ions should be inversely proportional to the ionic mass m_i .

Direct electron temperature measurements measured with the use of the Ariel satellite also show that T_e significantly increases with latitude (Reference 22) the steepest gradient centered at a geomagnetic latitude of about 20°. The midday T_e value given at the geomagnetic equator for an altitude of 400 km is about 900°K which compares favorably with T_e given by Harris-Priester for the pertinent level of solar activity and with the T_i measurements of Bowles. The trend of the latitude variation at 400 km obtained from the Ariel satellite is generally consistent with the latitude variation N_e , and thus with the ground-based results of both Bowles and Evans (Reference 22).

However, the situation above 400 km is more complicated. The Ariel results show T_e increasing with altitude up to maximum height of the observations at all latitudes. The continuing increase with altitude of T_e from Ariel at higher latitudes would be consistent with the 1962 results

adequacy of the Harris-Priester reference atmosphere, this would put an upper limit on T_e/T_g of 1.2 even during solar minimum conditions. Low values for T_e/T_g at high altitudes would be expected near the geomagnetic equator because of the generally higher values of N_e and because near this location vertical diffusion of photoelectrons tends to be inhibited. This supposes heating only by EUV radiation.

The incoherent backscatter results of Evans (References 19 and 27) taken near 50° north magnetic latitude show drastically different behavior of charged particle temperatures. This would be expected because of: (1) the generally lower value of N_e than would exist at the equator; and (2) the higher probability of the photoelectron diffusion effect, and (3) additional sources of ionization. The earlier results of Evans' taken in March-April 1962, show daytime ratios of T_e/T_i of up to 1.6

of Evans but not for the likely possibility which Evans offers for his 1963 results, that T_e decreases above 450 km. We suffer here in the comparison from a lack of simultaneity in the observations. An increase of T_e at all altitudes in 1962 is perhaps reconcilable with a possible decrease in T_e above 450 km in 1963 on the base of a lowering with solar activity of the $O^+ - He^+$ transition altitude.

The fate of the photoelectrons which apparently escape from the altitude of their formation is not yet clear. We have made a case that for the December 1962 mid-latitude profile the ratio of Q/Q_e possibly is large enough that the high values of T_e observed up to 500 km at mid-latitudes could be explained on the basis of the EUV effect and heat conduction in electron gas. In his interpretation of the daytime altitude behavior of T_e from the Ariel satellite, Willmore (Reference 22) finds that for altitudes up to 600 km, the altitude dependence of the heat input computed from the observed T_e and N_e (see Equation 1) follows the scale height of atomic oxygen and thus also concludes that the main energy input below 600 km is by the photoionization of atomic oxygen. Willmore also finds that the increase of T_e above 800 km can be explained by additional energy input from the photoelectrons diffusing from below together with the main energy loss mechanism being thermal conduction in the electron gas rather than collisions with positive ions. However, his conclusions depend on an assumed model atmosphere and assume that the photoionization of helium is unimportant.

NIGHTTIME CHARGED PARTICLE TEMPERATURE MEASUREMENTS

The charged particle temperature measurements of Figures 2 and 3 are too sparse and the dependency on the assumed reference atmosphere too critical to draw firm conclusions about departures from temperature equilibrium at night for mid-solar cycle conditions. Bowles, et al. (Reference 20) observe that T_e/T_i is unity at night at the geomagnetic equator with $T_i \approx 600^\circ K$, the latter value being in fair agreement with the Harris-Priester reference atmosphere. Remembering the different altitudes and times of the observations, Willmore, et al. (Reference 22) report that at 1000 km midnight values of T_e increase from about $800^\circ K$ at the equator to $1400^\circ K$ at 60° magnetic latitude. Evans (Reference 19) indicates a small but significant departure from temperature equilibrium in the F region at 50° north magnetic latitude. The definite evidence from the Ariel satellite for quite significant departures from temperature equilibrium at night at medium latitudes have been confirmed by rocket measurements (Reference 6). The Ariel results show that the nighttime departure from equilibrium becomes more pronounced at the higher latitudes. The nighttime source required to explain the Ariel observations has been estimated to be less than 30 percent of the daytime EUV heat input (Reference 22).

As an example of the sensitivity of nighttime electron temperatures to small sources of heat input, consider Equation 1 and the fact that for solar minimum conditions, N_e varies by a factor of 4 from day to night at 400 km (Reference 18). From these considerations, it can be shown that less than 10 percent of the daytime EUV heat input would be required at night to maintain the same temperature difference ($T_e - T_g$) throughout the day.

CONCLUDING REMARKS

For all temporal conditions and latitudes, large departures from temperature equilibrium ($T_e/T_g > 2$) are observed in the daytime lower F region at the altitude of maximum rate of electron productions. Moderate but significant daytime values for T_e/T_g are maintained to very high altitudes in winter at mid-latitudes in the middle of the solar cycle. Daytime mid-latitude data taken for summer and/or solar minimum conditions when electron densities generally are much lower reveal much larger values of T_e/T_g persisting to altitudes well above the F2 maximum. There is considerable evidence at least for altitudes below 600 km that the diurnal electron temperature maximum occurs in the early morning. Observed increases of daytime electron temperature with latitude follows the observed electron density which is under geomagnetic control. All of these temporal and latitudinal trends in the observed electron temperature are consistent with EUV as the predominant daytime source of electron heating. The uncertainties in calculating the EUV effect make it difficult to infer other possible daytime heat sources at the present time. The charged particle temperature observations strongly suggest the possibility that not all of the EUV energy is locally deposited—an important factor to be considered in the theories of formation of the ionosphere. There is some evidence, principally from backscatter experiments, that the ion temperature is controlled by electrons at very high altitudes.

Significant departures from temperature equilibrium at night have been observed especially for conditions close to solar minimum. The estimated intensity of this additional heat source increases with latitude but at all altitudes is only a fraction of the daytime EUV effect.

ACKNOWLEDGMENT

The author is grateful to S. J. Bauer, L. J. Blumle, J. V. Evans and K. Bowles, for early access to the results of their charged particle temperature observations.

REFERENCES

1. Aono, Y., Hirao, K., and Miyazaki, S., "Positive Ion Density, Electron Density and Electron Temperature in the Ionosphere by the Kappa-8-5 and -6 Rockets," *Japan Radio Res. Lab J.* 8(40): 453-465, November 1961.
2. Bourdeau, R. E., "Ionospheric Results with Sounding Rockets and Explorer VIII Satellite," in: *Space Research II: Proceedings 2nd International Space Sciences Symposium*: 554-573, New York: Interscience, 1961.
3. Spencer, N. W., Brace, L. H., and Carignan, G. R., "Electron Temperature Evidence for Nonthermal Equilibrium in the Ionosphere," *J. Geophys. Res.* 67(1): 157-175, January 1962.
4. Smith, L. G., "Electron Density Measurements by the Asymmetrical Bipolar Probe," *J. Geophys. Res.* 66(8): 2562, August 1961 (Abstract).

5. Aono, Y., Hirao, K., and Miyazaki, S., "Rocket Observation of Ion Density, Electron Density and Electron Temperature in Ionosphere," *Japan Radio Res. Lab J.* 9(46): 407-419, November 1962.
6. Brace, L. H., Spencer, N. W., and Carignan, G. R., "Ionosphere Electron Temperature Measurements and Their Implications," *J. Geophys. Res.* 68(19): 5397-5412, October 1, 1963.
7. Bauer, S. J., and Bourdeau, R. E., "Upper Atmosphere Temperatures Derived from Charged Particle Observations," *J. Atmospheric Sci.* 19(3):218-225, May 1962.
8. Bourdeau, R. E., "Ionospheric Research from Space Vehicles," *Space Sci. Rev.* 1(4):683-728, May 1963.
9. Hanson, W. B., "Electron Temperatures in the Upper Atmosphere," in: *Space Research III: Proc. 3rd International Space Sciences Symposium*: 282-302, New York: Interscience, 1963.
10. Hanson, W. B., and Johnson, F. S., "Electron Temperatures in the Ionosphere," *Mem. Soc. Roy. Sci. Liège* (Coll. in-8°), 4: 390-424, 1961.
11. Hanson, W. B., "Upper Atmosphere Helium Ions," *J. Geophys. Res.* 67(1): 183-188, January, 1962.
12. Dalgarno, A., McElroy M. B., and Moffett, R. J., "Electron Temperatures in the Ionosphere" *Planet Space Sci.* 11(5): 436-484, May 1963.
13. Hall, L. A., Damon, K. R., and Hinteregger, H. E., "Solar Extreme Ultraviolet Photon Flux Measurements in the Upper Atmosphere of August 1961," in: *Space Research III Proc. 3rd International Space Sciences Symposium*: 745-759, New York: Interscience, 1963.
14. Bourdeau, R. E., and Donley, J. L., "Explorer VIII Satellite Measurements in the Upper Ionosphere," *Proc Roy. Soc. A.* (To be published).
15. Hale, L. C., "Ionospheric Measurements with a Multigrid Potential Analyzer," *J. Geophys. Res.* 66(5): 1554, May 1961 (Abstract).
16. Taylor, H. A., Jr., Brace, L. H., Brinton, H. C., and Smith, C. R., "Direct Measurements of Helium and Hydrogen Ion Concentration and Total Ion Density to an Altitude of 940 Kilometers," *J. Geophys. Res.* 68(19): 5339-5347, October 1, 1963.
17. Bauer, S. J., "Some Implications of a Direct Measurement of the Hydrogen and Helium Ion Distribution in the Upper Atmosphere," *J. Geophys. Res.* 69(3): 553-555, February 1, 1964.
18. Bauer, S. J., and Blumle, L. J., "Mean Diurnal Variation of the Topside Ionosphere at Mid-Latitudes," *J. Geophys. Res.* 69(17): September 1, 1964 (In press).
19. Evans, J. V. and Loewenthal, M., "Ionospheric Backscatter Observations," presented at XV General Assembly of URSI, Washington, April 1964.
20. Bowles, K. L., Ochs, G. R., and Green, J. L., "On the Absolute Intensity of Incoherent Scatter Echoes from the Ionosphere," *J. Res. Nat. Bur. Stand. (D. Rad. Prop.)* 66D(4): 395-407, July-August 1962.

21. Brace, L. H., Spencer, N. W., and Dalgarno, A., "Electrostatic Probe Data and Interpretation," Presented at the AGU Meeting, April 21-24, 1964.
22. Willmore, A. P., *Proc. Roy. Soc. A.*, July-September, 1964 (In press).
23. Lockwood, G. K., and Nelms, G. L., "Topside Sounder Observations of the Equatorial Anomaly in the 75°W Longitude Zone," *J. Atmos. Terr. Phys.*, 26: 569-580, 1964.
24. Wright, J. W., "Cortes Verticales de la Ionòsfera a Travès del Ecuador Geomagnético," *National Bureau of Standards*, Boulder, Colo., TN 138; PB 161639, April 6, 1962.
25. King, J. W., Smith, P. A., Ecdes, D., and Helm, H., "The Structure of the Upper Ionosphere as Observed by the Topside Sounder Satellite, Alouette," Radio Research Station I.M. 94, July 1963.
26. Bowles, K., "Incoherent Backscatter from the Ionosphere," presented at XIV General Assembly of URSI, Tokyo, September 1963.
27. Evans, J. V., "Diurnal Variation of the Temperature of the F Region," *J. Geophys. Res.* 67(12):4914-4920, November 1962.
28. Bourdeau, R. E., Whipple, E. C., Jr., Donley, J. L., and Bauer, S. J., "Experimental Evidence for the Presence of Helium Ions Based on Explorer VIII Satellite Data," *J. Geophys. Res.* 67(2): 467-476, February 1962.
29. Bowen, P. J., Boyd, R. L. F., Raitt, W. J., and Willmore, A. P., "Ion Composition of the Upper F-Region," *Proc. Roy. Soc. A.* (to be published).
30. Gringauz, K. I., Gorozhankin, B. N., Shyutte, N. M., and Gdalevich, G. L., "Altitude Distribution of Charged Particles in the Ionosphere and the Transition Zone between Oxygen and Helium Ionic Layers and Revealed by Ion Trap Tests in the 'Cosmos-2' Satellite," *Dokl. Akad. Nauk SSSR*, 151(3): 560-563, July 21, 1963 (In Russian).

ON THE DIURNAL VARIATION OF THE UPPER ATMOSPHERE

by

Isador Harris

Goddard Space Flight Center

Wolfgang Priester*

Goddard Institute for Space Studies

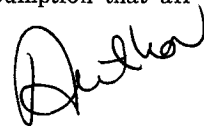
N65-29555

SUMMARY

29555

The diurnal variation of the upper atmosphere as revealed from satellite drag measurements has been further investigated on the basis of a simultaneous integration of the heat conduction equation and the hydrostatic law. In addition to the heat source due to absorption of solar extreme ultraviolet radiation and the hypothetical "second heat source," the heating due to absorption of solar radiation in the Schumann-Runge range by oxygen molecules has been included. The effects of time-dependent variations in the boundary conditions on the phase and amplitude of the diurnal variation in the upper thermosphere and exosphere have been investigated. Also the effects of lateral heat conduction and lateral convective heat transport on the diurnal variation of density and temperature are discussed.

The main purpose of the paper is to investigate several possibilities which could be thought to eliminate the requirement for the "second heat source." It is shown that neither the inclusion of absorption of solar radiation in the Schumann-Runge band by O_2 molecules in our heat source nor diurnal variations of the boundary conditions at 120 km can be invoked in order to explain the diurnal variation on the basis of an EUV heat source exclusively. Further the effect of horizontal conduction is found in a simplified analysis to be quantitatively insufficient to account for an energy transport toward the west large enough to explain the observed diurnal variation under the presumption that all heating comes from the solar EUV radiation.



INTRODUCTION

The diurnal variation of the atmospheric density at heights above 200 km has been determined from satellite drag measurements by several investigators. An extensive analysis has been given by Jacchia and Slowey (Reference 1). The diurnal density variation can be described as follows: During the morning the density increases until it reaches a maximum at about 14^h local

*NAS-NRC Senior Research Associate with the Goddard Institute for Space Studies; on leave from Bonn University.

time. Then it decreases rather rapidly in the afternoon and evening, followed by a less steep decrease during the night. The density minimum can be placed at around 04^h local time. This holds true for at least the altitude range from 350 to 660 km and for the time interval from 1958 through 1963, during which sufficiently accurate satellite drag data were available. It is particularly remarkable that almost for the entire decreasing phase of solar activity, the diurnal maximum is always found very close to 14^h local time (Reference 2). It furthermore should be noted that the density decrease is considerably less rapid during the hours around midnight than in the late afternoon. The description of the diurnal density variation is also applicable to the diurnal temperature variation to a good approximation.

By using Nicolet's set (Reference 3) of "static" models, Jacchia obtained temperature maxima and minima exactly at the same local times as for the densities. This results because Nicolet's models furnish a monotonic relationship between densities and temperatures independent of local time. Since the main physical processes which determine the time-dependent variation of the upper atmosphere (heating by absorption of solar energy and heat conduction) have different characteristics, some caution must be exercised when relying on this kind of transformation (for further details, see Reference 4). For this reason, we shall always use the observed density variations rather than the inferred temperatures, for the analysis in this paper.

Two years ago we investigated how the observed diurnal variation could be understood by assuming hydrostatic equilibrium and integrating the time-dependent heat conduction equation (Reference 5). We included an expression which represented the convective heat transfer due to the diurnal expansion and contraction of the atmospheric bulge. From this analysis we concluded that heating of the thermosphere due to absorption of the solar extreme ultraviolet (EUV) radiation alone cannot explain the observed diurnal variation of density and temperature, as extreme ultraviolet heating alone would yield the maximum value of the density at about 17^h local time instead of 14^h. Furthermore, if the EUV flux is adjusted to represent the observed average density of the diurnal variation, then the amplitude of the diurnal variation would greatly exceed the observed amplitude.

Also, comparison of the required flux with Hinteregger's measurements of the EUV flux (Reference 6) would require a very high efficiency for the conversion of EUV radiation into heat. Recent improved EUV measurements by Hall, Schweizer, and Hinteregger (Reference 7) yielded considerably higher fluxes than one would have expected for low levels of solar activity from the previous measurements. This might indicate that the solar spectrum in the EUV range does contain sufficient energy to provide the required heat exclusively. If so, it would eliminate the requirements for an extremely high efficiency, but does not affect the wrong phase and too large amplitude of the diurnal variation when calculated with an EUV heat source only by the aforementioned method.

Figure 1 illustrates the discrepancy between the diurnal density variation derived from observations (Reference 8) for an altitude of 600 km, and the calculated variation when only an EUV heat source is used (dotted line). In order to overcome this discrepancy we assumed the existence of a second heat source which has a maximum in the morning (at about 9^h or 10^h local time), a

rather low value in the afternoon, and a small contribution during the night. With this additional heat source one achieves a good agreement between observed and calculated densities. The calculated values are given in Figure 1 by the solid line. The line represents our model $S = 200$, wherein a peak flux of $0.93 \text{ erg/cm}^2\text{-sec}$ for the EUV heat source and of $1.03 \text{ erg/cm}^2\text{-sec}$ for the "second heat source" were used. These values correspond to the average level of solar activity in the fall of 1959. If we use an EUV heat source only, it would be necessary to employ a peak value of $\sim 2 \text{ erg/cm}^2\text{-sec}$ of the EUV flux, in order to obtain a diurnal average density in close agreement with the observed average density. If the efficiency for conversion of solar EUV radiation into heat in the thermosphere is 40 percent (Reference 9), the total flux in the EUV range below 1000 \AA would have to be as high as $5 \text{ erg/cm}^2\text{-sec}$ for a level of solar activity that occurred in the fall of 1959. But even with this rather large flux the problem of a wrongly phased variation remains. It is the purpose of this paper to investigate what the effects are on the diurnal variation if some of the simplifications made in the previous calculations are removed.

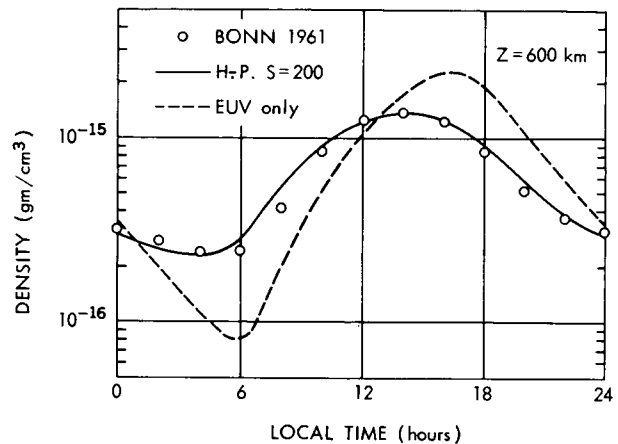


Figure 1—Diurnal variation of the density at a height of 600 km. The abscissa is the local time. The circles represent the observations as given in the Bonn model 1961 (Reference 8) which represents atmospheric conditions during the fall 1959. The dotted line is the calculated density variation if the absorption of solar extreme ultraviolet radiation is used as the only heat source. The solid line is the variation which is obtained if a "second heat source" is included in the calculations.

DISCUSSION OF THE BASIC EQUATIONS

In the attempt to understand the diurnal behavior of the upper atmosphere, it is important to determine to what extent the requirements for the second heat source are influenced by the simplifications employed in the basic equations.

The time dependent heat conduction equation is:

$$\frac{\partial}{\partial z} \left[K(T) \frac{\partial T}{\partial z} \right] - \rho C_p \frac{\partial T}{\partial z} T \int_{z_0}^z \frac{1}{T^2} \frac{\partial T}{\partial z} dz' + \sum_j Q_j = \rho C_p \frac{\partial T}{\partial t} \quad (1)$$

Since we use, in this paper, the same notations as in the previous ones, we shall not repeat all the details here. The equation includes a convective term for the vertical heat transport during the diurnal expansion-contraction of the atmospheric bulge. This is represented by the second term on the left side of Equation 1 and the appearance of C_p instead of C_v on the right side. A detailed derivation has been given earlier (Reference 5). The second term in Equation 1 has only a minor

influence on the energy balance, as calculations with and without this term have shown. It, therefore, is unimportant in our discussion of the effects of simplifications in the theory on the calculated diurnal variation.

The first term in Equation 1 accounts for the heat conduction in the vertical direction. $K(T)$ is the coefficient of heat conduction, taken as the weighted average of the coefficients. The weighting factor is the number density. The coefficient depends, furthermore, on the square root of the temperature (Reference 10).

The third term accounts for the heat sources and losses. The heat source due to absorption of solar EUV radiation is given by

$$Q_{\text{EUV}} = \sum_i \epsilon_i n_i(z, t) \int_0^{\infty} F_{\lambda} \sigma_i(\lambda) \exp\left[-\sum_i \tau_i(z, t, \lambda)\right] d\lambda, \quad (2)$$

where

$$\tau_i(z, t, \lambda) = \int_z^{\infty} \sigma_i(\lambda) \frac{n_i(z, t)}{\cos \theta(t)} dz. \quad (3)$$

$\sigma_i(\lambda)$ is the cross-section for absorption by the i^{th} constituent of radiation of wavelength λ in the region $d\lambda$, F_{λ} is the incident flux of wavelength λ in the region $d\lambda$ at the top of the atmosphere and ϵ_i is an efficiency factor for the conversion to thermospheric heat of energy in the extreme ultraviolet absorbed by the i^{th} constituent. θ is the zenith angle of the sun.

In our previous paper (Reference 5), the summation sign in the exponential function of Equation 2 was accidentally left out in the printing. The correct formula, however, was used in the computer program. The correct formula is also given in our paper which was printed in the proceedings of the Third International Space Science Symposium (Reference 11).

We summed Hinteregger's measurements of the solar EUV flux from 40 to 1000 Å and used appropriately averaged cross sections for the absorption by the different constituents. This simplification was made after calculations had shown that the temperature profiles of the thermosphere were only slightly affected whether the EUV region was divided into five different regions with appropriate mean cross sections or a proper average over the entire EUV region was used.

The efficiency for the conversion of solar EUV energy into heat was taken to be 37 percent in close agreement with the result of Lazarev's recent paper (40 percent) (Reference 9). The uncertainty of the above value is still quite large. Smaller values (15 to 30 percent) have been recommended by Hanson and Johnson (Reference 12) and Chamberlain (Reference 13). Therefore all arguments about the heating of the thermosphere which are based on the absolute values of solar EUV fluxes must be considered with caution.

In this paper we have investigated the effects of additional heating caused by the absorption of solar radiation in the Schumann-Runge range by oxygen molecules. A detailed discussion of this process and its heating efficiency is given in the next section.

Johnson argues in a recent paper (Reference 14) that it would not be entirely unreasonable that the generally used values for the heat conductivity might be too large by a factor of three or even ten. We have investigated the influence of different values for the conductivity. A smaller value would decrease the discrepancy in the thermospheric heat budget, but it would increase the discrepancy between the observed and calculated time of the diurnal maximum. This is an argument against considerably smaller values for the conductivity.

A shortcoming of our Equation 1 is the neglect of horizontal conduction as well as horizontal convection. This will be discussed later. The horizontal conduction depends, of course, on the horizontal temperature gradients. Due to the large distances involved, these gradients are rather small. MacDonald estimates in his recent view (Reference 15) that the average temperature gradient at an altitude of 1000 km is 3×10^{-7} °K/cm for a temperature difference of 600°K between the dark and the sunlit side of the earth. The corresponding heat flow is then only of the order of 10^{-2} erg/cm²-sec.

SCHUMANN-RUNGE ABSORPTION

In previous integrations of the time dependent heat conduction equation we included electromagnetic radiation in the EUV range only (40 to 1000 Å). As the number density of molecular oxygen at the 120 km level is still rather large and the flux in the Schumann-Runge region is large compared to that in the EUV region, such a neglect has been considered as an oversimplification. However, integrations of the time dependent heat conduction equation which includes heating from solar flux in the Schumann-Runge region show that our previous conclusions are not affected.

Walker (Reference 16) has estimated the amount of flux in the Schumann-Runge region that can be optimistically converted into local heating of the atmosphere above 120 km. His conclusion is that at most a flux of 0.5 erg/cm² sec can be converted into local heating. We have performed integrations of the time dependent heat conduction Equation 1 where we have included the absorption of Schumann-Runge radiation by molecular oxygen in addition to the heating due to extreme ultraviolet radiation. We used a cross section for absorption of 1.5×10^{-17} cm² (Reference 6).

In these calculations we obtain a behavior of the upper atmosphere which is qualitatively similar to our previous results: *The temperature still peaks at 17 hours local time and the amplitude of the diurnal variation is much too great.*

The inclusion of Schumann-Runge absorption has the effect of steeping the temperature gradient at the lower boundary. This makes it possible to obtain better agreement with the densities measured at the lower boundary altitude by the falling sphere method (Reference 17) and still to

maintain good agreement with the satellite drag data. Figure 2 is the comparison of the density profiles at the diurnal maximum (14^h) and minimum (4^h) with and without inclusion of absorption in the Schumann-Runge range.

VARIATION OF THE RATIO OF ATOMIC TO MOLECULAR OXYGEN

In all of our previous calculations (References 4, 5, 11, and 18) we have assumed that the number densities of the various constituents at our boundary level (120 km) do not vary within one day. This is reasonable for example, as the lifetime for recombination of atomic oxygen at this altitude is of the order of years (Reference 3). Also the lifetime for molecular oxygen due to dissociation is of the order of several days.

Since it has been suggested that the ratio of atomic to molecular oxygen might vary by a factor of three to four over a day-night cycle (References 15 and 19), calculations have been made

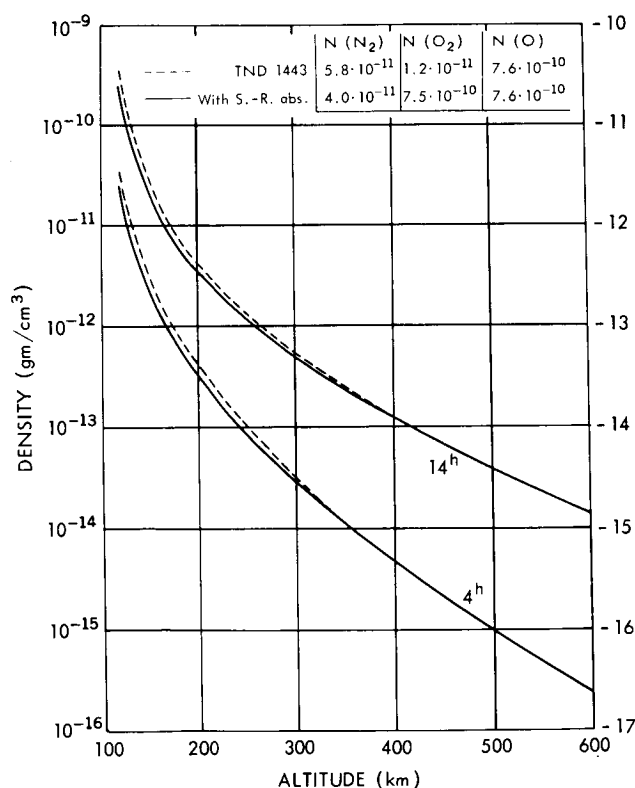


Figure 2—Density versus height from 120 to 600 km for 14 and 4 hours local time. The dotted line represents our model $S = 200$ (Reference 5) for mean atmospheric conditions during the fall 1959. The solid lines give the densities when, in addition, the absorption by oxygen molecules in the Schumann-Runge range is included in the calculations. In the legend the boundary number densities of N_2 , O_2 and O at 120 km are given.

to ascertain how this affects the calculated diurnal variation. However, it is difficult to see how such a variation at 120 km could influence the density variations of higher altitudes within one day as the diffusion time at 120 km is of the order of one day. Nevertheless, despite the above objections, we have performed calculations where we have varied the amount of atomic and molecular oxygen sinusoidally and in such a manner that the variation would correspond to photodissociation of molecular oxygen (or recombination of atomic oxygen) and maintain a constant density at 120 km. Thus the variation at 120 km chosen was the following:

$$N(O) = N_0(O) \left[1 + \frac{1}{3} \sin \frac{2\pi}{24} (t - 10) \right], \quad (4)$$

$$N(O_2) = N_0(O_2) \left[1 - \frac{1}{6} \frac{N_0(O)}{N_0(O_2)} \sin \frac{2\pi}{24} (t - 10) \right], \quad (5)$$

where $N_0(O)$, $N_0(O_2)$ are the diurnal average values of the number density of atomic and molecular oxygen, t is the local time in hours. The ten hour phase was chosen so as to have the number density of atomic oxygen increasing until 16^h local time. Equations 4 and 5 yield a variation of the ratio of atomic to molecular

oxygen of about a factor of 3. In the calculations only heating due to EUV and Schumann-Runge radiation corresponding to an average level of solar activity of autumn 1959 was included. Figure 3 presents the relative variation of the density at 600 km together with the observed variation. For comparison the calculations with constant boundary conditions are also shown. It is noticed that such a variation hardly affects the behavior of the diurnal variation, that is, the calculated variation still peaks at about 17^h local time with a too large amplitude. Thus such a variation at 120 km cannot account for the diurnal variation observed in the height range from 300 to 700 km. On the basis of these calculations it is also difficult to interpret the rocket measurements of the number densities of atomic and molecular oxygen at 190 km by Hall, Schweizer and Hinteregger (Reference 7) as a diurnal variation.

VARIATION IN THE TURBOPAUSE HEIGHT

The level at which diffusive equilibrium begins is not well known. Furthermore it might be that the height of the diffusive equilibrium level changes from day to night. For the various atmospheric constituents it may vary from about 100 to 120 km. For example if the level for the diffusive separation of atomic oxygen changes by 28 km from 90 to 118 km, then the number density of atomic oxygen would change by a factor of nine at 120 km. We have performed calculations in which we forced the number density of atomic oxygen at 120 km to vary diurnally so as to give good agreement with the observed densities at 600 km.

The diurnal variation we used is given in Figure 4. Again only extreme ultraviolet and the radiation in the Schumann-Runge region were used as heat sources. Figure 4 shows that a fairly good agreement can be obtained due to the manner in which the number density of atomic oxygen is varied at 120 km. Even perfect agreement could be obtained by an additional slight variation of the boundary conditions. But Figure 4 also shows that we cannot obtain good agreement simultaneously at lower altitudes between 200-400 km. Thus such an assumed diurnal variation of the

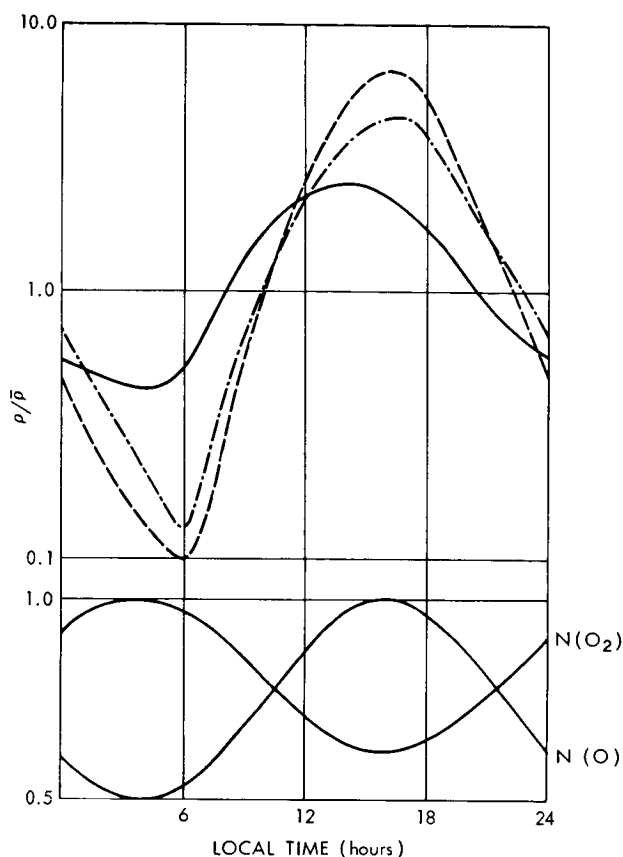


Figure 3—Diurnal density variation at 600 km calculated with time-dependent boundary conditions. The number densities of O_2 and O at 120 km were forced to vary according to formulas 4 and 5 (see lower part of the figure). The resulting density variation at 600 km is represented by the dashed line in the upper section of this figure. As heat sources, only the absorption of solar radiation in the EUV and Schumann-Runge range are used. For comparison, the dashed-dotted curve gives the densities when the number densities at 120 km are kept constant at the mean values. The solid line again shows our model $S = 200$, which represents the observed variation in the fall 1959.

height of the turbopause cannot account for the observed diurnal density variation in the 300 to 700 km range. Furthermore, since the diffusion time for atomic oxygen at 120 km is of the order of one day, it is difficult to understand how such an effect can be propagated upward within a day without smoothing out the variation at greater heights.

VARIATION OF THE BOUNDARY TEMPERATURE

The third type of variation we may use to explain the observed diurnal variation is the variation of the boundary temperature. As the characteristic conduction time (Reference 15) at 120 km is large compared to one day, we do not expect any appreciable diurnal variation in the temperature at 120 km. Thus any forced variation at the 120 km level, even if the total amplitude would be as large as 100°K, would be rapidly damped out with increasing altitude. This is borne out by actual calculations where we have varied the temperature at 120 km sinusoidally with a total variation of 100°K from 305 to 405°K, peaking at 6 hours local time. Again only EUV and Schumann-Runge radiation were used. In Figure 5 we compare the exospheric temperature obtained with the results for fixed boundary temperatures of 305°K, 355°K and 405°K. The results for the periodic boundary temperature variation do not deviate appreciably from the results when a constant boundary temperature of 355°K is used. This demonstrates that a periodic temperature variation at 120 km cannot propagate rapidly enough to affect the diurnal variation in the upper thermosphere.

Thus diurnal variations of the boundary conditions of the type illustrated above cannot account for the density peaking at 14^h local time (instead of 17^h) nor for the much lower observed ratio of daytime maximum temperature (or density) to minimum nighttime temperature (or density). Thus the considerations in sections 3 to 6 of this paper have no influence upon our requirement of an additional heat source which when included well represents the observations.

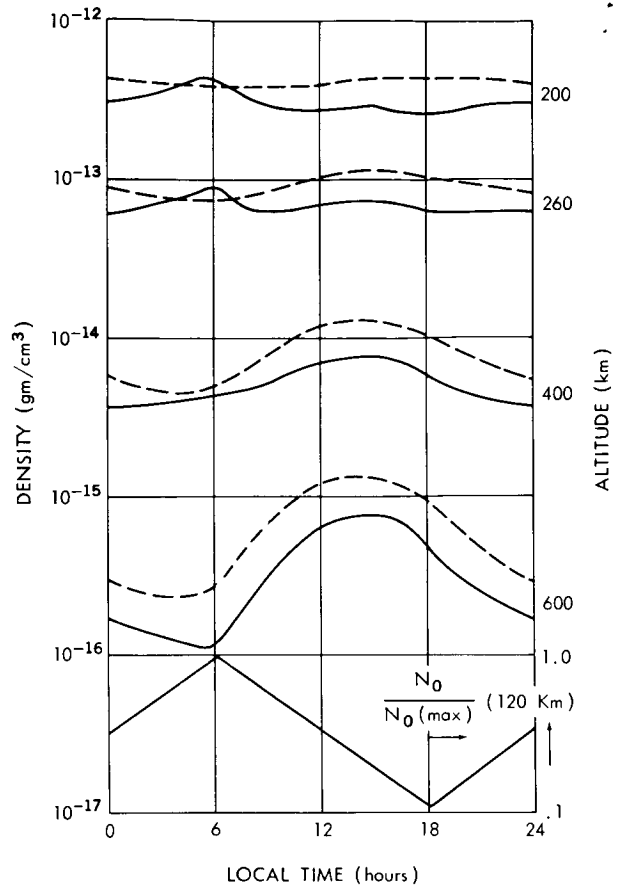


Figure 4—Diurnal density variations at 200, 260, 400 and 600 km calculated under the assumption that the height of the turbopause (diffusion level) changes diurnally from 90 km at 6 hours local time to 118 km at 18 hours local time. The corresponding variation of the number density of atomic oxygen at 120 km is given in the lower part of the figure. The solid lines in the upper part represent the calculated densities. For comparison again the densities of our model $S = 200$ are given (dashed lines). The agreement at 600 km is good, but agreement at the lower altitudes cannot be achieved simultaneously with height variations of the turbopause.

LATERAL HEAT TRANSPORT

The basic Equation 1 depends on height and time only. A complete treatment of two or three dimensions in space is not quite feasible with the high speed computers readily available at the present time. However, lateral heat conduction parallel to the equator can be included in our one-dimensional treatment by taking advantage of the relationship between the longitude and the local time. Lateral conduction is expected to be small as the lateral temperature gradients are small (of the order of the difference between maximum daytime temperature and minimum nighttime temperature divided by the circumference of the earth). At high altitudes, however, the lateral temperature gradient can be comparable to the vertical temperature gradient—but at these altitudes the heat content of the thermosphere is small so that such a lateral heat flow hardly affects the total heat budget in a given column of air. If horizontal conduction would be sufficient to decrease the diurnal amplitude, which is obtained when heating by EUV radiation alone is used, towards the observed value and also sufficient to shift the diurnal maximum towards 14^h local time, this might offer an immediate explanation of why the

local time of the maximum remains close at the same local time (14^h) for the whole solar cycle. If we calculate the local time of the maximum using only solar EUV radiation as the heat source for the entire solar-cycle, by changing the flux parallel to the solar activity we find that the maximum proceeds from 17^h for high solar activity towards 15^h for extreme low activity. Parallel to this, however, the temperature maximum and the diurnal amplitude of the temperature decreases. From the decrease of the latter it is plausible that the effectiveness of horizontal conduction also becomes gradually smaller. So it can only provide a smaller time-shift for the maximum at periods of low solar activity. This just might then result in having the maximum always at about 14 hours. Of course, this requires quantitative proof.

The method we employed to include lateral conduction along the equator is the following. It is illustrated in Figure 6. A horizontal displacement ds is equivalent to a change in local time dt , thus the lateral temperature gradient dT/ds can be replaced by $1/[\omega(R_0 + z)] \partial T/\partial t$, where ω is the angular velocity of the earth and R_0 the radius of the earth, and z the height. Thus the net heat

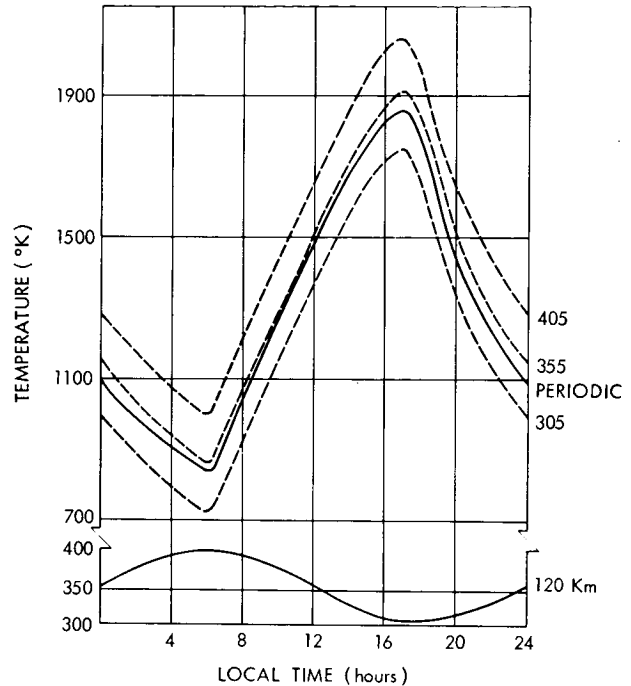


Figure 5—Diurnal variation of the exospheric temperature for different boundary temperatures at 120 km. As heat sources, only the absorption of solar radiation in the EUV and Schumann–Runge range are used with the same fluxes in all cases. The dashed curves give the temperature variations when the boundary temperature is kept constant at 305, 355 and 405°K respectively. The solid line represents the variation of the exospheric temperature when the boundary temperature at 120 km is forced to vary diurnally as given in the lower part of the figure.

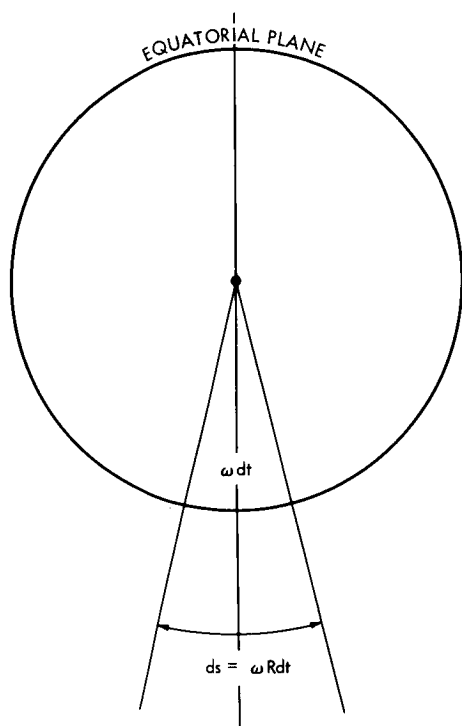


Figure 6—This figure demonstrates how the lateral conduction in longitude can be included in our formula 1 if we take advantage of a conversion of length units into time units.

properties of the upper atmosphere, that is, it does not shift the time of the diurnal maximum, nor does it decrease the ratio of the maximum to minimum temperature appreciably.

Another factor which can be thought of to influence the diurnal behavior of the upper atmosphere is lateral convective energy transport. From the temperature gradient one expects speeds of convective flow much too small to furnish any appreciable horizontal energy transport. In order to have an effective horizontal energy transport, large range flow velocities of the order of 10^4 cm/sec are required (Reference 15).

At present it cannot be proved or disproved whether this effect can be, indeed, large enough to account for a temperature difference of 250° at the bulge maximum between the "observed" temperature and the higher value which has been calculated on the basis of a sufficiently strong EUV heat source (no other source) and no horizontal convective energy transport. Quantitative proof is needed which is at present not yet feasible in order to see whether horizontal convection can provide the required time shift and flattening of the temperature maximum. As long as this cannot be done one will have to rely on a second heat source. There seem to be two different ways to interpret this source:

1. As a heat source other than the absorption of solar EUV radiation. This is particularly suggested if we relate the semi-annual variation to the solar wind, since, in this case, we surely

input to a given amount of air ($K \partial^2 T / \partial s^2$) can be included by adding the term

$$\frac{K(z)}{\omega^2 (R+z)^2} \frac{\partial^2 T}{\partial t^2} \quad (6)$$

to Equation 1. In this term we have ignored the explicit temperature dependence of the thermal conductivity as it is a small correction to a small term. Calculations have been made including this term as a perturbation and with EUV and Schumann-Runge radiation alone. The result is a change of the exospheric temperature by less than 25°K , too small to be of any significance. A comparison of the term given as Equation 6 with the net heat input due to vertical conduction (first term in Equation 1) showed that the former term only becomes comparable to the latter for heights above 500 km and times around 06^{h} and 18^{h} local time. Below 300 km it is always smaller by more than two orders of magnitude.

But we have, of course, to consider also the meridional component of the heat conduction. This can reasonably be expected to be of the same order as the longitudinal component. Thus lateral heat flow does not affect the gross

would need a "second source" which provides about the same amount of heat as the EUV radiation. Furthermore it was recently found that much stronger additional heating of the thermosphere occurs parallel to slight changes of geomagnetic activity during quiet periods than as anticipated before (References 20 and 21). This favors the assumption of additional heating other than solar EUV radiation.

2. If we assume that the solar EUV provides enough energy (a flux up to $6 \text{ erg/cm}^2 \text{ sec}$ for very high solar activity if the efficiency for conversion into heat is 40 percent or up to $12 \text{ erg/cm}^2 \text{ sec}$ if the efficiency is only 20 percent), then we might interpret the sum of the EUV heat source and the "correction term" which provides the agreement with the observed diurnal variation as the "effective heat source" of the upper atmosphere. This source then incorporates the horizontal energy transport in such a way that the simplified theory provides the agreement with the observations. This interpretation, however, depends strongly on a quantitative proof of whether horizontal convection is effective enough.

CONCLUSIONS

Herein, several possibilities have been investigated which could eliminate the requirement for a second heat source which we had to introduce in order to reproduce the observed diurnal variation by solving the time-dependent heat conduction equation as a function of height and time only. We were able to show that neither the inclusion of absorption of solar radiation in the Schumann-Runge band by O_2 molecules in our heat source nor diurnal variations of the boundary conditions can be invoked in order to explain the diurnal variation on the basis of an EUV heat source exclusively.

Further, the effect of horizontal conduction is insufficient to account for an energy transport toward the west large enough to explain the observed diurnal variation. A complete three-dimensional quantitative analysis which will eliminate the need of the artifice employed here would be useful. But this requires a much larger and faster computer than presently available.

ACKNOWLEDGMENTS

We express our appreciation to Mr. E. Monasterski for devising the numerical procedure and preparing the program for the IBM 7094 computer.

REFERENCES

1. Jacchia, L. G., and Slowey, J., "Accurate Drag Determinations for Eight Artificial Satellites; Atmospheric Densities and Temperatures," Smithsonian Astrophysical Observatory, Special Report No. 100, July 30, 1962.

2. Jacchia, L. G., "The Temperature Above the Thermopause," Smithsonian Astrophysical Observatory, Special Report No. 150, April 22, 1964.
3. Nicolet, M., "The Properties and Constitution of the Upper Atmosphere," in: *Physics of the Upper Atmosphere*, (Ratcliffe, J. A., ed.): 17-21, New York: Academic Press, 1960.
4. Harris, I., and Priester, W., "Relation between Theoretical and Observational Models of the Upper Atmosphere," *J. Geophys. Res.* 68(20):5891-5894, October 15, 1963.
5. Harris, I., and Priester, W., "Time-Dependent Structure of the Upper Atmosphere," *J. Atmos. Sci.* 19(4):286-301, July 1962; also NASA Technical Note D-1443.
6. Hinteregger, H. E., "Preliminary Data on Solar Extreme Ultraviolet Radiation in the Upper Atmosphere," *J. Geophys. Res.* 66(8): 2367-2380, August 1961.
7. Hall, L. A., Schweizer, W., and Hinteregger, H. E., "Improved Extreme Ultraviolet Absorption Measurements in the Upper Atmosphere," *J. Geophys. Res.* (In press).
8. Martin, H. A., Neveling, W., Priester, W., and Roemer, M., "Model of the Upper Atmosphere from 130 through 1600 km, Derived from Satellite Orbits," in: *Space Research II* (van de Hulst, H. C., de Jager, C., and Moore, A. F., eds.): 902-917, Amsterdam, North-Holland Publishing Co., 1961.
9. Lazarev, V. I., "The Ionizing Radiation and Heating of the Upper Atmosphere," *Geomagn. i. Aeronomiya* 3:842-849, 1963; NASA Draft Translation ST-AI-10094, 1964.
10. Chapman, S., and Cowling, T. G., "The Mathematical Theory of Non-Uniform Gases," 2d ed., Cambridge: University Press, 1952.
11. Harris, I., and Priester, W., "Heating of the Upper Atmosphere," in: *Space Research III* (Priester, W., ed.): 53-57, Amsterdam: North-Holland Publishing Co., 1963.
12. Hanson, W. B., and Johnson, F. S., "Electron Temperatures in the Ionosphere," *Mem. Soc. Roy. Sci. Liège* (Coll. in-8°), 4:390-424, 1961.
13. Chamberlain, J. W., "The Energies in the Spectra of the Airglow and Aurora," *Ann. Geophys.* 17(1):90-99, 1961.
14. Johnson, F. S., "Circulation at Ionospheric Levels," Southwest Center of Advanced Studies, Report on Contract Cwb-10531, 1964.
15. MacDonald, G. J. F., "The Escape of Helium from the Earth's Atmosphere," *Rev. Geophys.* 1(3):305-349, August 1963.
16. Walker, J. C. G., "The Day Airglow and the Heating of the Upper Atmosphere," Thesis, Columbia University, 1964.

17. Faucher, G. A., Procnier, R. W., and Sherman, F. S., "Upper-Atmosphere Density Obtained from Measurements of Drag on a Falling Sphere," *J. Geophys. Res.* 68(11):3437-3450, June 1, 1963.
18. Harris, I., and Priester, W., "Theoretical Models for the Solar-Cycle Variation of the Upper Atmosphere," *J. Geophys. Res.* 67(12):4585-4592, November 1962; also NASA Technical Note D-1444.
19. Kallmann-Bijl, H. K., and Sibley, W. L., "Diurnal Variation of Temperature and Particle Density between ~100 km and ~500 km," in: *Space Research IV* (Muller, P., ed.): 279-301, Amsterdam: North-Holland Publishing Co., 1964.
20. Jacchia, L. G., and Slowey, J., "Temperature Variations in the Upper Atmosphere during Geomagnetically Quiet Intervals," Smithsonian Astrophysical Observatory, Special Report No. 152, June 15, 1964.

RESULTS FROM THE IMP I RETARDING POTENTIAL ANALYZER

by

G. P. Serbu

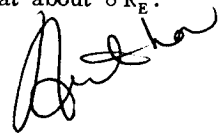
Goddard Space Flight Center

N65-29556

SUMMARY

29556

Some preliminary experimental results obtained with a planar geometry retarding potential analyzer flown on the IMP I satellite are presented. The plasma energy spectrum for both ions and electrons was measured in the range from 0 to 100 ev. Charged particle density measurements have been obtained for the complete range from 1000 km to $30 R_E$. The results show a sharp decrease of about an order of magnitude in charged particle density at about $4.5 R_E$ —similar to the decrease deduced from whistler observations. The electrons exhibited thermal energies for geocentric distances less than $4.5 R_E$; the average electron energy then increased gradually to values above 100 ev at about $8 R_E$. The observed satellite potential was less than 1 v positive.



INTRODUCTION

Measurements of the ionized plasma enveloping the earth have been reported by numerous investigators to date. The region to 30 earth radii (R_E) has been traversed extensively by a number of satellites; beyond this distance measurements have been made from the Soviet Lunik probes and the American Mariner series. Primarily the energy spectrum of positively charged particles, presumably protons, has been investigated, and only a few measurements on the electron spectrum below 10 kev are available to date. Presented are some preliminary experimental results obtained with a retarding potential experiment designed to measure the number density and the energy of ions and electrons in the energy range below 100 ev at distances to $30 R_E$.

INSTRUMENTATION

The retarding potential analyzer gives information on the arrival direction and energy distribution of both ions and electrons with energies up to 100 ev. The detector is a charged particle trap of planar geometry which is programmed with appropriate voltages such that the number of

charged particles of either polarity can be measured separately as a function of a given energy interval.

The charged particle trap, a circular cup 7 cm in diameter mounted so that the aperture is flush with the satellite skin, looks out at right angles to the spin axis of the satellite. The outside aperture is a hole of 5 cm² in area over which is stretched a fine wire mesh with 95 percent light transmission. Surrounding the aperture is a tungsten surface of 35 cm² area which is electrically connected to the aperture grid. Spaced parallel to the aperture and 4 mm behind it is the retarding grid. The collector, a tungsten disk is parallel to and 5 mm behind the retarding grid.

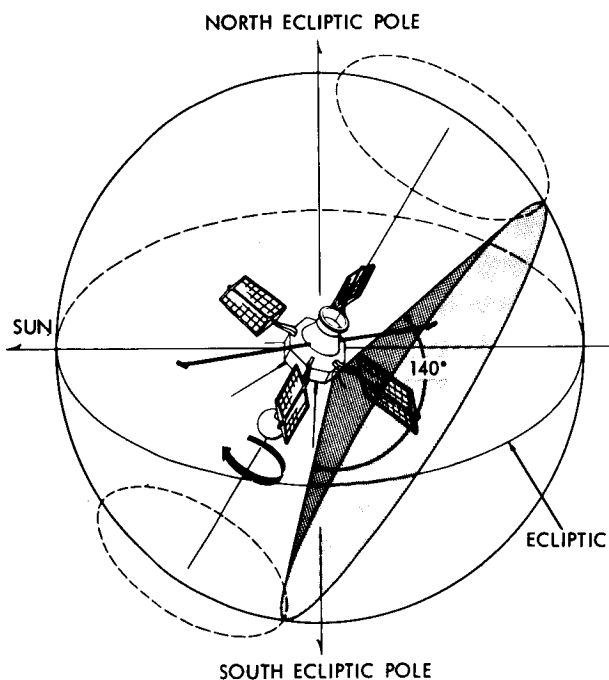


Figure 1—Location and viewing sphere of the retarding potential analyzer aboard the IMP 1 satellite.

The collector, a tungsten disk is parallel to and 5 mm behind the retarding grid. The geometry and size of the aperture and the relative spacings provide a viewing angle for the trap of 5 steradians. Figure 1 shows the total viewing direction of the trap as it was spin-modulated at the satellite spin rate of 22 rpm. Nearly all directions are viewed during one revolution, with the sun vector lying within 20 degrees of the normal to the trap once each revolution.

The collector current is measured by a logarithmic amplifier whose analog output is presented directly to telemetry. The electrometer sensitivity is from 10⁻¹¹ to 10⁻⁶ amps of either polarity. An internal current calibrator is used to check the electronics in flight.

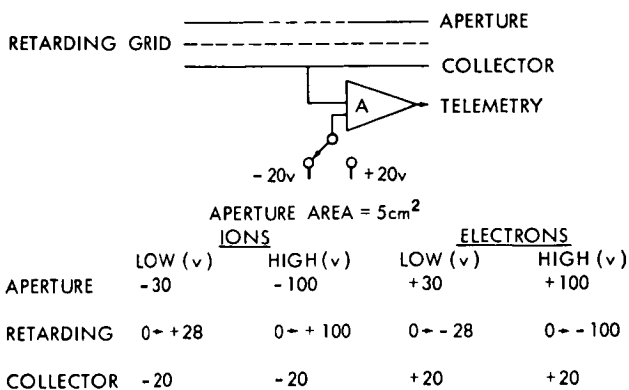


Figure 2—Schematic diagram of sensor and the various programmed voltages.

Figure 2 shows the sensor schematically and also the sequence of voltages programmed to the various trap elements in order to define the four modes of operation: low (30 ev) and high (100 ev) ion spectrum and the low (30 ev) and high (100 ev) electron spectrum. A mechanical programmer, which operates synchronously with the telemetry system, is used to switch the voltages to the trap. For example, the low energy (30 ev) ion spectrum is done as follows. The aperture grid and guard electrode are maintained at -30 v with respect to the satellite skin, thus all electrons with energy less than 30 ev are excluded from the trap and all positive ions are accelerated through the aperture. The retarding

grid voltage is changed in fifteen equal steps between 0 and +28 v. A current measurement is made and telemetered at each retarding potential step. Only those ions with energies in excess of the retarding potential will pass through the retarding grid and impinge on the collector. In this manner a current voltage characteristic is obtained for ions with energy below 30 ev.

During the ion measurement, photoemission current from the collector appears as a positive current, the expected magnitude being about 10^{-8} amps. As the collector views the sun the photoemission current amplitude will vary as the cosine of the angle between the sun vector and the trap normal and it will be repetitive with the spin cycle, thus corrections in the data can be made for the photocurrent. A highly accurate solar aspect sensor is used to find the precise time that the sun vector lies in the plane normal to the trap.

The electron mode of operation is such that the positive 20v potential on the collector suppresses all photoelectron emission from the collector. However, photoelectrons can be emitted from the grids and will appear as a negative current, the expected value being 5.10^{-10} amps. Also corrections for grid photoemission currents can be easily made in the electron data.

The 30 ev and 100 ev ion spectra are obtained and then the trap voltages are reversed and the 30 ev and 100 ev electron spectra are obtained. The entire ion and electron sequence is repeated once every 10 minutes; each individual 15 step spectrum analysis is done within 5.4 seconds.

RESULTS

Figure 3 shows a 30 ev electron spectrum which was obtained at $2.2 R_E$ geocentric distance. The data points are the measured current values, plotted on a logarithmic scale as a function of the known retarding potential voltage. The resultant semilogarithmic plot of a current-voltage characteristic yields information on the mean energy and the density of electrons. The observed decrease of two orders of magnitude in collector current with 2v negative retardation suggests a maxwellian distribution

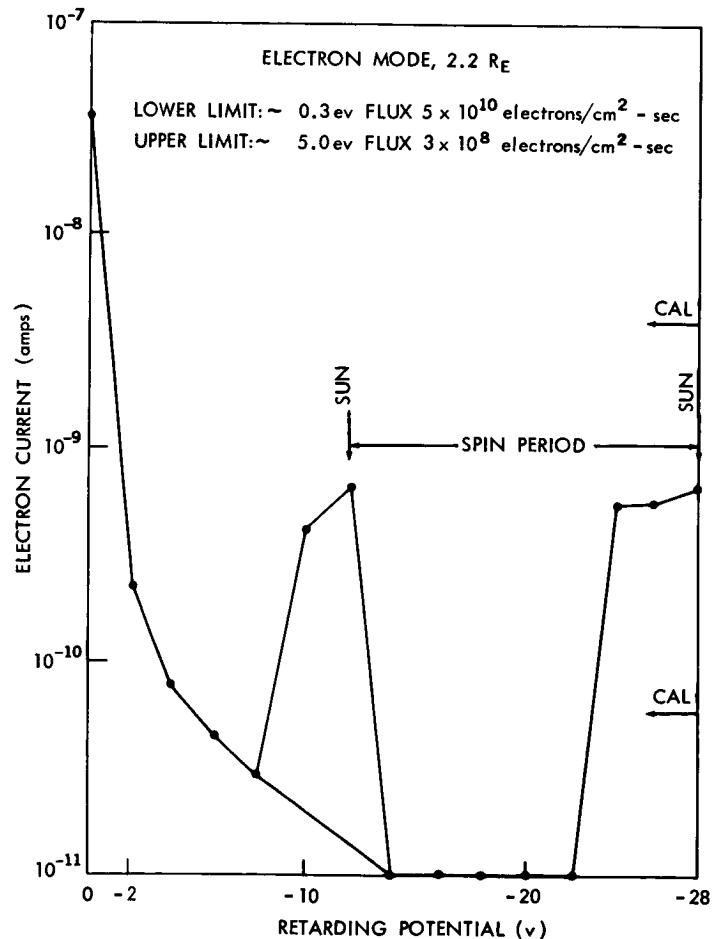


Figure 3—The 30 ev electron spectrum for $2.2 R_E$ geocentric.

of electron velocities. A second component or high-energy "tail" to the distribution is noted beyond 2 v. The primary slope yields an energy value of 0.3 ev or an equivalent electron temperature of 3500°K. From the governing equation:

$$I_- = \frac{1}{4} N_e \bar{v}_- e A e^{-ve/kT_e}, \quad (1)$$

where I_- is the measured current, N_e the electron density, \bar{v}_- the most probable velocity, A the area, v the retarding potential, e the electronic charge, k Boltzmann's constant and T_e the electron temperature. We can compute the electron density if A , the effective area is known. Low energy electrons which normally would not impinge on the aperture are deflected into the aperture along the accelerating +30 volt electric field lines; thus a uncertainty in the effective collection area exists. Using the geometric aperture area, we compute a flux of 5×10^{10} electrons/cm²-sec; this flux could be a factor of 10 too large due to the collection area uncertainty. Using Equation 1 a flux of 5.10^{10} electrons/cm²-sec with a mean energy of 0.3 ev at $2.2 R_E$, if maxwellian in distribution, represents an electron density of 3.5×10^3 electrons/cm³. The high energy component of 5.0 ev has an upper flux value of 3.10^8 electrons/cm²-sec. It has been suggested by Hanson (Reference 1) that at 7000 km, approximately this altitude, a 10^8 electron/cm²-sec flux of 5 ev photoelectrons exists. These photoelectrons are formed at altitudes above 300 km and diffuse along magnetic field lines; Mariani (Reference 2) extended the work of Hanson and describes the role that these photoelectrons may play in the explanation of the "equatorial" or "geomagnetic" anomaly. Since these electrons are constrained to follow field lines, the flux will drop off with the cube of the distance; thus beyond $3 R_E$ this flux should be below the minimum sensitivity of this experiment.

In Figure 3 the current to the trap decreases below the minimum sensitivity at retarding potentials greater than -12 v, thus fewer than 1×10^7 electrons/cm²-sec exist within excess of 12 ev. The two photoemission peaks correlate well with the indicated sun position. The magnitude of the photoemission current is consistent with the value of 5×10^{-10} amps computed on the basis of solar illumination of the 95 percent transparent grid.

Satellites, in general, are negatively charged (References 3 and 4), owing to the high velocity of electrons compared with either the velocity of the satellite or the thermal velocity of ambient ions. However, at very high altitudes and in interplanetary space, where the electron concentrations are small, a satellite might tend to have a net positive charge due to the photoelectric effect (Reference 5).

A direct measurement of the net charge, or the resultant potential difference between satellite and plasma as a consequence of the accumulated charge, can be based on observed current-voltage characteristics (Reference 6) such as these in Figure 3. Since a positive potential will accelerate ambient electrons to the satellite the measured electron current will not be retarded until an opposing voltage of magnitude equal to that of the satellite potential is reached. At that potential the characteristic will change slope and a further increase in negative voltage will retard the electron current. It is evident from the data of Figure 3 that a break in the curve could exist

for potentials more negative than +2 volts; therefore, the satellite potential is not more than 1 volt positive—more probably it is only a few tenths of a volt negative. There is no evidence throughout the magnetosphere that the satellite potential is ever positive.

The 30 ev electron spectrum obtained at $4.6 R_E$ geocentric, is shown in Figure 4, which yields an electron energy value of 1.4 ev, or an equivalent gas temperature of $16,400^\circ K$. A maximum flux of 9×10^9 electrons/cm²-sec is computed from the data, assuming the effective area to be equal to the geometric area. By converting to energy units, the data of Figure 4 yield, a value of 2.2×10^{-2} ergs/cm²-sec. Thus when we compare this to the value of 1 to 10 ergs/cm²-sec for particles with $E \geq 200$ ev obtained by the Explorer XII Cadmium Sulphide Total Energy Detector (Reference 7), it is apparent that a large number of low energy electrons ($E \leq 1.4$ ev) exist in the second radiation belt, however, their energy content represents only a small fraction of the total particle energy. Gringauz, et al. (Reference 8) infer from the Soviet charge particle traps that in this region an electron flux of 10^9 electrons/cm²-sec with $E < 200$ ev is present.

Figure 5 shows a consecutive series of 30 ev electron spectra obtained between 7.2 and $8.3 R_E$. From all the spectra it is apparent that a residual negative current component is measured even at the maximum retardation voltage of 28 v. Similar data, obtained at $9.2 R_E$, is shown in more detail in Figure 6. The residual current amplitude is not roll modulated; thus at $8.2 R_E$, on the

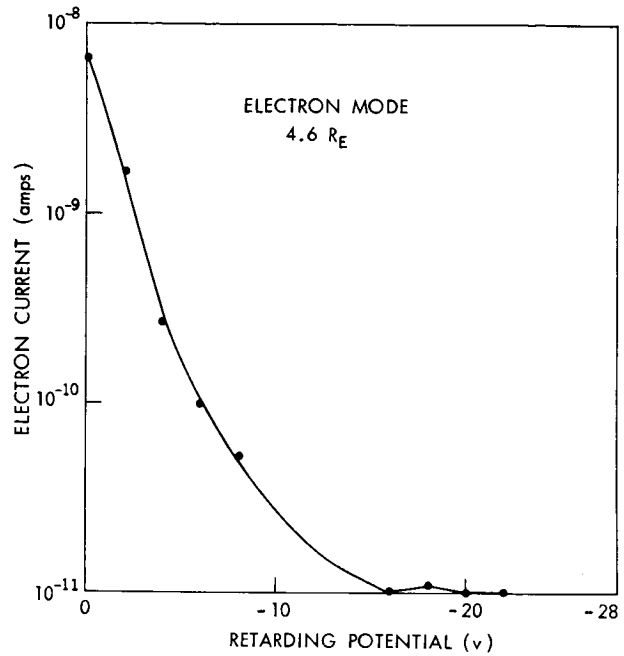


Figure 4—The 30 ev electron spectrum for $4.6 R_E$ geocentric.

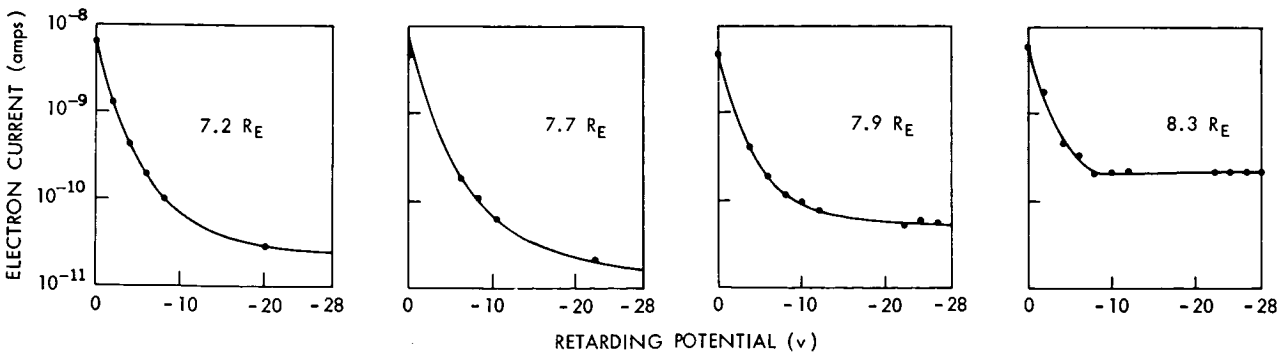


Figure 5—A successive series of 30 ev electron spectra depicting the transit into a region characterized by a residual current in the trap, due to an omnidirectional flux of electrons.

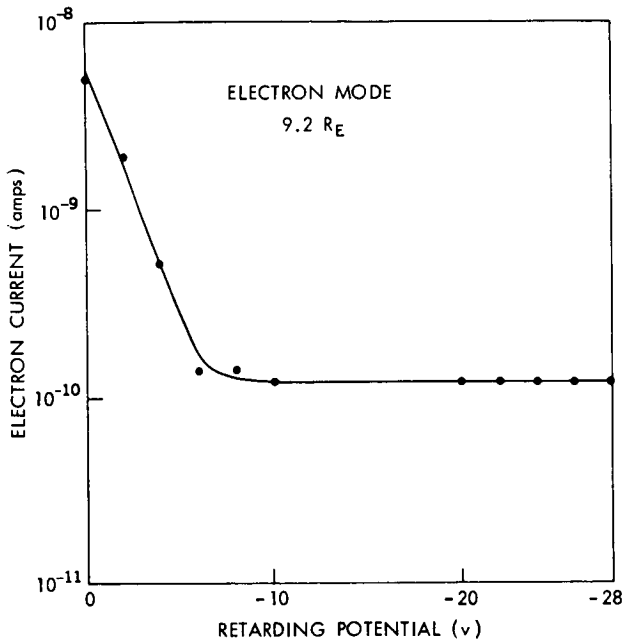


Figure 6—The 30 ev electron spectrum for 9.2 R_E geocentric.

sunlit side of earth, the satellite crosses into a region of omnidirectional electrons with energy in excess of 100 ev at a flux value of 1.5×10^8 electrons/cm²-sec. Gringauz, et al. (References 9, 10, and 11) observed, with Lunik 1 and also with Lunik 2 and Mars 1, a flux of $1-2 \times 10^8$ electrons/cm²-sec at these distances with electron energies greater than 200 ev, and thus called this region "the outermost belt of charged particles."

Figure 7 shows the 100 ev ion and electron spectra obtained at 9.0 and 9.1 R_E . The omnidirectional current residual in both traps at 100 v retardation indicates that both ions and electrons are present in the outermost belt of charged particles with energies in excess of 100 ev.

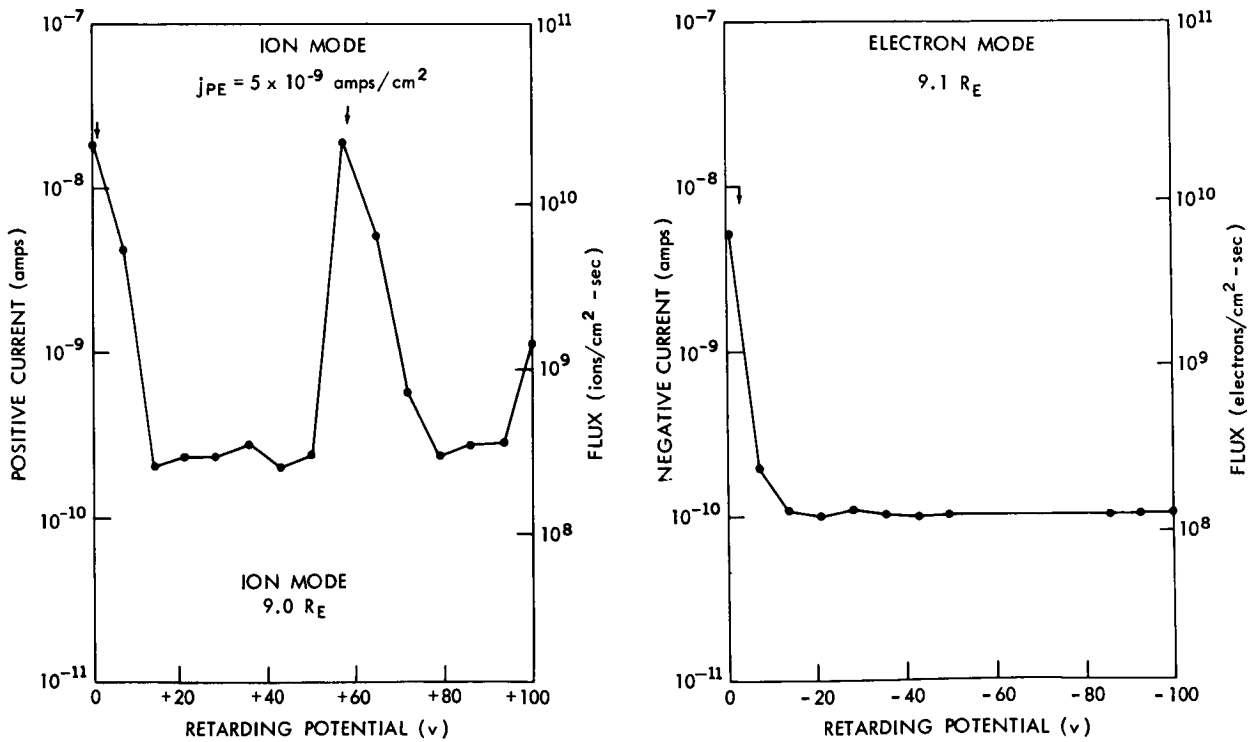


Figure 7—The 100 ev ion and electron spectra obtained at 9.0 R_E and 9.1 R_E geocentric.

The data of Figure 7 may also be used to illustrate that the net current flow to the satellite is essentially zero. At zero retardation, the current flow to the collector should be representative of any given area on the surface of the satellite, thus in order to maintain a constant satellite to plasma potential it must be shown that the net current flow to the satellite is zero. The photoemission current, which acts over the illuminated cross sectional area of the satellite, constitutes a positive current flow, i.e., electrons flowing outward from the satellite. The negative current is, on the other hand, effective over the entire area of the satellite, since the ambient electron velocity exceeds the satellite velocity, and so electrons diffuse inward from all directions. In order to have a net zero current flow the ratio of the photocurrent to electron current must be equal to 4, which is the inverse ratio of the areas in which these current flows are effective. From Figure 7 the current ratios at zero volt retardation are seen to be 4; thus the trap currents at zero retardation are inferred to be representative of the overall current flow to the satellite and we deduce that the equilibrium potential in sunlight is stabilized near zero volts.

The data in Figure 8 is representative of the trap currents at distances beyond $16.2 R_E$ geocentric. Positive and negative currents have been plotted as a function of orientation relative to the sun; this presentation was chosen since attempts at plotting the currents as a function of retarding voltages were useless. After disregarding the data points due to photoemission (the dashed curve), a residual net current in both traps is evident at 90-degree clockwise rotation from the sun; in the anti-solar direction the currents to the trap drop below 1×10^{-11} amps. Since

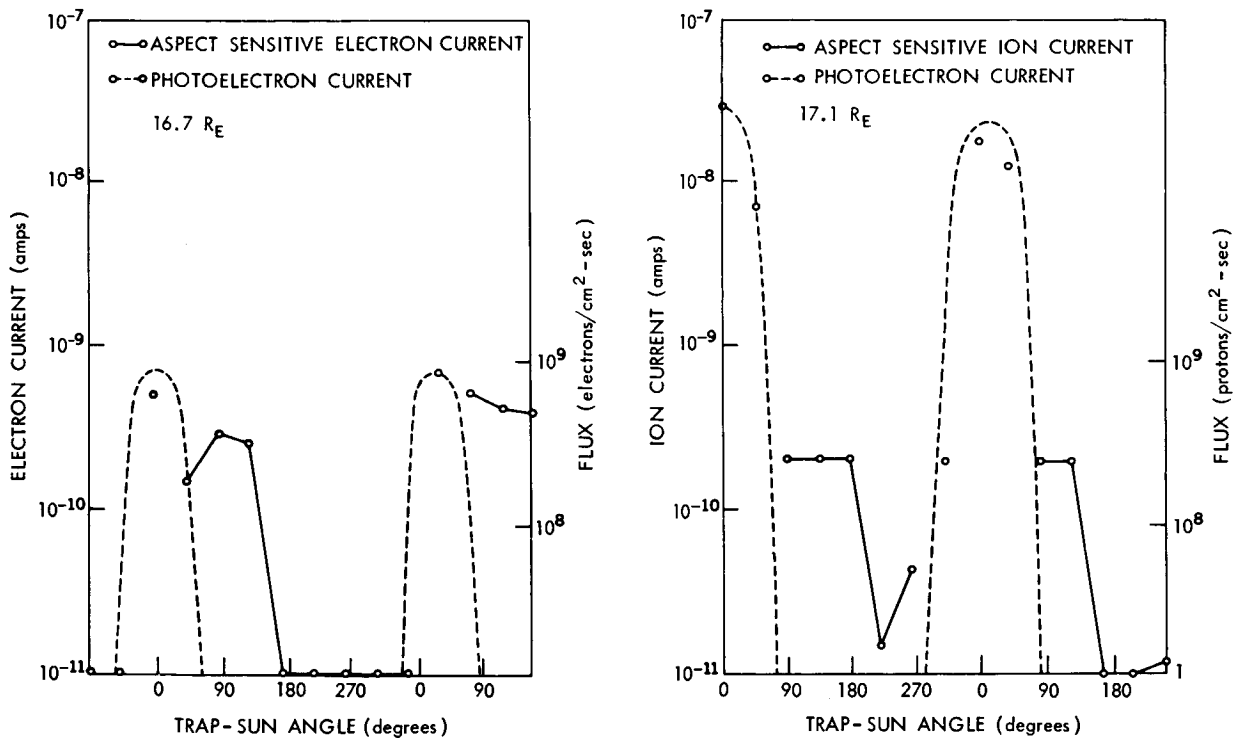


Figure 8—The ion and electron currents plotted as a function of trap-sun angle orientation. These responses typify the data obtained at distances beyond $16.2 R_E$ geocentric on the first IMP I orbit.

the retarding potentials do not effect the trap currents, it is evident that the negative current measurement represents a net negative charge entering the trap with energies in excess of 100 ev, and that the positive current measurement represents a sum of net positive charge plus secondary electron emission. With the assumption of a secondary electron emission efficiency of 100 per cent, these observations are consistent with the computation that what is seen beyond $16.2 R_E$ (i.e., in the solar wind region) is a net flux of both ions and electrons of the order of 10^8 particles/cm²-sec with energies in excess of 100 ev.

CONCLUSIONS

An overall summary of these observations may be made by using Figure 9, which is a plot of the electron flux as a function of geocentric distance. The three plotted curves were computed

from the negative current in the trap found in the 0 to -5 v retardation interval, the -5 to -10 v and the greater than -100 v interval.

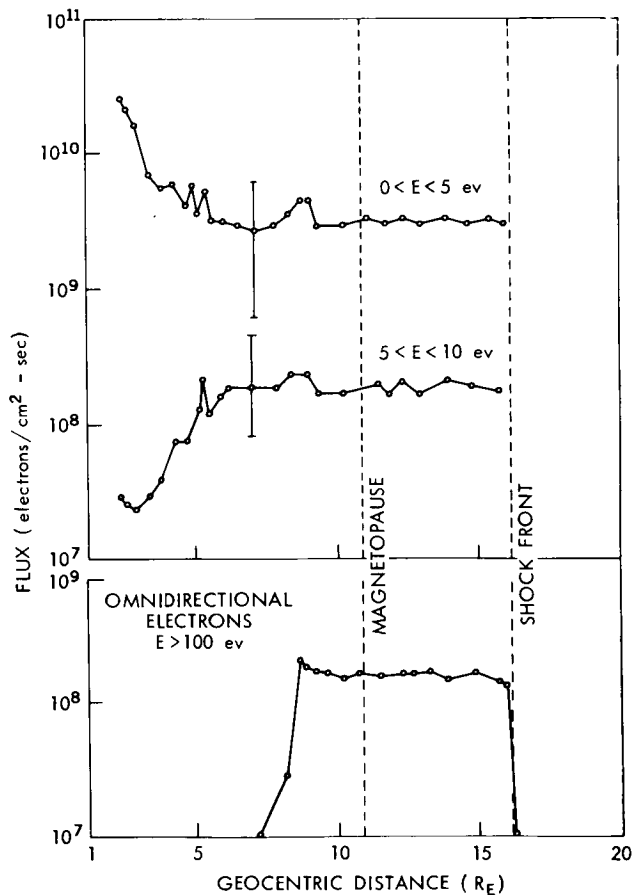


Figure 9—Plot of the electron flux as a function of geocentric distance. Three electron energy intervals are shown.

The flux of electrons with energies $0 \leq E \leq 5$ ev shows a steep decrease with distance between 3 and $5 R_E$. This type of electron drop off is in agreement with whistler observations; Carpenter (Reference 12) refers to this decrease as the "equatorial knee" and points out that the equatorial knee moves further out, i.e., beyond $3 R_E$, during magnetically quiet periods. Out to about $3 R_E$ we note that the flux in the energy interval $5 \leq E \leq 10$ ev is decreasing with distance. This energy interval contains the previously mentioned Hanson photoelectrons, which are evident in Figure 2. Furthermore the drop off in flux in Figure 9 lends credulity to the belief that in this region we observe the flux of trapped photoelectrons produced at altitudes above 300 km.

Beyond $3 R_E$ an increase in the flux of electrons with energy $5 \leq E \leq 10$ ev is noted; and at $7 R_E$ this flux is comparable to the flux of lower energy electrons. The error bars in the figure reflect the previously

discussed uncertainty in the "effective collection area." Thus the overall picture is one of an initial sharp decrease in thermal electron concentration accompanied by an increase in the average energy of electrons, such that, at some $7 R_E$ geocentric there are nearly as many electrons with energy greater than 5 ev as there are those with energy below 5 ev. At $8.2 R_E$ geocentric, on the sunlit side of earth, with a payload-earth-sun angle of 25 degrees, a flux of 2×10^8 electrons/cm²-sec omnidirectional electrons with $E > 100$ ev is observed. There is no significant variation in this flux rate across the magnetosphere (the magnetosphere boundary was determined through the IMP I magnetometer data of Ness*). Beyond $16.2 R_E$ the flux of these omnidirectional particles drops off sharply. Whereas the crossing of the magnetosphere boundary is not evident from the trap data, the crossing of the shock front is. On the earth side of the shock front the trap currents are governed by the retarding potential voltages; outside the shock front the trap currents are governed by the trap-sun angle orientation.

The recent controversy (References 13 and 14) concerning the observations of particles in the outermost belt of charged particles and whether or not these particles are trapped is not resolved on the basis of these IMP observations, since it is possible to explain the observed constant flux across the magnetosphere boundary either on the basis of some unknown mechanism for solar wind penetration as suggested by Gringauz or on the basis that the total trapped flux inside the boundary just equals the flux outside the boundary, a possibility not excluded by the measurements of Explorer XII and IV (Reference 15).

ACKNOWLEDGMENTS

Messrs. W. J. Archer and J. Luce were responsible for the instrumentation associated with this experiment. Also acknowledged are the helpful discussions with Mr. R. E. Bourdeau.

REFERENCES

1. Hanson, W. B., "Electron Temperatures in the Upper Atmosphere," in: *Space Research III: Proc. 3rd International Space Sciences Symposium*: 282-302, Amsterdam: North-Holland Pub. Co., 1963.
2. Mariani, F., "Pitch-Angle Distribution of the Photoelectrons and Origin of the Geomagnetic Anomaly in the F₂ Layer," *J. Geophys. Res.* 69(3):556-560, February 1, 1964.
3. Jastrow, R., and Pearse, C. A., "Atmospheric Drag on the Satellite," *J. Geophys. Res.* 62(3):413-423, September 1957.
4. Beard, D. B., and Johnson, F. S., "Charge and Magnetic Field Interaction with Satellites," *J. Geophys. Res.* 65(1):1-8, January 1960.

*Norman F. Ness, Private communication.

5. Al'pert, Ja. L., Gurevic, A. V., and Pitaevskij, L. P., "Effects due to an Artificial Earth Satellite in Rapid Motion through the Ionosphere or the Interplanetary Medium," *Space Sci. Rev.* 2(5):680-748, November 1963.
6. Loeb, L. B., "Basic Processes of Gaseous Electronics," Berkeley: University of California Press, 1955, pp. 331-371.
7. Freeman, J. W., Van Allen, J. A., and Cahill, L. J., "Explorer 12 Observations of the Magnetospheric Boundary and the Associated Solar Plasma on September 13, 1961," *J. Geophys. Res.* 68(8):2121-2130, April 15, 1963.
8. Gringauz, K. I., et al., "Results of Experiments with Three-Electrode Charged-Particle Traps in the Second Radiation Belt and in the Outermost Charged-Particle Belt," *Iskusst. Sputniki Zemli*, no. 15:92-97, 1963, Trans. in: Planet. Space Sci. 12:175-179, 1964.
9. Gringauz, K. I., et al., "A Study of the Interplanetary Ionized Gas, Energetic Electrons and the Corpuscular Radiation of the Sun by Means of 3-Electrode Collectors for Charged Particles in the Second Soviet Cosmic Rocket," *Dokl. Akad. Nauk SSSR*, 131(6):1301-1304, April 21, 1960, Trans. in: Sov. Phys.-Doklady, 5(6):1225-1228, May-June 1961.
10. Gringauz, K. I., et al., "Ionized Gas and Fast Electrons in the Vicinity of the Earth and in Interplanetary Space," *Iskusst. Sputniki Zemli*, no. 6:108-112, 1961, Trans. in: Planet. Space Sci. 9(1):21-25, January-February 1962.
11. Gringauz, K. I., et al., "Measurements Made in the Earth's Magnetosphere by Means of Charged Particle Traps Aboard the Mars 1 Probe," in: *Space Research IV: Proceedings 4th International Space Sciences Symposium*, Amsterdam: North-Holland Pub. Co., 1963.
12. Carpenter, D. L., "Whistler Measurements of the Equatorial Profile of Magnetospheric Electron Density," *J. Geophys. Res.* 68(6):1675-1682, March 15, 1963.
13. Gringauz, K. I., "Remarks on Papers by J. W. Freeman, J. A. Van Allen and L. J. Cahill, 'Explorer 12 Observations of the Magnetosphere Boundary and the Associated Solar Plasma on September 13, 1961,' and by L. A. Frank, J. A. Van Allen and E. Macagno, 'Charged-Particle Observations in the Earth's Outer Magnetosphere'," *J. Geophys. Res.* 69(5):1007-1010, March 1, 1964.
14. Van Allen, J. A., "Remarks on Accompanying Letter by K. I. Gringauz," *J. Geophys. Res.* 69(5):1011-1013, March 1, 1964.
15. Frank, L. A., Van Allen, J. A., and Macagno, E., "Charged-Particle Observations in the Earth's Outer Magnetosphere," *J. Geophys. Res.* 68(12):3543-3554, June 15, 1963.

N65-29557

INITIAL RESULTS OF THE IMP I MAGNETIC FIELD EXPERIMENT*

by

Norman F. Ness, Clell S. Scearce

and Joseph B. Seek

Goddard Space Flight Center

SUMMARY

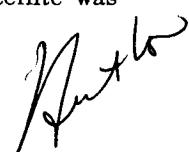
29557

The Interplanetary Monitoring Platform (IMP I), Explorer XVIII (1963 46A), launched on November 27, 1963 has provided the first accurate measurements of interplanetary magnetic fields. The initial apogee of the satellite was located 197,616 km on the sunlit side of the earth, with an apogee-earth-sun angle of 25°. Detailed measurements of the interplanetary magnetic fields and the interaction of the solar wind with the geomagnetic field have been performed. This paper presents the initial results of the magnetic field experiment.

The strength of the interplanetary magnetic field is found to vary between 4 and 7γ with extreme values as low as 1 and as high as 10γ . The magnitude, however, is extremely stable over time scales of hours, although directional changes are significant. The average direction of the interplanetary magnetic field lies slightly below the plane of the ecliptic and approximately along the streaming angle predicted for a steady state solar wind. A significant feature of the magnetic field measurements is the discovery of fields pointed diametrically opposite the streaming angle indicating filamentary structure of interplanetary fields. Associated with the fields of opposite direction are null surfaces between the filaments and in the overall field structure.

The complex interaction of the solar wind and geomagnetic field shows a variety of significant magnetic field fluctuations and transition characteristics. The discovery at $13.4 R_E$, of the collisionless magnetohydrodynamic shock wave at the stagnation point associated with the super Alfvénic flow of solar plasma is one of the major results of this experiment. Details of the fluctuations are discussed as well as the gross structure and shape of the magnetospheric surface ($10.2 R_E$ at the subsolar point) and the shock wave from the subsolar point to the nighttime geomagnetic tail. The transition region between the shock wave and the magnetopause is one of high turbulence in the magnetic field.

A unique aspect of the magnetic field data is the detection of the magnetohydrodynamic wake of the moon during the fifth orbit when the satellite was eclipsed by the moon's magnetosphere while in interplanetary space.



*Published in *J. Geophys. Res.* 69(17):3531-3570, September 1964.

INTRODUCTION

The Interplanetary Monitoring Platform (IMP I), Explorer XVIII (1963 46A), was launched from the Atlantic Missile Range, Cape Canaveral, Florida on November 27, 1963 at 0230:01.07 UT. The 63 kg spacecraft (Figure 1) was placed into a highly elliptical orbit by a three stage Thor-Delta vehicle with an initial orbital period of 93.5 hrs, inclination to the earth's equator of 33.33° and eccentricity of 0.937. The initial apogee was on the sunlit side of the earth at an angle to the sun of 25.6° and at a geocentric distance of 197,616 km (initial perigee, 192 km). The spacecraft was spin stabilized at an initial rate of 22.27 rpm with an initial spin axis-satellite-sun angle measured by the spacecraft optical aspect sensor of 111° . The right ascension and declination of the spacecraft spin axis were initially 116.6° and -23.5° , respectively.

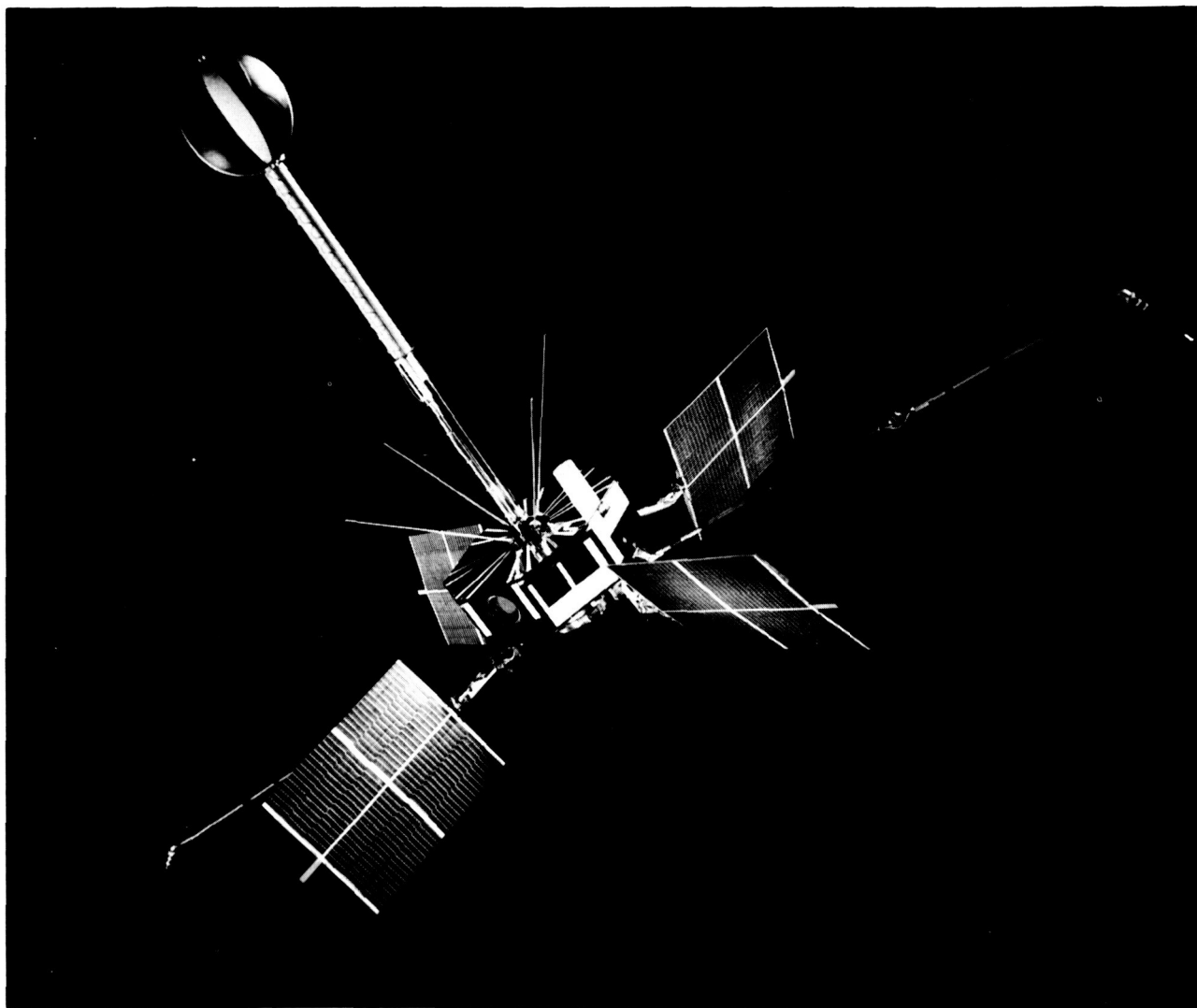


Figure 1—IMP I spacecraft in flight configuration with all appendages (solar paddles, fluxgate magnetometer booms, and rubidium vapor magnetometer tube) fully deployed.

An important physical force acting on the dynamically spin stabilized satellite and its solar paddles is solar radiation pressure. This force, or more properly, the torque effect associated with this force has led to both a gradual increase of the satellite spin rate and a precessional motion of the spin axis in celestial inertial coordinates. When the spacecraft aspect angle to the sun decreases below 90° the net effect of the solar radiation pressure torque will be to decrease the spin rate. After 70 days in orbit the spin rate was 24.30 rpm at an aspect angle of 125° to the sun with the location of the spin axis given by a right ascension of 111.1° and declination of -30.6° . The maximum solar aspect was 129° after 47 days in orbit. The lifetime of the satellite is expected to be at least 160 days and may well be 360 days or longer.

It is the purpose of this paper to discuss primarily the results of the magnetic field experiment on board the IMP I spacecraft. At this early date approximately 70 days of data collected by the spacecraft have been acquired, processed, and analyzed. It is important to note that our initial impressions of the significance of certain features of the data and their interpretations may be changed as the quantity of information returned from the satellite is increased and as our overall statistics and characteristics of the magnetic fields and associated phenomena become better understood.

The primary mission of the magnetic field experiment was four-fold:

1. The *interplanetary magnetic field* — its magnitude, direction and temporal variations as correlated with solar and terrestrial phenomena;
2. The *transition region* associated with the interaction of the solar wind with the geomagnetic field which leads to the study of two characteristic boundary surfaces; namely,
3. The *collisionless magnetohydrodynamic shock wave* surface separating the undisturbed interplanetary medium from the transition region, and
4. The *magnetopause boundary* separating the transition region from the magnetosphere, that region of space containing the geomagnetic field and encompassing the earth in the classical concept of the Chapman-Ferraro geomagnetic cavity.

These four major phenomena have been investigated in considerable observational detail thus far by this experiment but we shall attempt to summarize them at this time. Future publications concerning the IMP I magnetic field experiment will consider in substantially more detail the results of the magnetic fields in space and their solar-terrestrial correlations and also the correlations with other sensing elements carried on board the same spacecraft measuring importantly related phenomena such as the low energy proton flux "solar wind" and the higher energy proton-electron particle fluxes.

An additional feature investigated by the spacecraft has been the interaction of the solar wind with the moon, forming a magnetohydrodynamic (MHD) wake. This unexpected event occurred during December 1963 when the satellite was in an approximately lunar eclipsed position with respect to solar plasma propagation from the general direction of the sun. An even more fortuitous event studied occurred near the apogee of the satellite's second orbit during which time a geomagnetic

sudden commencement (SC) storm occurred on December 2, 1963 at 2117 UT.* A clearly unique event was observed to occur in the interplanetary magnetic field data three minutes prior to the terrestrial magnetic field event.

HISTORICAL BACKGROUND

The existence, general description, and temporal behavior of the interplanetary magnetic field have been deduced in the past from a variety of terrestrial observations notably the analysis of energetic particle trajectories impacting the earth. An analysis by McCracken (Reference 1) is indicative of the most recent efforts in this respect. Direct measurements in space by Pioneer V (Reference 2) with a search coil magnetometer were initially interpreted as consistent with a steady field component of 2.5γ normal to the ecliptic plane. In addition it was also reported that fluctuations as large as 50γ were detected during times of magnetic disturbance (Reference 3). Recent efforts to reanalyze and reinterpret the Pioneer V data by Greenstadt[†] (Reference 4) have yielded results inconsistent with the initial findings in that the fields are now found to have been much nearer to being in the plane of the ecliptic with a magnitude of $5-10\gamma$.

A steady field normal to the plane of the ecliptic is inconsistent with a number of models of the interplanetary magnetic field in which solar magnetic lines of force are stretched out away from the sun by the highly conducting streaming solar plasma (Reference 5). The low energy proton flux detected by Explorer X (Reference 6) was directed at all times away from the sun but fluctuated in magnitude and energy spectra as a function of time. Measurements by the Mariner spacecraft (References 7 and 8) have indicated that the flux of low energy plasma from the sun gives a spectrum with considerable temporal and energy variation but which, in general, is in agreement with the extrapolated results of Explorer X (1961 $\alpha 1$).

Measurements of the interplanetary magnetic field by Explorer X (Reference 9) were distorted by a strong interaction between the streaming plasma and the magnetic field of the earth which led to the formation within the plasma stream of a cavity containing the geomagnetic field. The magnetometer measurements on the Mariner (1962 $\alpha\rho 1$) spacecraft (Reference 10) are incomplete for total vector information, because of unknown spacecraft magnetic fields, and do not provide accurate vector data on the interplanetary magnetic field. The data are consistent with an interplanetary field in the plane of the ecliptic with a strength of approximately 5γ normal to a sun-satellite direction. The magnitude of this field component compares somewhat favorably with Pioneer V (1960 $\alpha 1$) but the direction is different by 90° . Recent data on galactic fields (Reference 11) indicate that they are on the order of 0.5γ and may be up to 2.5γ in interstellar space.

In summary the interplanetary magnetic field has been estimated by various methods to be approximately $1-10\gamma$ average value, although steady periods might be infrequent. The variability of the interplanetary magnetic field and the extreme variations expected during solar disturbances

*Final classification of this event is not as an SC.

[†]Greenstadt, E. W., Private communication, 1963.

indicated a wide dynamic range was required as well as precise and accurate measurements in order to achieve the desired scientific objectives of this experiment.

INSTRUMENTATION

The IMP I satellite experiment complement included two types of magnetic field instruments: A Rb^{87} vapor magnetometer and two monoaxial fluxgate magnetometers. The purpose of the rubidium vapor magnetometer was to allow extremely accurate measurements of the interplanetary magnetic field to be performed and also to provide a wide dynamic range for magnetic field measurements within the magnetosphere and near its boundary, the magnetopause. The two monoaxial fluxgate magnetometers were employed to delineate precisely the vector characteristics of the interplanetary magnetic field. Their zero levels were calibrated inflight on the spacecraft through a combined use of the rubidium vapor magnetometer data. The dynamic range of the fluxgates is $\pm 40\gamma$ with a sensitivity of $\pm 1/4\gamma$ while the dynamic range of the rubidium vapor magnetometer is 3-500 γ with a sensitivity dependent upon the magnitude of the field; the 0.1 percent precision of the ground digitization system leading to maximum errors of $\pm 0.5\gamma$ at the upper limit.

The rubidium vapor magnetometer measures the absolute scalar intensity of the magnetic field by measuring the Zeeman splitting of the sub-levels in the ground state of the atom (Reference 12). For the Rb^{87} isotope the separation between adjacent levels is 6.99592 cps/ γ . In order to detect these separations, a technique known as optical pumping is employed to selectively populate one of these sub-levels. As the vapor in the absorption cell is "pumped" by a spectral lamp it absorbs the light until a final state is reached in which the cell becomes transparent. The application of a weak ac magnetic field at the frequency corresponding to the separation of the Zeeman sub-levels (which is the Larmor frequency) then results in the redistribution of the population to all the levels and hence re-absorption of the incident light. It is possible to couple the modulated light produced and subsequently detected by a silicon photocell to the coil producing the ac magnetic field. Such a feedback loop with the appropriate phasing of signals operates the magnetometer as an atomic self-oscillator with the resonant frequency being the Larmor frequency. A "flashlight" configuration (Reference 13) of one lamp and absorption cell has been employed in the particular configuration used on the IMP spacecraft (Figure 2).

Although the Larmor frequency is dependent only upon the magnetic field intensity the inherent signal-to-noise ratio depends upon the angle α between the optical axis of the system (along the spin axis in IMP I) and the magnetic field as approximately $\sin 2\alpha$. This leads to the formation of two null regions of field orientation, polar and equatorial relative to the spin axis, in which the magnetometer will not self-oscillate with sufficient signal-to-noise ratio for accurate quantization by the ground digitization system. The fluxgate magnetometers however do measure the magnetic field vector at an extended range when in the null regions of the rubidium vapor magnetometer and thus provide complete coverage of the magnetic field in interplanetary space over the range 0.25 to 40 γ or more.

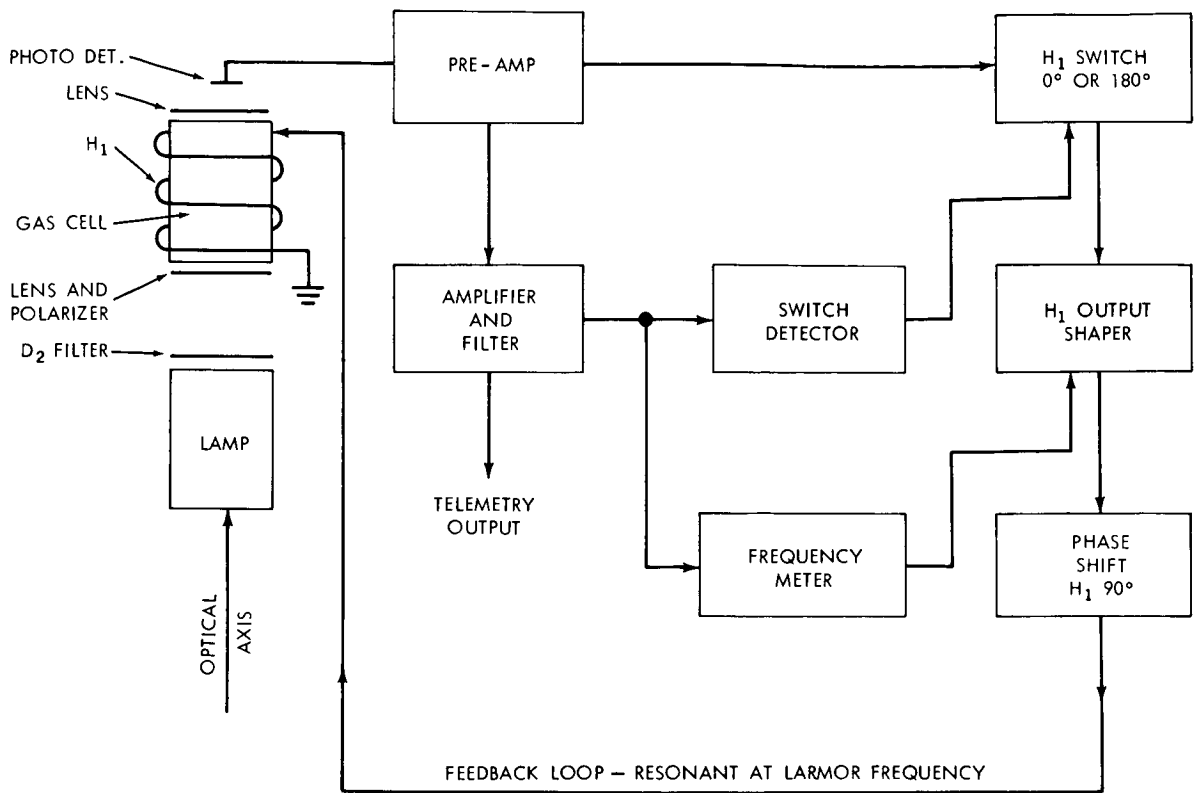


Figure 2—Functional block diagram of single absorption cell self-resonant rubidium vapor magnetometer instrumented for IMP I.

It is possible to convert the scalar Rb^{87} magnetometer to a vector instrument by application of a sequence of known triaxial bias magnetic fields. On a spin stabilized spacecraft, the rotation of the structure reduces the complexity of the bias coil system so that only one set of coils and one bias vector field is required. By a proper choice of the orientation and magnitude of the bias field the instrument will measure vector magnetic fields with an accuracy dependent upon the unknown vector field magnitude and orientation. An additional purpose of the bias coil system is to provide a means for inflight calibration of the fluxgate magnetometer zero field levels since it is possible to measure the unknown vector field simultaneously with two vector instruments.

Let F be the magnitude of unknown magnetic field; α , the polar angle of F to spin axis; B , the magnitude of bias magnetic field; θ , the polar angle of B to spin axis; R , the magnitude of resultant field measured; and ω , the spin frequency of spacecraft. Then

$$R = \sqrt{F^2 + B^2 + 2FB \cos \alpha \cos \theta + 2FB \sin \alpha \sin \theta \cos \omega t} \quad (1)$$

The analysis of $R(t)$ will yield values of F and α , if B and θ are known.

A major problem associated with the utilization of a rubidium vapor magnetometer in satellite applications is the necessity to maintain both the lamp used for optical pumping as

well as the gas cell for resonance absorption at optimum temperatures. These unfortunately range over only limited values and for the gas cell an optimum temperature is approximately $42.5^\circ \pm 5^\circ\text{C}$. The temperature at the lamp bulb base support structure is optimally $110^\circ \pm 10^\circ\text{C}$. The development of the IMP Rb^{87} vapor magnetometer was predicated upon the necessity to include active thermal control circuits and heating coils on the lamp and gas cell. Because of the difference in optimum temperatures required it was necessary to operate three completely independent temperature control systems: one for the lamp and two for the gas cell. Figure 3 illustrates the results of the active thermal control system on the spectral lamp from telemetered temperatures of the lamp bulb. It is seen that shortly after launch the temperature of the bulb begins to rise until it reaches the critical value of 120°C at which time the heat source is turned off. When the temperature reaches the lower limit of 100°C the active thermal control once again begins to heat the bulb to raise its temperature and this cycle has continued since launch stabilizing at a periodicity of approximately 32 minutes. This is indicative of the thermal time constants of the lamp bulb housing and the radiative properties of the support structures enclosing the rubidium spectral lamp. The temperature of the gas cell has always been above its lower limit and has not

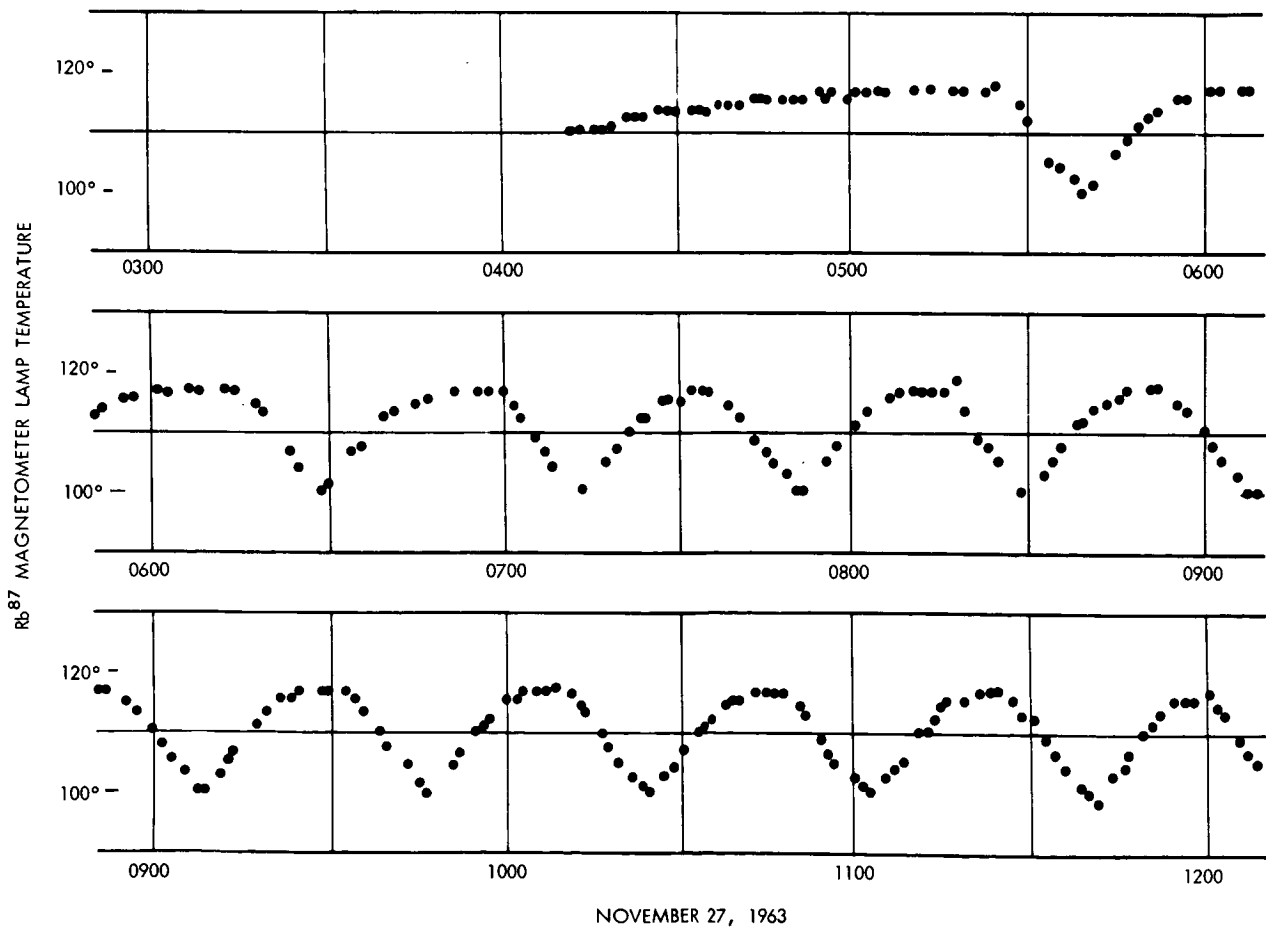


Figure 3—Representative cycling of active thermal control on spectral lamp of Rb^{87} vapor magnetometer following launch of IMP I.

cycled thus far. It remains at approximately 47°C being heated by the thermal losses from the physically adjacent spectral lamp. The IMP I rubidium magnetometer is completely transistorized. The additional power required for controlling the environmental temperatures of these elements is a fraction of the total power (approximately 4.5 watts) required by the system.

The characteristics of the fluxgate magnetometers are considerably less sensitive to temperature and their operation is proper and within the specified limits over a very wide temperature range. Thus no measurement of the temperatures of the fluxgates was required and their operation has proceeded normally. Standard calibrations on the sensitivity of the fluxgates are conducted in flight and have been within the desired range. The operation of the instrumentation for the magnetic field experiment on the IMP I spacecraft has been excellent since date of launch and no failures have been experienced to date.

In order to provide a uniform environment for the rubidium magnetometer system, a 13-inch-diameter spherical enclosure encompasses the lamp and gas cell mounted on top of the spacecraft (see Figure 1). This sphere, appropriately surface-coated for passive thermal control, provides a uniform temperature regime in which thermal equilibrium of the sensing elements can be maintained with minimum power. In addition this sphere supports a set of McKeenan coils (Reference 14) for generating the known bias fields. The strength of the magnetic bias field employed on the IMP I spacecraft was 20γ at an angle of $54^{\circ} 45'$ to the spin axis. These values were chosen to optimize the directional sensitivity of the resulting vector magnetometer for interplanetary magnetic fields. The output frequency from the magnetometer was used to directly phase modulate the 136 Mc carrier of the satellite telemetry system. Subsequent digitization of the signal on the ground via a period count procedure was employed using a multiplied reference frequency recorded on the raw analog data tape as the counter. This eliminated to first order the wow and flutter errors associated with data record and playback.

The fluxgate magnetometer measures the relative magnetic field intensity along the axis of the sensing element. The fluxgate sensor consists essentially of a saturable magnetic core which is driven at a high rate (10 kc) from positive to negative saturation by a solenoidal drive coil. Any second harmonic signal generated is due to the presence either of an ambient field component along the axis of the element or to permanent magnetization of the core material. The voltage output (0 to +5) represents the discriminated second harmonic output which is calibrated to yield the magnitude of the field component parallel to the sensor axis while the phase indicates the direction, parallel or antiparallel. Figure 4 presents a block diagram of the fluxgate magnetometers used on IMP I.

The pulsed frequency modulation (PFM) telemetry system employed on IMP I encoded the fluxgate data by applying it to a voltage controlled oscillator whose frequency output (333 cps to 938 cps) modulated the 136 Mc carrier. The fluxgate signals were digitized on the ground through the combined use of a contiguous set of narrow bandpass filters specifically designed for the PFM telemetry scheme and commonly referred to as a "comb filter". This led to a precision in the digitization of $\pm 0.4\gamma$ associated with the precision of the comb filters (± 1 percent of full scale range).

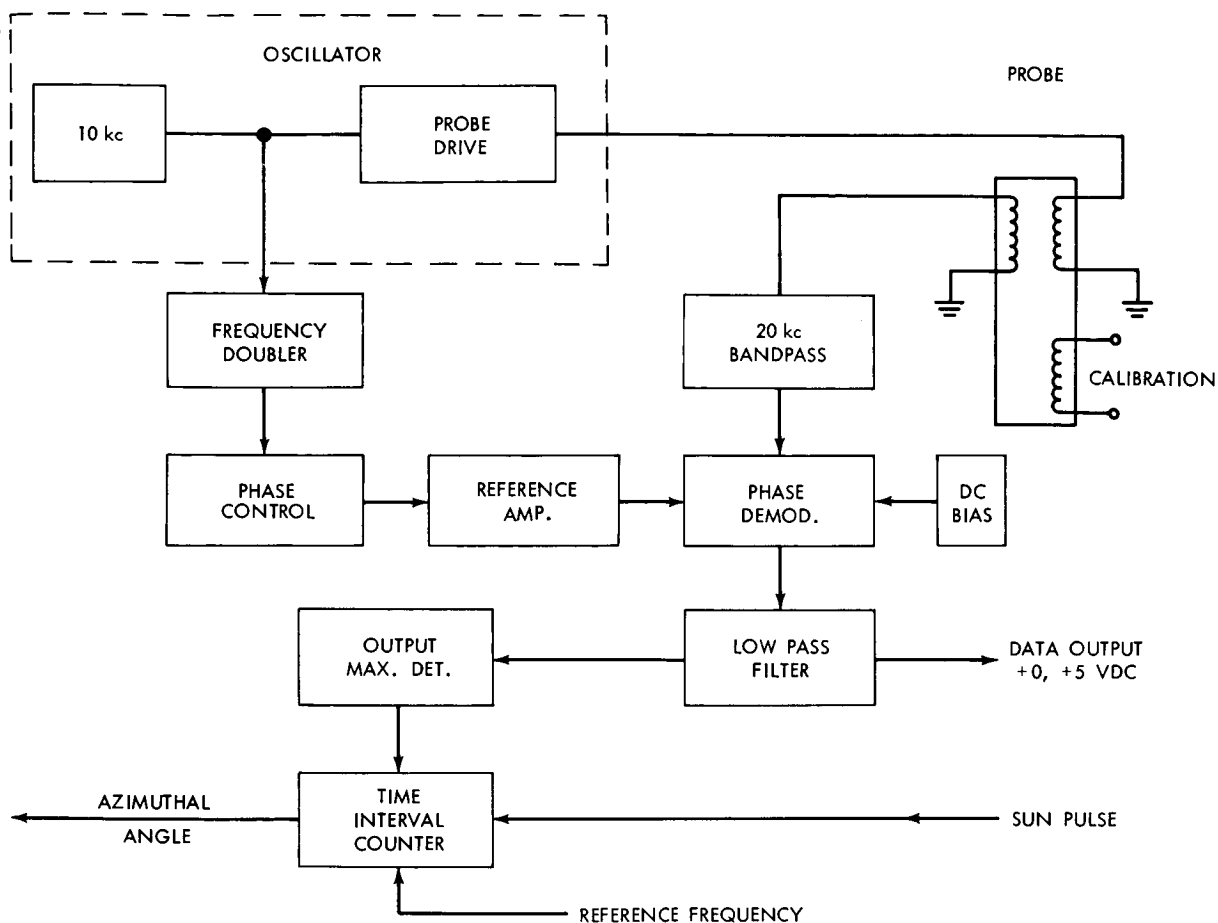


Figure 4—Functional block diagram of monoaxial fluxgate magnetometer and on-board data processor of azimuthal angle instrumented for IMP I.

SPACECRAFT STRUCTURE AND MAGNETIC CLEANLINESS

In order to insure the success of the magnetic field experiments on the IMP spacecraft it was absolutely essential that permanent or induced magnetic fields associated with the structure and/or the electronics and instrumentation be kept to an absolute minimum. In the design and fabrication of all subsystems, components that were highly magnetic were replaced by nonmagnetic equivalents and all circuit leads and welding material were chosen to be nonmagnetic or minimally magnetic. Considerable care was taken in the design and wiring of the spacecraft harness and power distribution system so that no net circulating currents and/or ground loops existed. In some instances this necessitated complex wiring techniques between and within subsystems. In addition, each solar cell module (8 × 15 series-parallel individual cell arrangement) was back wired within the paddle structure for compensation so that cell and module degradation did not change the compensating currents required. All power leads between subsystems and within subsystems at current levels above 20 ma were bifilar or twisted pair wound.

Extensive tests of individual subsystems and illuminated solar paddles at the Goddard Space Flight Center Magnetic Test Facility and finally of the entire spacecraft in flight configuration at the Naval Ordnance Laboratory Magnetic Ship Modeling Facility and the U. S. Coast and Geodetic Survey, Fredericksburg Magnetic Observatory provided confidence that minimum magnetic fields would be enjoyed on the satellite after launch. Mapping of the actual spacecraft magnetic fields due to permanent, induced, and stray magnetic fields indicated contamination levels at the fluxgate sensors of less than 0.6γ and contamination levels at the rubidium vapor magnetometer of less than 1γ . These limits were set by the natural ambient magnetic field variations at the two facilities since it was not possible to completely cancel out the normal geomagnetic field fluctuations. In addition extensive tests were performed on the vibration effects of ferro-magnetic materials in the earth's magnetic field to evaluate the potential "perming" which might result from the vibration of the satellite during the launch maneuver. These tests indicated contamination fields which were significantly less than the sensitivity of the experiment. The inflight measurements (see Figure 7) showed that the spacecraft fields actually achieved by the IMP I were less than $\pm 0.25\gamma$ and represented one of the "cleanest" satellites carrying magnetometers launched to date.

Figure 5 illustrates a schematic cross section of the IMP satellite showing the geometrical configuration and positional location of the three magnetic field sensing elements. In spite of all the precautions taken to restrict spacecraft magnetic fields to an absolute minimum it was still necessary to place the magnetometer sensors at as remote a distance from the spacecraft as possible. The rubidium vapor magnetometer was contained within the spherical enclosure mounted on top of a telescoping two section boom. This was erected at the same time the spacecraft was separated from the third stage ABL-258 rocket motor during the launch maneuver. This placed the Rb^{87} magnetometer resonance gas cell at a distance of 1.65 meters (65") from the center of the spacecraft. The two monoaxial fluxgate magnetometers were mounted at the extremities of double sectioned folding booms. These were also erected at 3rd stage separation and placed the sensors

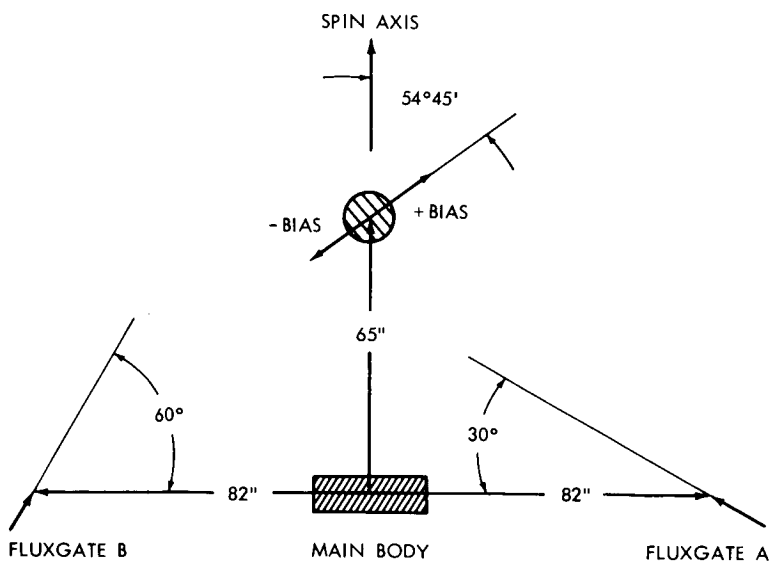


Figure 5—Schematic cross section of the IMP satellite illustrating location and orientation of sensors for magnetic field measurements.

2.1 meters (82") from the center of the spacecraft. The use of two booms was part of the experiment design to yield a spacecraft structure that was both statically and dynamically stable. Their axes were oriented so as to both lie in the same meridian plane containing the spin axis of the satellite but at different angles to the spin axis. The purpose of the two angles was to allow the sampling of magnetic fields larger than 40γ by either one of the two sensors depending upon the orientation of the unknown field to the spin axis. This is illustrated in Figure 6 in which the allowable magnitude as a function

of polar angle α is shown for the θ angles, $\theta_A = 30^\circ$ and $\theta_B = 60^\circ$, chosen for the two sensors. It is seen that by use of the two angles whose sum equals 90° the sensors tend to compliment each other in their capability to accurately and in an undistorted manner measure fields of intensities greater than 40γ . It was the intent of the experiment to extend the effective range of the fluxgate magnetometers beyond 40γ and thereby compliment the rubidium vapor magnetometer for field orientations that were nearly parallel or perpendicular to the spin axis of the spacecraft because of its signal-to-noise degradation at these orientations.

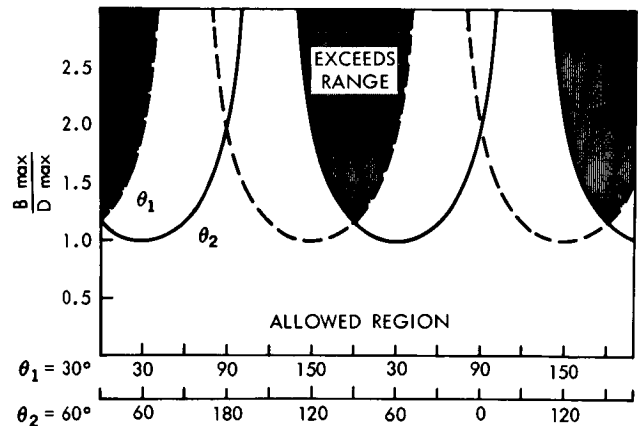


Figure 6—Dynamic range of IMP I fluxgate magnetometers as a function of sensor and field orientation. Allowed region is defined to be such that the detected output of the sensor is linearly related to the component of the field parallel to the sensor axis.

DATA SAMPLING AND ANALYSIS PROCEDURES

Magnetic field data are transmitted by the satellite sequentially in a format which time multiplexes the magnetic field information with the other scientific sensors and spacecraft performance parameters in a predetermined time shared manner. Figure 7 illustrates on a linear time scale four sequences of 16 frames containing fluxgate and rubidium vapor magnetometer data extending over a time interval of 327.65 seconds. Each normal telemetry sequence is 81.9144 seconds in length and contains four samples of real-time fluxgate magnetometer data consisting of continuous transmissions for 4.8 seconds at intervals of 20.5 seconds. Four such samples per sequence are shared between the two fluxgates, A and B, previously referred to in the description of the location of sensors on board the spacecraft. This procedure is repeated in an identical manner for the next two sequences. Every fourth sequence transmitted, however, is uniquely different from the previous three in that it contains only rubidium vapor magnetometer data continuously transmitted for a period of 81.91 seconds with gaps associated with the synchronization time channels required by the PFM telemetry format every 5.12 seconds.

Figure 7 illustrates the effects due to the different θ angles of the monoaxial fluxgate sensors as indicated by the difference in amplitude of the spin modulated sine wave for fluxgates A and B. In addition during the first few samples of each fluxgate a sensitivity calibration is performed which linearly adds a field of 10γ to the measured field. By measuring the difference in the recorded fields, and taking into account the rotation of the spacecraft, the verification of the sensor's sensitivities can be performed.

The programming of the rubidium vapor magnetometer bias coil system is also evident. During the first four frames of the 4th sequence the rubidium bias field is in a positive direction pointing forward relative to the spin axis. During the next eight frames the bias coil is programmed off and during the last four frames the current through the bias coils is directed in the reverse sense so as to yield a bias vector which points aft of the spacecraft.

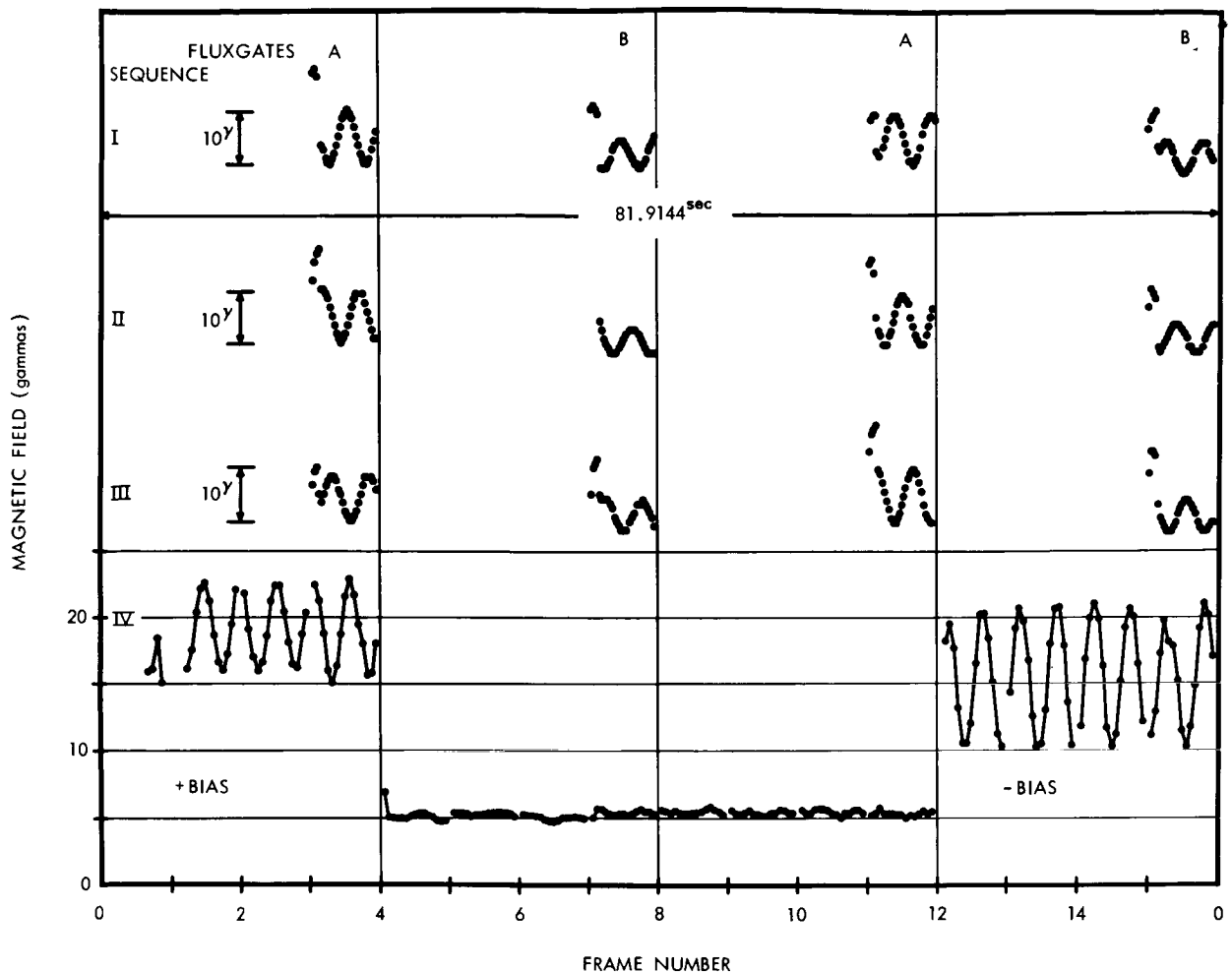


Figure 7—Sample telemetry data format for IMP I taken at a distance of 100,000 km illustrating interlacing of fluxgate and rubidium vapor magnetometer data.

The design of the experiment was contingent upon a measurement of interplanetary magnetic fields ranging between 1 and 10γ . Utilization of a bias magnetic field of 20γ and the illustrated programming sequence allows a unique and a complete determination of the vector magnetic field characteristics through the use of mathematical procedures to analyze the resultant fields given in Equation 1. These data were obtained at an elevation of approximately 10^5 km during the first month's operation of the satellite and is representative of the general characteristics of magnetic field data obtained in interplanetary space on the IMP I spacecraft.

A principal problem with the use of fluxgate magnetometers is the fact that they are relative devices whose absolute zeros can only be calibrated by physically reversing the sensor in a stationary magnetic field. Although the spacecraft rotates about its spin axis and thereby allows a unique determination of the magnetic field component perpendicular to the spin axis F_{\perp} , the component parallel to the spin axis F_{\parallel} is not capable of unique and absolute determination from the fluxgate data alone. Thus it has been necessary to calibrate the fluxgate magnetometer zero levels through the

use of the absolute rubidium vapor magnetometer data while in flight. Figure 8 compares the fluxgate magnetometer data and the rubidium vapor magnetometer data when viewed in a coordinate system in which magnetic field data is represented by perpendicular and parallel component values.

In this representation the magnetometer data from Fluxgate A has been used without any adjustment of its zero level. The data from Fluxgate B has been adjusted taking into account a zero offset of -2.1γ . Throughout the satellite's first 70 days, the fluxgate magnetometer data and the rubidium vapor magnetometer data have compared very well with the zero offset for Fluxgate A remaining constant at $0 \pm 0.25\gamma$ which is equal to the sensitivity of the analysis and the noise level of the instrument. The zero offset for Fluxgate B has changed from approximately -2.1 to -2.5γ . The fluxgate magnetometers were manufactured by the Schonstedt Instrument Corporation. The rubidium spectral lamp and absorption cell were manufactured by Varian Associates. The ancillary electronics for Fluxgate A and the complete electronics for the rubidium vapor magnetometer were fabricated at Goddard Space Flight Center.

A natural coordinate system to use in the initial reduction of magnetic field data on a spin stabilized spacecraft is associated with the spin axis of the satellite and the satellite-sun direction. In the payload coordinate system defined in Figure 9, the Z-axis is coincident with the spin axis of

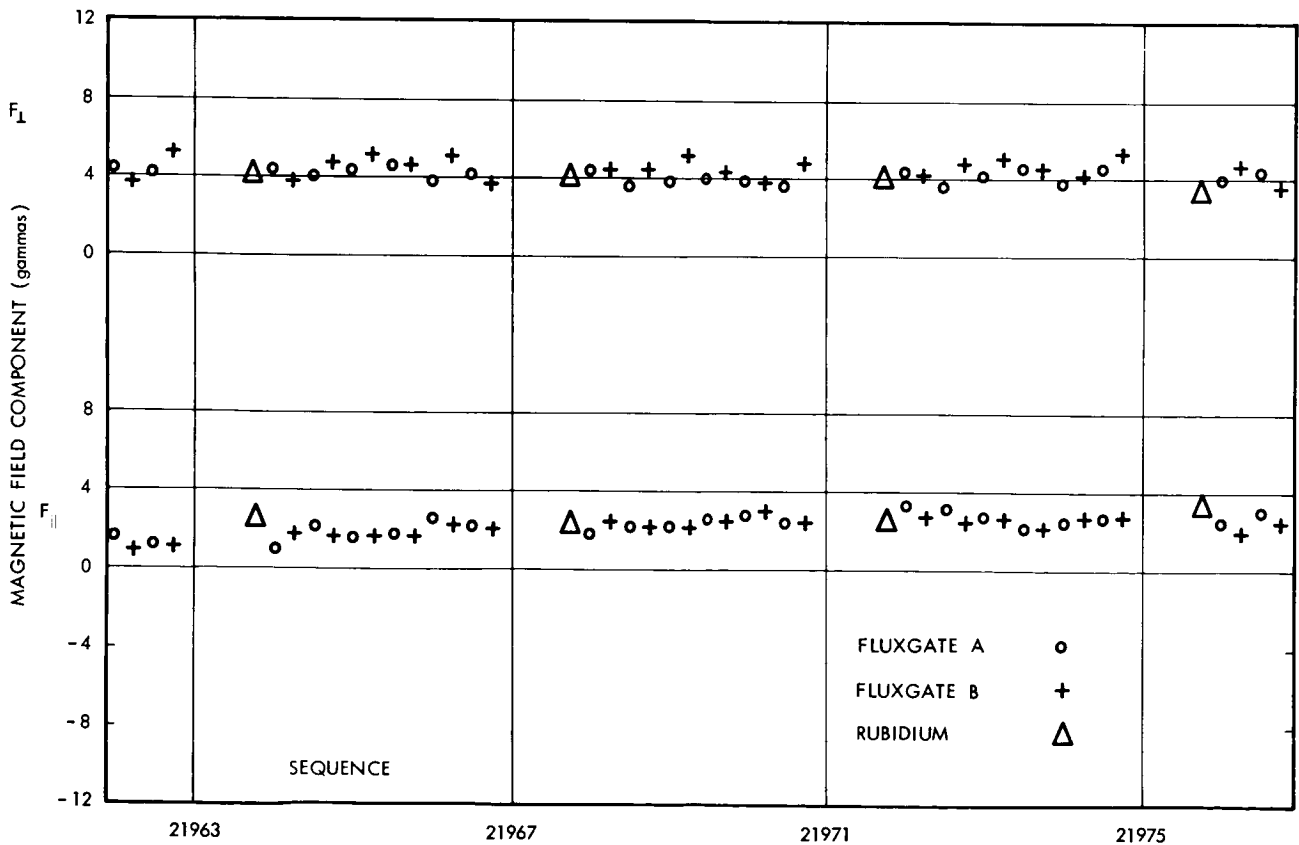
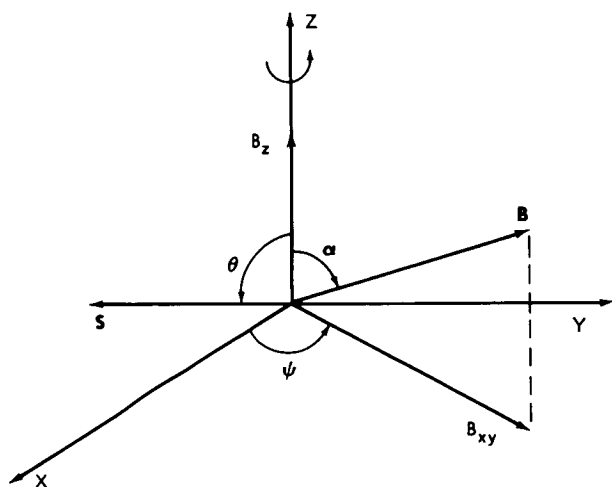


Figure 8—Results of calibration of fluxgate magnetometer zero levels with rubidium vapor magnetometer data obtained while IMP I was in orbit.



- Z = Spin axis of spacecraft
- B = Unknown vector field
- S = Sensor axis $|S| = 1$
- ψ = Azimuthal angle of B_{xy}
- ω = Angular spin frequency
- X, Y, Z = non rotating RH Coordinate system
- Detector Output = $D = B \cdot S = B \cos \alpha \cos \theta + B \sin \alpha \sin \theta \cos (\omega t - \psi)$

$$\frac{\delta D}{\delta t} = -\omega B_{xy} \sin \theta \sin (\omega t - \psi)$$

$$\frac{\delta^2 D}{\delta t^2} = -\omega^2 B_{xy} \sin \theta \cos (\omega t - \psi)$$

$$B_{xy}^2 = \left[\left(\frac{\delta D}{\delta t} \right)^2 \omega^2 + \left(\frac{\delta^2 D}{\delta t^2} \right)^2 \right] / \omega^4 \sin^2 \theta$$

$$\psi = \tan^{-1} \left[\omega \frac{\delta D}{\delta t} / \frac{\delta^2 D}{\delta t^2} \right]$$

Figure 9—Payload coordinate system and analysis procedure to obtain vector fields with monoaxial fluxgate magnetometers on a spin stabilized spacecraft.

the spacecraft; the X-Z plane contains the satellite-sun vector; and the Y-axis is chosen to form a right-handed coordinate system. The analysis of the monoaxial fluxgate data has proceeded through the use of numerical filters designed to extract from the spin modulated magnetometer signal the first harmonic and the first and second time derivatives of the magnetometer signal at a particular instant of time. As illustrated in Figure 9, it is possible to combine the first and second time derivatives to determine both the component of the magnetic field perpendicular to the spin axis, $B_{xy} = B \sin \alpha$, and also the azimuthal angle of the magnetic field ψ . These two quantities and the first harmonic then determine the component of the magnetic field parallel to the spin axis, $B \cos \alpha$. These three quantities: parallel, perpendicular, and azimuthal angle completely specify the vector magnetic field B. A similar procedure is used to deduce the vector fields from the rubidium magnetometer data.

A limited amount of onboard processing of the Fluxgate A magnetometer data was performed on IMP I as shown in Figure 4. A signal peak detector was developed to provide a pulse in time coincident with the maximum field value which occurred each spin period. A counter using the optical-aspect-sun pulse to open a gate and start a 100 cps count rate was terminated by this peak pulse. By this means an onboard measure of the azimuthal angle ψ was made once each telemetry sequence and provided an accurate check on the numerical procedures used to demodulate the spin modulated magnetometer data. Angle accuracies are more precisely determined for azimuth because of this and are accurate to $\pm 2^\circ$. The angular error of the polar angle α is dependent upon direct measurements of B_{\perp} and B_{\parallel} and thus can be larger for certain ratios of B_{\perp} and B_{\parallel} . This angular error is not significant in the transformation of the data from the initial payload coordinate system to another coordinate system by using a rotation matrix since $B_{\perp} \sin \psi$, $B_{\perp} \cos \psi$, and B_{\parallel} are used directly. The uncertainties in the field values and azimuth angle combine so that an estimate of the general directional accuracy of $\pm 5^\circ$ is conservative.

Each fluxgate magnetic field vector measurement is obtained from a sample of data 4.8 seconds in length containing 30 discrete samples of the magnetic field with a sensitivity of 0.4γ . The bandpass of the magnetometer sensors is flat with negligible phase shift from 0 to 5 cps and falls off at 6 db per decade for higher frequencies. The analysis procedure employed to obtain a vector measurement from the sampling of the magnetic field limits the final information bandwidth in the analysis to approximately 0 to 0.1 cps. As shown in Figure 7, the field samples from the fluxgates are obtained once every twenty seconds.

It is important to note from Figure 7 that during the interval when the rubidium vapor magnetometer bias coil was off the spin modulation observed on the total magnetic field output is less than $\pm 0.25\gamma$. During this particular time interval the magnetometer is sensitive to contamination fields which are perpendicular to the spin axis of the satellite at the position of the rubidium vapor sensor. The fluxgates always measure the component of the magnetic field perpendicular to the spacecraft spin axis accurately, independent of spacecraft contamination fields and zero offsets of the sensors. The agreement of the fluxgate and Rb magnetometer fields F_1 (shown in Figure 8) combined with the absence of spin modulation in the Rb⁸⁷ data gives assurance that the magnetic field data being discussed is accurate to $\pm 0.25\gamma$ and is not affected by spacecraft fields.

COORDINATE SYSTEM FOR RESULTS

The primary mission of the IMP magnetic field experiment was the delineation of the characteristics and statistics of the interplanetary magnetic field. However, the particular satellite chosen for these measurements was earth-orbiting so that all data collected were obtained in the vicinity near the earth. A geocentric solar ecliptic coordinate system has been defined which reflects both the interplanetary nature of the data and takes into account the motion of the earth around the sun. This is identical to the coordinate system used previously in the Explorer X data analysis and interpretation (Reference 9). In this coordinate system (Figure 10), the origin is at the center of the earth, the X_{se} -axis points to the sun, the Z_{se} -axis is normal to the ecliptic plane and Y_{se} is chosen to form a right-handed coordinate system. These coordinates have proven extremely successful in the analysis and interpretation of the magnetic field data.

The vector magnetic field will be presented as a magnitude F and two angles: θ represents the latitude of the magnetic field being positive above the plane of the ecliptic and negative below and ϕ the longitude, being 0° when it points to the sun and 180° when it points away from the sun. As will become evident from studying the results of this experiment, the choice of a

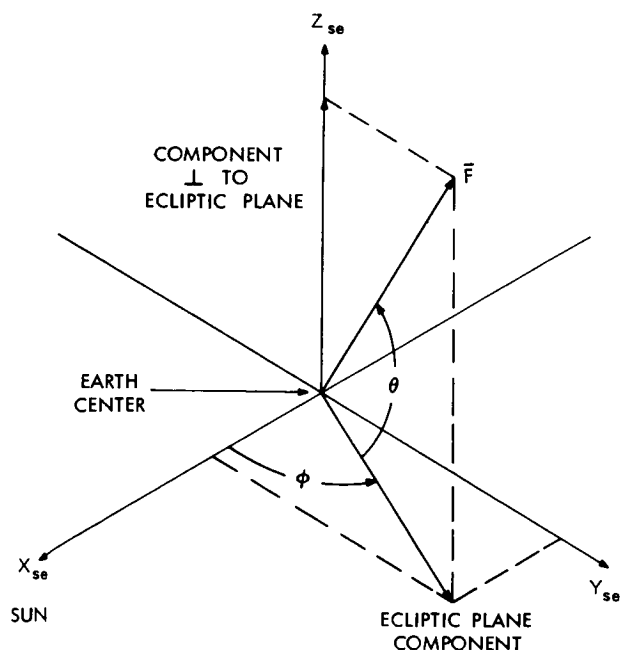


Figure 10—Solar ecliptic coordinate system and associated parameter nomenclature and definitions.

magnitude and two angle representation of the vector magnetic field appears to have more clearly elucidated its unique characteristics rather than the alternate representation using three components of the magnetic field. It should be noted that the coordinate system is not stationary in inertial coordinates but rotates about two principal axes and maintains its orientation at all times as shown in Figure 10. Viewed from a non-rotating solarcentric position the coordinate system moves around the sun once each year following the orbital motion of the earth.

In addition to its utility in the investigation of the interplanetary magnetic fields, the solar ecliptic coordinate system is also useful for studying the magnetic field phenomena associated with the interaction of the solar wind with the geomagnetic field. Since this interaction leads to the formation of a geomagnetic cavity which is strongly solar oriented, the coordinate system chosen is particularly meaningful in presenting the magnetic field data in a frame of reference which illustrates the intimate solar-terrestrial phenomena being studied.

The magnetic field results herein presented represent the time average of the 12 fluxgate measurements occurring in the telemetry transmission in sequences I, II, and III, and yield a sampling interval of 5.46 minutes. The solar ecliptic components for these 12 measurements are averaged by simple addition and no special numerical filters are employed. For the X_{se} component, if X_{se}^i represents the i^{th} value of the magnetic field in the sample set,

$$\bar{X}_{se} = \frac{1}{N} \sum_{i=1}^N X_{se}^i \quad (2)$$

where N is less than or equal to 12 depending upon the percentage of missing data points in the original 30 point data samples. If the number of missing points due to either digitization errors or transmission errors is greater than 10 percent, the corresponding vector field sample is not used in the analysis to determine the 5.46 minute average.

These average values for the three components are used to compute the magnitude \bar{F} and the two angles θ and ϕ . In addition the average value for the components is used in computing estimates of the variance of the magnetic field for the 12 sample data set. The variance is defined as

$$\delta X_{se} = \sqrt{\frac{1}{N} \sum_{i=1}^N (X_{se}^i - \bar{X}_{se})^2} \quad (3)$$

for the X_{se} component and similarly for Y_{se} and Z_{se} . The rubidium vapor magnetometer data have not been included in this initial field averaging because its directional sensitivity for magnetic fields is not as high as the fluxgate magnetometers.

In summary, the magnetic field data are represented by the following six parameters sampled at 5.46 minute intervals:

1. The magnitude of the average components,

$$F = \sqrt{(\bar{X}_{se})^2 + (\bar{Y}_{se})^2 + (\bar{Z}_{se})^2} ;$$

2. The latitude of the field direction,

$$\theta = \tan^{-1} \left\{ \frac{\bar{Z}_{se}}{[(\bar{X}_{se})^2 + (\bar{Y}_{se})^2]^{1/2}} \right\} ;$$

3. The longitude of the field measured in the plane of the ecliptic,

$$\phi = \tan^{-1} \left[\frac{\bar{Y}_{se}}{\bar{X}_{se}} \right] ; \quad (4)$$

4. δX_{se} , variance of the field in the X_{se} direction;
5. δY_{se} , variance of the field in the Y_{se} direction; and
6. δZ_{se} , variance of the field in the Z_{se} direction.

ORBIT CHARACTERISTICS

The orbit of IMP I is highly eccentric with an apogee of approximately $31.7 R_E$ (earth radii). The projection of the first four orbits as a function of time on the plane of the ecliptic or XY solar ecliptic plane is shown in Figure 11. The figures placed on the projection of the trajectory reference the date of the month and/or the time of the day measured in hours (UT) at which the satellite is located at the particular position shown. The location of the satellite at the time of the sudden commencement geomagnetic storm on December 2 is indicated by a cross on orbit 2. The data from this particular orbit will be presented later and discussed in detail with regard to the propagation of magnetic storms in interplanetary space.

A unique feature of highly eccentric orbits is related to the basic dynamics of satellites orbiting the central force field of the earth. At apogee the satellite moves very slowly in longitude so that with IMP I the spacecraft is located beyond $20 R_E$ for 66 percent of its orbital period. Thus the measurements of properties of interplanetary space is enhanced with respect to total time of possible observations. However, because of the high eccentricity of the IMP I orbit it is severely affected by the gravitational field of the moon. The selection of an appropriate "launch window" for IMP must take into account the multiplicity of spacecraft requirements for favorable solar aspect for power and thermal control as well as lifetime in orbit before lunar perturbations lead to a perigee which intersects the earth's surface. IMP I has a lifetime on this basis of approximately two years.

The highly elliptical orbit does not place the satellite far above nor far below the ecliptic plane (see Figure 12). Here a projection of orbit 1 is made on a plane perpendicular to the ecliptic

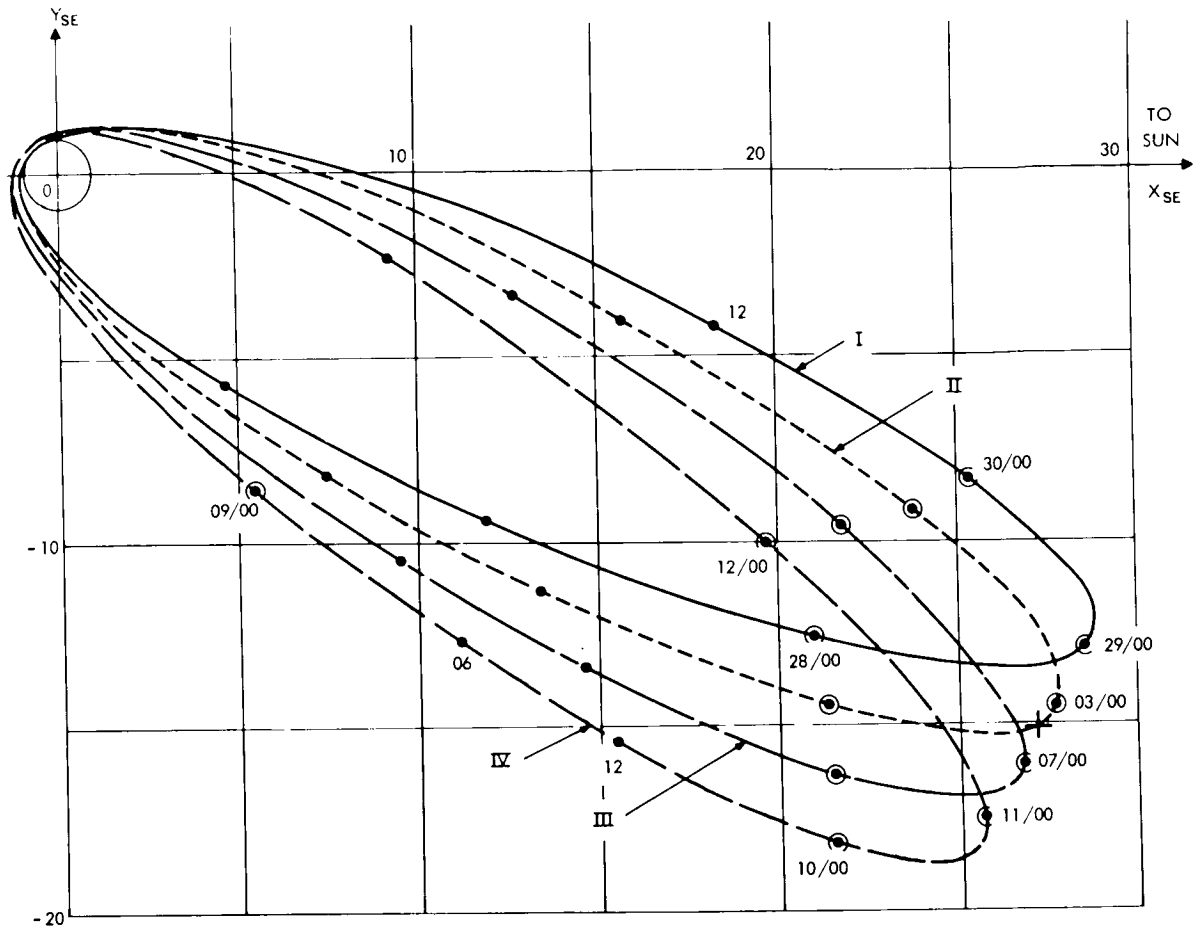


Figure 11—Projection on solar ecliptic XY plane of orbits 1 through 4. Cross indicated location of satellite at time of the December 2 sudden commencement geomagnetic storm.

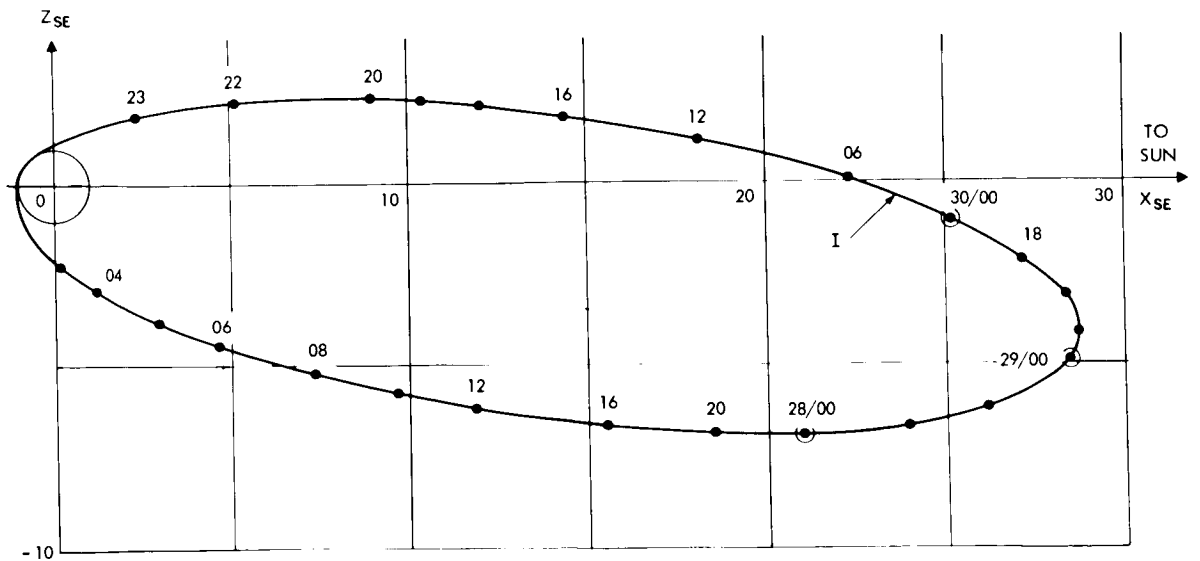


Figure 12—Projection on solar ecliptic XZ plane of orbit 1.

plane passing through the earth and the sun, which is the X-Z plane in solar ecliptic coordinates. As time since launch increases, the projection becomes foreshortened on this particular plane as the earth moves about the sun until the apogee eventually occurs behind the earth, 160 days after launch. Figure 13 illustrates the predicted variation of the apogee-earth-sun angle as a function of lifetime of the satellite.

The fact that the apogee-earth-sun angle never is 180° or 0° is due to the inclination of the line of apsides to the ecliptic plane. The magnitude of the inclination is determined from this figure to be 5° . The spacecraft spin axis-sun angle shown is important for certain of the directional sensors on board the spacecraft such as the two plasma probes, whose response is principally associated with solar originating and radially directed plasma flux. The solar aspect angle is also important in determining the effects of solar radiation pressure on the spin period of the satellite since the four solar paddles were all pitched in the same sense and at the same angle and a spin up or spin down of the spacecraft occurs dependent upon whether the sun is below or above the equatorial plane of the satellite.

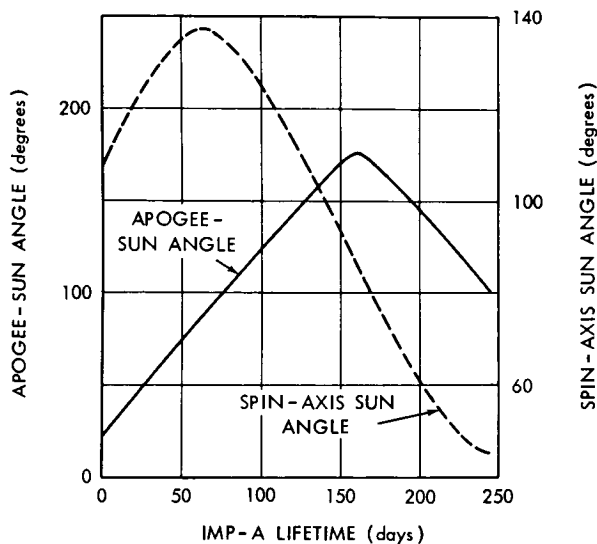


Figure 13—Predicted variation of apogee sun-angle and solar aspect angle for IMP I.

MAGNETIC FIELD RESULTS

A selection of one particular orbit of the available and already analyzed 19 orbits of the IMP satellite has been made to illustrate the characteristics of the data obtained and the format in which the data will be presented. The initial studies reported herein are preliminary only in the sense that detailed correlations of magnetic fields with other sensors on board and certain other solar and terrestrial phenomena have yet to be completed. The data themselves are final as no other changes, corrections, or calibrations are necessary since all have been included in this presentation.

However as the data are further studied certain characteristic features may become more evident than they are at the present time. The study of long term statistics of the interplanetary fields and the quantitative descriptions of the shock wave and magnetopause boundaries statistically are subjects for future studies.

The magnetic field data obtained on an outbound portion of orbit 11 on January 5, 1964 are presented in Figure 14. As previously indicated the data are presented in a magnitude and two angle representation. The RMSE or variance of the solar ecliptic components is indicated in the

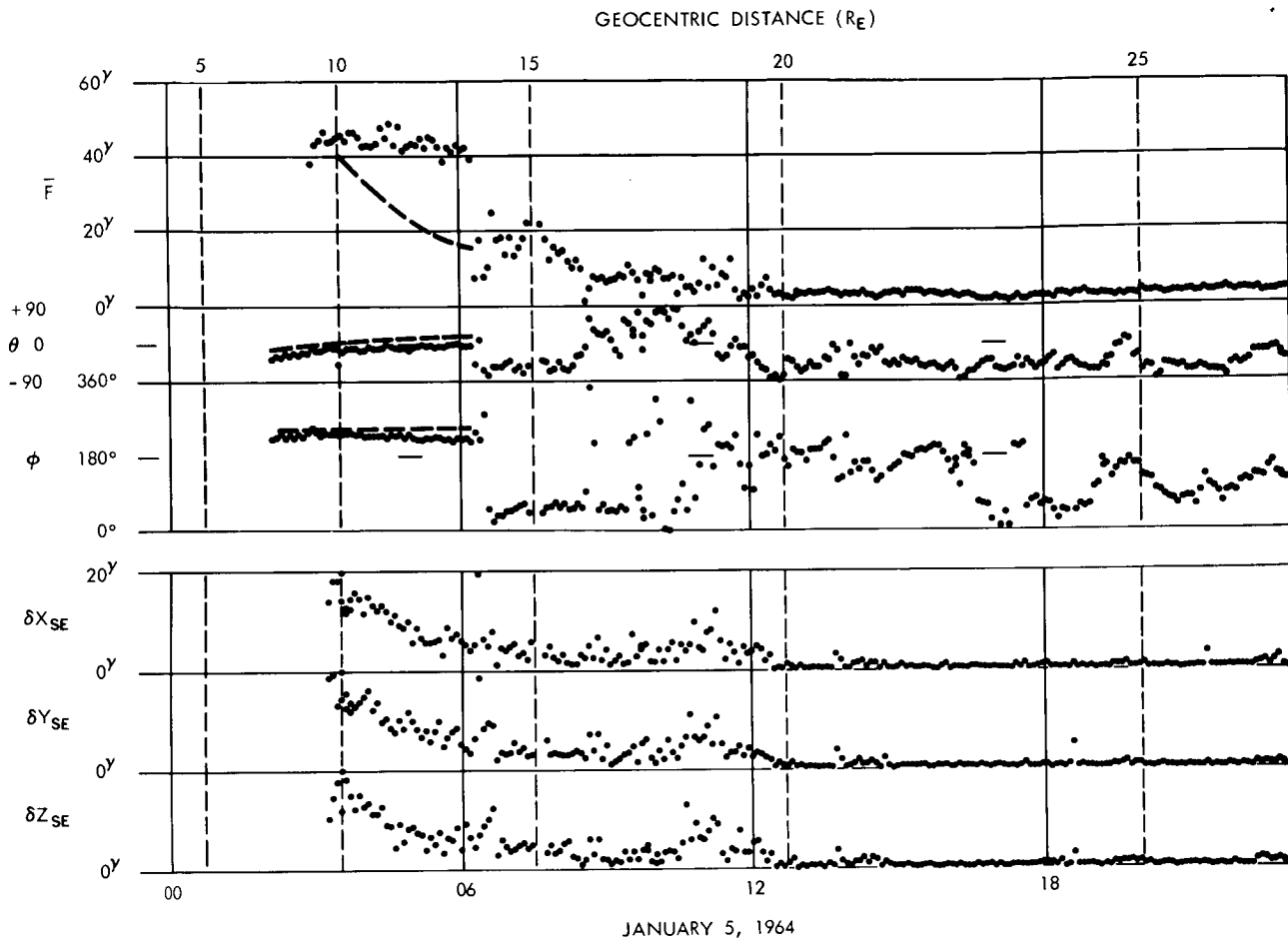


Figure 14—Magnetic field data from orbit 11 (January 5, 1964) illustrating outbound traversal of magnetopause at $13.6 R_E$ and shock wave at $19.7 R_E$.

lower three curves. The numerical values at the bottom refer to UT (hours) on the date indicated while the values at the top indicate the geocentric distance of the satellite in earth radii. By inspection of the data and reference to previous results on Explorer X (Reference 9) and Explorer XII (References 15 and 16), it is clear that the magnetopause boundary has been traversed by the IMP I satellite at a distance of $13.6 R_E$ at 0630 on January 5, 1964.

As the satellite moved away from the earth the measured magnetic field began to increase above the predicted value at about $10 R_E$, and proceeded to increase to more than twice that expected on the basis of the Finch and Leaton coefficients (Reference 17) for spherical harmonic expansion of the earth's terrestrial fields. In addition there were slight but regular angular deviations of the magnetic field increasing in importance until at $13.6 R_E$ there was an abrupt change in the character of the magnetic field in both magnitude and direction. The direction of the magnetic field appears to reverse by 180° while the magnitude, simultaneously and just as suddenly, decreases to less than 50 percent of its original value. The magnetic field then begins to fluctuate appreciably in its average magnitude and direction as the satellite continues moving further away.

Although the direction of the field remains roughly stable pointing generally back toward the sun and below the ecliptic plane, the magnetic field continues to display large deviations in the three solar ecliptic components which indicate a turbulent characteristic out to a distance of $19.7 R_E$. At this point in space the magnetic field becomes stable both in magnitude and direction as evidenced in the \bar{F} , θ , ϕ presentation but shown much more dramatically in the presentation of the variance results. This sudden decrease in the variance from several gammas to less than 0.4γ is a consistently remarkable feature of the IMP I data. This value is equivalent to the noise level of the instrument and the analysis procedure. For the next twelve hours the magnetic field is approximately 4 to 5γ in magnitude and pointed about 30° to 40° below the ecliptic plane while directed either away or generally towards the sun. The change in character and quantitative values describing the field at $19.7 R_E$ is identified as the collisionless shock wave suggested by Zhigulev (Reference 18), Axford (Reference 19), Gold (Reference 20), Kellogg (Reference 21), and Rossi (Reference 22), associated with the standing bow wave due to the super Alfvénic streaming velocity of the solar wind impacting the geomagnetic field. Theoretical aspects of these data will be discussed in a later section.

Continuing through orbit 11, Figure 16 illustrates data taken on January 6, 1964 immediately following that shown in Figure 15. In this case it is seen that the interplanetary field remains very steady at a level of 4 to 7γ and in general is below the plane of the ecliptic by 10° to 20° although

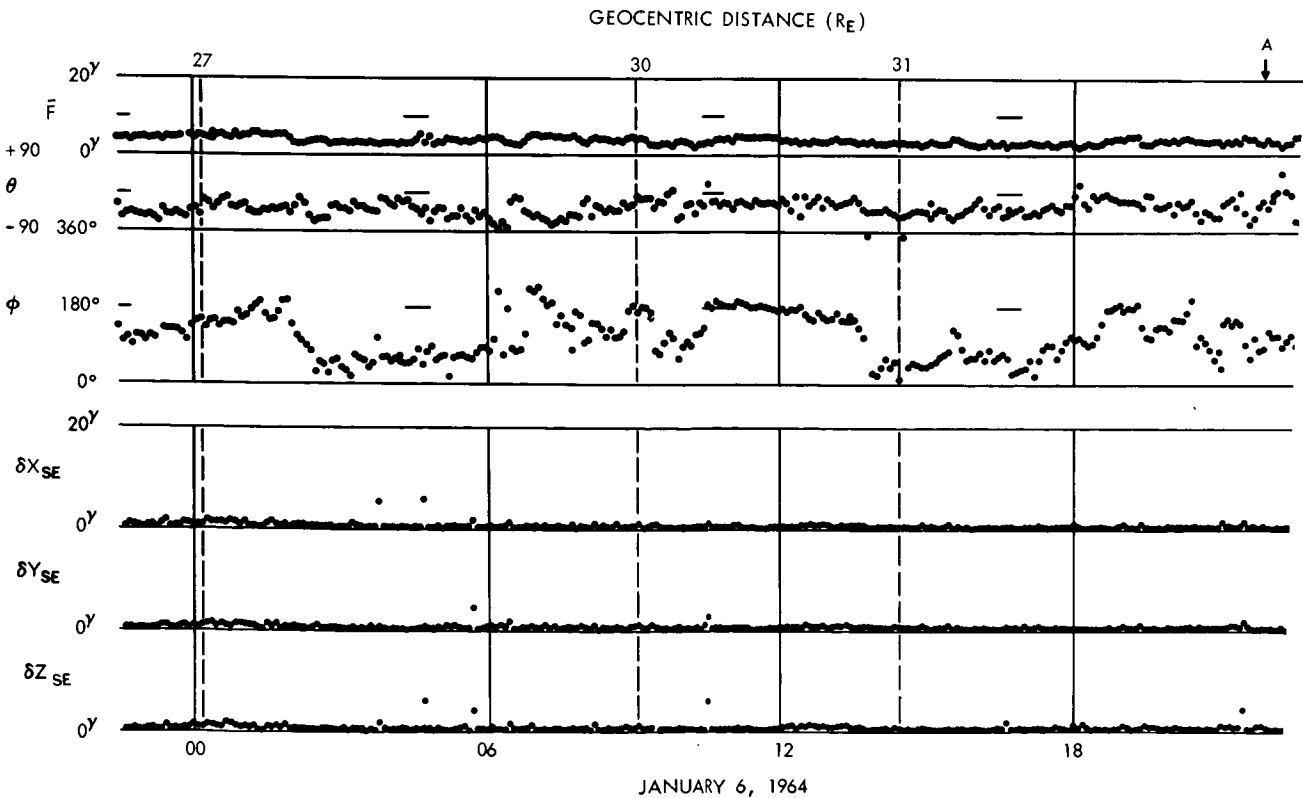


Figure 15—Magnetic field data from orbit 11 (January 6, 1964) illustrating interplanetary magnetic field.

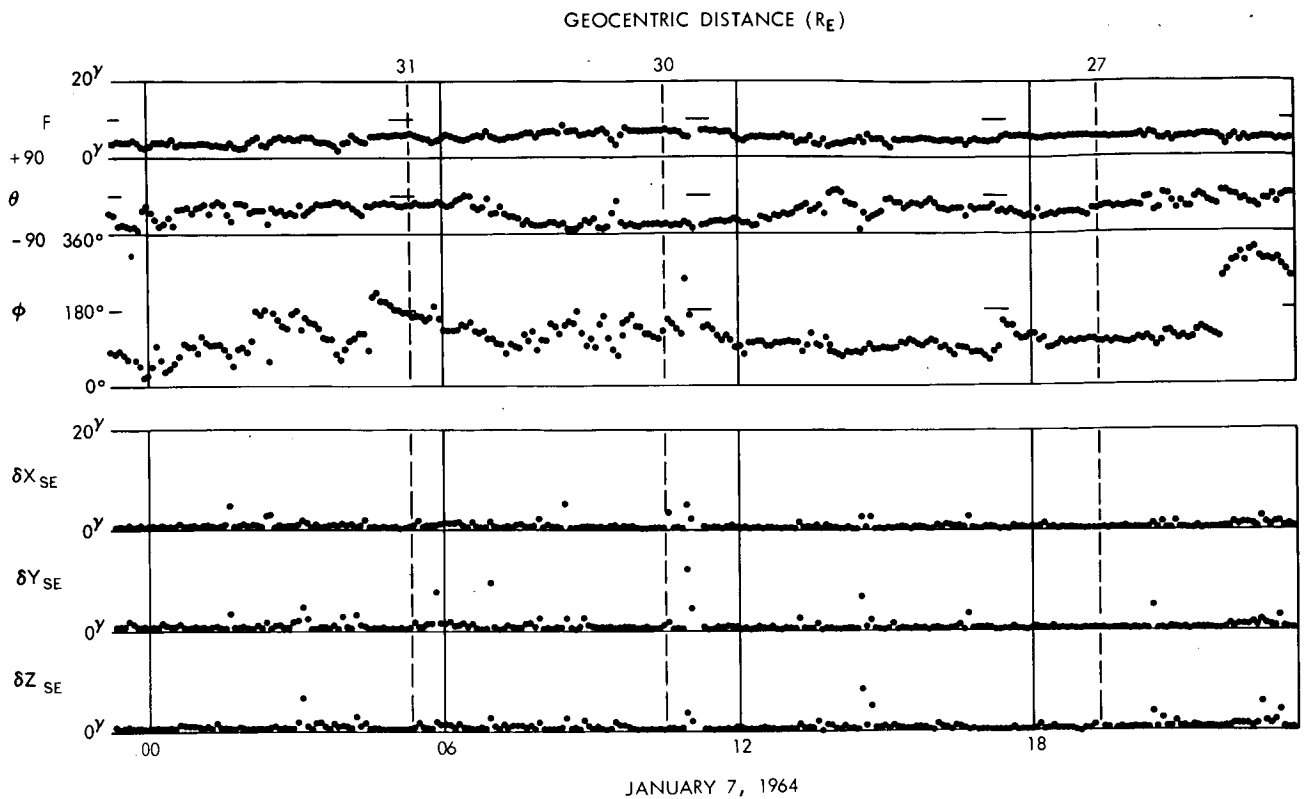


Figure 16—Magnetic field data from orbit 11 (January 7, 1964) illustrating interplanetary magnetic field and null surface separating filaments.

the sense of the field is to point either away from the sun at approximately the streaming angle associated with steady state models of coronal expansion or towards the sun at the streaming angle. A significant feature in Figure 16 is the occurrence of a reversal of field direction at 2300 UT on January 7. At the same time as the field changed from being along the streaming angle to 180° opposite the streaming angle, the magnitude abruptly decreased within 10 minutes. Detailed inspection of the data at this time shows that the field went to zero as the field changed directions which is indicative of a *neutral surface* in interplanetary space.

The variance of the field remains quite low and clearly indicates a relatively stable magnetic field configuration somewhat in contrast to the Mariner 2 results previously reported by Coleman et al. (Reference 10). Figure 17 continues the presentation of data from orbit 11 on January 7, 1964 and supports the general statements of the stability of magnitude of the interplanetary field between 4γ while the directional changes in general are slow, on time scales of hours to several hours, and average directions correspond to pointing towards and away from the sun at the streaming angle.

The inbound pass on orbit 11 shows the magnetic field data obtained on January 8, 1964 (Figure 17). The presentation of data is such that time always increases from left to right and the satellite is identified as being either on the inbound or outbound portion of its orbit by the sense

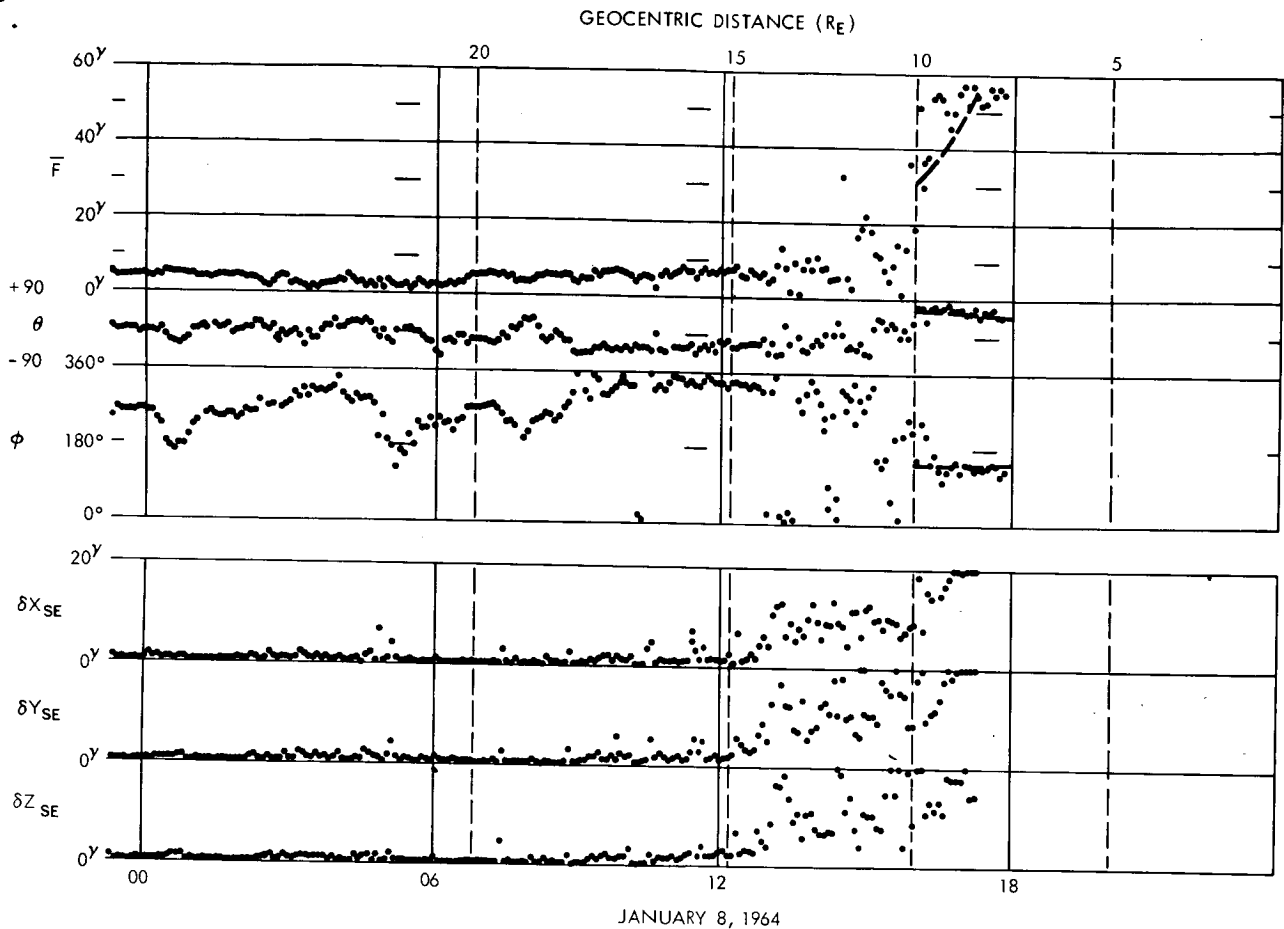


Figure 17—Magnetic field data from orbit 11 (January 8, 1964) illustrating inbound traversal of magnetopause at $9.7 R_E$ and shock wave at $16.0 R_E$.

in which the geocentric distance increases. Figure 17 illustrates two more traversals of the boundaries characteristically found throughout the lifetime of the IMP satellite. The shock wave (identified as before on the basis of the increased turbulence in the magnetic field) is shown in this sample as an abrupt and very distinct increase in magnetic field strength at $16.0 R_E$. The magnetopause boundary — at which the field jumps rapidly to very large values more than twice those theoretically predicted, at the same time as its direction abruptly changes — is found to occur at $9.7 R_E$. These data very briefly summarize the salient features of the 19 orbits which have been studied to date on the IMP I satellite.

The general characteristics of all the orbital passes are those shown in orbit 11: namely, traversal of two characteristic boundaries twice in each orbit. As the satellite orbit has progressed around from the sun-earth line the distance at which the magnetopause boundary and the shock wave boundary have been found to occur has changed. These changes have been correlated with a number of phenomena and will be discussed shortly. However, the most unique aspect of the boundary crossings in general has been their consistent and readily identifiable occurrence on all of the orbits.

The most important feature of the interplanetary magnetic field results has been, in general, that the interplanetary magnetic field magnitude is quite steady and varies only over fractions of a gamma on the relatively long time scale (hours). This stability of the field magnitude but variability of direction may lend support to the studies by Dessler and Walters (Reference 23) and Walters (Reference 24) as to the effects of the streaming magnetized plasma on terrestrial magnetic activity and magnetospheric geometry. The correlation between directional changes of the interplanetary magnetic field and the associated terrestrial activity as indicated by various indices, including K_p and A_p , is currently being investigated in detail. Previous experimental studies by Snyder, Neugebauer and Rao (Reference 25), Greenstadt (Reference 4), and Maer and Dessler (Reference 26) have not been completely consistent although they have generally indicated a definite correlation between K_p , or A_p , and solar wind velocity. These results are somewhat contradictory to the theoretical suggestions of Dessler and Fejer (Reference 27), who deduced a correlation between K_p and changes in the solar wind velocity. It is important to note that the time variations of the interplanetary magnetic field observed reflect mainly the structural variations within the interplanetary medium. This is because the proper frame of reference moves with the bulk velocity of the solar plasma.

Although the statistics are not as yet complete it appears that in general there is a preference over this portion of time in the solar cycle for the interplanetary magnetic field to lie generally below the plane of the ecliptic by approximately 10° to 20° . At the same time the projected vector on the ecliptic plane appears to have two preferred orientations to which it returns and near which it is observed most of the time. In order of duration these two directions are:

1. At the streaming angle associated with the theoretical models of the solar wind; and
2. At the anti-streaming angle (i.e., exactly 180° opposite to the streaming angle theoretically predicted).

These results of the IMP I magnetic field experiment suggest very strongly the existence of a filamentary structure in the interplanetary medium associated with unique and separate sources of solar associated magnetic fields. These fields are stretched out away from the sun by the highly ionized streaming solar plasma as modeled and discussed by Parker (Reference 5). In between these streaming filamentary elements evidence has been found of magnetic field magnitudes decreasing abruptly to zero so as to essentially be in consonance with the idea of a null surface separating regions of interplanetary magnetic fields which are of opposite directions. Throughout the lifetime of the satellite thus far, approximately 12 such readily identifiable filamentary structures have been observed.

A comparison of the observed streaming angle with those predicted by steady models assuming an axially symmetrical expanding solar plasma flux is made in Figure 18. The observed interplanetary magnetic field is close to $\psi = 130^\circ$ to 150° , or 310° to 330° for the streaming or anti-streaming angles, respectively. These directions are consistent with velocities of the solar wind of 300 to 700 km/sec — the values found by the Mariner II probe (Reference 8). The detailed characteristics of the angular deviations of the interplanetary magnetic field are currently being studied and in the future detailed correlations with the plasma probes on board the satellite as well as additional solar and terrestrial indices will be made.

At the present time it appears that the results of the IMP magnetic field experiment have indicated an impressive consistency with the theoretical models proposed mainly by Parker, but also by Gold (References 28 and 29). Those of Parker are substantiated on the basis of the interplanetary field direction dependence upon plasma velocity which compares very favorably with observation. The general directions of the field lines emphasize the principal fact that a rotating sun continuously emitting plasma will lead to a gross superposed spiral field structure under most circumstances. The filamentary structures appear to indicate specific sources, as proposed by Gold (Reference 29), must be considered in the modeling of realistic solar coronal phenomena. It is also possible that the data are consistent with the magnetic "bottle" ideas of Gold (Reference 20) in which cutting of lines of force near the sun generates field topologies which do not include the sun.

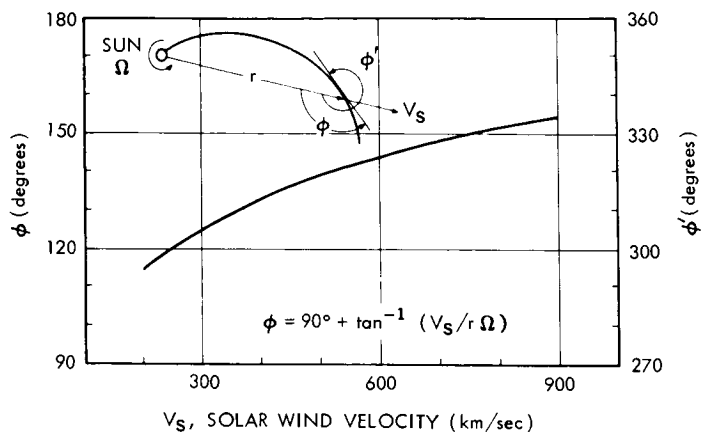


Figure 18—Theoretical direction of interplanetary magnetic field ϕ as a function of solar wind velocity V_s .

Additional data from the magnetic field experiment shown in Figure 19 for orbit 15 on January 21, 1964 clearly illustrate the crossing of the magnetopause at $15.7 R_E$, while the shock wave traversal is not observed to occur until $22.7 R_E$.

A particularly significant feature of the outbound traversal of the shock wave on this orbit is the appearance at $24.5 R_E$ of an increased variance for 10-30 minutes. Not in evidence on every orbit although clearly indicated here, this feature of the IMP I magnetic field data is very important. This limited increase in variance is also spatially associated with the position of the shock wave and when observed is usually found to be several earth radii beyond the shock wave. This is identified as a precursor to the shock and is suggested to be indicative of characteristic plasma instabilities or particle resonances whereby the presence of the shock wave can be communicated "upstream" to the plasma by a mechanism that depends upon the individual particle dynamics of the plasma rather than the continuum dynamics of the collective particles. For orbit 15, the interplanetary field on January 22, 1964 is shown in Figure 20. The characteristics of the data are quite similar to those shown for orbit 11 although the boundary positions are considerably beyond those observed in orbit 11 and, correspondingly, the boundary positions detected during orbit 11 occur at larger distances than detected during early orbits. An important feature of the turbulent field structure is that fluctuations occur about a specific orientation so that there is an appreciable sense of directionality to the magnetic field, even though it is not stable in magnitude.

The data from orbit 6 inbound is being investigated in detail since it followed an interval of time during which the interplanetary field was disturbed because of the interaction of the moon's magnetosphere with the solar wind. It is clear from Figure 21 that the characteristic boundaries

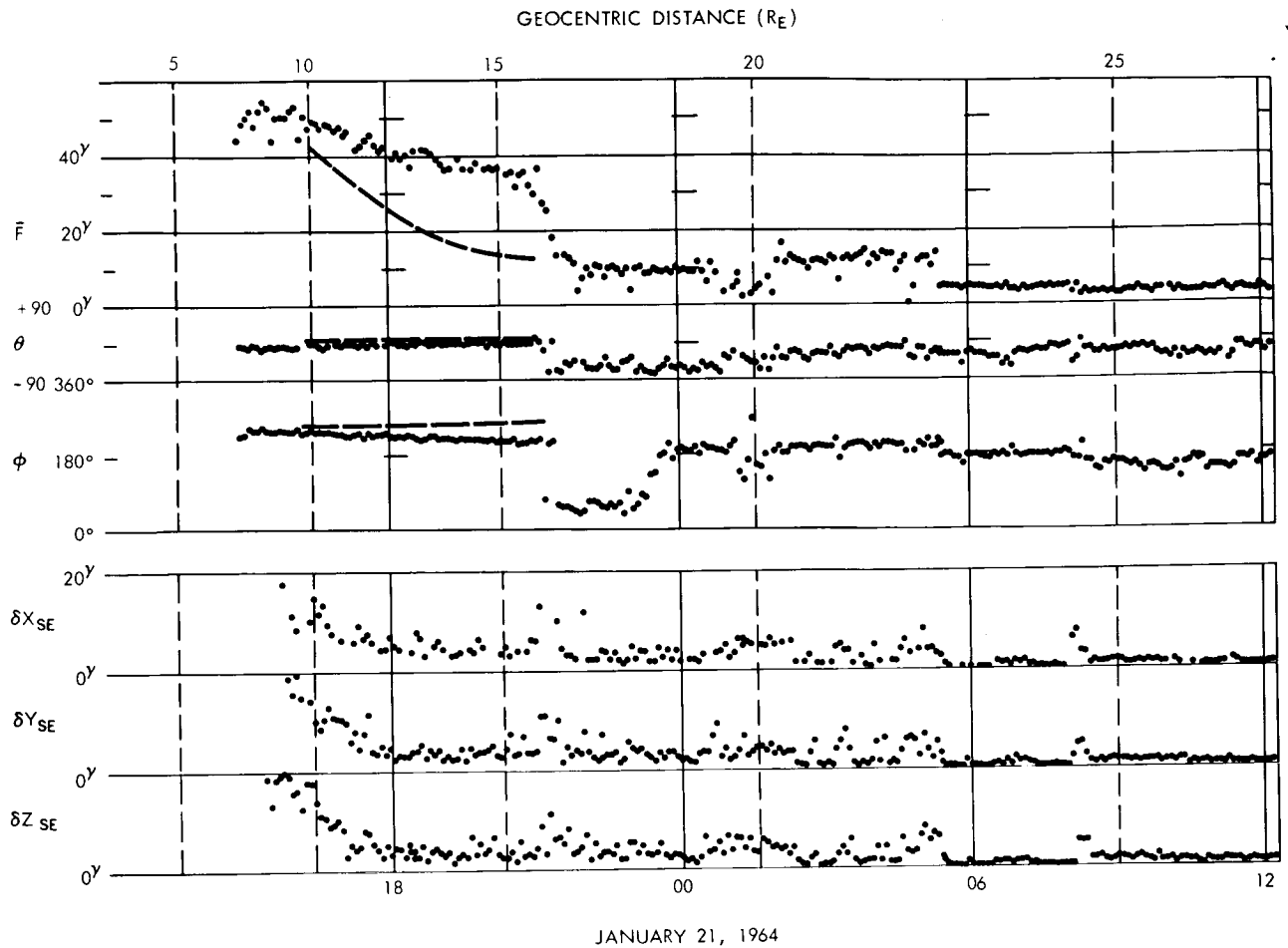


Figure 19—Magnetic field data from orbit 15 (January 21, 1964) illustrating outbound traversal of magnetopause at $15.7 R_E$, shock wave $22.7 R_E$ and precursor at $24.5 R_E$.

observed on all other traversals (37 in all) are not evidenced here in the same manner. Principally the variance remains at the instrument noise level until a distance of $10.8 R_E$ is reached. Secondly, the abrupt directional changes in magnetic field are not coincident with abrupt changes in the magnetic field strength. The data strongly suggest the absence at this time of the collisionless shock wave probably due to the increased field strengths and possibly low plasma densities leading to Alfvén velocities sufficiently high that a shock situation does not exist. These data are also consistent with the study by Alfvén, Danielsson, Falthammer and Lindberg (Reference 30) on the direct entry of solar plasma into the geomagnetic field when fields external to the cavity are parallel to internal fields.

SUMMARY CHARACTERISTICS OF MAGNETIC FIELD PHENOMENA

It is appropriate to summarize the many details of the interplanetary magnetic field data and the characteristics of the magnetic field at the shock wave and the magnetopause boundaries as

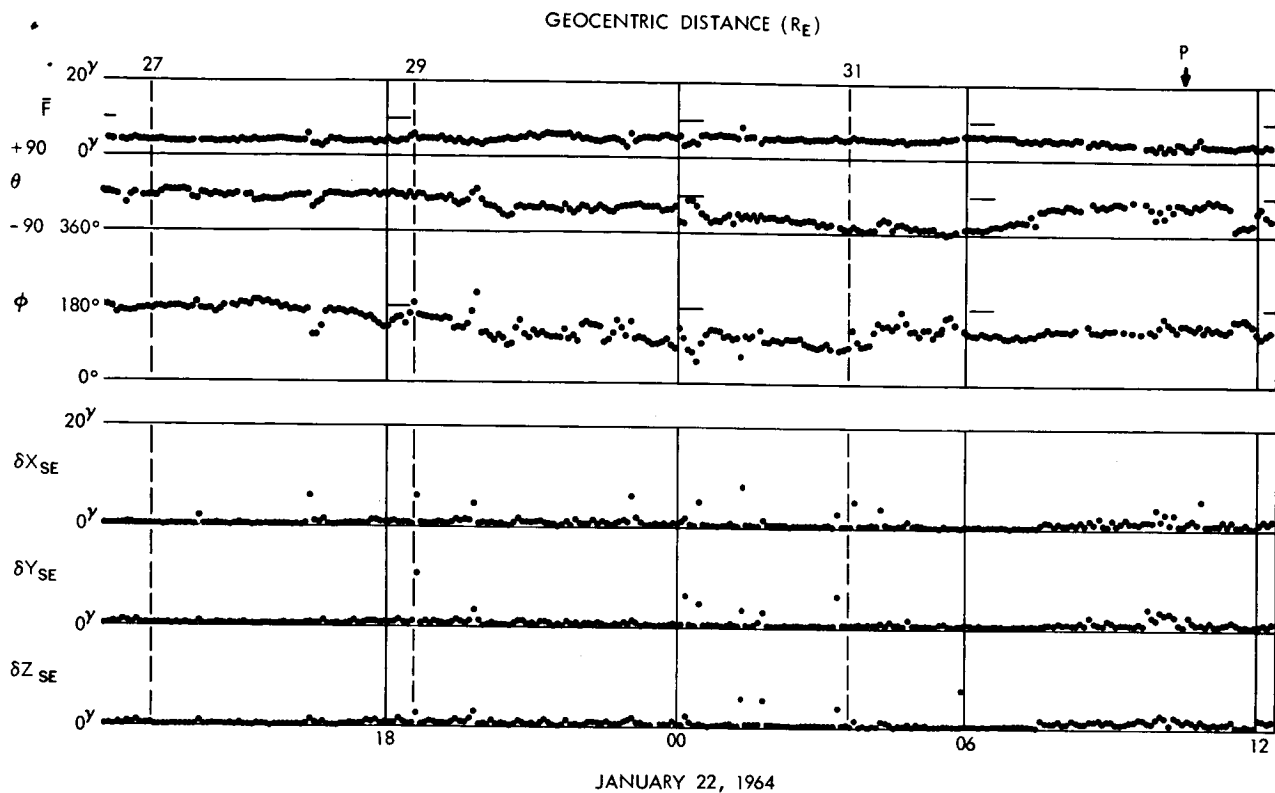


Figure 20—Magnetic field data from orbit 15 (January 22, 1964) illustrating interplanetary magnetic field.

well as the characteristics of the data for the transition region. Certain features are clear and have been already stated. The omission of certain characteristics which may become obvious to the reader should not be taken to indicate their dismissal by the authors as insignificant aspects. It is quite impossible to discuss in this first publication all of the results which have been obtained from this particular experiment.

The orbit of the IMP I satellite and the data obtained is such that it suggests logically separating the region of space surrounding the earth into three physical regions for discussion.

1. The *Magnetosphere*: that region of space including the earth and its radiation belts and separated by the magnetopause boundary from region 2. This geomagnetic cavity corresponds to a persistent containment of the geomagnetic field along the concepts initially developed for magnetic storm theory by Chapman and Ferraro (References 31, 32, and 33); Ferraro (References 34, 35, and 36) and reviewed by Chapman (References 37 and 38).
2. The *transition region* extends from the magnetosphere to the interplanetary medium or more appropriately the interaction region between the streaming solar plasma and the geomagnetic field which is separated by the collisionless magnetohydrodynamic shock wave from region 3.
3. The *interplanetary medium* in which the plasma flux and magnetic fields are undisturbed and undistorted by the presence of the earth in interplanetary space. This region of space

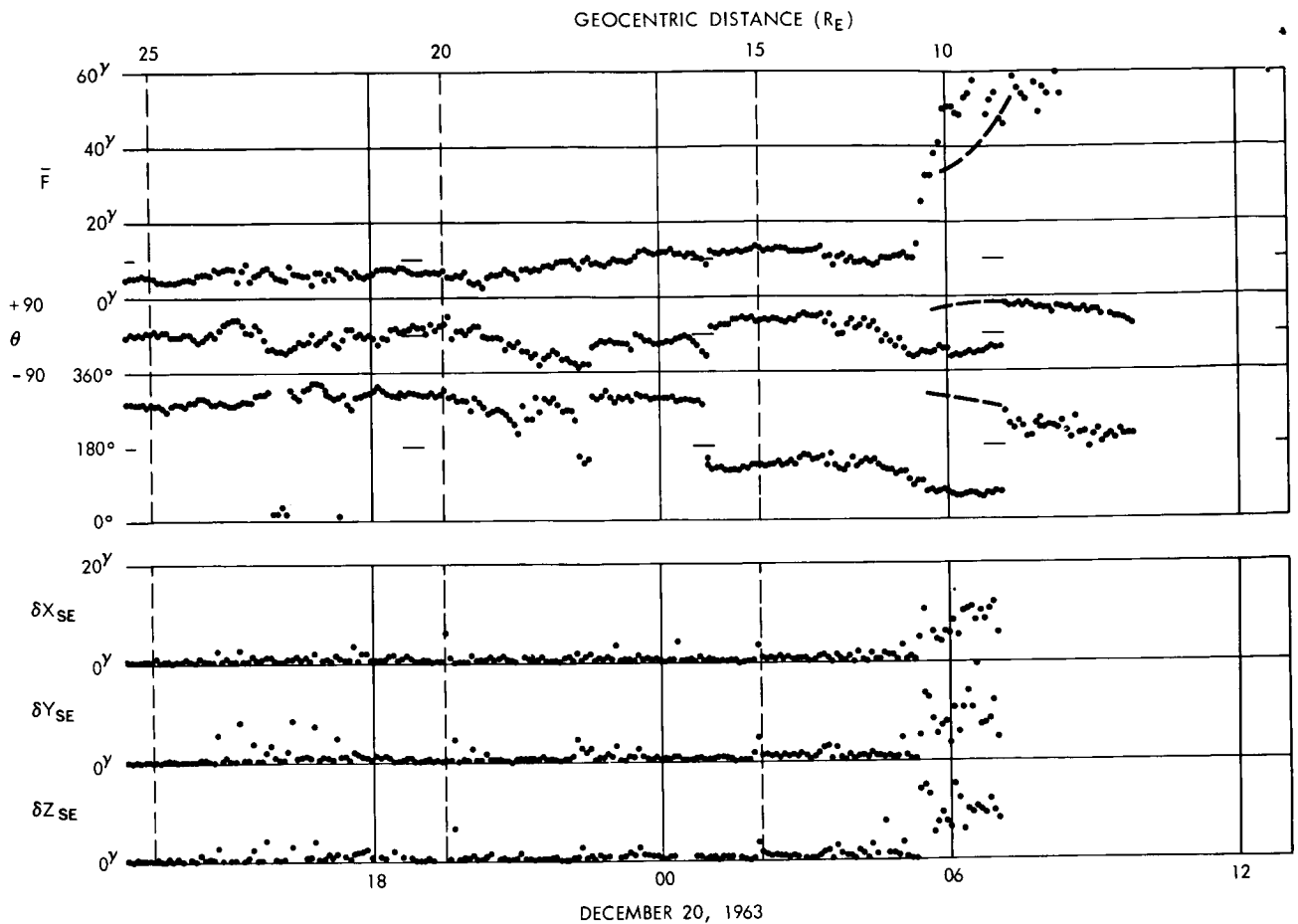


Figure 21—Magnetic field data from orbit 6 (December 20, 1963) illustrating inbound traversal of magnetopause at $10.8 R_E$ and questionable shock wave at $16.3 R_E$.

and its physical characteristics represent the principal region of interest for the IMP I measurements.

The physical characteristics of the magnetic fields in these three regions and the description and discussion of the boundary properties is given in the following paragraphs.

The dynamics of charged particle motion in the magnetosphere region is dominated by the magnetic field of the earth. Measurements on the IMP I show that deviations of direction and magnitude of the observed magnetic field when compared with theory do not become significant until an elevation of $7-10 R_E$ is reached. The deviations beyond this distance are consistent with the characteristics of a contained geomagnetic field with the strength increasing to at least a factor of two greater than normally expected without the formation of a magnetopause.

The directional distortion is consistent with the fields being oriented approximately tangential to the magnetopause surface. Although it requires further investigation in the future it is possible

to state that the magnetic fields near the boundary on the sunlit hemisphere interior to the magnetopause are not stable as argued by Dessler (References 39 and 40) and that appreciable energy must be transmitted into the magnetosphere in the form of magnetohydrodynamic waves. The fluctuations observed are generally smaller than could have been detected by Explorer XII, because of its limited sensitivity of $\pm 12\gamma$ (Reference 15) and show characteristic values of 10γ rms or less and corresponding values of $\delta F/F$ of 0.05 to 0.3.

The magnetopause, reviewed by Hines (Reference 41) is identified by the abrupt discontinuity in the character and quantitative description of the magnetic field as the satellite passes from Region 1 to Region 2. Near the subsolar point this is found to occur at approximately $10 R_E$. The magnetic field rapidly decreases from values of $30-60\gamma$ to $5-20\gamma$ and the corresponding variances from small $\delta F/F$ to large $\delta F/F$, approximately 0.5 to 2.0. The thickness of the magnetopause is difficult to determine unambiguously but upper limits can be placed assuming that the boundary is stationary on a time scale such that the total time for motion of the satellite across the magnetopause is small. At distances of $10 R_E$ the satellite radial velocity from the earth is approximately 2.7 km/sec.

In general the analysis procedures and definitions currently employed to determine the location of the magnetopause are such that ± 2.5 to ± 15 minutes is a good measure of the uncertainty in precisely specifying where the boundary is traversed. The spacecraft velocity combined with this time uncertainty together yields thicknesses of 810 to 4860 km. This is quite reasonable since the proton Larmor radius for a 1 keV proton in a magnetic field of 10γ is 450 km and should be a reasonable scale length to consider in estimating the magnetopause thickness since all plasma flux is presupposed to be reflected and excluded by the geomagnetic field from entering the magnetosphere (Reference 42).

The direction of the fields at the magnetopause boundary strongly suggest that both internally and externally to the magnetopause, the fields are tangential to the magnetopause surface at least locally, i.e., not far from the boundary. Furthermore the directional changes suggest that although the magnetic fields are oppositely directed on either side of the magnetopause for a number of the crossings studied thus far, there are cases in which the fields appear to be crossed perpendicular with respect to each other on opposite sides of the boundary.

The transition region is one of great instability of the magnetic field suggesting that turbulent phenomena occur in this region and that statistical descriptions of the field will be most appropriate in their study. The vector field fluctuates rapidly in magnitude and direction with $\delta F/F$ ranging from 0.5 to 2.0. At times however the magnetic field direction and magnitude stabilized for time scales of 20 to 60 minutes with values corresponding to those of Regions 1 or 3. Although suggested by the Explorer XII results, this is not considered to be representative of the general characteristics of Region 2. It is not interpreted to be indicative of rapid spatial movements of the magnetopause as it expands and contracts. Actually in a region of turbulence there is a finite probability that the field orientations will equal those of other regions. The region of high turbulence encompassing and enclosing the magnetosphere is well established by the IMP data and quantitative statistical descriptions of the magnetic field and its topology in the vicinity of the magnetopause will be presented in future publications.

The collisionless shock wave boundary separates the interplanetary region 3 from the turbulent region 2, and is observed experimentally at $13.4 R_E$ at the subsolar point. The identification of its position as the satellite traversed it in space is based upon the striking physical differences between Regions 2 and 3. The abruptness of the changes in character of the fields at the outer boundary of the turbulent region is not always as sharply defined as at the inner boundary. In general, the interplanetary fields are very stable and characteristically show very small variances, less than 0.4γ for extended times yielding $\overline{\delta F/F} < 0.1$. Inside the shock wave boundary the field is observed to be randomized in direction and the total energy density in the magnetic field increases: both the dc value, as measured by $B^2/8\pi$ and the fluctuating field as measured by the variances δX_{se} , δY_{se} , and δZ_{se} . This means that the total energy of the magnetic field increases by factors of 5-10 and can play an important role in the flow of plasma around the cavity. It should be noted that although the identification of the shock wave boundary is generally unique based upon the above physical criteria, certain samplings of the shock region show a *precursor* in the Region 3 which stands off from the shock wave by several R_E . This precursor does not show the characteristic of large fields but does display large variances, up to 5γ , in each component for time scales of ≤ 40 minutes. At these distances, the satellite is moving radially outward at approximately 1.8 km/sec. Thus the spatial width of the precursor is ≤ 4000 km. Since the satellite is moving more slowly when it traverses the shock wave, the longer times required do not indicate a more diffuse boundary than is the case of the magnetopause.

The existence of the collisionless magnetohydrodynamic shock wave was anticipated on the basis of theoretical analyses relying principally on the analogy with high speed aerodynamic flow. Various aspects of this general approach have been reviewed by Levy, Petschek and Siscoe (Reference 43). Their specific interest and results were mainly to deduce certain aspects of the overall plasma flow around the geomagnetic cavity. Analytical studies on the structure of collisionless shocks in magnetohydrodynamics have proceeded in some work by modification of the appropriate form of the Rankine-Hugoniot conditions derived by De Hoffman and Teller (Reference 44). Theoretical studies by Adlam and Allen (Reference 45), Auer, Hurwitz and Kilb (References 46 and 47), Fishman, Kantrowitz and Petschek (Reference 48), Morawetz (References 49 and 50), and Morton (Reference 51) have attempted to treat in varying degree the detailed description of the shock characteristics and sufficient conditions for its existence. The present situation appears to be one in which the characteristics of the plasma flow are grossly described, at least in the location of the shock and magnetopause, on a basis of the analogy with fluid dynamics. However, the physical structure of the fields and plasmas in the observed three dimensional case of the earth are not immediately derived by such simplifying considerations. In particular the discovery of the shock precursor is obviously indicative of the necessity to treat the flow of plasma more specifically as a two stream flow of non-cold electrons and protons (References 52 and 53). A more detailed study of the observed shock wave with regard to the theoretical descriptions is presently in progress. However, it is reasonably certain that the IMP I satellite and its experiments have provided the first physical measurements of the physical structure of a collisionless magnetohydrodynamic shock which heretofore has never been observed because of the "scaling problems" in laboratory research.

The interplanetary region 3 is defined most readily by the stability of the magnetic field as measured by the variances δX_{se} , δY_{se} , and δZ_{se} . These are observed to be less than 0.4γ with corresponding magnitudes of 4 to 7γ although excursions to values as low as 1 and to as high as 10γ for extended time intervals have been observed. The extreme stability of the magnitude of the field is in contrast to the more variable directional characteristics of the field. In general the fields lie on average slightly below the plane of the ecliptic ($\theta = 10^\circ$ or 20°) and at the streaming angle of 130° - 150° or anti-streaming angle 310° - 330° . The gross structure of the interplanetary field is in remarkably good agreement with the general concepts of spiral field configurations originally proposed by Parker (Reference 5). Associated with the two preferred orientations of the field, along or opposing the traces of the plasma flux, are regions of abrupt change to low values on time scales of less than 5 minutes. These are identified as neutral surfaces of zero field strength separating magnetic field filaments oppositely directed.

LOCATION AND GEOMETRY OF MAGNETOPAUSE AND SHOCK WAVE

A summary of the positions of shock wave and magnetopause traversals as a function of time associated with preliminary K indices from the Fredericksburg, Virginia magnetic observatory are shown in Figures 22-25. In addition, the geomagnetic latitude of the subsolar point χ_{ss} has

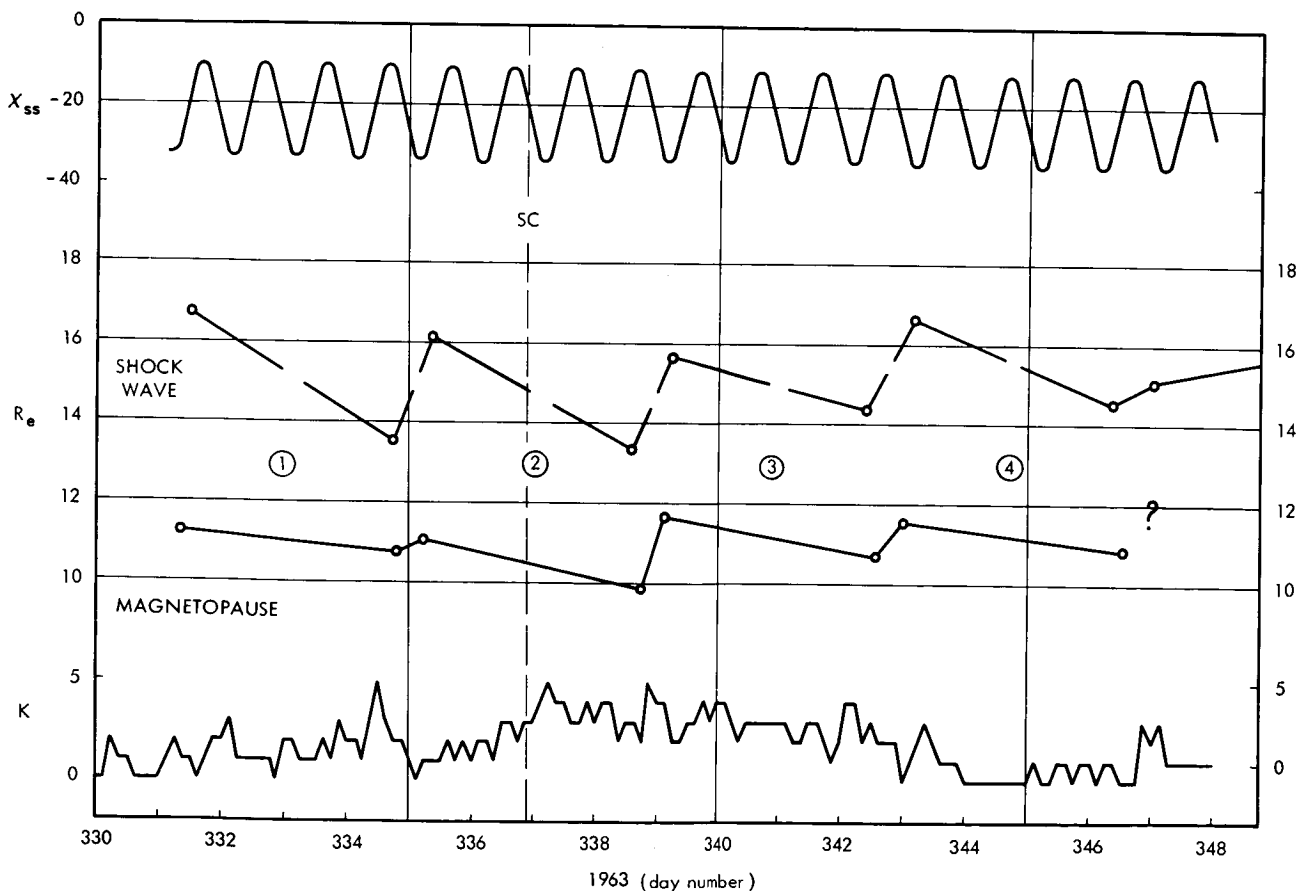


Figure 22—Time characteristics of geomagnetic latitude of subsolar point χ_{ss} , magnetopause and shock wave locations and K indices for days 330 to 348, 1963.

been included since it is an important factor in the interpretation of the position of the boundary crossings and the manner in which they relate to theoretical models of the magnetopause and the shock wave surfaces. In these figures the orbit number is enclosed in a large circle while the boundary crossings are indicated by small circles. These are connected from inbound to outbound passes by straight lines if successive boundary crossings are uniquely identifiable. In some cases the position of the boundary is not sufficiently clear (e.g., on the outbound portion of orbit 5) to uniquely specify its position and a question mark is displayed. This is related to the difficulty associated with the definition of the characteristics of the boundaries as deduced from the magnetic field data alone.

Certain aspects of the position of the boundary crossings are immediately evident upon inspection of these data. Principally seen is the periodic difference in position of the boundary

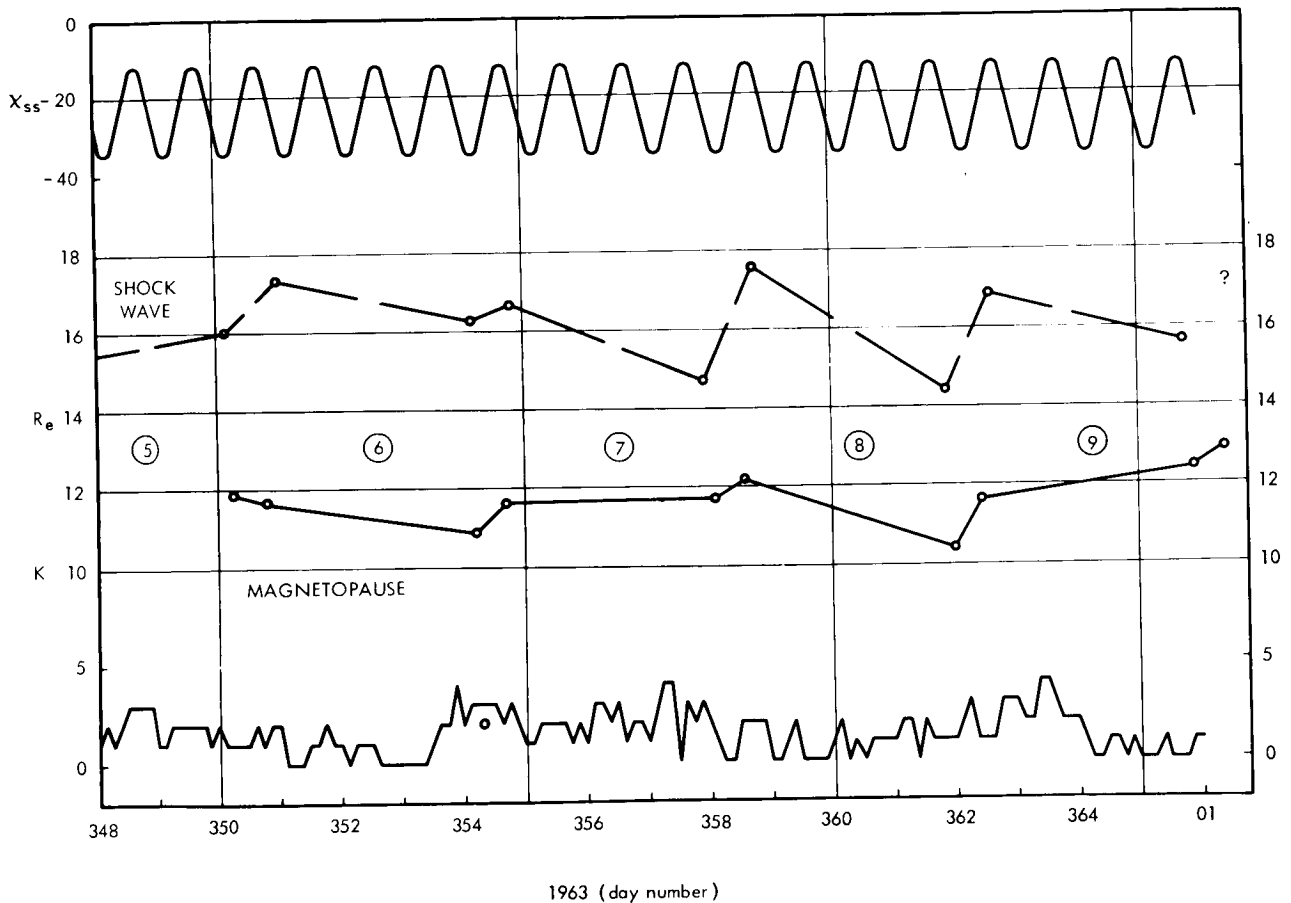


Figure 23—Time characteristics of geomagnetic latitude of subsolar point X_{ss} , magnetopause and shock wave locations and K indices for days 348, 1963 to 01, 1964.

crossings associated with outbound and inbound passes of the satellite. Characteristically the outbound pass shows the position of both boundaries to be greater than that associated with the next successive inbound pass. Upon further investigation it is found that following the sudden commencement storm in December 1963 (Figure 22), the magnetopause and shock wave boundaries were located at smaller distances than normally to be expected on the basis of previous passes.

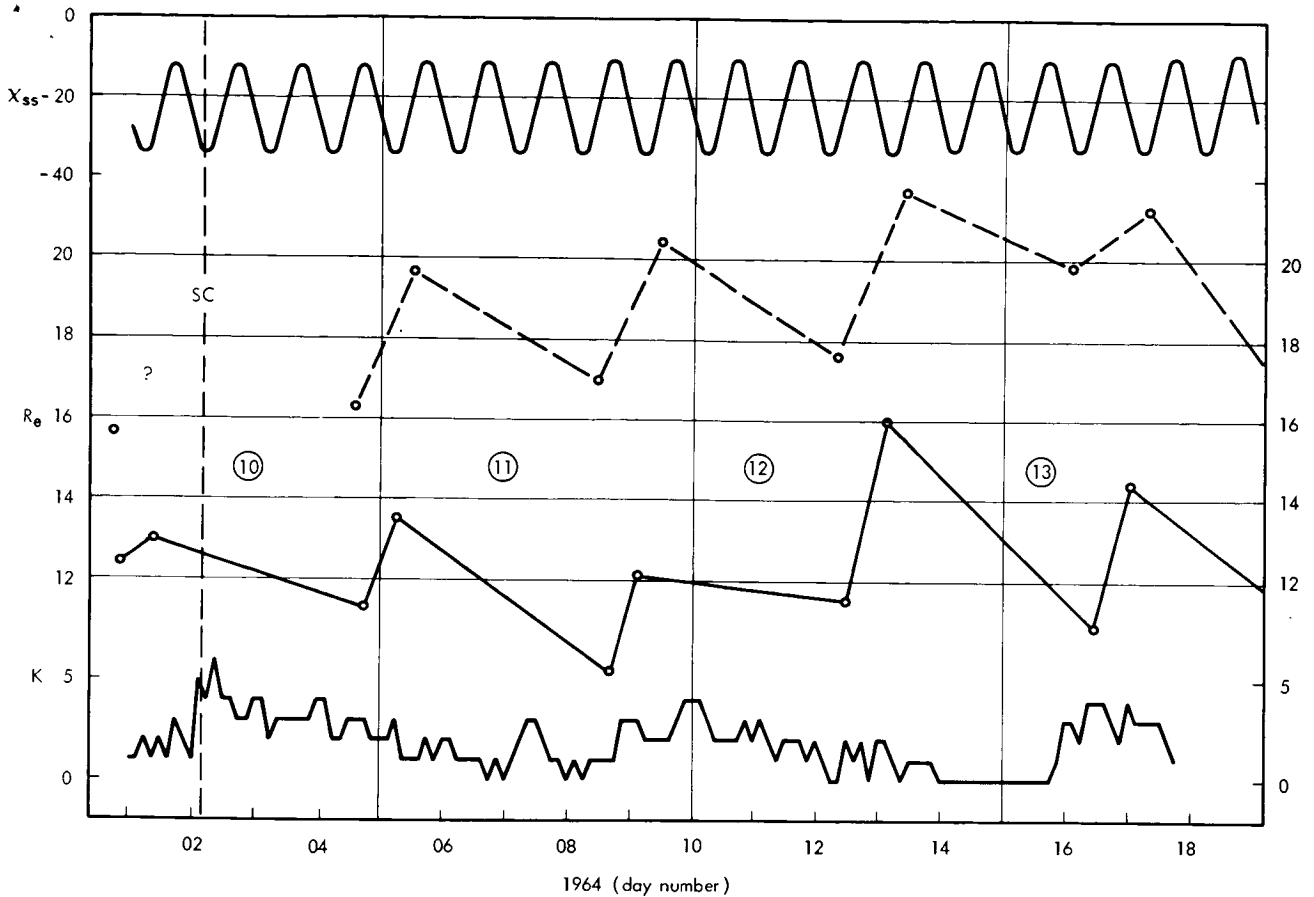


Figure 24—Time characteristics of geomagnetic latitude of subsolar point χ_{ss} , magnetopause and shock wave locations and K indices for days 01 to 19, 1964.

Also over the 70 day interval covered by these data, it is clear that the position of the magnetopause boundary and shock wave boundary increase as the satellite moves away from the earth-sun line. The two boundaries do not increase by the same amount. The shock wave increases more rapidly implying a wider transition region away from the subsolar point. It is noted that the satellite motion is roughly normal to these surfaces for early orbits, but becomes more oblique for later orbits.

Superimposed upon this spatial variation of the boundaries is the fact that the position of the boundary must be sensitive to the varying geomagnetic latitude of the subsolar point during successive crossings. This is seen by inspecting the condition for balance of magnetic and particle pressure at the boundary. The original developments by Chapman and Ferraro (References 31 through 33) the recent works by Beard (Reference 54), Davis and Beard (Reference 55), Spreiter and Briggs (References 56 and 57) have led to agreement of the proper form. The location of the boundary at the stagnation point is given by

$$\frac{B_t^2}{8\pi} = 2mnV_s^2, \quad (5)$$

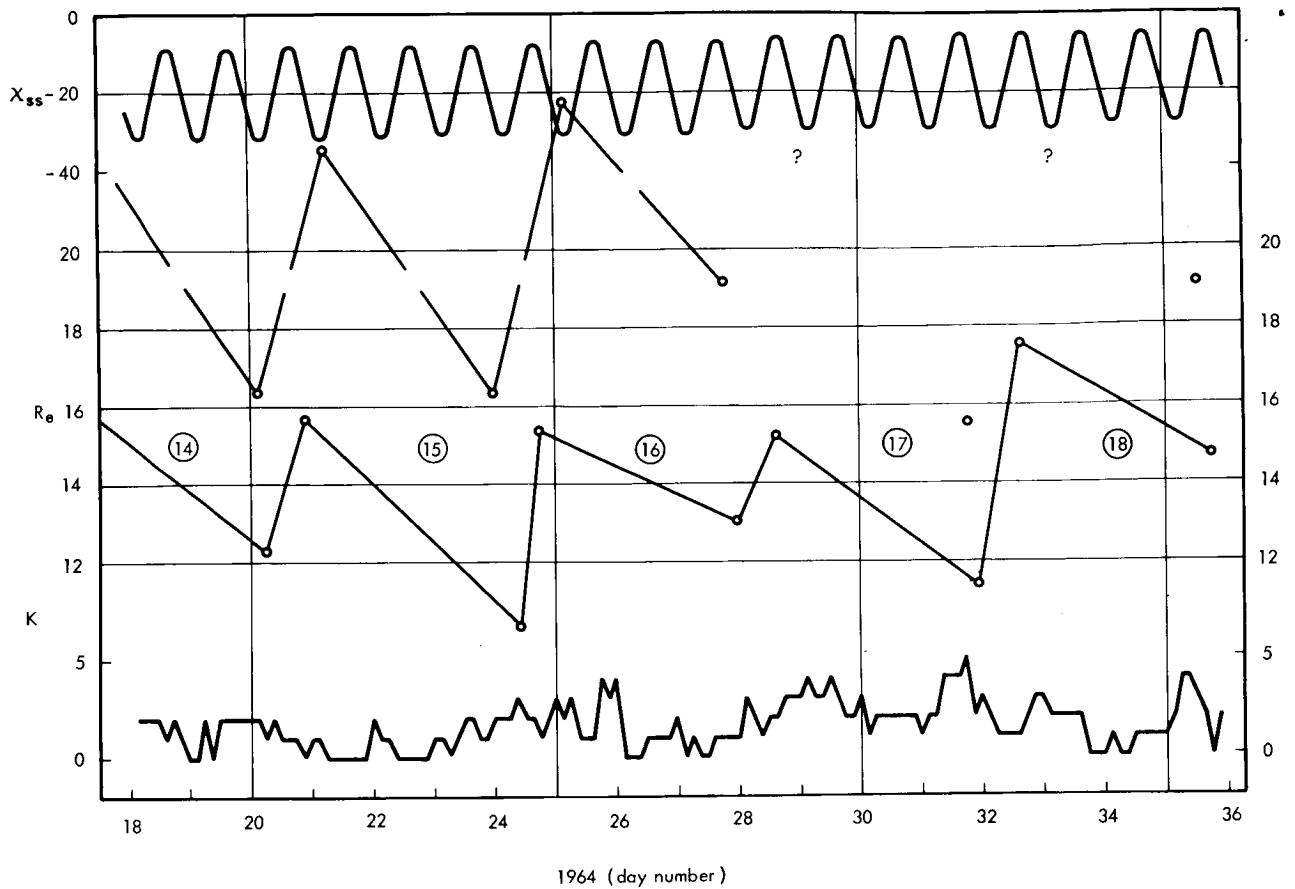


Figure 25—Time characteristics of geomagnetic latitude of subsolar point χ_{ss} , magnetopause and shock wave locations and K indices for days 18 to 36, 1964.

where m is proton mass, n the proton density, V_s the solar wind velocity, and B_t the net magnetic field tangential to the magnetopause boundary, which is commonly taken to be given by

$$B_t = 2fB_c, \quad (6)$$

where f is a factor less than or equal to 1 (usually taken as unity) and B_c is the theoretical and undisturbed geomagnetic field. However

$$B_c = B_0 \frac{R_e^3}{R_c^3} \sqrt{1 + 3 \sin^2 \chi_{ss}}, \quad (7)$$

where χ_{ss} is the geomagnetic latitude at the stagnation point where the flow velocity is normal to the surface and B_0 the terrestrial equatorial field strength.

Combining Equations 5 through 7 yields

$$R_c = R_e \left[\frac{B_0^2 (1 + 3 \sin^2 \chi_{ss})}{4\pi mn V_s^2} \right]^{1/6}, \quad (8)$$

where χ_{ss} is the geomagnetic latitude of the subsolar point. Clearly the distance at which the magnetopause is predicted depends upon the angle of the earth's dipole to the solar plasma. This concept has been included in the final data summary and has been employed to rectify the position of the boundary crossings to a geometry which allows comparison with the simplified theoretical treatments. In these analyses the solar stream is assumed normally incident upon the axis of the magnetic dipole, implying coincidence of the geomagnetic equatorial plane and the ecliptic plane.

A summary of the location of the magnetopause and shock wave traversals rotated into the ecliptic plane as a function of position of the satellite is presented in Figure 26. The effect of motion of the line of apsides of the satellite relative to the sun-earth line is evident. Figure 26 shows all boundary crossings which have been uniquely identified on the basis of magnetic field information alone. These data do not include any corrections for time variations of the solar wind, the planetary indices of the geomagnetic field, nor the geomagnetic latitude of the subsolar point χ_{ss} . These boundary crossing positions have been rotated from their actual position to the

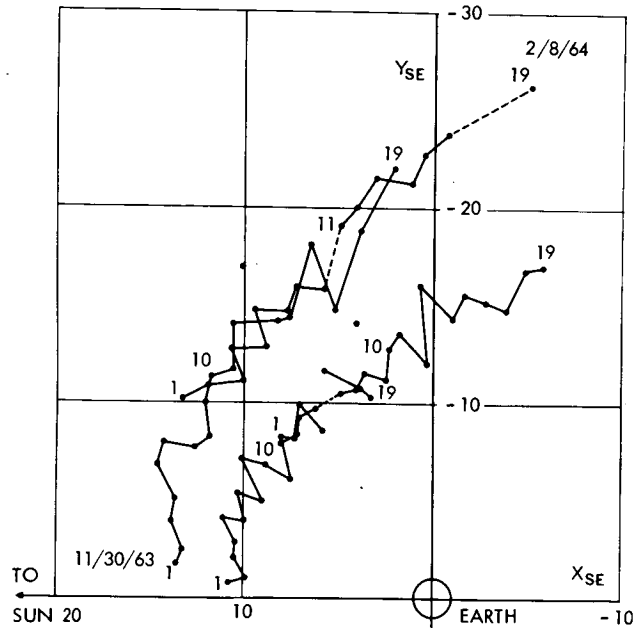


Figure 26—Location of magnetopause and shock wave boundary traversals rotated onto ecliptic XY plane.

ecliptic plane in a meridian plane through the Z_{se} axis. This essentially assumes a constant radius of curvature in each meridian plane. An alternative procedure — not employed — is to rotate the positions into the ecliptic plane about the X_{se} axis which presumes cylindrical symmetry about the X_{se} axis.

Clearly evident in this figure is the fact that the magnetopause is not spherical, but actually on the nightside hemisphere of the earth, the boundary flares out in consonance with the ideas originally resulting from measurements on the Explorer X satellite (reviewed by Bridge, Reference 58, and Ness, Reference 59). In addition, it is seen that the shape of the shock wave boundary when projected on the ecliptic plane is approximately hyperbolic. The angle which the hyperbola asymptotically approaches is referred to as the Mach angle and, if measured, could indicate the velocity of solar wind propagation relative to the interplanetary magnetic field strength and plasma density by defining the Mach number of the super Alfvénic flow of the solar wind.

In order to make a first order correction for the variation of the geomagnetic latitude of the subsolar point and thereby take into account the variable magnetic field strength which the solar wind meets at the stagnation point, an expansion factor K has been computed. This is dependent upon the geomagnetic latitude of the subsolar point and the strength of the magnetic field of an assumed dipole at the center of the earth. From Equation 8, K is defined as:

$$K = \left[1 + 3 \sin^2 \chi_{ss} \right]^{1/6} \quad (9)$$

The maximum inclination of the earth's magnetic dipole axis to the solar wind direction is 35.1° being the sum of 11.7° , the tilt of the magnetic axis to the rotation axis, and 23.4° , the obliquity of the rotation axis to the ecliptic. The maximum expansion is seen in Figure 27 to be 12 percent assuming a constant pressure of the solar wind. The time of launch of IMP I is such that the maximum inclination was achieved during the first month of operation of the satellite (the winter solstice), and since that time the earth's rotational axis has approached perpendicularity to the earth-sun line. This is seen in Figures 22 through 25 in which the diurnal variation of χ_{ss} is seen to become more negative, reaching a minimum in December 1963 and then becoming less negative as time progresses. The average values of χ_{ss} over one day indicate the angle between the normal to the earth-sun line (X_{se} axis) and the direction of the earth's rotation axis.

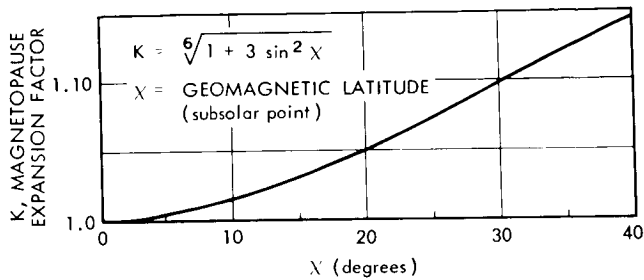


Figure 27—Magnetopause expansion factor K to compensate for variable tilt of earth's magnetic field axis to the "angle of attack" of solar wind.

In comparing theoretical and observed boundary geometries, it has been assumed that the only model currently available is that provided by the computations of Spreiter and Jones (Reference 60) using a blunt body profile representing the earth's magnetosphere to determine the shape of the shock wave surface based upon a strict analogy with high speed aerodynamic flow.

The blunt body profile used is that which is obtained by rotating the trace of the magnetopause in the geomagnetic equatorial plane about the X_{se} axis. The shape has been determined by a number of workers — among these are Beard, Hurley, Midgley and Davis, Slutz, Spreiter and Briggs, and Mead and Beard (References 54, 61, 62, 63, 56 and 57, and 64, respectively) — and all their results are generally in good agreement as long as the region near the null points in the polar regions is not considered. None of these analyses has included an interplanetary magnetic field in determining the shape nor physical characteristics of the magnetopause boundary, particularly in view of the importance of the collisionless shock wave. This omission has been partially rectified in the work of Lees (Reference 65) by inclusion of the interplanetary magnetic field. The ramification of the shock on the field configuration external to the magnetopause has been considered by Beard (Reference 66). The results for the particular model which Spreiter and Jones (Reference 60) utilized have been slightly adjusted to match the actual observation of standoff distances of the geomagnetic cavity boundary and the shock wave boundary at the subsolar point. In addition all boundary crossings have been rectified by dividing the observed distance by the appropriate value of the expansion factor K so as to reduce all distances to a geometry in which the solar wind is normally incident upon the axis of the earth's magnetic dipole. The results of these rectifications and the adjustment of the theoretical models are compared in Figure 28 with the theoretical results indicated by solid curves through the experimental data. The theoretical magnetopause geocentric distance at the subsolar point is taken to be $10.25 R_E$ while that of the

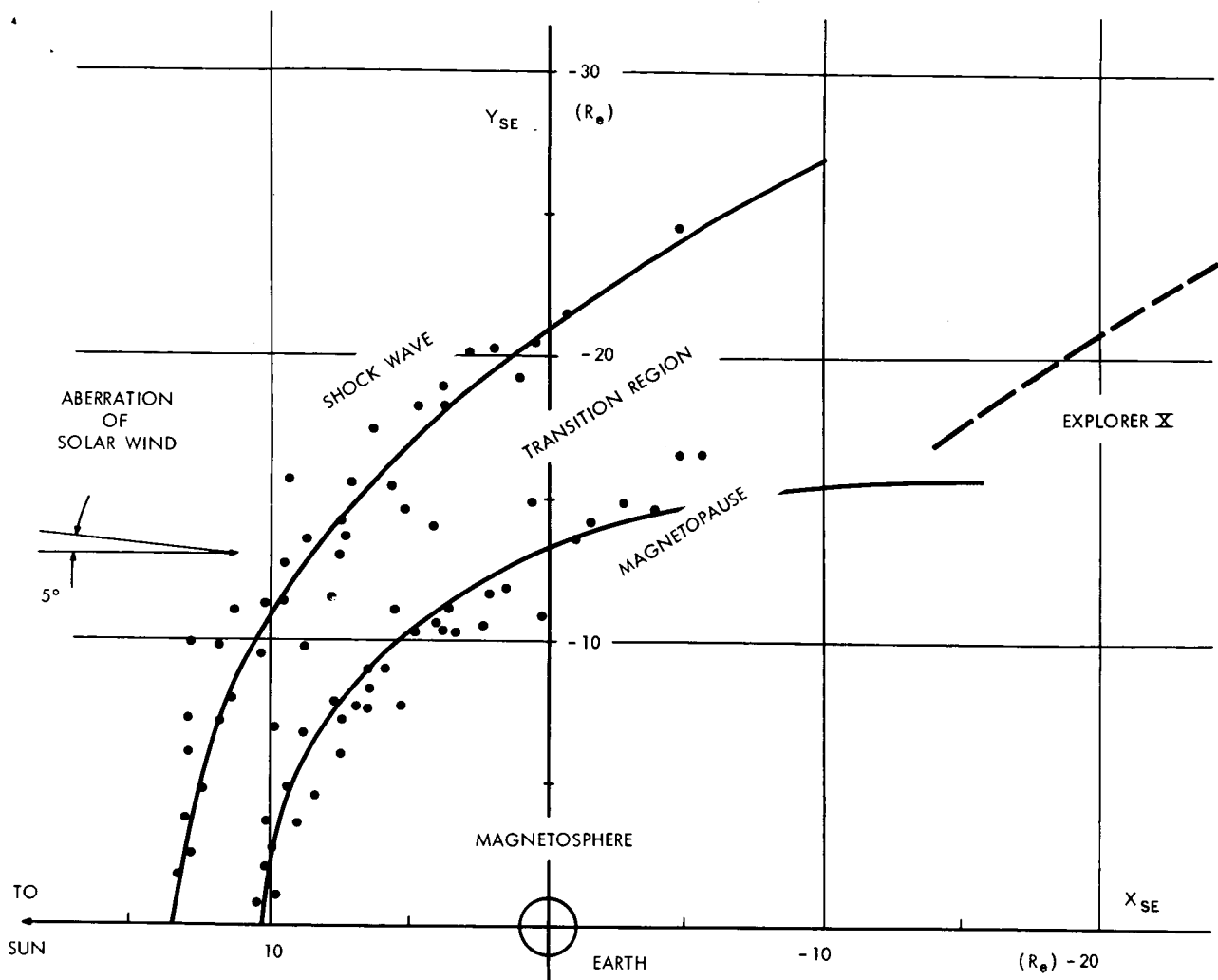


Figure 28—Summary of location of rectified shock wave and magnetopause crossings and comparison with theoretical predictions using analogy with supersonic fluid flow.

shock wave is taken as $13.4 R_E$. It has been necessary to rotate the theoretical model by 5° about the Z_{SE} axis to obtain the demonstrated agreement. This is comparable with the aberration effect due to the earth's orbital motion of 30 km/sec when compared to the solar wind velocities. For values of v_s between 300 and 400 km/sec the aberration effect changes from 5.7° to 4.6° and the value of 5° is taken to be a representative average.

An important parameter describing the flow of the solar plasma and its interaction with any planetary object is the velocity at which disturbances can be propagated. In the highly ionized magnetized plasma being studied, the appropriate modes of propagation are the magnetoacoustic modes. Considering the important mode to be the simple Alfvén transverse magnetohydrodynamic mode, we have the relevant velocity given by

$$v_A = \frac{B}{\sqrt{4\pi\rho}} \quad (10)$$

and shown in Figure 29 for the range of parameters observed in space. Since in general representative values of these parameters are

$$4 \leq B \leq 7\gamma ,$$

$$3 \leq \rho \leq 10 \text{ protons/cm}^3 ; \quad (11)$$

therefore

$$25 \leq V_A \leq 90 \text{ km/sec} .$$

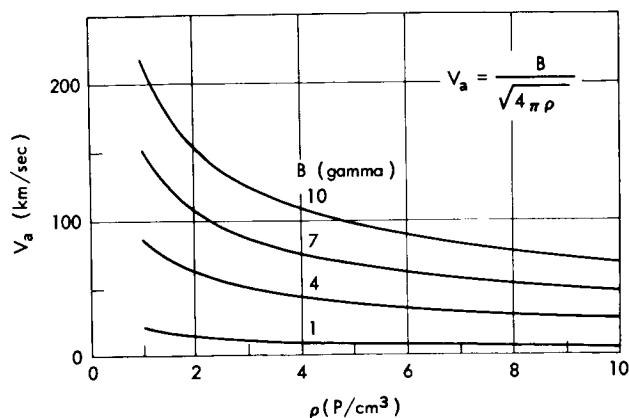


Figure 29—Alfvén magnetohydrodynamic phase velocity of wave propagation as function of magnetic field strength and plasma density.

Now the directed stream velocity of the solar wind is observed to be

$$300 \leq V_s \leq 700 \text{ km/sec} .$$

Thus the ratio of directed velocity to Alfvén velocity measures the super Alfvénic ratio, or Mach number corresponding to the gas dynamic analogy, and is found to be

$$3.3 \leq M_A \leq 28 , \quad (12)$$

and the mean value is

$$\bar{M}_A = 5-10 . \quad (13)$$

A general review of the applicability of the gasdynamic analogy used in treatments of the flow of plasma around the geomagnetic field has been given by Levy, Petschek and Siscoe (Reference 43).

The comparison between theory and observation of the position of the shock wave surface is good. It is clear however that the comparison is possible at the present time only near the stagnation point. Here the shape of the surface is not critically dependent upon Mach number or the equivalent gas specific heat ratio used. The experimental data however do suggest an outward flaring of the magnetopause — first observed on Explorer X and is seen to be consistent with the present observations on IMP. The portion of the Explorer X trajectory over which the magnetopause boundary was observed is indicated in Figure 28, where the magnetopause boundary has been rotated about the X_{se} axis into the ecliptic plane ahead of the earth. The extrapolation of the IMP observations coincides reasonably well with these earlier measurements. It indicates a fundamental discrepancy between theory and observation in that all theoretical models using a real, thermalized plasma lead to a closure of the magnetopause at distances of 30-50 R_E on the dark side of the earth. However, the observations indicate that an outward flaring of the magnetopause surface at a half-cone angle of 10-15° occurs. The magnetic fields interior to the magnetopause for orbits 11 and beyond are directed at $\phi = 205-215^\circ$ which is consistent with an outward flaring, if the fields are tangential to the bounding geomagnetic cavity surface.

The relative position of the subsolar geocentric distance to the shock wave, R_s , and the magnetopause boundary, R_c , is presented as a function of the Alfvén Mach number in Figure 30. The solid lines indicate the theoretical models for a sphere and blunt body as predicted by Spreiter and Jones (Reference 60). The circled data represent the values deduced by Kellogg (Reference 21) in his analysis using the analogy of supersonic flow in gasdynamics and the theoretical results of Hida (Reference 67) for a spherical object. The observed value of the ratio of R_s/R_c is shown as a horizontal solid line, experimentally determined to be 1.31 ± 1 percent. The correspondence between theory and observation is very good and although the use of the blunt body profile does not yield the proper ratio, it is increased in the proper sense. The present discrepancy between theory and observation can be readily resolved through use of $\gamma < 2$ and slightly altering the magnetopause shape.

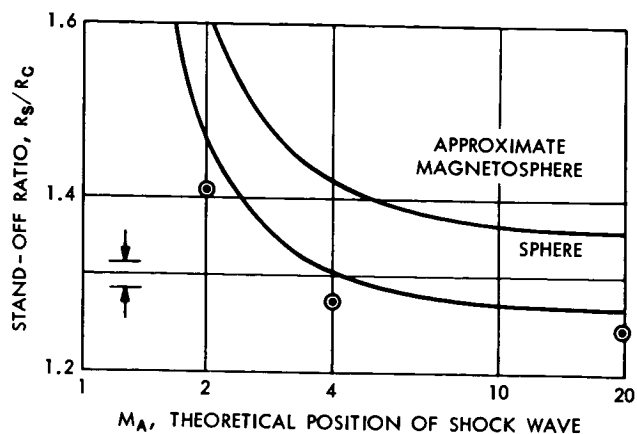


Figure 30—Theoretical stand-off ratio R_s/R_c of shock wave surface to magnetopause boundary and comparison with observations.

The totality of IMP observations on the location and geometry of the magnetopause and collisionless shock wave boundary are in generally good agreement with theoretical models using the analogies between supersonic fluid flow and the super Alfvénic flow of the solar wind with the interplanetary magnetic field acting to couple the particles together as described by Axford (Reference 19) and Kellogg (Reference 21) rather than direct particle collisions. Obayashi (Reference 68) has reviewed all previous satellite measurements with respect to their significance in the detection and identification of the magnetopause and shock wave boundary positions.

Since the satellite has yet to complete mapping the nighttime magnetospheric tail, it is not possible to definitely state that an extended flaring of the cavity far behind the earth is the only possible interpretation of the data. It appears to be a reasonable assumption, however, and it is anticipated that during orbits 20-40 the IMP satellite will provide extremely important data on the actual geometry and physical characteristics of the magnetopause boundary and the magnetic field topology within the geomagnetic tail. Studies on the magnetosphere tail magnetic field topology have been performed by Axford and Hines (Reference 69), Harrison (Reference 70), Hones (Reference 71), and Johnson (Reference 72). Quantitative estimates of the field characteristics in the magnetosphere near the stagnation point have been performed by Mead (Reference 73). In the traversals of the magnetopause boundary the direction of the magnetic fields appear to be tangent to the apparent magnetopause surface within $\pm 10^\circ$. At present one of the major theoretical uncertainties is the reason for the outward flaring shape of the cavity boundary on the nightside of the earth.

SOLAR TERRESTRIAL TRANSIENTS

The general level of terrestrial magnetic activity throughout the lifetime of the IMP satellite has been extremely low as seen by the K values in Figures 22-25. This is associated with the decrease of solar activity which will meet its absolute minimum within the next eighteen months. Fortunately, however, there have been a few specific isolated magnetic disturbances associated with the limited solar activity and these have been observed definitely by the IMP satellite in interplanetary space. In particular, the December 2, 1963 sudden commencement storm beginning at 2117 UT occurred at a very favorable time in the second orbit of the satellite. At this time, as shown in Figure 11, the satellite was approaching apogee and essentially was stationary in space except for its motion through the interplanetary medium at the heliocentric orbital velocity of the earth.

The regular run magnetograms from a number of standard observatories in the US Coast and Geodetic Survey net are presented in Figure 31 for the time interval preceding and following the

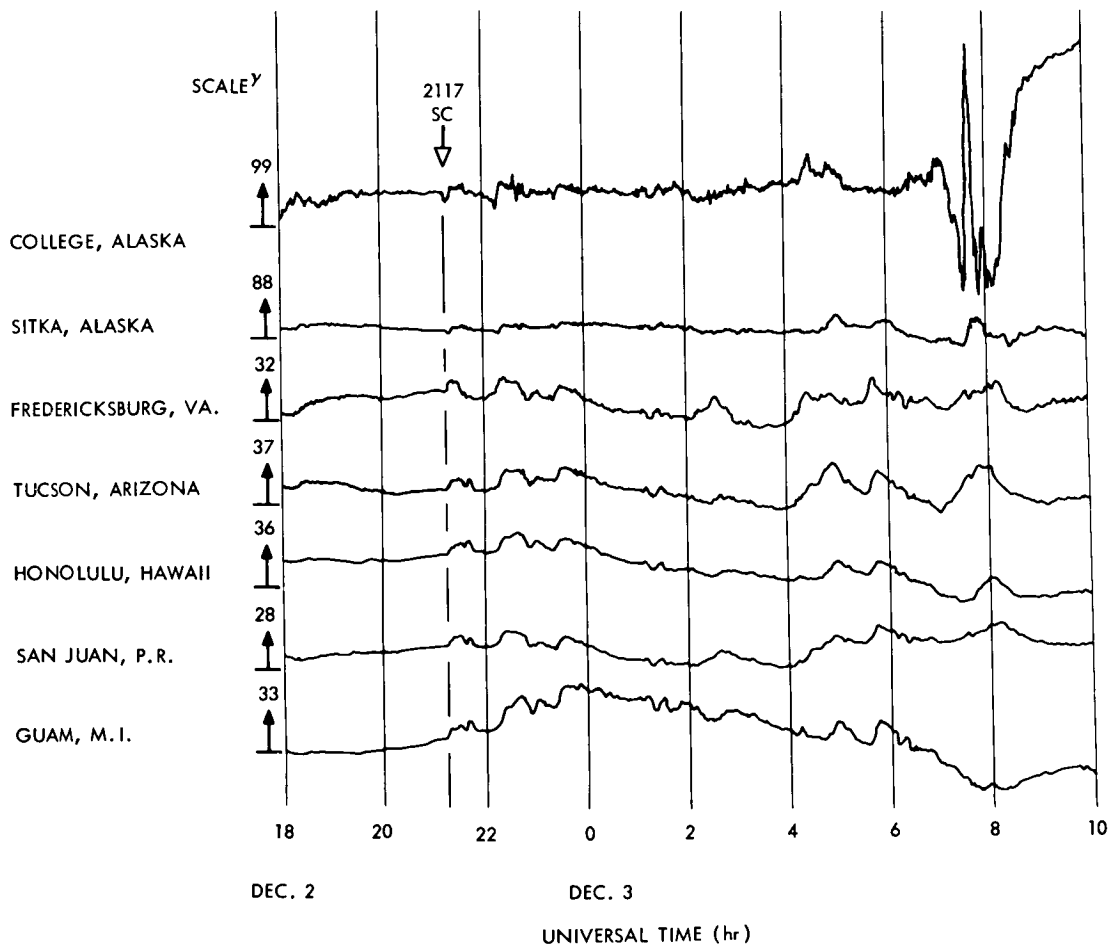


Figure 31—Regular-run observatory H component magnetograms for December 2, 1963 sudden commencement storm period.

sudden commencement storm. It is clear from inspection of the records that this sudden commencement showed similar characteristics at a number of stations for several hours after the initial onset. In order to accurately establish the time of occurrence of the sudden commencement at terrestrial stations, the rapid-run magnetograms from certain of these same stations are illustrated in Figure 32 (in which the time scale is considerably expanded). It is seen that the onset time of 2117 is easily identifiable as there is no discrepancy in its unique characteristic.

The magnetic field data obtained on the outbound portion of the orbit 2 on December 1, 1963 are shown in Figure 33. At this time the boundary of the magnetopause was observed at $11.1 R_E$; but the shock wave was observed at $16.2 R_E$. In general the interplanetary magnetic field conditions were quiet although the field was somewhat larger than previously observed, approximately 6γ , varying somewhat in direction and illustrating the filamentary structure previously referred to in the summary of the overall characteristics of the interplanetary magnetic field. Data from the portion of the second orbit during which the storm occurred are shown in Figure 34. The interplanetary magnetic field was undisturbed prior to the occurrence of the sudden commencement, although the magnitude increased gradually. Shortly before the terrestrial observations of the sudden commencement the field decreased very rapidly, and varied somewhat for several hours, eventually returning to a configuration similar to that prior to the storm. An expanded time

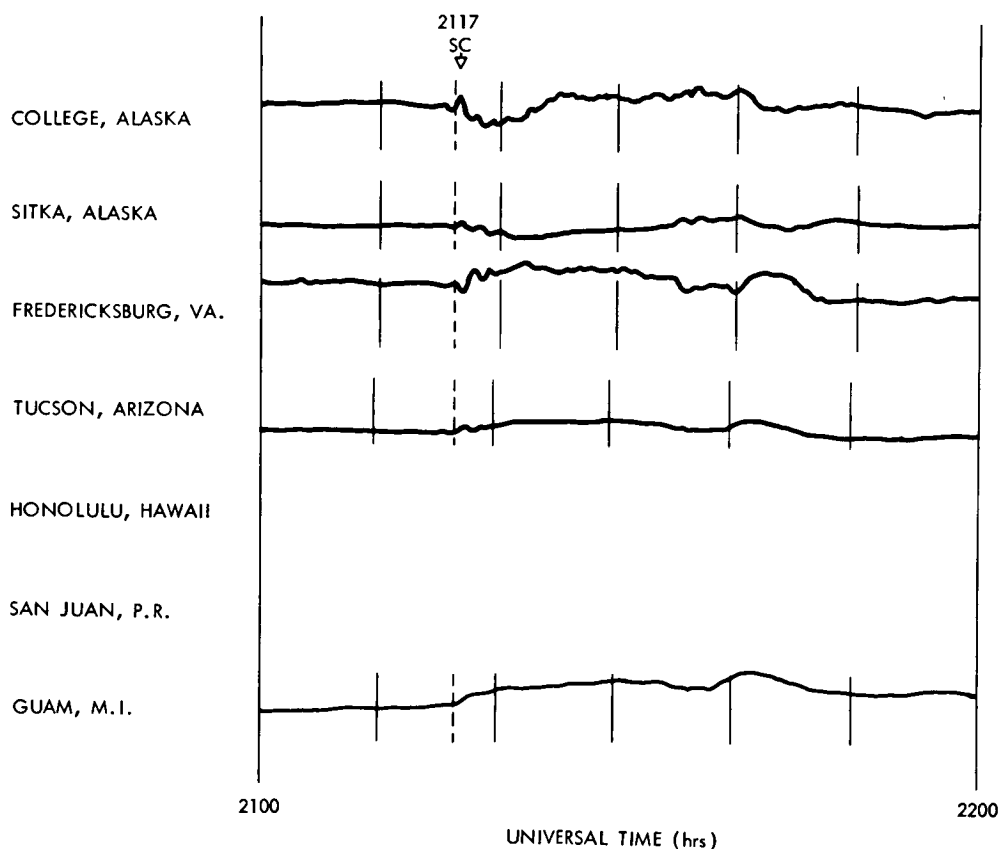


Figure 32—Rapid-run observatory H component magnetograms for December 2, 1963 sudden commencement storm period.

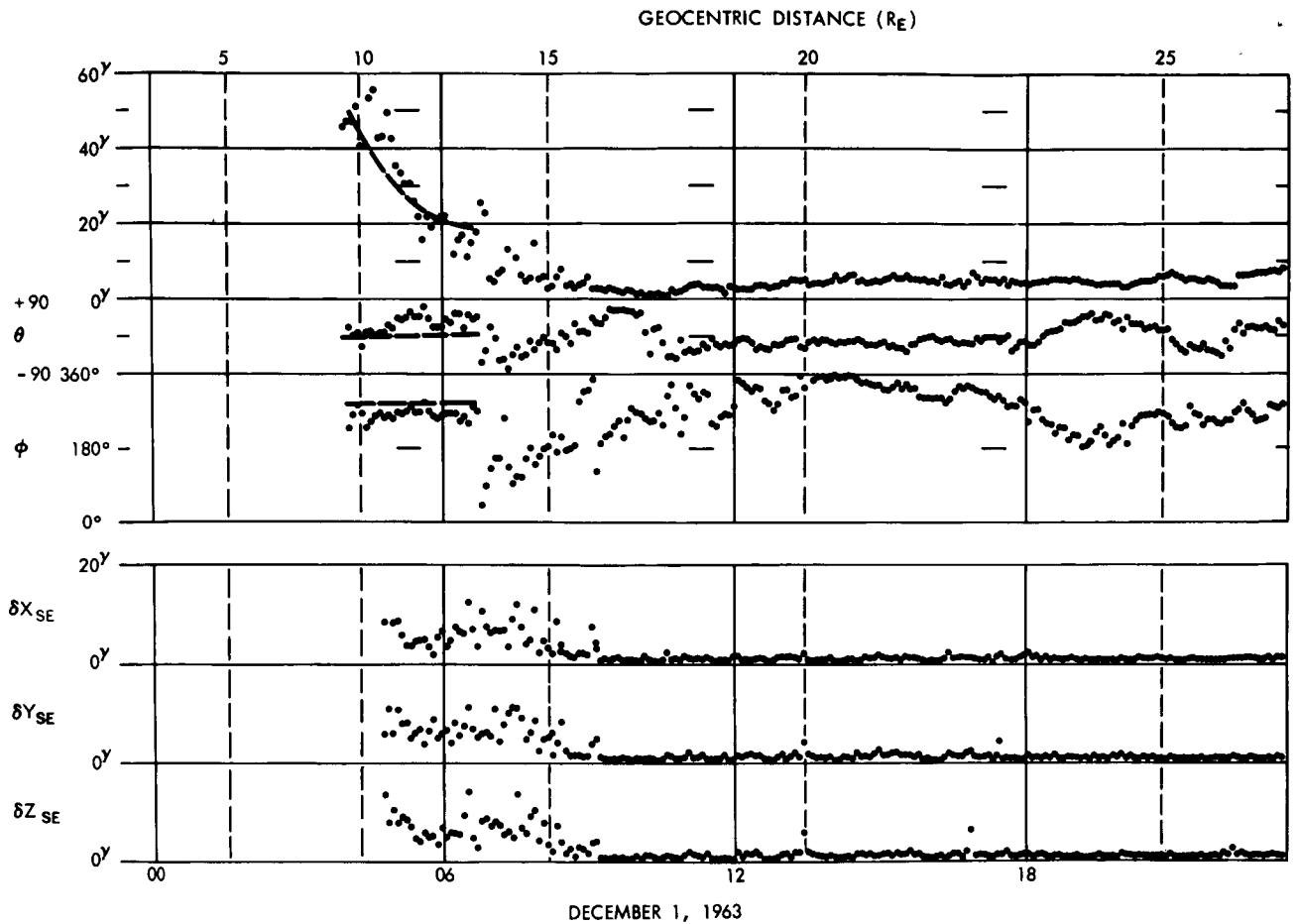


Figure 33—Magnetic field data from orbit 2 (December 1, 1963) indicating traversal of magnetopause boundary at 11.1 R_E and shock wave boundary at 16.2 R_E .

scale presentation of the interplanetary magnetic field is presented in Figure 35 in a payload coordinate system. Instead of 5.46 minute averages, the 12 sample values in that interval are presented separately with a time spacing of 20 seconds. It is clear that the occurrence of the sudden commencement indicated by the initial onset of the magnetic field disturbance occurs at 2114 on December 2 at the satellite. Assuming radial propagation of the plasma front and the associated magnetic field distortions to the surface of the earth yields a propagation velocity of 700 km/sec. This velocity is an apparent value of velocity of propagation, since it does not include the physical propagation of the storm transient itself to the surface of the earth, and it assumes the direction of propagation of the storm front and that the magnetic field disturbance and the plasma disturbance occur at the same place in the solar plasma stream. This value of 700 km, however, is consistent with the transit time associated with the projected solar region responsible for the storm, and is equivalent to particle energies of 2.5 kev. By assuming a propagation velocity of 700 km/sec and by observing the time interval during which the magnetic field is disturbed and presumed to be associated with the propagation of the shock front surface, the shock front surface thickness is 0.005 AU. This is consistent with particle measurements yielding scale lengths of scattering centers in interplanetary space at the time of magnetic disturbances.

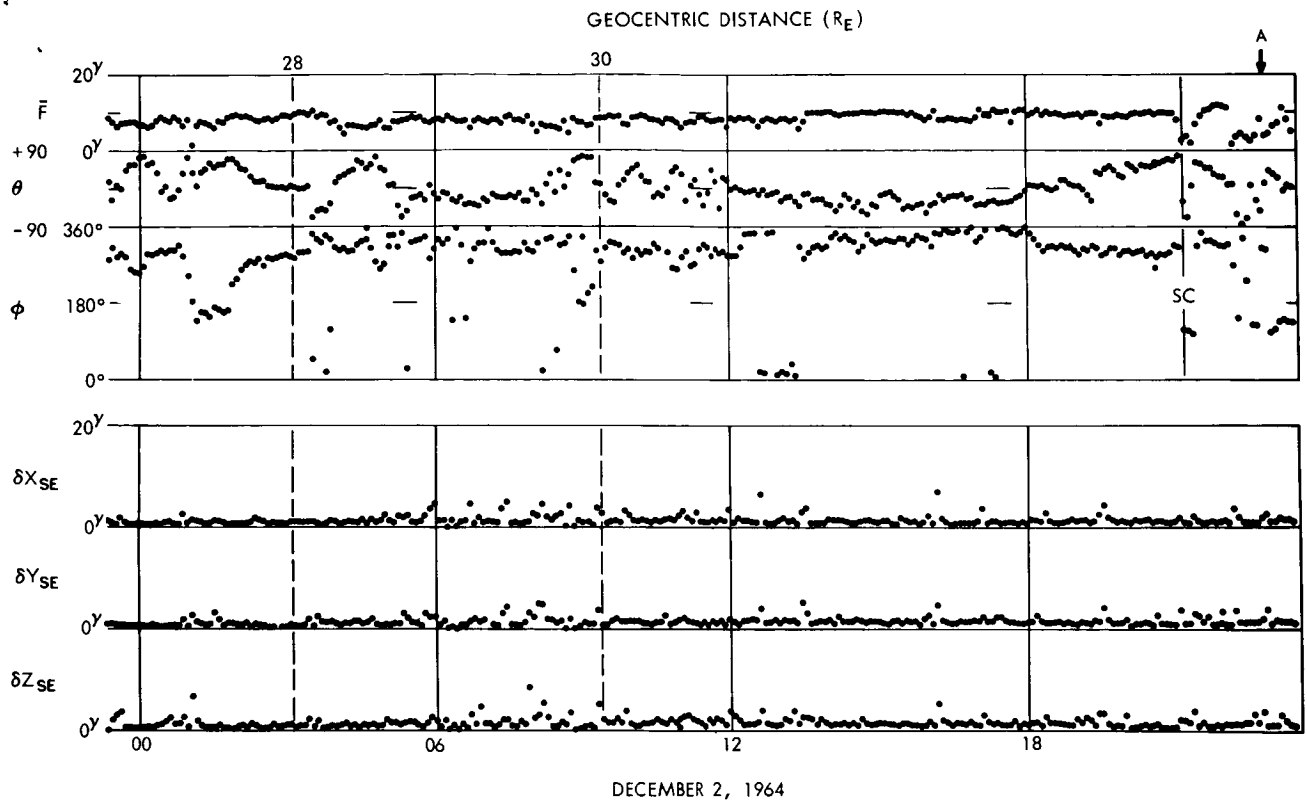


Figure 34—Magnetic field data from orbit 2 (December 2, 1963) illustrating interplanetary magnetic field at time of sudden commencement storm.

Another important feature of the storm is that there is a null surface observed during the transit of the storm front surface across the spacecraft. The structure may well be consistent with Parker's "blast wave" model of sudden commencement storms if we include the fact that if the compressed interplanetary fields are filamentary in their topology, then null surfaces must occur. This suggests that magnetic field annihilation as proposed by Petschek (Reference 74) may be the mechanism whereby acceleration of particles in the shock front occurs. The present sample of magnetic fields associated with SC's in interplanetary space does not show the large fields, up to 50γ , previously reported by Coleman et al., (Reference 3) for Pioneer V data. Indeed the experimental results appear to be in the main contradictory since Pioneer V also did not measure a null surface. At the present time, it is suggested that these differences only reflect the great variability in storm characteristics and intensities.

INTERPRETATIONS OF SOLAR STREAM PROPERTIES

The location of the magnetopause and shock wave boundaries as observed by the magnetic field experiment permit an extrapolation to the characteristics of the streaming solar plasma. The streaming angles indicated by the magnetic fields are used in computing the characteristics of the

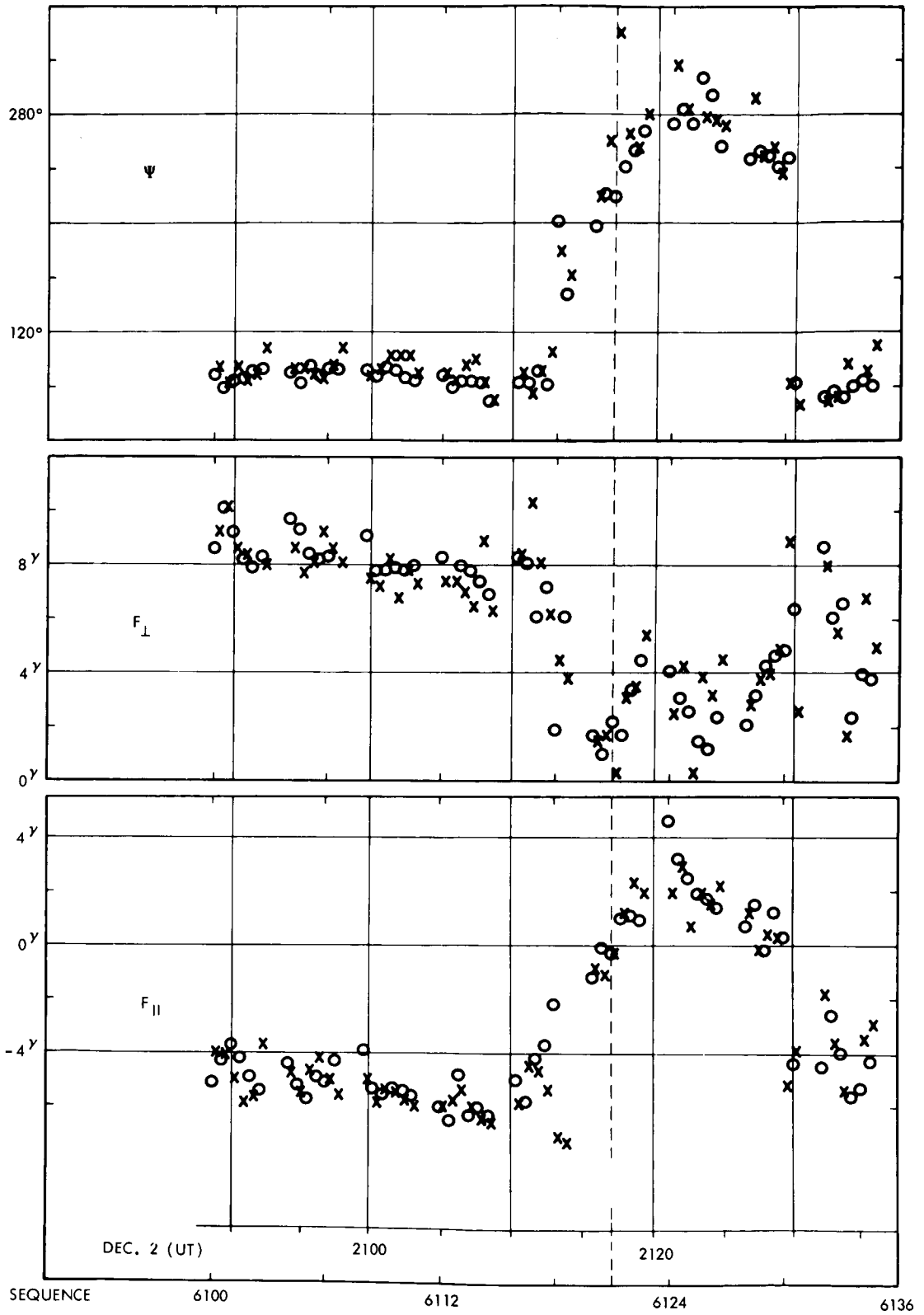


Figure 35—IMP 1 magnetic field data on expanded time scale in payload coordinates at time of December 2, 1963 sudden commencement storm. Circles refer to fluxgate A data while crosses reference fluxgate B.

solar stream. The interpretation assumes that the streaming angle provides a reasonable estimate of the particle velocity (Figure 36) and gives the particle density and velocity that would be consistent with the observed location of the magnetopause if the plasma were directly incident upon the magnetopause. This density and velocity represent an effective description of the plasma flux pressure, which is balanced by the magnetic field pressure. The actual solar wind velocity and density must be adjusted in terms of the boundary conditions which exist at the shock wave. On the assumption of particle velocities between 300-700 km/sec and the observed location of the magnetopause boundary of $10.25 R_E$, it is seen that the corresponding proton density is between 1 and 5 protons/cm³. This yields a flux value of 0.7 to 1.5×10^8 protons/cm²/sec, which is in good agreement with previous plasma data extrapolated from Explorer X (Reference 6) and the direct measurements on the Mariner II spacecraft (Reference 7).

MAGNETOHYDRODYNAMIC WAKE

OF THE MOON

A unique phenomena occurred in interplanetary space during the fifth orbit of the satellite. At that time the interplanetary magnetic field was observed to fluctuate much more so than had been previously observed or was subsequently observed and also to reach a maximum value of 14.6γ for a period of 4 hours on December 14, 1963. This high value of both the magnitude and the variance had never been observed throughout the previous 4 orbits of the spacecraft when in the interplanetary medium and some concern was expressed initially as to whether or not the operation of the instrument and/or the telemetry digitization system was proper at the time. The integrity of the operation of the telemetry system and the sensor has been verified and the conclusion is irrevocable that the basic data are valid. At this time the satellite was located between 28 to 31 R_E from the earth at approximately an angle of 40° to the sun-earth line and far beyond the shock wave location.

Investigation of solar conditions prior to the anomalous field behavior, extending from 0100 UT, December 14 to 1000 UT December 15, has not revealed any significant features that might have led to disturbed conditions in interplanetary space. The characteristics of the fluctuations are quite unlike those of the magnetic fields associated with the sudden commencement storm on

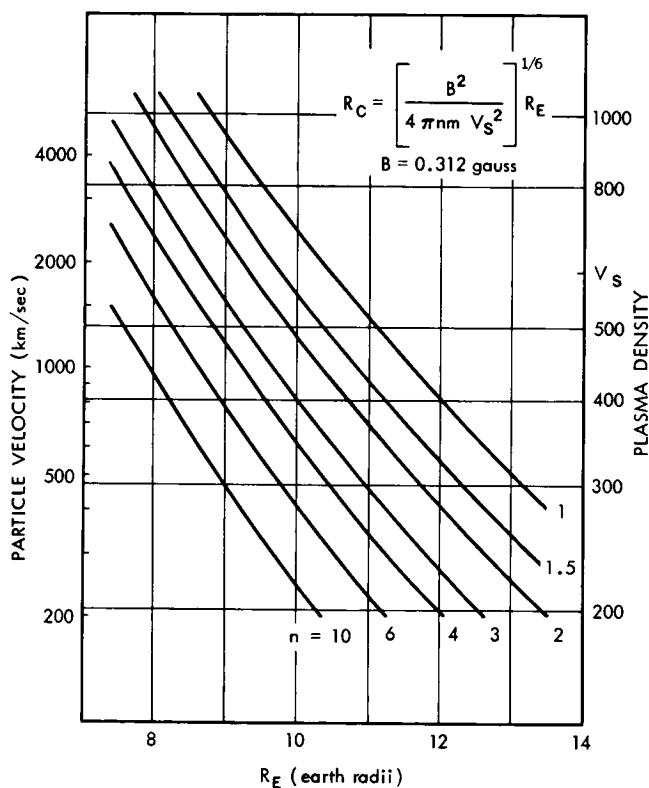


Figure 36—Theoretical stagnation point distance R_c of magnetopause boundary as function of particle velocity (or energy) and plasma density.

December 2, 1963. Indeed the characteristics are similar to those observed when sampling the transition region associated with the solar wind impacting the geomagnetic field.

The explanation offered is that the relative location of the sun, moon and satellite was unique and that the interaction of the solar wind with the moon and its magnetosphere formed a magnetospheric tail which IMP I traversed. This extended far behind the moon much in the manner of cometary tails (Reference 75) and as may be the case of the earth's tail. An inspection of the ephemerides of the moon, sun and IMP I satellite has shown that this is a reasonable interpretation. Thus it provides the first direct measurements of magnetic field phenomena associated with the moon and indeed may provide quantitative estimates of the lunar field strength upon subsequent detailed analysis.

The projected locations of the relevant celestial objects on the ecliptic plane is shown in Figure 37. To illustrate the fact that the satellite was not sampling the region of interplanetary space influenced by the presence of the earth the location of the magnetopause and the shock wave boundaries are included. The numbers on both the IMP I and moon orbits indicate the location of the respective object at 00 hours UT on the particular day in December 1963. The projected view of the same days on the solar ecliptic YZ plane is shown in Figure 38. Certain physical

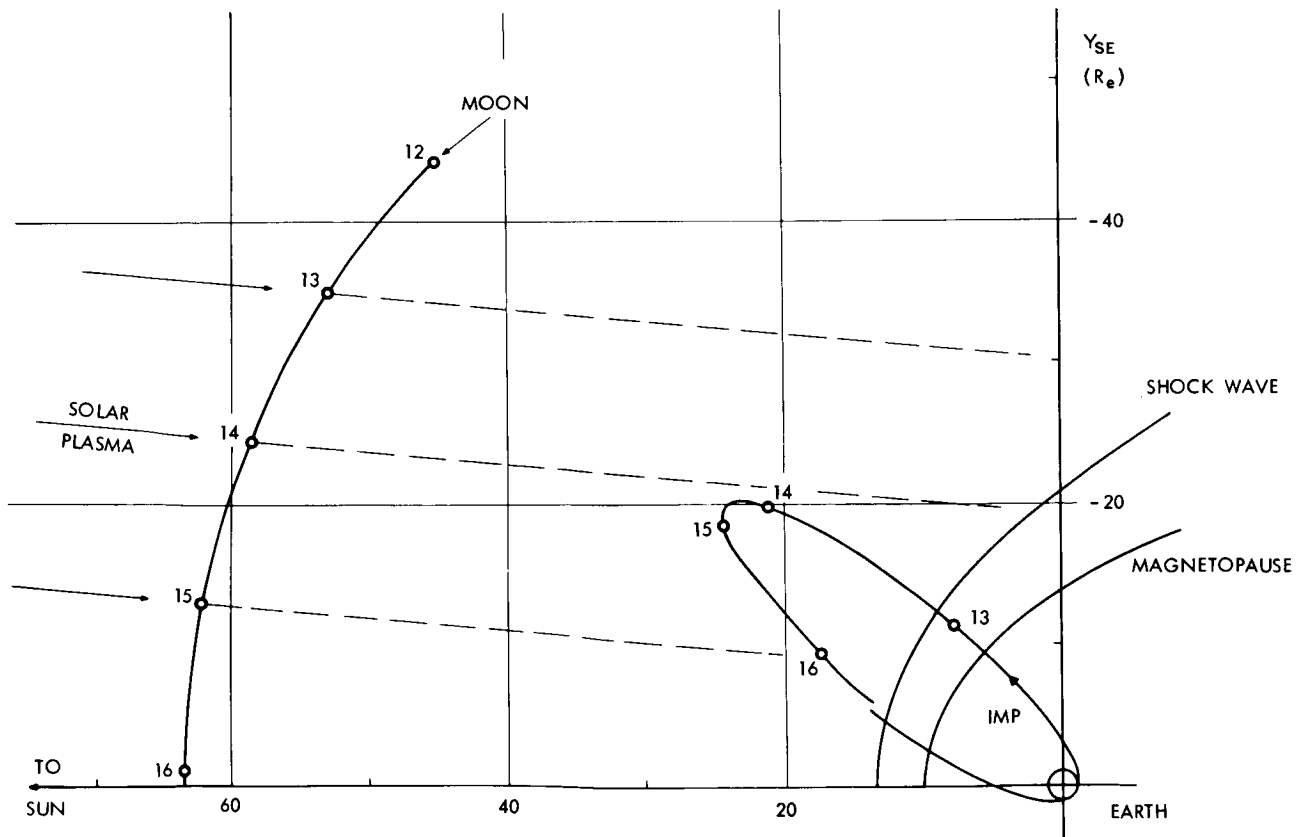


Figure 37—Relative location of IMP I satellite, earth and moon during period December 12-16, 1963 when lunar magnetospheric wake was detected by the magnetic field experiment.

parameters important in specifying the relative location of the sun, moon and IMP I are defined as follows:

\mathbf{D} = vector distance from satellite to moon,

$$\mathbf{D} = D_x \mathbf{i}_x + D_y \mathbf{i}_y + D_z \mathbf{i}_z,$$

$$D_{sm} = |\mathbf{D}| = [D_x^2 + D_y^2 + D_z^2]^{1/2},$$

$$D_{xy} = [D_x^2 + D_y^2]^{1/2} = \text{projected distance in XY plane,}$$

$$D_{yz} = [D_y^2 + D_z^2]^{1/2} = \text{projected distance in YZ plane,}$$

$\cosine \lambda_{xy} = D_x/D_{xy} = \text{cosine of angle between } \mathbf{D} \text{ and } \mathbf{i}_x \text{ projected into XY plane,}$

$\cosine \lambda_{yz} = D_z/D_{yz} = \text{cosine of angle between } \mathbf{D} \text{ and } \mathbf{i}_z \text{ projected into YZ plane.}$

The distance D_{yz} and the angle λ_{yz} are illustrated in Figure 38. For an optical occultation $D_{yz} = 0$ while when $\lambda_{yz} = 0$ it implies that the sun, moon, and IMP I define a plane that is perpendicular to the ecliptic plane.

A summary of the above critical parameters as a function of time in December is shown in Figure 39 as well as the indicated traversals of the shock wave boundary. The parameter D_{yz} refers to the projected distance on a plane rotated by 5° from the YZ plane to take into account the aberration of the solar wind. The "closest" distance from the satellite to the moon is $7.9 R_E$ in the

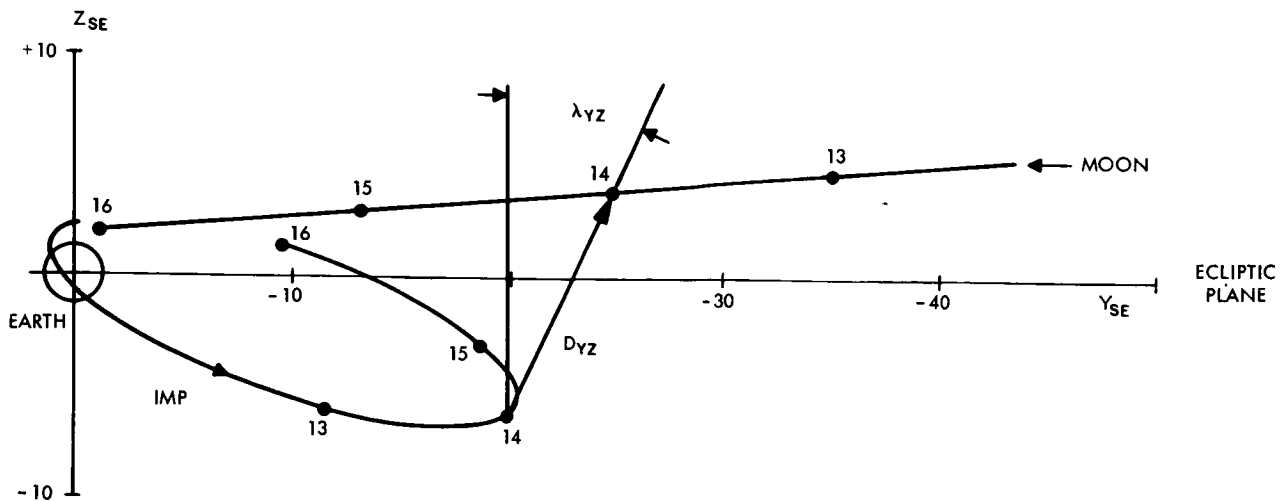


Figure 38—Relative location of IMP I satellite, earth and moon projected on plane perpendicular to earth-sun direction, the solar-ecliptic, YZ plane during period December 12-16, 1963.

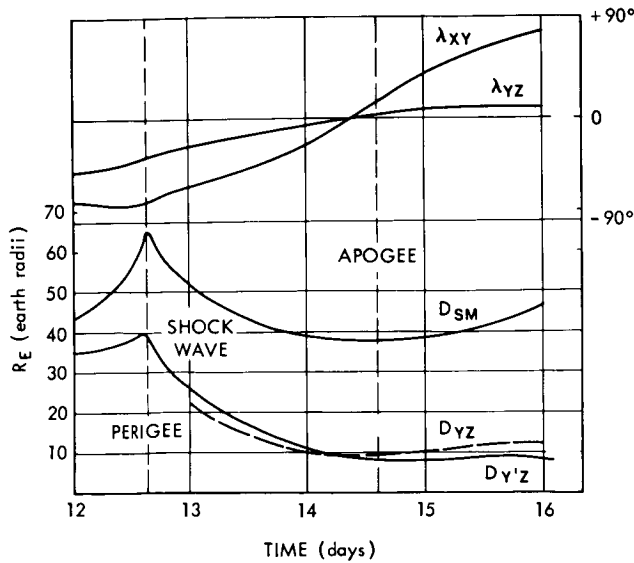


Figure 39—Critical parameters related to "shadowing" by the moon's magnetosphere or IMP I magnetic field measurements during December 12-16, 1963.

YZ plane where the satellite is $38 R_E$ from the moon. Converted to lunar radii, R_M , the length of the moon's magnetospheric tail is at least $150 R_M$ while the apparent diameter of the tail at that distance is at least $30 R_M$. These values indicate a magnetospheric wake with a half-cone angle of approximately 11° , a value consistent with the Mach angle associated with the solar wind interaction with a moon possessing a weak magnetic field.

The direct measurement of the lunar magnetic field and a precise determination of its geometrical properties is of vital importance in the study of the origin of the earth-moon system. The interpretation of terrestrial data suggests the non-existence of a lunar magnetic field similar in origin to the earth's in which a dynamo system of currents circulates in a

fluid core. The presence of a lunar magnetic field may be indicative of a permanent state of magnetization which reflects an ancient field at the time of origin of the moon. It has been suggested by Gold (Reference 20) that the streaming magnetized solar plasma may provide a mechanism whereby the interplanetary magnetic field is captured by the finite electrical conductivity of the moon. This would then lead to a magnetic field configuration which could be interpreted as a lunar magnetic field.

Russian measurements of the lunar magnetic field on the second Cosmic rocket (Reference 76) indicate a surface field of less than 50 to 100γ which corresponds to a magnetization intensity of less than 0.25 percent of the earth's. The streaming solar plasma is sufficiently strong that it will greatly distort a lunar magnetic field regardless of its origin (Reference 77). Thus it can reasonably be expected that a cavity and geomagnetic tail similar to that observed on Explorer X (in the anti-solar direction behind the earth) and thus far suggested by IMP I, will also develop around the moon.

The detailed measurement and accurate vector mapping of such a lunar magnetic field and associated magnetospheric tail can only be accomplished with a spacecraft orbiting the moon. The present IMP I measurements may provide information sufficient to indicate the nature of the lunar magnetic field. A detailed study of the magnetic field results is currently being conducted and a future publication will discuss the lunar wake.

CONCLUSIONS

The IMP I satellite has provided the first direct measurements of interplanetary magnetic fields with high accuracy. The spacecraft fields are found by analysis of inflight data to be less

than $\pm 0.25\gamma$. The observed field strengths in the interplanetary medium range generally from 4 to 7γ with temporary excursions to values as low as 1 and as high as 10γ . The magnitude is impressively steady although directional changes occur fairly frequently on time scales of several hours. These steady magnitudes are a feature of the fields which had not been anticipated.

A significant feature of the vector field and the inferred interplanetary field configuration is the gross feature of spiral structure associated with the rotation of the sun, in directions consistent with observed solar plasma velocities. At times the field reverses directions on a time scale of 5-20 minutes, going through zero rapidly, indicating neutral surfaces separating the filamentary elements of magnetic fields. The overall Archimedean spiral structure in which the distinctive filaments are imbedded strongly suggests a merging of theoretical field topologies — as discussed by Parker (Reference 5) and Gold (Reference 20). However, the fields have only been sampled recently and further analysis will be required to determine whether the "magnetic

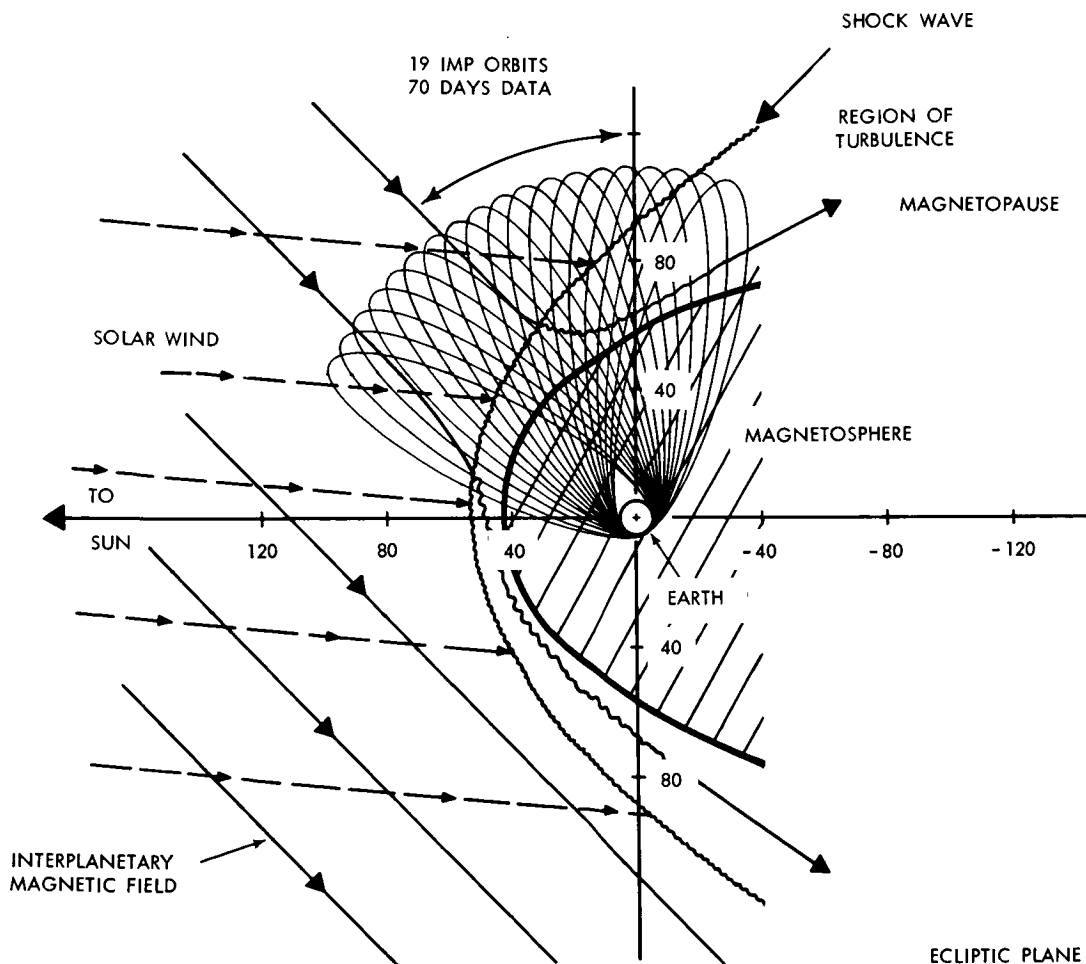


Figure 40—Illustration of IMP I magnetic field data interpretation showing solar wind, interplanetary fields collisionless shock wave and magnetopause locations on ecliptic plane. The distances are in thousand miles.

bottles" of Gold (Reference 28) are also consistent with the data. Indeed with only one sample point in space it may not be possible to delineate between such features.

The IMP I observations of the solar wind interactions have experimentally confirmed the existence of the collisionless shock wave predicted by theoretical analogies with supersonic gas dynamics. Indeed the position of the shock wave is impressively consistent with the theoretical models showing a departure of only a few percent. The magnetosphere boundary, the magnetopause, is clearly observed and found to be separated from the shock wave by a region of high turbulence in the magnetic field. An interpretive graphical summary of the initial results of solar wind interaction with the earth is shown in Figure 40. The geocentric distance to the magnetopause is found to be $10.25 R_E$ at the stagnation point. The distance to the shock wave is $13.4 R_E$ yielding a stand-off ratio of 1.31 ± 1 percent.

The detection of the extended lunar magnetospheric wake into interplanetary space at least 150 lunar radii behind the moon is important evidence in confirming the general aspects of the understanding of solar wind interactions with planetary objects. The field strengths and directions are indicative of the magnetohydrodynamic interaction of the solar wind with the moon's magnetosphere and may provide evidence on the lunar magnetic field strength. The lunar wake geometry is illustrated in Figure 41.

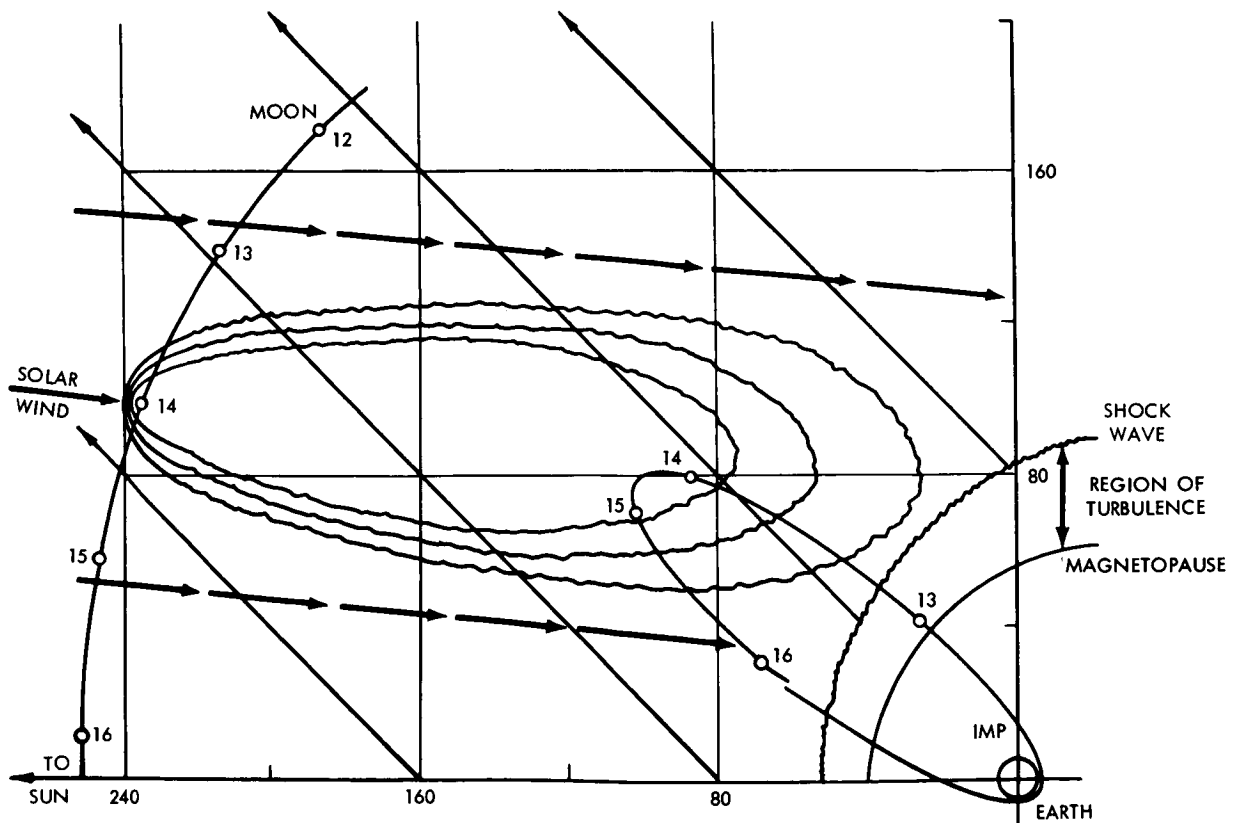


Figure 41—Interpretation of IMP I magnetic field data indicating characteristics of interplanetary and cislunar space and MHD wake of the moon at time of lunar magnetosphere detection. The distances are in thousand miles.

ACKNOWLEDGMENTS

The success of the magnetic field experiment is due in large part to the outstanding effort by the technical staff at Goddard Space Flight Center, the other experimenters and the IMP project staff in restricting the spacecraft fields to an absolute minimum. We are particularly indebted to those individuals without whose cooperation and contributions the final cleanliness of the spacecraft could not have been achieved. In addition the contributions of additional individuals too numerous to separately mention in the overall IMP spacecraft mission is hereby gratefully acknowledged.

REFERENCES

1. McCracken, K. G., "The Cosmic-Ray Flare Effect. I. Some New Methods of Analysis. II. The Flare Effects of May 4, November 12, and November 15, 1960. III. Deductions Regarding the Interplanetary Magnetic Field," *J. Geophys. Res.* 67(2):423-458, February 1962.
2. Coleman, P. J., Jr., Davis, L., and Sonett, C. P., "Steady Component of the Interplanetary Magnetic Field: Pioneer V," *Phys. Rev. Letters* 5(2):43-46, July 15, 1960.
3. Coleman, P. J., Jr., Sonett, C. P., and Davis, L., "On the Interplanetary Magnetic Storm: Pioneer V," *J. Geophys. Res.* 66(7):2043-2046, July 1961.
4. Greenstadt, E. W., "A Comparison of Preliminary Mariner 2 Plasma Data with Solar Wind Velocities Deduced from Pioneer V Magnetic Field Measurements," *J. Geophys. Res.* 69, 1964 (In press).
5. Parker, E. N., "Dynamics of the Interplanetary Gas and Magnetic Fields," *Astrophys. J.* 128(3): 664-676, November 1958.
6. Bonetti, A., Bridge, H. S., Lazarus, A. J., Rossi, B., and Scherb, F., "Explorer 10 Plasma Measurements," *J. Geophys. Res.* 68(13):4017-4064, July 1, 1963.
7. Neugebauer, M., and Snyder, C. W., "The Mission of Mariner II: Preliminary Observations. Solar Plasma Experiment," *Science*, 138(3545):1095-1096, December 7, 1962.
8. Snyder, C. W., Neugebauer, M., "Interplanetary Solar Wind Measurements by Mariner II," in: *Space Research IV: Proceedings 4th International Space Sciences Symposium* (In press).
9. Heppner, J. P., Ness, N. F., Scarce, C. S., and Skillman, T. L., "Explorer 10 Magnetic Field Measurements," *J. Geophys. Res.* 68(1):1-46, January 1, 1963.
10. Coleman, P. J., Davis, L., Smith, E. J., and Sonett, C. P., "The Mission of Mariner 2: Preliminary Observations, Interplanetary Magnetic Fields," *Science*, 138(3545):1099-1100, December 7, 1962.

11. Davies, R. D., Verschour, G. L., and Wild, P. A., "Measurement of Magnetic Fields in Interstellar Clouds," *Nature*, 196:563, November 10, 1962.
12. Bloom, A. L., "Principles of Operation of the Rubidium Vapor Magnetometer," *Applied Optics*, 1(1):61-6S, January 1962.
13. Ruddock, K. A., "Optically Pumped Rubidium Vapor Magnetometer for Space Experiments," in: *Space Research II: Proceedings 2nd International Space Sciences Symposium*: 692-700, New York: Interscience, 1961.
14. McKeehan, L. W., "Combinations of Circular Currents for Producing Uniform Magnetic Fields," *Rev. Sci. Instrum.* 7(3):150-153, March 1936.
15. Cahill, L. J., and Amazeen, P. G., "The Boundary of the Geomagnetic Field," *J. Geophys. Res.* 68(7):1835-1844, April 1, 1963.
16. Freeman, J. W., Van Allen, J. A., and Cahill, L. J., "Explorer 12 Observations of the Magnetospheric Boundary and the Associated Solar Plasma on September 13, 1961," *J. Geophys. Res.* 68(8):2121-2130, April 15, 1963.
17. Finch, H. F., and Leaton, B. R., "The Earth's Main Magnetic Field-Epoch 1955.0," *Monthly Notices Royal Astronom. Soc., Geophys. Suppl.* 7(6):314-317, November 1957.
18. Zhigulev, V. N., "On the Phenomenon of Magnetic 'Detachment' of the Flow of a Conducting Medium," *Soviet Phys. Doklady*, 4(3):514-516, December 1959.
19. Axford, W. I., "The Interaction between the Solar Wind and the Earth's Magnetosphere," *J. Geophys. Res.* 67(10):3791-3796, September 1962.
20. Gold, T., "Magnetic Storms," *Space Sci. Rev.* 1(1):100-114, June 1962.
21. Kellogg, P. J., "Flow of Plasma around the Earth," *J. Geophys. Res.* 67(10):3805-3812, September 1962.
22. Rossi, B., "Interplanetary Plasma," in: *Space Research III: Proceedings 3rd International Space Sciences Symposium*: 529-539, New York: Interscience, 1963.
23. Dessler, A. J., and Walters, G. K., "Hydromagnetic Coupling Between Solar Wind and Magnetosphere," *Planet. Space Sci.* 12(3):227-234, March 1964.
24. Walters, G. K., "Effect of Oblique Interplanetary Magnetic Field on Magnetosphere Shape and Behavior," *J. Geophys. Res.* 69, 1964 (In press).
25. Snyder, C. W., Neugebauer, M., and Rao, U. R., "The Solar Wind Velocity and its Correlation with Cosmic-Ray Variations and with Solar and Geomagnetic Activity," *J. Geophys. Res.* 68(24):6361-6370, 1963.

26. Maer, K., Jr., and Dessler, A. J., "Comment on Paper by Conway W. Snyder, et al., 'The Solar Wind Velocity and Its Correlation with Cosmic-Ray Variations and with Solar and Geomagnetic Activity,'" *J. Geophys. Res.* 69(13):2846, July 1, 1964.
27. Dessler, A. J., and Fejer, J. A., "Interpretation of K_p Index and M-Region Geomagnetic Storms," *Planet. Space Sci.* 11(5):505-511, May 1963.
28. Gold, T., "Magnetic Field in the Solar System," *Nuovo Cimento Suppl.* 13(1):318-323, 1959.
29. Gold, T., "Magnetic Field Configurations Near the Sun and in Interplanetary Space," *Proc. Pontifical Academy*, 431-457, 1963.
30. Alfvén, H., Danielsson, L., Falthammar, C. G., and Lindberg, L., "On the Penetration of Interplanetary Plasma into the Magnetosphere," 1963 (Preprint).
31. Chapman, S., and Ferraro, V. C. A., "New Theory of Magnetic Storms," *Terrest. Mag. Atoms. Elect.* 36:77-97, 171-186, June-September 1931.
32. Chapman, S., and Ferraro, V. C. A., "New Theory of Magnetic Storms," *Terrest. Mag. Atoms. Elect.* 37:147-156, 421-429, June-December 1932.
33. Chapman, S., and Ferraro, V. C. A., "New Theory of Magnetic Storms," *Terrest. Mag. Atoms. Elect.* 38:79-96, June 1933.
34. Ferraro, V. C. A., "On the Theory of the First Phase of a Geomagnetic Storm: A New Illustrative Calculation Based on an Idealized (Plane not Cylindrical) Model Field Distribution," *J. Geophys. Res.* 57(1):15-49, March 1952.
35. Ferraro, V. C. A., "An Approximate Method of Estimating the Size and Shape of the Stationary Hollow Carved Out in a Neutral Ionized Stream of Corpuscles Impinging on the Geomagnetic Field," *J. Geophys. Res.* 65(12):3951-3953, December 1960.
36. Ferraro, V. C. A., "Theory of Sudden Commencements and of the First Phase of a Magnetic Storm," *Rev. Modern Phys.* 32(4):934-940, October 1960.
37. Chapman, S., "Idealized Problems of Plasma Dynamics Relating to Geomagnetic Storms," *Rev. Mod. Phys.* 32(4):919-933, October 1960.
38. Chapman, S., "Solar Plasma, Geomagnetism and Aurora," in: *Geophysics: The Earth's Environment*, (C. DeWitt, J. Hieblot, and A. Lebeau, eds.): 373-502, New York: Gordon and Breach, Science Publishers, 1963.
39. Dessler, A. J., "The Stability of the Interface between the Solar Wind and the Geomagnetic Field," *J. Geophys. Res.* 66(10):3587-3590, October 1961.
40. Dessler, A. J., "Further Comments on Stability of Interface between Solar Wind and Geomagnetic Field," *J. Geophys. Res.* 67(12):4892-4994, 1962.

41. Hines, C. O., "The Magnetopause: A New Frontier in Space," *Science*, 141(3576):130-136, July 12, 1963.
42. Grad, H., "Boundary Layer between a Plasma and a Magnetic Field," *Phys. Fluids*, 4(11):1366-1375, November 1961.
43. Levy, R. H., Petschek, H. E., and Siscoe, G. L., "Aerodynamic Aspects of the Magnetospheric Flow," Avco-Everett Research Lab., Everett, Mass., Report no. RR170; AD 430410, December 1963.
44. De Hoffmann, F., and Teller, E., "Magneto-Hydrodynamic Shocks," *Phys. Rev.* 80:692-703, November 15, 1950.
45. Adlam, J. H., and Allen, J. E., "The Structure of Strong Collision-Free Hydromagnetic Waves," *Phil. Mag.* 3:448-455, May 1958.
46. Auer, P. L., Hurwitz, H., Jr., and Kilb, R. W., "Low Mach Number Magnetic Compression Waves in a Collision-Free Plasma," *Phys. Fluids*, 4(9):1105-1121, September 1961.
47. Auer, P. L., Hurwitz, H., and Kilb, R. W., "Large-Amplitude Magnetic Compression of a Collision-Free Plasma. II. Development of a Thermalized Plasma," *Phys. Fluids*, 5(3):298-316, March 1962.
48. Fishman, F. J., Petschek, H. E., and Kantrowitz, A., "Magneto-hydrodynamic Shock Wave in a Collision-Free Plasma," *Rev. Mod. Phys.* 32(4):959-966, October 1960.
49. Morawetz, C. S., "Magneto-hydrodynamic Shock Structure without Collisions," *Phys. Fluids*, 4(8):988-1006, August 1961.
50. Morawetz, C. S., "Modification for Magneto-hydrodynamic Shock Structure without Collisions," *Phys. Fluids*, 5(11):1447-1450, November 1962.
51. Morton, K. W., "Large-Amplitude Compression Waves in an Adiabatic Two-Fluid Model of a Collision-Free Plasma," *J. Fluid Mech.* 14(3):369-384, November 1962.
52. Bernstein, W., Fredricks, R. W., and Scarf, F. L., "A Model for a Broad Disordered Transition between the Solar Wind and the Magnetosphere," *J. Geophys. Res.* 69(7):1201-1210, April 1, 1964.
53. Morton, K. W., "Finite Amplitude Compression Waves in a Collision-Free Plasma," Courant Inst. of Mathematical Sciences, New York University, NYO-10434, January 15, 1964.
54. Beard, D. B., "The Interaction of the Terrestrial Magnetic Field with the Solar Corpuscular Radiation," *J. Geophys. Res.* 65(11):3559-3568, November 1960.
55. Davis, L., Jr., and Beard, D. B., "A Correction to the Approximate Condition for Locating the Boundary between a Magnetic Field and a Plasma," *J. Geophys. Res.* 67(11):4505-4507, October 1962.

56. Spreiter, J. R., and Briggs, B. R., "Theoretical Determination of the Form of the Boundary of the Solar Corpuscular Stream Produced by Interaction with the Magnetic Dipole Field of the Earth," *J. Geophys. Res.* 67(1):37-51, January 1962.
57. Spreiter, J. R., and Briggs, B. R., "Theoretical Determination of the Form of the Hollow Produced in the Solar Corpuscular Stream by Interaction with the Magnetic Dipole Field of the Earth," NASA Technical Report R-120, 1961.
58. Bridge, H. S., "Plasmas in Space," *Physics Today*, 16(3):31-37, March 1963.
59. Ness, N. F., "Observations of the Geomagnetic Cavity Boundaries," The Catholic University of America Symposium on Plasmas in Space, 1963 (To be published).
60. Spreiter, J. R., and Jones, W. P., "On the Effect of a Weak Interplanetary Magnetic Field on the Interaction between the Solar Wind and the Geomagnetic Field," *J. Geophys. Res.* 68(12): 3555-3564, June 15, 1963.
61. Hurley, J., "Interaction of a Streaming Plasma with the Magnetic Field of a Two-Dimensional Dipole," *Phys. Fluids*, 4(7):854-859, July 1961.
62. Midgley, J. E., and Davis, L., "Computation of a Bounding Surface of a Dipole Field in a Plasma by a Moment Technique," *J. Geophys. Res.* 67(2):499-504, February 1962.
63. Slutz, R. J., "Numerical Method for Calculating the Equilibrium Configuration of a Free-Surface Plasma," *Amer. Phys. Soc. Bull.* II 8(2):165, 1963.
64. Mead, G. D., and Beard, D. B., "Shape of the Geomagnetic Field Solar Wind Boundary," *J. Geophys. Res.* 69(7):1169-1179, April 1, 1964.
65. Lees, L., "Interaction between the Solar Plasma Wind and the Geomagnetic Cavity," New York Meeting of AIAA, January, 1964 (Preprint 64-88).
66. Beard, D. B., "The Effect of an Interplanetary Magnetic Field on the Solar Wind," *J. Geophys. Res.* 69(7):1159-1168, April 1, 1964.
67. Hida, K., "An Approximate Study on the Detached Shock Wave in Front of a Circular Cylinder and a Sphere," *Phys. Soc. Japan J.* 8:740-745, November-December 1953.
68. Obayashi, T., "Interaction of Solar Plasma Streams with the Outer Geomagnetic Field," *J. Geophys. Res.* 69(5):861-867, March 1, 1964.
69. Axford, W. I., and Hines, C. O., "A Unifying Theory of High-Latitude Geophysical Phenomena and Geomagnetic Storms," *Canad. J. Phys.* 39(10):1433-1464, October 1961.
70. Harrison, E. R., "The Earth's Distant Magnetic Field," *Geophys. J.* 6(4):479-492, June 1962.
71. Hones, E. W., Jr., "Motions of Charged Particles Trapped in the Earth's Magnetosphere," *J. Geophys. Res.* 68(5):1209-1220, March 1, 1963.

72. Johnson, F. S., "The Gross Character of the Geomagnetic Field in the Solar Wind," *J. Geophys. Res.* 65(10):3049-3051, October 1960.
73. Mead, G. D., "Deformation of the Geomagnetic Field by the Solar Wind," *J. Geophys. Res.* 69(7):1181-1195, April 1, 1964.
74. Petschek, H. E., "Magnetic Field Annihilation," Avco-Everett Research Lab., Everett, Mass., AMP-123; AD-425751, October 1963.
75. Biermann, L., "Kometenschweife und solare Korpuskularstrahlung," *Z. Astrophys.* 29(3):274-286, September 1951.
76. Dolginov, S. S., Eroshenko, E. G., Zhuzgov, L. N., Pushkov, N. V., and Tyurmina, L. O., "Magnetic Measurements with the Second Cosmic Rocket," in: *"Artificial Earth Satellites,"* 5:490-502, New York: Plenum Press, 1961.
77. Neugebauer, M., "Question of the Existence of a Lunar Magnetic Field," *Phys. Rev. Letters*, 4(1):6-8, January 1, 1960.

N65-29558

THEORETICAL STUDIES OF PROTONS IN THE OUTER RADIATION BELT

by

M. P. Nakada, J. W. Dungey* and W. N. Hess

Goddard Space Flight Center

SUMMARY

The variations in the energy spectra with pitch angle and L of the relatively stable 0.1 to 5 Mev protons in the outer radiation belt have been found to be in good agreement with the results of a model that permits rapid motion of the protons in L space. In this model, the protons violate the third adiabatic invariants. Changes in fluxes with L are not consistent with Liouville's theorem. Both the departure from Liouville's theorem and variations in energy spectra seem to indicate that the source of these protons is at large L.

29558

Rush

INTRODUCTION

In the $L = 2$ to 5 range in the outer radiation belt, Davis, Hoffman, and Williamson (Reference 1) found that the spectra of the relatively stable 0.1 to 5 Mev protons show smooth but large variations with L and equatorial pitch angle α_0 . Protons near the earth and at α_0 near 90° are more energetic than those at larger L and at smaller α_0 . The spectra are well represented by ϱ^{-E/E_0} ; E_0 varies by about a factor of 10 with L and by a factor of 2 with α_0 . In this study a model is proposed for the explanation of these spectral variations.

Kellogg (Reference 2) first suggested that the radiation belt might be formed through magnetic disturbances in which the third adiabatic invariant of trapped particles is violated without violating the first and second invariants. Violation of the third invariant allows motion in L-space. As particles move closer to the earth they tend to gain energy with the maintenance of the 1st invariant since, for example, E/B is a constant for 90° pitch angles. Thus this process can accelerate the protons. Kellogg's suggestion has been adopted for this study although the mechanism for motion in L-space is unspecified. It has further been assumed that motion in L-space is rapid compared to loss and scattering processes and that the geomagnetic field is sufficiently well represented by a dipole.

*Imperial College, London, England.

ENERGY AND ANGLE VARIATIONS

If the first and second adiabatic invariants of trapped particles are maintained during motion in L-space, changes in both the energy and equatorial pitch angle can be calculated. The first invariant is

$$\mu = \frac{E \sin^2 \alpha_0}{B_0} = \frac{EL^3 \sin^2 \alpha_0}{.312} , \quad (1)$$

where B_0 is the equatorial magnetic field. The second invariant is:

$$J = m \oint v \cos \alpha \, dS \quad (2)$$

where m is the mass, v the velocity, α the local pitch angle and S is along the guiding center. The integration is over a complete north-south oscillation. For a dipole magnetic field, Equation 2 becomes

$$J = v L F(\alpha_0) ,$$

with

$$F(\alpha_0) = 4m r_e \int_0^{\lambda_m} \sqrt{\left[1 - \frac{\sin^2 \alpha_0 (4 - 3 \cos^2 \lambda)^{\frac{1}{2}}}{\cos^6 \lambda} \right]} (4 - 3 \cos^2 \lambda) \cos \lambda \, d\lambda , \quad (3)$$

where r_e is the radius of the earth, λ is the latitude, and λ_m is the mirror latitude.

Since μ and J are constants, Equation 1 may be divided by the square of Equation 3 to give

$$L \left[\frac{\sin \alpha_0}{F(\alpha_0)} \right]^2 = \text{constant} . \quad (4)$$

From this, the changes in α_0 with respect to L can be evaluated as seen in Figure 1. Two features of these results are worthy of note: (1) Changes in α_0 with L are relatively small for $L > 2.5$ and, as Davis and Chang (Reference 3) have indicated, particles diffusing inwards assume flatter helices; and (2) Changes in α_0 with L are independent of energy for non-relativistic particles.

These changes in α_0 with L and Equation 1 may be used to find the variation in energy with L and α_0 . Results are shown in Figure 2 for protons having α_0 values at $L = 7$ as indicated on the curves. The energies shown are relative to energies at $L = 7$.

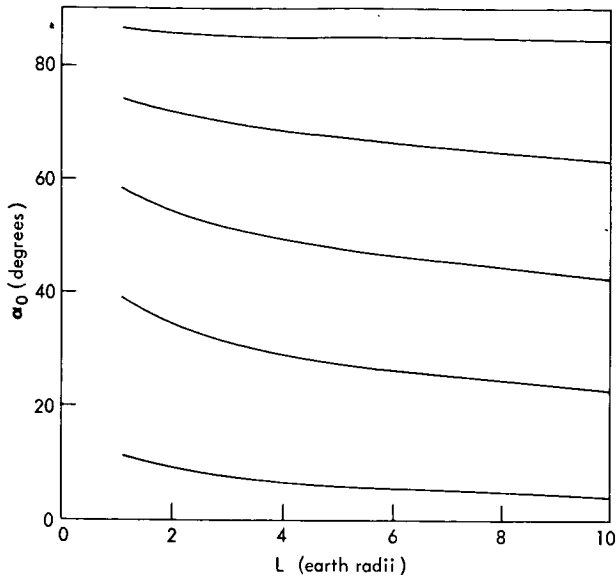


Figure 1—Variation in equatorial pitch angle with L when μ and J are constant.

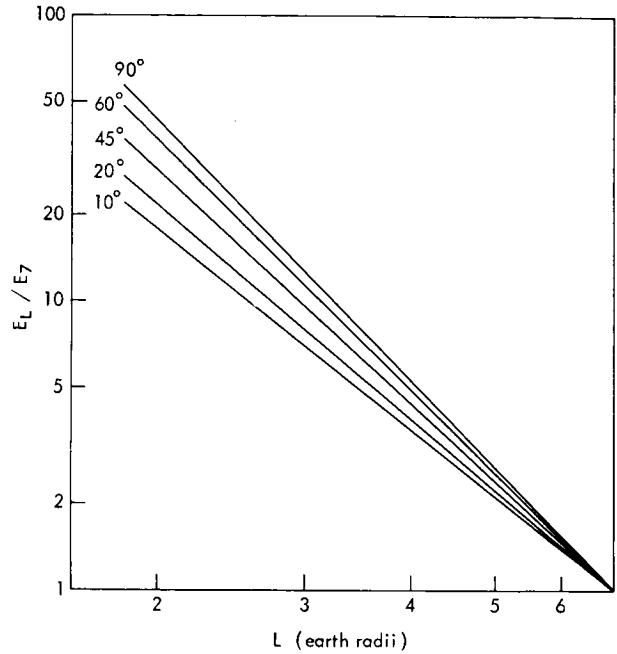


Figure 2—Relative variation in proton energy with L when μ and J are constant.

COMPARISON OF SPECTRA WITH EXPERIMENTAL RESULTS

The proton spectrum that we would expect at some L and α_0 depends on the location and nature of the source and on the energy dependence of motion in L-space. The source is assumed to be at a single L and to consist of a single proton spectrum. The result of the superposition of sources at different L and of different spectra can be obtained by using the above assumption. The energy dependence of motion in L-space has been examined for two processes where the third invariant only is violated. When the violation mechanism involves electric fields, the velocity of L-space motion is proportional to the vector product of the electric and the magnetic fields and does not depend on particle energy. Another process that violates only the third invariant depends on asymmetric distortions of the geomagnetic field such as those occurring with sudden commencements and sudden impulses (Reference 4). Motion in L-space for this process depends on the guiding center of particles following magnetic field lines during rapid changes in the field and is also independent of energy. Thus the motion in L-space, when only the third invariant is violated, appears to be independent of energy.

With the above results and assumptions and the results and assumption of the previous sections, changes in spectra for motion in L-space are readily obtained. If the injection spectrum is a power law, the spectrum remains a power law with the same exponent. If the injection spectrum has an exponential form, e^{-E/E_0} , the spectrum remains exponential after L-space motion and E_0 varies in the same way with L and α_0 as has been calculated for a single particle in the previous section.

These two predictions of the model may be compared with experiment. The first prediction, that the spectrum retains its exponential form, is in agreement with experiment. To test the second prediction, measured E_0 (Reference 1) have been plotted in Figure 3 as a function of L with appropriate changes in α_0 with L . The labels on these curves refer to values of α_0 at $L = 7$. The dashed curves in Figure 3 are taken from Figure 2 for corresponding changes in E with L and α_0 . This comparison, too, shows good agreement between the model and experimental results.

If the dashed curves in Figure 3 are extended, they intersect near $L = 10$. This intersection is the L value where the spectrum is independent of α_0 and therefore may be interpreted as the source location.

COMPARISON WITH LIOUVILLE'S THEOREM

Thus far only the spectra of particles have been compared with the model. Now, the fluxes in L -space will be compared with predictions of Liouville's theorem to see what might be learned about the mechanisms of L -space motion. With motion in L -space, the fluxes may: (1) Obey Liouville's theorem; (2) Obey Liouville's theorem but be altered by loss processes; (3) Not obey Liouville's theorem. The third possibility could occur, for example, if motion in L -space is due to diffusion.

The measured directional fluxes, $j(L, E, \alpha_0)$, have been given in units of particles/cm²-sec-ster-Mev (Reference 1). If Liouville's theorem were to hold, the conserved quantity is j/E . In the comparison between measurements and Liouville's theorem both E and α_0 are varied with L as is appropriate for following a particle's trajectory when the first two adiabatic invariants are maintained.

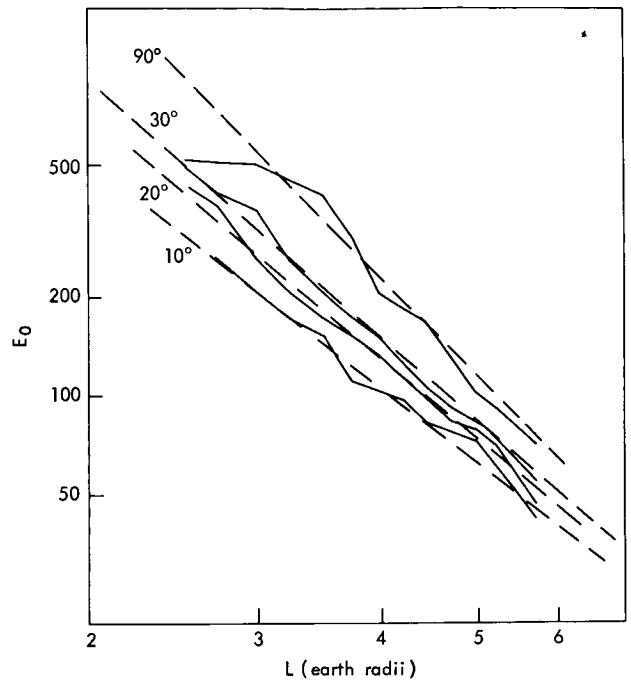


Figure 3—Comparison between measured and predicted variations in E_0 with L and α_0 .

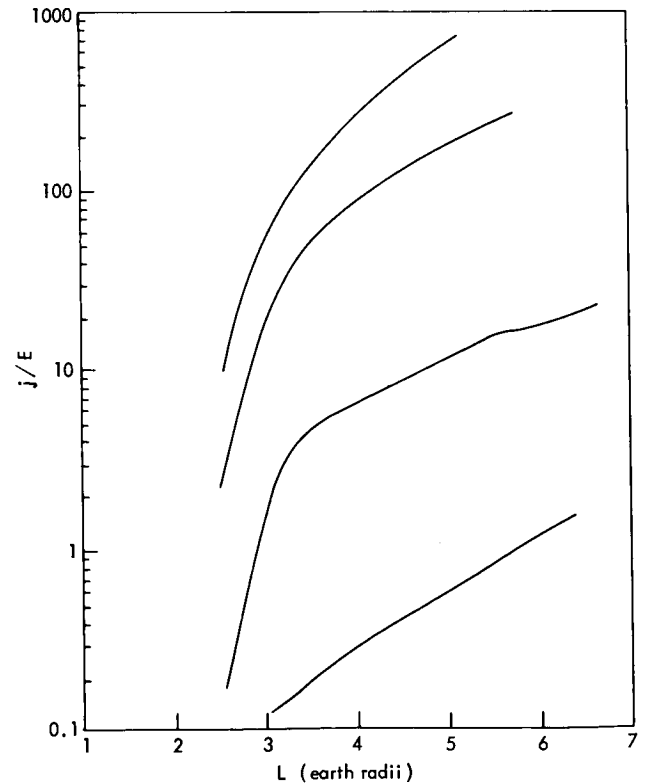


Figure 4—Relative variation of j/E with L .

Figure 4 shows results which are typical of the experimental data. Since j/E is not conserved, the first possibility above is ruled out.

An interesting feature of Figure 4 is the fact that j/E increases monotonically with L . This also indicates that the source is at large L .

CONCLUSIONS

In this study a rather simple model has been found which successfully explains spectral changes of the protons in the outer radiation belt with respect to L and α_0 . The trends in the variations in the spectra and in comparison of fluxes with Liouville's theorem both indicate that the source is near the edge of the magnetosphere. According to this model, the protons are moved within the outer radiation belt and accelerated by some mechanism that violates the third adiabatic invariant of charged particle motion without violating the first two invariants. Since these fluxes do not obey Liouville's theorem, the mechanism is of the diffusion type or one where losses must be considered along with the motion of fluxes obeying Liouville's theorem.

REFERENCES

1. Davis, L. R., Hoffman, R. A., Williamson, J. M., "Observations of Protons Trapped Above 2 Earth Radii," (abstract) *Trans. American Geophysical Union*, 45(1):84, March 1964; Presented at the 45th Annual Meeting American Geophysical Union, April 21-24, 1964, Washington, D. C.
2. Kellogg, P. J., "Van Allen Radiation of Solar Origin," *Nature*, 183:1295-1297, May 9, 1959.
3. Davis, L., Jr., and Chang, D. B., "On the Effect of Geomagnetic Fluctuations on Trapped Particles," *J. Geophys. Res.* 67(6):2169-2179, June 1962.
4. Parker, E. N., "Geomagnetic Fluctuations and the Form of the Outer Zone of the Van Allen Radiation Belt," *J. Geophys. Res.* 65(10):3117-3130, October 1960.

N65-29559

SOLAR CYCLE CHANGES IN INNER ZONE PROTONS

by

Robert C. Blanchard*

and

Wilmot N. Hess

Goddard Space Flight Center

SUMMARY

Time dependent calculations of the inner Van Allen belt proton population show that large changes of the population, up to a factor of 50, will take place during the solar cycle. The effect is most pronounced for the region of B-L space corresponding to minimum altitudes of 300-700 km. Because different energy protons respond to the changing solar cycle at different rates the proton energy spectra will change with time also.

29559



INTRODUCTION

The purpose of this paper is to calculate the expected changes in inner zone proton populations with time in the solar cycle.

Freden and White (Reference 1) identified the penetrating component of the inner zone of the Van Allen belt as that due to energetic protons and measured the energy spectrum of the protons of $E > 75$ Mev. This and subsequent experimental work on Atlas rockets (References 2, 3, and 4) has confirmed and extended this finding and we now have a well established proton energy spectrum at $L \sim 1.4$, $B \sim .20$ (which is about apogee for these flights) for near solar maximum (Figure 1). The analysis of the spectrum (Reference 2) has shown conclusively that the protons are produced by neutron decay.

One feature of this radiation belt component is the time constancy. Measurements after a solar flare (Reference 3) gave essentially the same fluxes of protons as before the flare. For $L > 1.6$ changes in proton spectra are seen (References 5 and 6) to be associated with solar proton events (Reference 7). These may be explainable in terms of neutrons produced in the polar regions by solar protons (References 8 and 9). For $L < 1.6$ only gradual changes in the proton populations have been observed on Explorer VII (Reference 7). It was originally suggested (Reference 7) that such changes implied that neutrons could not produce all inner zone protons but this does

*Done as partial fulfillment of the requirements for a Master's Degree from the College of William and Mary.

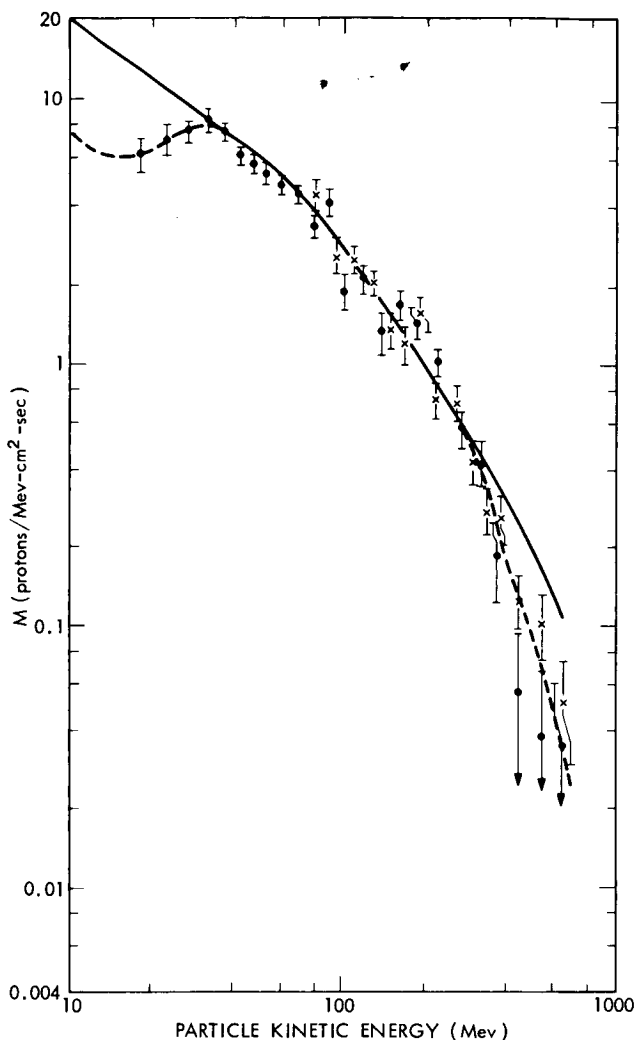


Figure 1—The experimentally measured inner zone proton energy spectrum (Reference 3) for $L \sim 1.4 B \sim .20$.

not seem to be the case. Hess (Reference 10) showed that slow changes in proton population were expected due to changes in the galactic cosmic ray flux during the solar cycle and, more importantly, due to changes in the upper atmospheric density during the solar cycle. We will now make a quantitative discussion of the expected changes in proton populations for $L < 1.6$.

The continuity equation for protons is usually written (References 2, 11, and 12):

$$\frac{dN(E)}{dt} = +S(E) - L(E) + \frac{d}{dE} \left[N(E) \frac{dE}{dx} v \right] = 0, \quad (1)$$

and this is solved for the steady state population of protons $N(E)$. However, we are now interested in time variations so we shall write this equation in its time dependent form:

$$\frac{dN(E, t)}{dt} = +S(E, t) - L(E, t) + \frac{d}{dE} \left[N(E, t) \frac{dE}{dx} (t) v \right] \quad (2)$$

The source term $S(E, t)$ will use the neutron decay source strength of Hess (Reference 11) for solar maximum $S(E)$ multiplied by a function of time $f(t)$ to consider the solar cycle variation in galactic cosmic ray flux as determined by McDonald and Webber (Reference 13):

$$S(E, t) = S(E) f(t) = \frac{0.8E^{-2.0}}{\nu_\gamma T_n} \frac{r_e^3}{r} f(t), \quad (3)$$

where $f(t)$ varies from 1.0 at solar maximum to 1.25 at solar minimum in a way similar to that of Figure 2.

For the loss term $L(E, t)$ following Freden and White (Reference 2) we consider nuclear collisions:

$$L(E, t) = N(E, t) v \sum_i \sigma_i \bar{\rho}_i(t), \quad (4)$$

where $\bar{\rho}_i(t)$ is the average atmospheric density of atmospheric component i (O_2 , O , N_2 or He) and σ_i is the inelastic cross section for collisions (assumed geometric).

The last term in Equation 2, the change in proton population due to slowing down, varies with the solar cycle due to the atmospheric density change:

$$\frac{dE}{dx} = \left[\frac{\bar{\rho}(t)}{2.69 \times 10^{19}} \right] \cdot \left. \frac{dE}{dx} \right|_{NTP} \quad (5)$$

where $\bar{\rho}(t)$ is the average atmospheric density of equivalent oxygen atoms. The variation of $\bar{\rho}_i(t)$ and $\bar{\rho}(t)$ with time in the solar cycle is the major reason for the change in proton population.

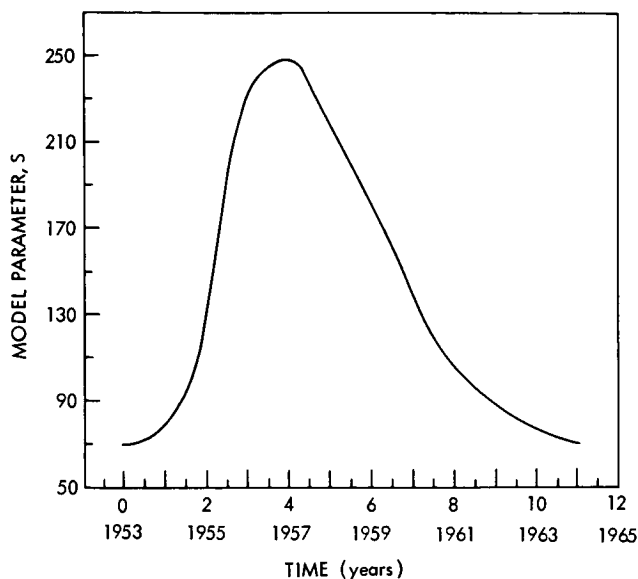


Figure 2—Solar cycle used in these calculations S is the Harris and Priester (References 14 and 15) model parameter which is related to but not the same as the 10 cm flux intensity.

AVERAGE ATMOSPHERIC DENSITIES

A major part of this problem was to determine the average atmospheric densities used in calculating the loss rate of trapped protons by coulomb scattering. To do this the theoretical model of the upper atmosphere developed by Harris and Priester (References 14 and 15) was used. This model gives the time dependences of the atmosphere for both solar cycle and diurnal variations. It agrees well with several measurements of density by satellite drag (References 16 and 17) and recently has been checked by preliminary density data from the Explorer XVII satellite (Reference 18). This model atmosphere is the most complete description of the time dependence of atmospheric densities available and agrees well with the current experimental data. We must perform several operations on the H and P model data to get it in form to use for this problem. Harris and Priester give the atom densities n_i of the several atmospheric constituents i in the form

$$n_i(h, t, S)$$

where h is altitude above the earth, t local time, and S a model parameter related to, but not the same as, the intensity of the average 10-cm solar flux \bar{F} , in $\text{watts/m}^2\text{-cps} \times 10^{-22}$. Recent studies of atmospheric densities (Reference 19) show that the model number S is the same as \bar{F} near solar maximum but near solar minimum $S > \bar{F}$. For example, $\bar{F} = 70$ corresponds to the model $S = 100$. Figure 2 shows the solar cycle variation of S we have used based on the last solar cycle.

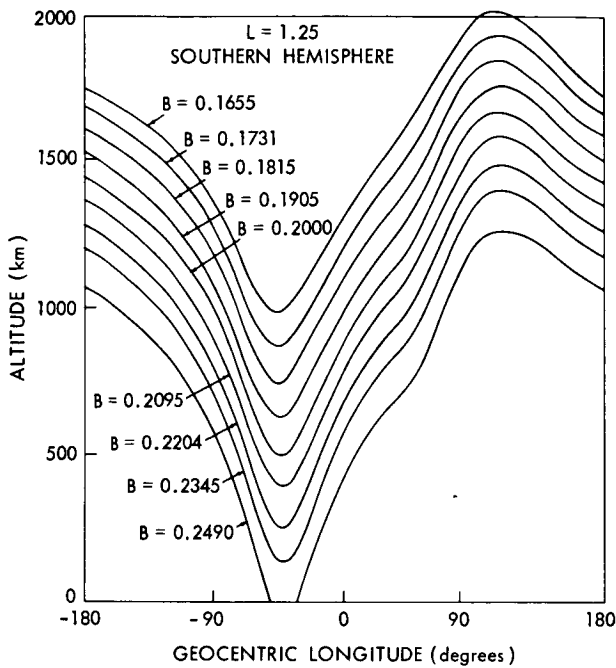


Figure 3—Variation of the altitude of B-L rings with longitude.

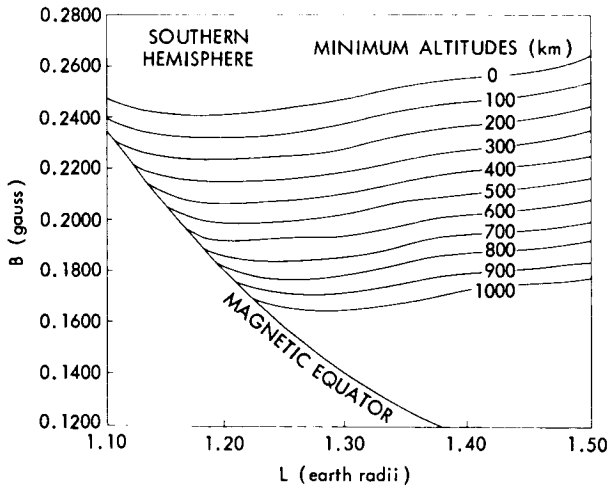


Figure 4—B-L map of minimum altitudes.

missible to average the density in this fashion. A dipole field is assumed in carrying out this step. Ray (Reference 20) gave the bounce averaging process as

$$\rho = \frac{\int \rho(\lambda) ds}{\int ds}, \quad (6)$$

The first operation on the H and P atmosphere is to average over local time. The protons we shall consider live long enough so that they will encounter the midday density bulge and the nighttime minimum many times and will average them out.

Secondly, we shall perform a longitude average. As the particles drift around the earth, their mirror points do not stay at constant altitude but rather follow a certain path in B-L space. Several such constant B-L rings are shown in altitude-longitude coordinates (Figure 3). The particles dip lowest in the South Atlantic due to the nature of the earth's magnetic field. A B-L map of minimum altitudes is shown in Figure 4. Due to the variation in altitude of the protons' mirror point, longitude averages were made using the B-L rings every ten degrees in both northern and southern hemispheres. This step gives the average mirror point density for a proton's motion. Walt has recently shown that the protons do not drift in longitude at a constant rate because of the variation of the magnetic field gradient and field line curvature. This effect is ignored here. It probably amounts to about a 20 percent correction on average densities. Values atmospheric densities are not known that well now anyway.

The third operation on the H and P atmosphere is to average over a bounce from one mirror point to the conjugate mirror point. Since the protons live much longer than a bounce period, and since no change in direction of the proton is considered during slowing, it is per-

where the element of length along the particle's orbit is

$$ds = \frac{v dt}{\cos \alpha} = \frac{d\ell}{\cos \alpha}, \quad (7)$$

where $d\ell$ is the element of length along the field line. Using

$$d\ell^2 = dr^2 + r^2 d\lambda^2 \quad (8)$$

and

$$r = L \cos^2 \lambda \quad (9)$$

with the mirror equation and the expression for the magnetic field variation along a field line and combining and substituting in Equation 6, we obtain

$$\bar{\rho}_i = \frac{\int \rho_i(\lambda) A(\lambda) d\lambda}{\int A(\lambda) d\lambda}, \quad (10)$$

where

$$A(\lambda) = \frac{\cos^4 \lambda (1 + 3 \sin^2 \lambda)}{\left[\cos^6 \lambda (1 + 3 \sin^2 \lambda_m)^{1/2} - \cos^6 \lambda_m (1 + 3 \sin^2 \lambda) \right]^{1/2}}. \quad (11)$$

Here, the subscript m corresponds to the particles' mirror point. This bounce averaged density has been integrated on a computer.

The last step is to combine the five i constituents N_2 , O_2 , O , He, and H to give the averaged number of equivalent oxygen atoms:

$$8 \bar{\rho} = 14 \bar{\rho}(N_2) + \bar{\rho}(O) + 16 \bar{\rho}(O_2) + 2 \bar{\rho}(He) + \bar{\rho}(H) \quad (12)$$

Values of $\bar{\rho}$ at different times in the solar cycle for $L = 1.25$ are shown in Figure 5.

We can use the data on the rate of energy loss dE/dx for oxygen at NTP (Reference 21) in Equation 5 with this averaged density $\bar{\rho}$ to calculate the loss rate.

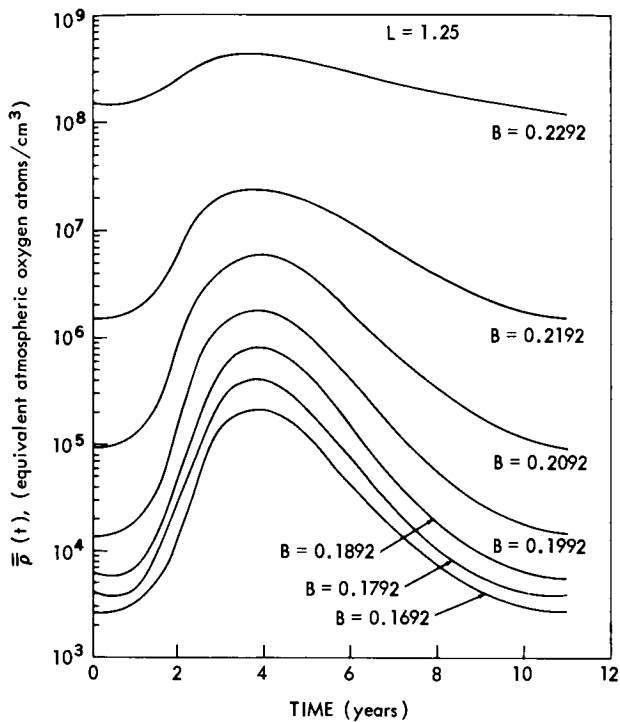


Figure 5—Average atmospheric densities at different times of the solar cycle at different B-L points.

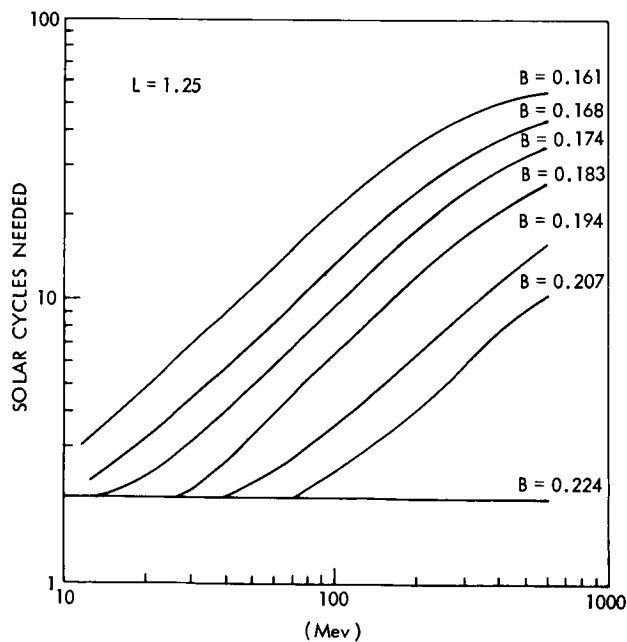


Figure 6—The number of solar cycles needed for a group of protons to come within 1 percent of its final oscillating population for $L = 1.25$ starting with $N(E) = 0$ at $t = 0$.

RESULTS

Equation 2 is integrated stepwise starting with $N(E) = 0$ at $t = 0$ to build up to an oscillating proton population which is the same from one solar cycle to the next. In Figure 6 is shown the number of solar cycles after which the population change per cycle is less than 1 percent for $L = 1.25$. After achieving this final condition the proton energy spectrum varies during one solar cycle as shown in Figures 7-11; the dashed curves in these figures are what the proton spectrum would be if steady state

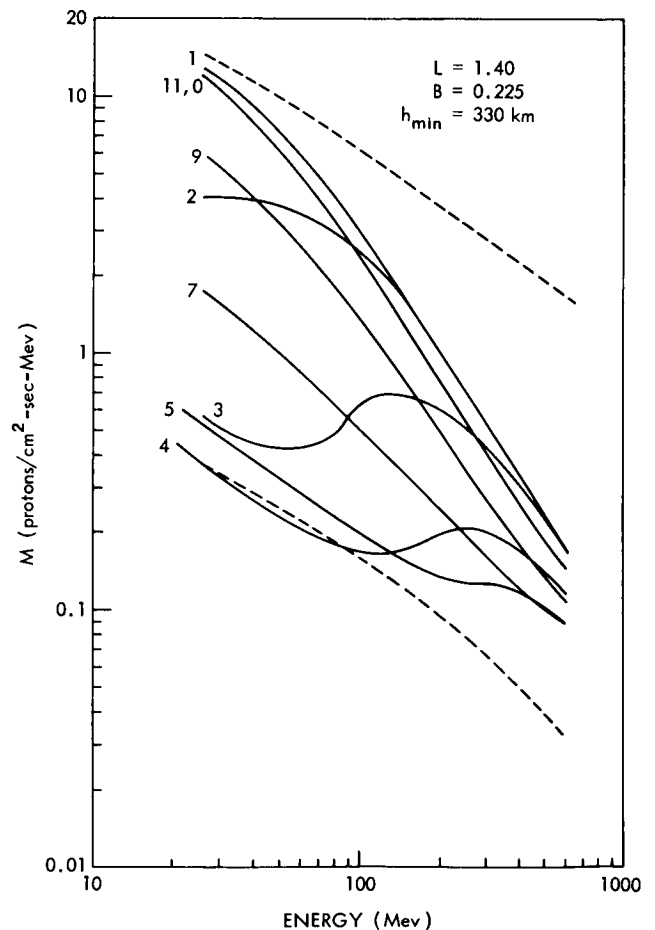


Figure 7—Proton energy spectra at different times in the solar cycle for $L = 1.40$, $B = .225$; the curves are labeled by the time in years from solar minimum.

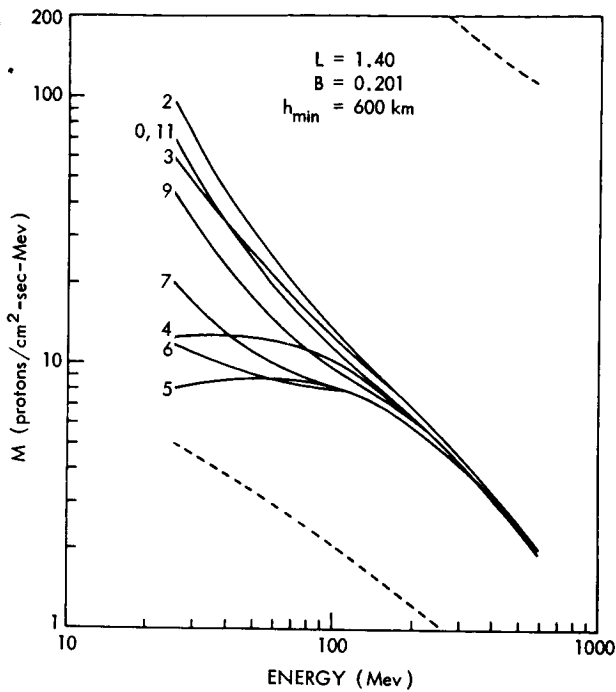


Figure 8—Proton energy spectra at different times in the solar cycle for $L = 1.40$, $B = .201$; the curves are labeled by the time in years from solar minimum.

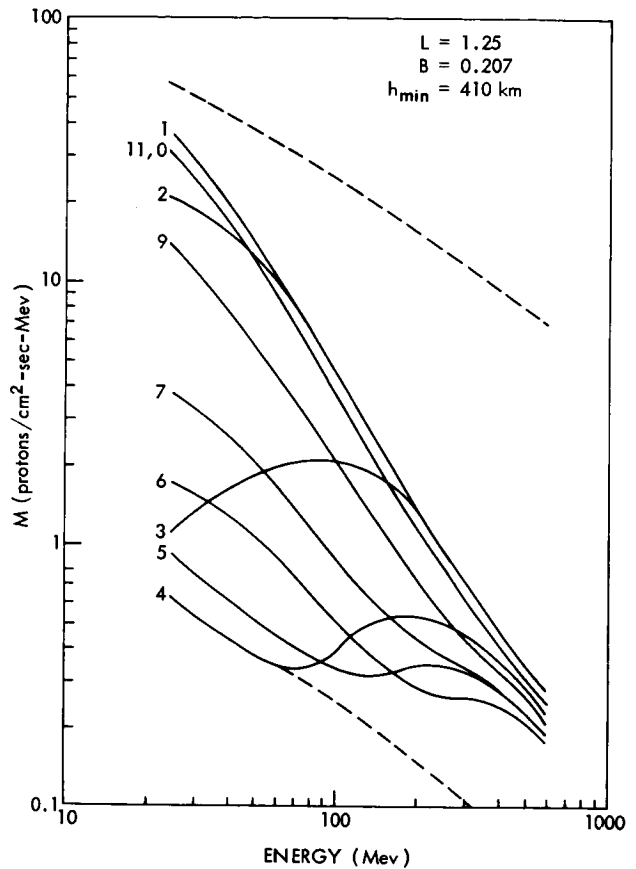


Figure 10—Proton energy spectra at different times in the solar cycle for $L = 1.25$, $B = .207$; the curves are labeled by the time in years from solar minimum.

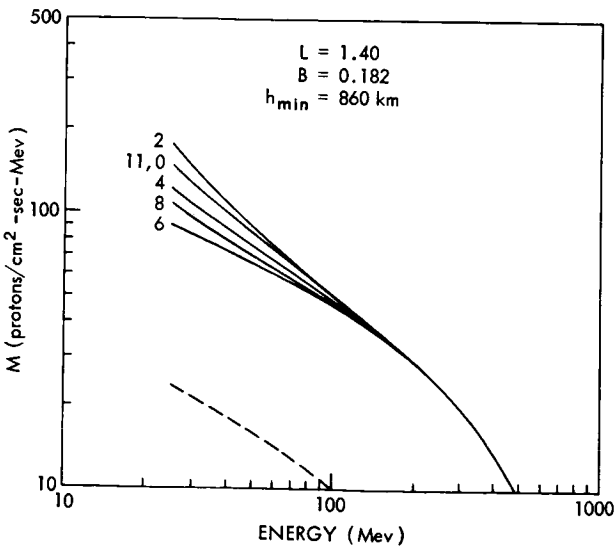


Figure 9—Proton energy spectra at different times in the solar cycle for $L = 1.40$, $B = .181$; the curves are labeled by the time in years from solar minimum.

conditions were achieved at solar maximum and solar minimum. Steady state clearly is not achieved for high energy protons or for high altitudes.

It is also interesting that this calculation predicts a spectral peak above 100 Mev for certain conditions (Figure 7, Year 3) owing to the time lag in different energy protons adjusting to solar cycle changes.

Figures 12 and 13 show time histories for various conditions. Large variations from solar maximum to solar minimum populations are seen in these figures. The amplitude of these changes for $L = 1.25$ and 1.40 are shown in Figures 14 and 15.

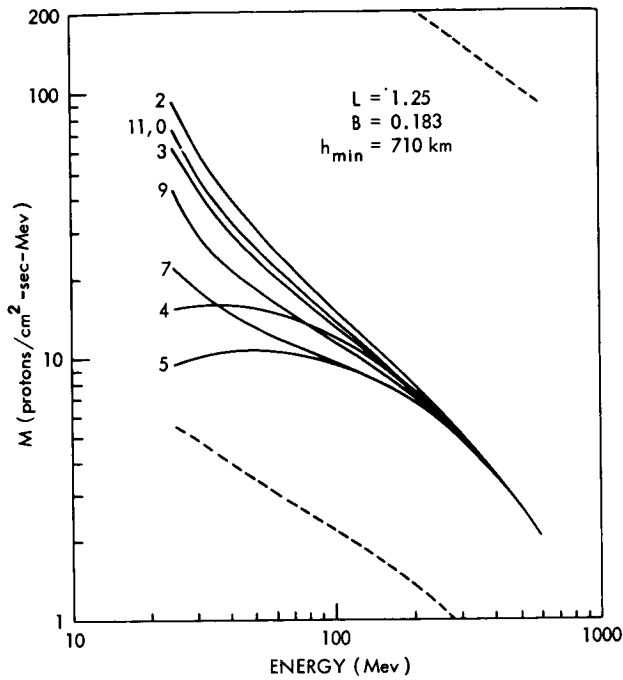


Figure 11—Proton energy spectra at different times in the solar cycle for $L = 1.25$, $B = .183$; the curves are labeled by the time in years from solar minimum.

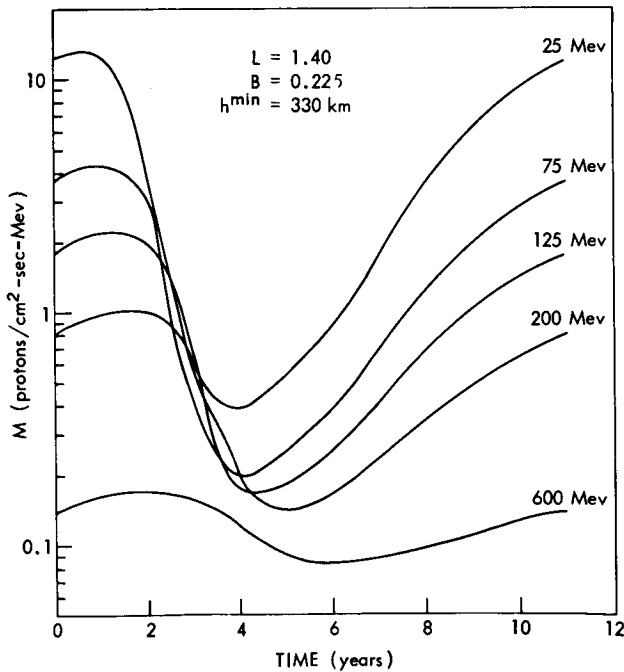


Figure 12—Proton time histories for $L = 1.40$, $B = .225$.

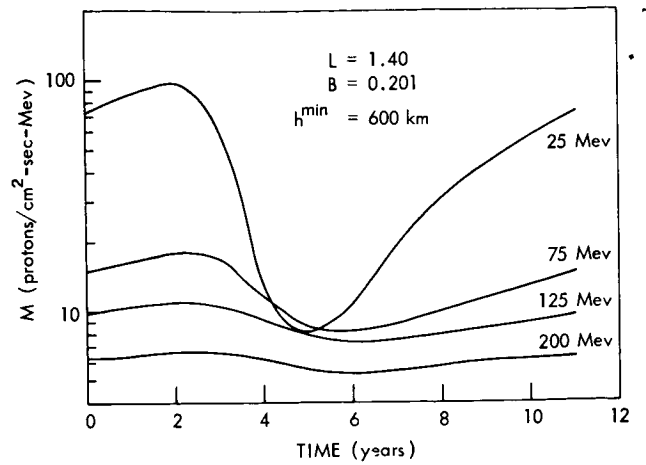


Figure 13—Proton time histories for $L = 1.40$, $B = .201$.

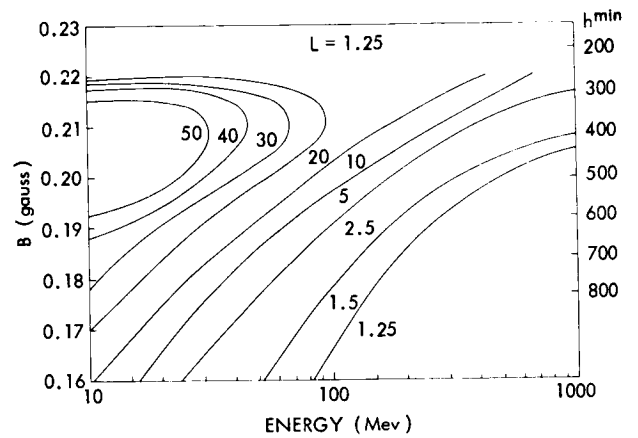


Figure 14—The amplitude of the proton population change during the solar cycle for $L = 1.25$.

A comparison of past experimental results and the calculations of this paper is shown in Table 1. In discussing these experiments we can consider three types of information.

In comparing time changes of the proton fluxes two situations occur:

1. Some individual experiments run long enough (a year or more) so that they should see proton flux changes directly. From Table 1, Experiments c and d are of this type. Although in Experiment d

it is not one experiment on one satellite, it is many identical experiments on essentially identical satellites, and therefore this experiment falls in this category.

2. Different experiments on different satellites can be compared to provide data on proton flux changes. Data of this type is given in Experiments a, e, and f of Table 1.

The third type of data is given by:

3. Direct measurement of the proton energy spectrum in one experiment. Experiments a, b, e, f, and g are of this type.

In comparing flux time change experiments of Type 1 with the calculations, the agreement is good. Two experiments covering the period 1959 to 1962 give results consistent with the calculations.

Comparison with Type 2 data does not work as well. The observed changes of flux with time agree qualitatively with those predicted but not quantitatively. The experimental flux ratios are smaller than the calculated ones. Two remarks are in order here. First, Type 2 data usually has larger errors attached to it than Type 1 because it involves the systematic errors of two experiments while Type 1 data involves no systematic errors—only statistical errors are involved in the time variations in the flux. Because of this the experimental flux ratios using Type 2 data are probably not as accurate as those using Type 1 data. Secondly all the comparisons of Type 2 data involve Explorer IV data; so there is no independent check of experimental consistency.

We may have over-estimated the amplitude of the change of proton populations in this present calculation by as much as a factor of two because our solar cycle model uses $S = 70$ at solar minimum while recent data of Harris and Priester (Reference 19) shows that $S = 100$ is probably more appropriate. Changing the shape of the model solar cycle (Figure 2) will also affect the results of the calculation. The solar cycle must rise more rapidly towards solar maximum than it falls to solar minimum in order to produce the changes in spectrum calculated herein. Solar cycle 16 was quite symmetrical and should not give the calculated results.

Of the five experiments of Type 3 that help understand the proton energy spectrum the first two, a and b, in 1960 showed a modest sized peak at about $E = 40$ Mev. The more recent experiment, g, of Rowland et al. (Reference 22) in 1962 shown in Figure 16 does not show such a peak. The solid curve on Figure 16 compared with the data of Rowland is the normalized results of the present calculations. The agreement is fairly good. Recent experiments f and g show a large low energy proton population but cannot be compared with early experiments because the early ones

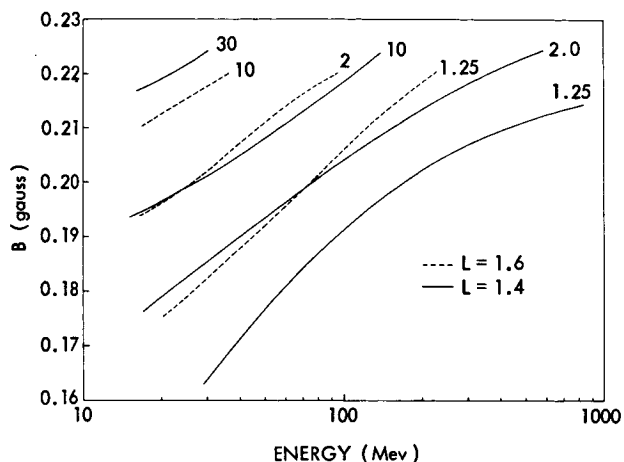


Figure 15—The amplitude of the proton population change during the solar cycle for $L = 1.4$ and 1.6 .

Table 1
Experimental Data on Proton Spectra.

Experiment	Date of Experiment	Time in Solar Angle	L	B	H Minimum (km)	Results of Experiment	Predictions from Present Paper
(a) Naugle and Kniffen (1963)—Emulsions on NERV	Sept., 1960	6.7	(a) 1.54 (b) 1.47	.209	610	Spectrum ~ flat from 20 to 60 Mev $\frac{J_0(31)}{J_0(31)}$ at 6.7 $\frac{J_0(31)}{J_0(31)}$ at 4.1 (Exp. IV) ~ k	Spectrum should fall about a factor of 3 in this energy range (Figure 8, curve 7) $\frac{J_0(31)}{J_0(31)}$ at 6.7 = 1.3 (Figure 8) $\frac{J_0(31)}{J_0(31)}$ at 4
(b) Freden and White (1962)—Emulsions on Atlas	1960	6.5	~1.40	~.202	600	Spectrum ~ flat from 20 to 100 Mev $\frac{J_0(31)}{J_0(31)}$ at 6.7 $\frac{J_0(31)}{J_0(31)}$ at 4.1 (Exp. IV) ~ 2.5	Spectrum should fall about a factor of 4 in this energy range (Figure 7, curve 7) $\frac{J_0(31)}{J_0(31)}$ at 6.7 = 3.5 (Figure 7) $\frac{J_0(31)}{J_0(31)}$ at 4
(c) Pizzella, McIlwain and Van Allen—GM counter on Explorer VII	Oct. 1959 to Dec. 1960	5.8 to 7.0	1.40	.22	390	Spectrum peaks at ~40 Mev $\frac{J_0(20)}{J_0(40)}$ ~ .75 $\frac{J_0(40)}{J_0(40)}$ ~ .75	No spectral peak at t = 6.5 (Figure 8) $\frac{J_0(20)}{J_0(40)}$ ~ 2.0 $\frac{J_0(40)}{J_0(40)}$ ~ 2.0 but at t = 5 do have spectral peak $\frac{J_0(20)}{J_0(40)}$
(d) Filz and Yagoda—Emulsions on Discover	Dec. 1960 to June 1962	7.0 to 8.5	varying	varying	400	$\frac{J_0(E > 18)}{J_0(E > 18)}$ at 7.0 ~ 2.3 $\frac{J_0(E > 18)}{J_0(E > 18)}$ at 6.0 ~ 2.3	$\frac{J_0(E = 25)}{J_0(E = 25)}$ at 7.0 = 2.0 (Figure 12) $\frac{J_0(E = 25)}{J_0(E = 25)}$ at 6.0
(e) Heckman and Nakano—Emulsions on Low altitude polar satellites	Sept. 1962 to Sept. 1963	8.7 to 9.7	varying	varying	400	$\frac{J_0(65)}{J_0(65)}$ at 8.5 ~ 2.0 $\frac{J_0(65)}{J_0(65)}$ at 7.0 $\frac{J_0(65)}{J_0(65)}$ at 9.5 = 1.0 + .10 $\frac{J_0(65)}{J_0(65)}$ at 9.0 $\frac{J_0(65)}{J_0(65)}$ at 9.5 $\frac{J_0(65)}{J_0(65)}$ at 4.1 (Exp. IV) ~ 3	$\frac{J_0(65)}{J_0(65)}$ at 9.5 = 1.2 $\frac{J_0(65)}{J_0(65)}$ at 9.0 $\frac{J_0(65)}{J_0(65)}$ at 9.5 = 12 $\frac{J_0(65)}{J_0(65)}$ at 4.1
(f) Freden and Paulikos—Solid state counters on Polar satellites	Sept. and Oct., 1962	8.8	1.30	.200	530	$\frac{J_0(7)}{J_0(85)}$ ~ 13 $\frac{J_0(7)}{J_0(85)}$ ~ 23 $\frac{J_0(7)}{J_0(85)}$ ~ 43 $\frac{J_0(65)}{J_0(85)}$ ~ 3	$\frac{J_0(10)}{J_0(85)}$ ~ 11 (Figure 7) $\frac{J_0(10)}{J_0(85)}$ ~ 24 (Figure 8) J (E = 50) at 8.8 = 13 J (E = 50) at 4.1
(g) Rowland Bakke, Imhof, Smith (1963)—Scintillators on Atlas pods	March, 1963	9.2	1.27	.216	340	no maximum at 40 Mev $\frac{J_0(20)}{J_0(40)}$ ~ 2.0 $\frac{J_0(10)}{J_0(60)}$ ~ 8.0	$\frac{J_0(20)}{J_0(40)}$ = 2.2 (Figure 10) $\frac{J_0(10)}{J_0(60)}$ = 9.0

did not cover such low energies. Figures 7 through 11 show that the calculated spectral shape should not change much during the period of these measurements—from 6 to 9 years solar cycle time. The proton fluxes should increase but the shape of the spectrum stays nearly the same. Striking changes in spectral shape should occur on the upswing of the solar cycle. The agreement with spectral shape in Figure 16 is not bad but the peaks in Experiments a and b should not occur at $t = 6$. It may be that a neutron absorption, as suggested by Freden and White (Reference 3), is required to explain the peak.

All of the information presented so far on Figures 6 through 15 are mirror point fluxes M , that is, the flux of protons mirroring per unit volume at one particular B and L. For low altitudes where the atmosphere changes rapidly with altitude it is nearly correct to compare this flux with measured omnidirectional flux values. For these low altitudes the omnidirectional flux is very nearly the same as the mirror point flux. To show a more complete picture of the solar cycle proton changes we have converted to omnidirectional fluxes using Equations 24 of Hess and Killeen (Reference 23). Figure 17 shows a calculated $R-\lambda$ map of the 25 Mev proton omnidirectional fluxes J at solar maximum and solar minimum. An isoflux contour is clearly at lower R for solar minimum.

In conclusion we have shown that large changes in proton fluxes will take place during the solar cycle for those regions of B-L space corresponding roughly to minimum altitudes of about 300-700 km. Changes in proton spectra will occur also. Comparison of the calculations with available experimental information are not conclusive. Some kinds of experimental data agree quantitatively with the calculations. Other data agrees qualitatively but not quantitatively. The crucial tests of the calculations will involve measuring changes in the proton flux and spectrum

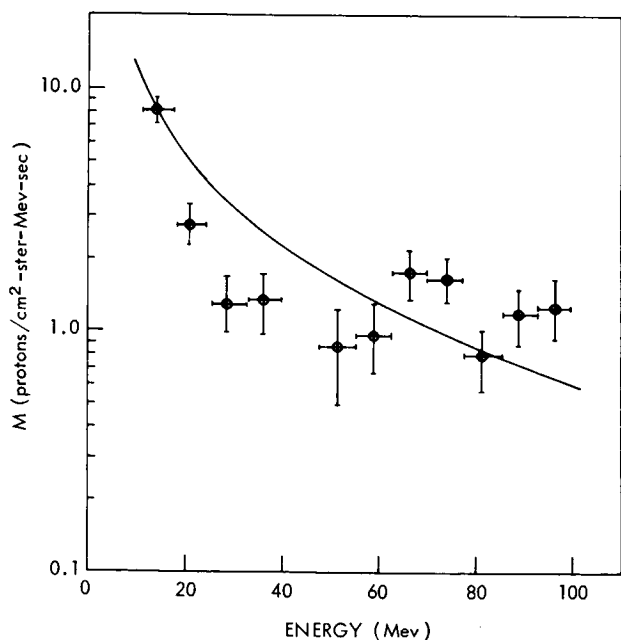


Figure 16—The energy spectrum of inner zone protons measured by Rowland (Reference 22) on an Atlas pod at $L = 1.27, B = .216$ shown for comparison is the spectrum calculated in this paper for $L = 1.27, B = .207, t = 9$.

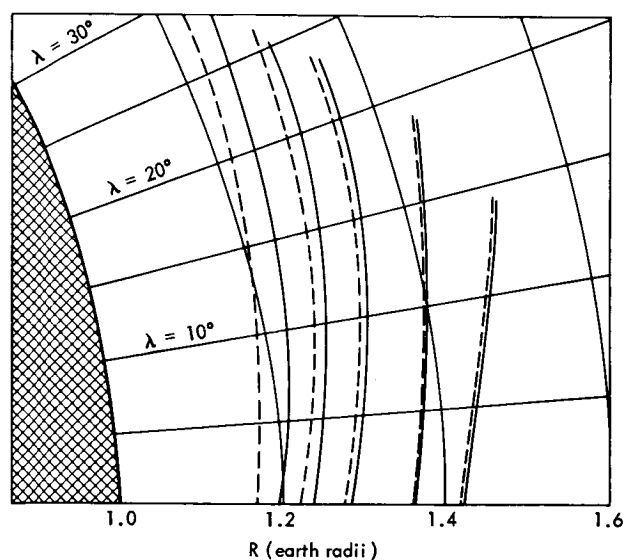


Figure 17—An $R - \lambda$ map of the omnidirectional flux of $E = 25$ Mev protons at solar maximum (solid line) and solar minimum (dashed line).

as we approach solar maximum during 1966-68. We know experimentally (Reference 16) that the atmospheric density changes used in the calculation are reasonable. These calculated effects must take place with about the magnitudes shown here unless there are features of the inner belt protons which we do not now understand.

REFERENCES

1. Freden, S. C., and White, R. S., "Protons in the Earth's Magnetic Field," *Phys. Rev. Letters*, 3(1):9-11, July 1, 1959.
2. Freden, S. C., and White, R. S., "Particle Fluxes in the Inner Radiation Belt," *J. Geophys. Res.* 65(5):1377-1383, May 1960.
3. Freden, S. C., and White, R. S., "Trapped Proton and Cosmic-Ray Albedo Neutron Fluxes," *J. Geophys. Res.* 67(1):25-29, January 1962.
4. Armstrong, A. H., Harrison, F. B., Heckman, H. H., and Rosen, L., "Charged Particles in the Inner Van Allen Radiation Belt," *J. Geophys. Res.* 66(2):351-357, February 1961.
5. Naugle, J. E., and Kniffen, D. A., "Flux and Energy Spectra of the Protons in the Inner Van Allen Belt," *Phys. Rev. Letters*, 7(1):3-6, July 1961.
6. Naugle, J. E., and Kniffen, D. A., "Variations in the Proton Energy Spectrum with Position in the Inner Van Allen Belt," *J. Geophys. Res.* 68(13):4065-4078, July 1, 1963.
7. Pizzella, G., McIlwain, C. E., and Van Allen, J. A., "Time Variations of Intensity in the Earth's Inner Radiation Zone," *J. Geophys. Res.* 67(4):1235-1254, April 1962.
8. Lenchek, A. M., "On the Anomalous Component of Low-Energy Geomagnetically Trapped Protons," *J. Geophys. Res.* 67(6):2145-2157, June 1962.
9. Lingenfelter, R. E., to be published.
10. Hess, W. N., "Discussion of Paper by Pizzella, McIlwain, and Van Allen 'Time Variations of Intensity in the Earth's Inner Radiation Zone. October 1959 Through December 1960'," *J. Geophys. Res.* 67(12):4886-4887, November 1962.
11. Singer, S. F., "Trapped Albedo Theory of the Radiation Belt," *Phys. Rev. Letters*, 1(5):181-183, September 1, 1958.
12. Hess, W. N., "Van Allen Belt Protons from Cosmic-Ray Neutron Leakage," *Phys. Rev. Letters*, 3(1):11-13, July 1, 1959.
13. McDonald, F. B., and Webber, W. R., "A Study of the Rigidity and Charge Dependence of Primary Cosmic Ray Temporal Variations," *J. Phys. Soc. Japan* 17(Suppl. A II):428-435, January 1962.

14. Harris, I., and Priester, W., "Time-Dependent Structure of the Upper Atmosphere," *J. Atmos. Sci.* 19(4):286-301, July 1962.
15. Harris, I., and Priester, W., "Theoretical Models for the Solar-Cycle Variation of the Upper Atmosphere," NASA Technical Note TN D-1444, August 1962.
16. King-Hele, D. G., "Decrease in Upper-Atmosphere Density Since the Sunspot Maximum of 1957-58," *Nature*, 198:832-834, June 1, 1963.
17. Bryant, R., "Densities Obtained from Drag on the Explorer XVII Satellite," to be published.
18. Spencer, N. W., Brace, L. H., Corignan, C. R., Tausch, D. R., and Niemann, H., "The Concentration and Temperature of Molecular Nitrogen and Electrons in the 120 to 350 km Region"; Brace, L. H., and Spencer, N. W., "Geophysical Implications of Explorer XVII Electrostatic Probe Measurements"; Horowitz, R., and Newton, G. P., "First Direct In-Site Measurements of Atmospheric Density from Explorer XVII"; and Reber, C. C., "Preliminary Results Regarding Neutral Atmosphere Composition from the Explorer XVII Satellite", abstracts at the Boulder AGU Meeting, Dec. 1963, *Transactions of AGU* 44 884, 1963.
19. Harris, I., and Priester, W., "Relation between Theoretical and Observational Models of the Upper Atmosphere," *J. Geophys. Res.* 68(20):5891-5894, October 15, 1963.
20. Ray, C. E., "On the Theory of Protons Trapped in the Earth's Magnetic Field" *J. Geophys. Res.* 65(9):1125-1134, April 1960.
21. Aron, W. A., et al., "Range-Energy Curves," 2d rev. ed., Oak Ridge: U. S. Atomic Energy Commission, Technical Information Service Extension, 1957.
22. Rowland, J. H., Bakke, J. C., Imhof, W. L., and Smith, R. V., "Radiation Environment Experiment" Lockheed Missiles and Space Co. Tech. Report SSD-TDR.
23. Hess, W. N., and Killeen, J., "Spatial Distribution of Electrons from Neutron Decay in the Outer Radiation Belt," *J. Geophys. Res.* 66(11):3671-3680, November 1961.

N65 29560

SOLAR X - RAY BURSTS IN THE 20 TO 100 KEV RANGE OBSERVED BY OSO-I

by
Kenneth J. Frost
Goddard Space Flight Center

SUMMARY

29560

During the months of March, April, and May, 1962, instrumentation aboard OSO-I observed five solar-flare associated high-energy x-ray bursts. The instrumentation which observed these bursts was designed to monitor the solar x-ray flux in the 20 to 100 keV energy range. The beginning and the end of each event was observed. All events were accompanied by radio bursts of impulsive character in the microwave range. Plots of flux density versus wavelength for the associated microwave outbursts yield curves similar to the curves which Kundu found to be associated with previously observed x-ray bursts. Sudden ionospheric disturbances also accompany each high energy x-ray burst.

Consideration of the radio data, the short duration of the x-ray bursts, and the energy of the bursts lead to the conclusion that we are observing a process which is located in the chromosphere and is non-thermal in character.

Author

INTRODUCTION

Among the experiments carried by OSO-I (1962 1) in the pointed section was a scintillation counter designed to detect hard solar x-ray bursts in the 20 to 100 keV energy range. The scintillation counter consisted of a cylindrical NaI(Tl) crystal 0.3 cm high and 2.24 cm in diameter and an RCA C-7151 photomultiplier tube. The photomultiplier tube and crystal assembly was placed in a cylindrical copper shield which through an opening in the front end provided a field of view of 0.3 steradian. The copper shield had a wall thickness of 1 cm. The 3.8 cm² area of the front surface of the crystal was held normal to the solar direction by the pointing of the satellite. An aluminum disc of 0.08 cm thickness was placed over the front surface of the crystal. The efficiency of the detector in the 20 to 100 keV interval was approximately 0.90.

The electronics associated with the detector consisted of lower and upper level discriminator circuits and a logarithmic ratemeter. The lower and upper level discriminator circuits were set to select only those pulses from the photomultiplier which corresponded to an energy loss of between 20 to 100 keV in the crystal. The pulses accepted by the discriminator circuits were then passed on to the logarithmic ratemeter. The output of the ratemeter was a voltage level between zero

and 5 volts which corresponded to an input count rate between 10 and 10^4 counts/second. The output of the ratemeter was able to respond to changes in count rate that occurred in a time longer than 10 milliseconds.

The satellite telemetry system sampled the voltage level at the output of the ratemeter continuously for 2 seconds once every 20 seconds. This sampling format was operative during the entire daylight part of an orbit.

DATA

With the return of the first hundred orbits of reduced data the response of the detector to the general spacecraft x-ray background and the response to the regions of trapped radiation was determined. In addition it was found that the experiment responded to the electron warm spots detected by an electron-proton spectrometer placed aboard the spacecraft by Schrader et al, (Reference 1). When passing through regions not including trapped radiation or electron warm spots the detector was found to produce a count rate for a 2-second sample that consistently fell between limits of 10.5 to 14.5 counts/second.

On March 17, 1962 a short-lived increase in count rate occurred while the satellite was passing through a region where the count rate normally fell in the background range of 10.5 to 14.5 counts/second. The increase in count rate started at 19:39:49 UT and ended at 19:40:08 UT. A record of the satellite telemetry signal for the orbit containing this time period indicated conclusively that the fluctuation in count rate was real and could not be attributed to telemetry noise that had been erroneously digitized by the automatic data reduction system. Reference to the available solar data revealed that a solar flare had been observed by the McMath-Hulbert and Lockheed Observatories between the times of 1934 to 1959 UT and 1936 to 2003 UT, respectively. The flare was observed on the east limb of the sun and was classified by McMath-Hulbert as an importance 1 flare and by Lockheed as an importance 2 flare. Also at this time an impulsive radio burst of 3-minute duration beginning at 19:39 UT and reaching maximum at 19:40:12 UT was observed at 2800 Mc/sec by Ottawa. Furthermore an SID accompanied the flare beginning at 19:40 UT and reaching maximum at 19:44 UT. The very close correlation in the time for these events and the fluctuation of the 20 to 100 keV count rate suggested that the most plausible explanation of the fluctuation was a burst of energetic x-rays produced by the flare.

During succeeding orbits of the spacecraft four more instances of rapid excursions in count rate were observed during the presence of a flare on the sun which produced an impulsive radio burst in the microwave range and an SID. These excursions in count rate were also interpreted as solar flare x-ray bursts. The history of these five events is presented graphically in Figures 1 through 5 (Reference 2).

DISCUSSION

Prior to the launch of OSO-I eight occurrences of high energy x-ray bursts accompanying solar flares had been observed (References 3 through 7). Kundu has analyzed the radio data associated with each of these events (Reference 8). He found that an impulsive microwave burst was associated with every x-ray burst whereas type III bursts and other meter wave events did not show as strong a correlation. Furthermore the general character of the microwave spectrum was found to be such that the peak flux observed at wavelengths in the 3 to 10 cm range was stronger than that observed at wavelengths in 10 to 20 cm range. The radio data associated with the OSO-I x-ray bursts as indicated in Figures 1 through 5 appear to lend strong support to Kundu's analysis. Additional information of interest to this analysis is the fact that as far as can be determined from spectral observations in the meter wave range, no type III bursts occurred during the x-ray events.

1⁺ FLARE 1 SID RADIO DATA

Station and Frequency (Mc)	Start (UT)	Max (UT)	Duration (min)	Type	Peak Flux *
2800 OTT	1939	2000	101	S	2
2800 OTT	1939	1940.2	3	S	6
18 NBS	1940	1949	135		

* In units of $10^{-22} \text{ w m}^{-2} (\text{c/sec})^{-1}$

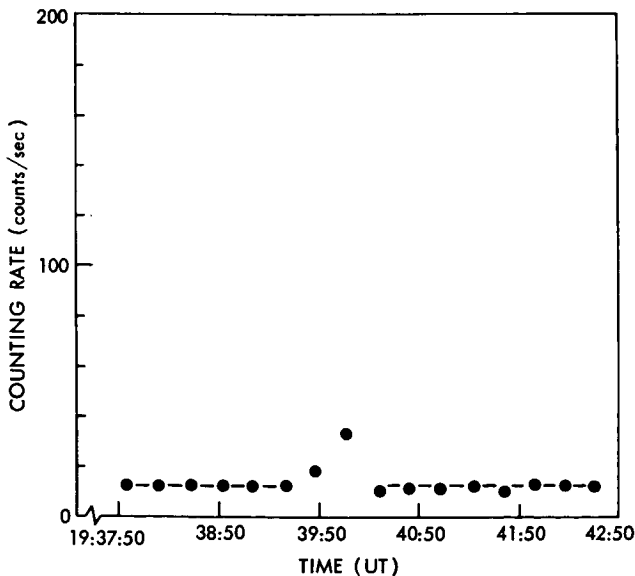


Figure 1—High energy x-ray burst, OSO-I;
 $20 < E_{\gamma} < 100 \text{ kev}$, March 17, 1962.

1⁺ FLARE 1 SID RADIO DATA

Station and Frequency (Mc)	Start (UT)	Max (UT)	Duration (min)	Type	Peak Flux *
9100 NED	0848.1	0849.2	4.5	S	102
2980 NED	0848.0	0849.2	4.5	S	122
1500 HHI	0848.0	0849.6	22.0	S	38

* In units of $10^{-22} \text{ w m}^{-2} (\text{c/sec})^{-1}$

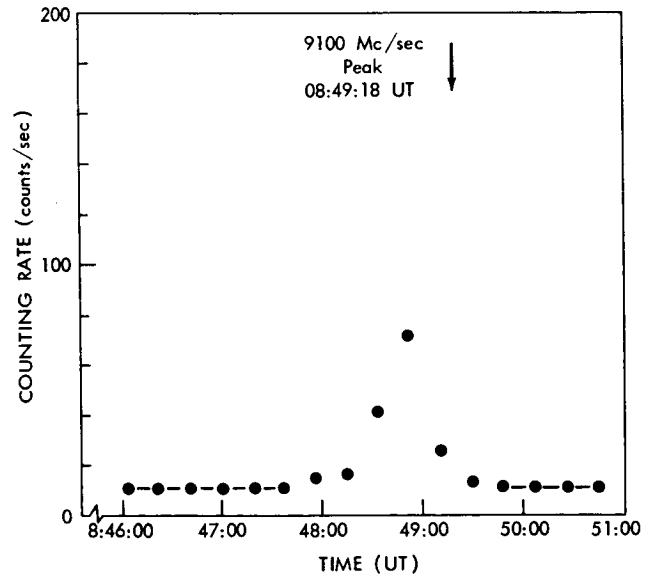


Figure 2—High energy x-ray burst, OSO-I;
 $20 < E_{\gamma} < 100 \text{ kev}$, April 13, 1962.

1⁺FLARE 1 SID RADIO DATA

Station and Frequency (Mc)	Start (UT)	Max. (UT)	Duration (min)	Type	Peak Flux *
2800 OTT	1935	1936.3	8	S	165

* In units of $10^{-22} \text{ w m}^{-2} (\text{c/sec})^{-1}$

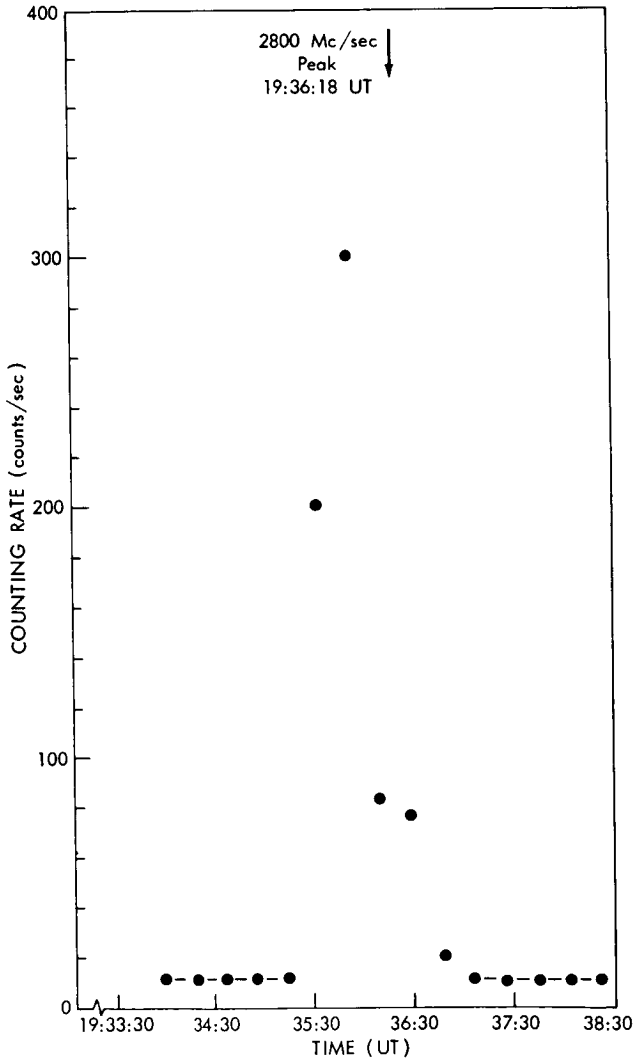


Figure 3—High energy x-ray burst, OSO-I; $20 < E_{\gamma} < 100$ kev, April 19, 1962.

1⁺FLARE 1 SID RADIO DATA

Station and Frequency (Mc)	Start (UT)	Max. (UT)	Duration (min)	Type	Peak Flux *
9500 TOK	0203.5	0203.8	1	C	419
3750 NAG	0203.5	0204.2	2.5	C	330
2000 NAG	0203.5	0204.2	2.5	C	73
1000 NAG	0203.5	0204.3	2.5	S	37
222 SEA	0203.5	0204.0	1	S	110

* In units of $10^{-22} \text{ w m}^{-2} (\text{c/sec})^{-1}$

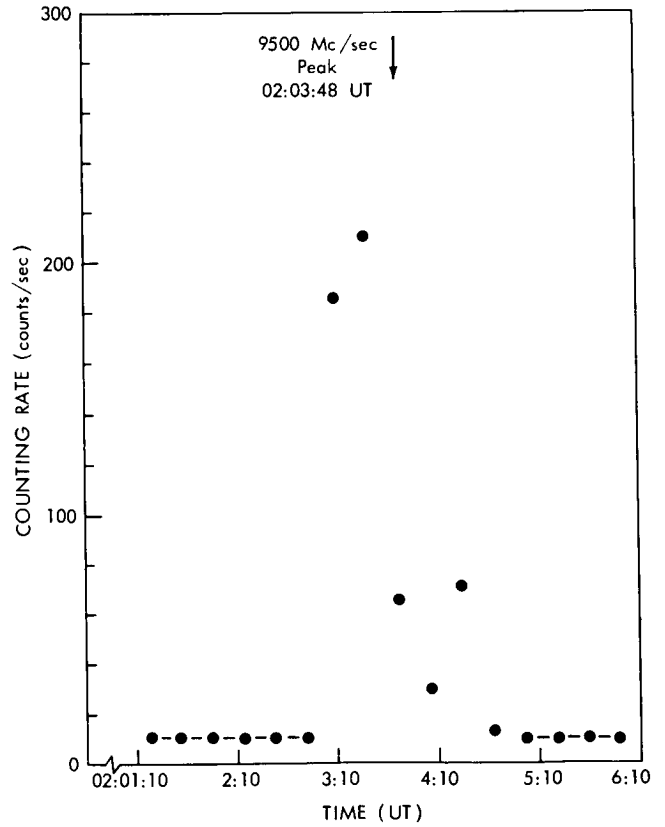


Figure 4—High energy x-ray burst, OSO-I; $20 < E_{\gamma} < 100$ kev, April 21, 1962.

2 FLARE 2 SID RADIO DATA

Station and Frequency (Mc)	Start (UT)	Max (UT)	Duration (min)	Type	Peak Flux *
9400 NAG	0647.5	—	5	—	> 80
3750 NAG	0647.5	0650.2	5	C	270
2000 NAG	0647.5	0654.9	10	C	80
1500 HHI	0643	0650.0	16.7	f	73
1000 NAG	0647.5	0654.3	10	C	30
545 NED	0648	—	0.8	C	70
200 NED	0648	0649.7	15	C	65

* In units of $10^{-22} \text{ w m}^{-2} (\text{c/s})^{-1}$

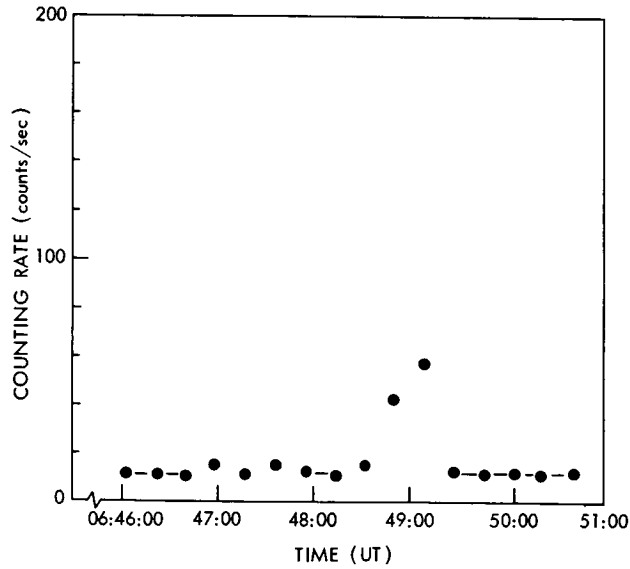


Figure 5—High energy x-ray burst, OSO-1;
 $20 < E_r < 100 \text{ kev}$, May 1, 1963.

REFERENCES

1. Schrader, C., Kaifer, R. C., Wagner, J. A., Zinger, J. H., and Bloom, S., "Proton, Electron Fluxes (75 kev) from OSO," Presented at AGU Spring Meeting, April, 1963.
2. Flare, SID, and Radio Data, taken from: *Quart. Bull. Solar Activity*, no. 137, January-March 1962, and no. 138, April-June 1962.
3. Peterson, L. E., and Winckler, J. R., "Gamma-Ray Burst from a Solar Flare," *J. Geophys. Res.* 64(7): 697-707, July 1959.
4. Chubb, T. A., Friedman, H., and Kreplin, R. W., "X-Ray Emission Accompanying Solar Flares and Non-Flare Sunspot Maximum Conditions," in: *Space Research: Proceedings 1st International Space Science Symposium*: 695-701, New York: Interscience, 1960.
5. Winckler, J. R., May, T. C., and Masley, A. J., "Observation of a Solar Bremsstrahlung Burst of 1926 U. T., August 11, 1960," *J. Geophys. Res.* 66(1): 316-320, January 1961.
6. Vette, J. I., and Casal, F. G., "High-Energy X-Rays during Solar Flares," *Phys. Rev. Letters* 6(7): 334-336, April 1, 1961.
7. Anderson, K. A., and Winckler, J. R., "Solar Flare X-Ray Burst on September 28, 1961," *J. Geophys. Res.* 67(11): 4103-4117, October 1962.
8. Kundu, M. R., "Centimeter-Wave Radio and X-Ray Emission from the Sun," *Space Sci. Rev.* 2:438-469, September 1963.

N65-29561

DETECTION OF INTERPLANETARY 3- TO 12-MEV ELECTRONS

by

T. L. Cline, G. H. Ludwig,

and F. B. McDonald

Goddard Space Flight Center

~~29561~~

In this Letter we report the direct observation of interplanetary electrons of energy above 3 Mev with the IMP 1 satellite (Explorer XVIII).

Electrons observed in the primary interplanetary radiation in the Bev energy region by Earl (Reference 1) and in the 200-Mev energy region by Meyer and Vogt (Reference 2) are believed to be of galactic origin because their energies are as high as those assumed to be necessary for their penetration into the inner solar system and because their measured intensity agrees with that which was anticipated to account for galactic radio emission. Support was lent to this hypothesis when the modulation characteristics of these particles were observed (Reference 3) to be similar to those of cosmic-ray protons and their positron-to-electron ratio was found to be compatible with an origin of at least half of them in meson-producing cosmic-ray interactions in the interstellar medium (Reference 4). We feel that the existence of an interplanetary flux of electrons lower in energy by orders of magnitude is interesting because of the possibility that these too may have a cosmic origin. If so, their study should yield entirely new information about the galactic electron sources and modulation characteristics. If they are of solar origin, there are analogous implications. We wish to demonstrate here that the flux of lower-energy electrons we observe is indeed a primary component of the interplanetary radiation, and to discuss its properties in terms of its possible origin, either galactic or solar.

The observations reported here were made with a scintillator telescope on Explorer XVIII, a satellite placed in an elliptic orbit with an apogee height of 193,000 kilometers. Data were taken from the launch, on 27 November 1963, until 6 May 1964 when the satellite passed into a long period in the earth's shadow, causing failure of the detector. During this time interval the apogee moved from the sunlit side of the earth beyond the magnetosphere (terminating at about 70,000 km) and beyond the earth's shock front (observed with a magnetometer*) and plasma sensor (Reference 5 at about 100,000 km) to the region behind the earth and inside the shock front. Electron data taken only when the satellite was beyond 125,000 kilometers are reported here; throughout the life of the instrument these data continued to be free from effects due to the trapped radiation.

*See pp.

The detector was developed (Reference 6) to study low-energy cosmic-ray protons, electrons and light nuclei. It is composed of three scintillators: two in coincidence, measuring energy loss and total energy, and a guard counter in anticoincidence. When a table of intensity versus measured energy loss versus measured total energy is constructed from data taken at apogee, there is seen a distinct counting rate component of minimum-ionizing energy loss and of low apparent energy. An analysis of the topology of distributions in energy loss and in total energy through this minimum-ionizing component indicates that indeed it is composed of three distinct particle groups: One group with total energies corresponding to electrons that stop within the detector, a much smaller group with a high apparent total energy equal to or exceeding the energy loss of a minimum-ionizing cosmic ray traversing the detector, and a third group with very low total energies. We believe that the latter two components are surely secondary radiations composed of, respectively, cosmic rays that avoid detection by the guard counter (for example, by turning into neutrals through reactions within the detector) and gamma rays made locally in the spacecraft, producing random and coherent coincidences between the energy loss and total energy detectors.

These secondary effects were eliminated to produce Figure 1a, which shows the energy spectrum of electrons obtained during the first orbit (27 to 30 November 1963) at a time when the observed electron intensity was at a typical minimum and when there were no measurable time variations. Figure 1b shows, for comparison, a spectrum of the difference between the first statistically significant intensity increase (13 to 16 January 1964) and the immediately preceding intensity (9 to 12 January). No background corrections were necessary to produce the latter distribution since the electron intensity increase was unaccompanied by an increase of either secondary gamma rays or spurious cosmic rays; it was therefore possible to determine the intensity to higher energies. The nearly identical shapes of the two corrected spectra suggest that the electrons seen daily may have the same origin as the extra ones seen on days of increased electron flux. The integral intensity of electrons of energy between 2.7 and 7.5 Mev is $210. \pm 10.$ electrons/m²-sec-ster., and that of the increase between 3. and 12.5 Mev an additional $100. \pm 10.$ electrons/m²-sec-ster.

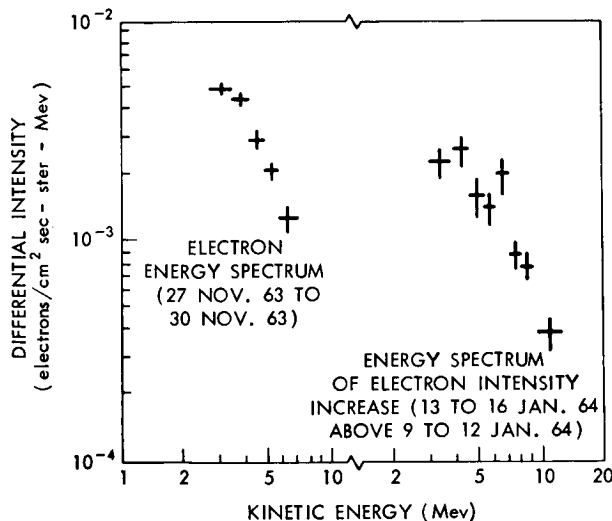


Figure 1—Differential energy spectra of electrons observed beyond 125,000 kilometers from the earth. The first spectrum is from the apogee of the first orbit; the second is the difference between measurements from the 13th and 12th orbits and indicates the first significant increase in intensity.

To demonstrate that most of the observed electrons are not of local or secondary origin at the satellite (e.g., such as knock-on or cascade-shower electrons produced in or near the detector) we consider their time variations. Figure 2 shows the counting rate of these electrons, partially corrected for slow gain drifts in the detector, plotted in the form of one-quarter-orbit averages throughout the

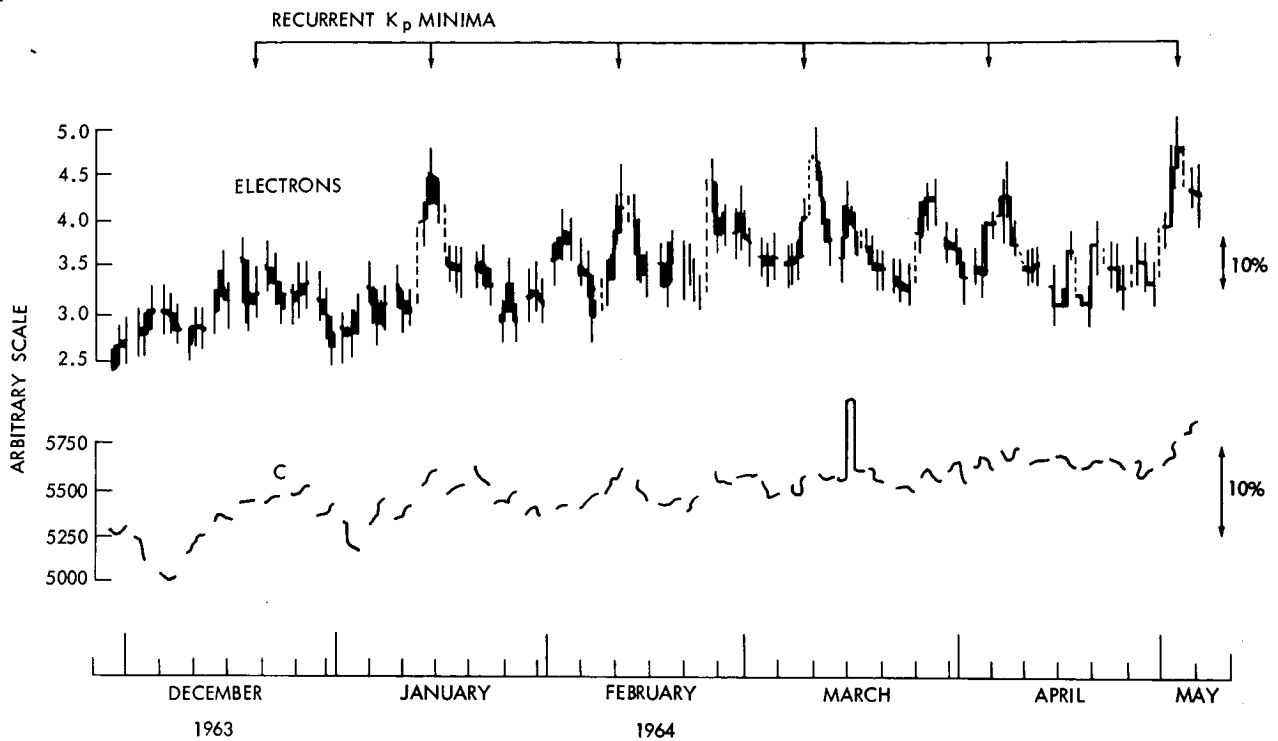


Figure 2—Integral counting rate of electrons throughout the active life of the instrument plotted in quarter-orbit averages. The counting rate "C" of cosmic rays into a thinly shielded scintillator and the times of one recurrent minimum of the interplanetary index K_p are also shown. Recurrent Forbush decreases are seen in the cosmic rays in early December and January and a small solar proton event occurs in March; other increases can be largely attributed to the electron mixture in the cosmic rays.

active life of the instrument. (The gaps in the data occur at times when the satellite is within 125,000 kilometers; the other three points per orbit are plotted so that each center one represents data taken from beyond 185,000 kilometers.) Also shown are a comparison plot "C" of the integrated cosmic-ray flux into a scintillator with about 0.3 gram cm^{-2} shielding, and the times of a recurrent minimum in the interplanetary magnetic activity index K_p with a period of one solar rotation.

A dominant feature of the electron rate is the appearance of many statistically meaningful intensity increases, including one series apparently coincident with the recurrent K_p minimum. These electron intensity increases were not accompanied by comparable increases in the integral cosmic-ray intensity above 15 Mev: the magnitude of the electron modulation is 50 percent on occasions, while the cosmic rays undergo modulations of less than 5 percent. Further, following the flare of 16 March 1964 there was a solar-proton event, accompanied by Type IV solar radio emission*, during which the flux of protons of energy between 15 and 75 Mev briefly increased by several orders of magnitude, while the 3- to 8-Mev electron flux rose less than 50 ± 25 percent.

*A. Maxwell, Private communication.

(Figure 2 shows the quarter-orbit average of the total integrated cosmic ray flux increasing at that time by about 10 percent.) These comparisons demonstrate that, at most, an insignificant fraction of the electron modulation results from modulations of cosmic rays of energy about 15 Mev.

Modulations of protons with energies below 15 Mev, such as 27-day recurrent solar proton events similar to those observed (Reference 7) with Explorer XII, were not monitored with our apparatus; but these would be expected at the times of recurrent Forbush decreases and geomagnetic activity, rather than at the time of our repeating electron increases. Several such 1- to 10-Mev proton intensity increases were observed early in the life of the satellite by Fan, Gloeckler and Simpson (Reference 8) but these were about two weeks out of phase with our electron enhancements and appear to be accompanied by, if anything, decreases in the electron intensity and in the galactic cosmic rays.

Finally, a study of 3-hour averages of the observed intensity of these electrons indicates no variation with distance from the earth, either during orbits of minimum intensity or during times of increased intensity; the electron rate is constant through the shock front to a distance of up to 50 percent beyond it. Further, the satellite's passage through the wake of the moon* was unaccompanied by an electron intensity variation. Thus, these electrons are not secondary to cosmic rays or solar protons or due to geophysical processes.

We feel that the question of whether these primary electrons originate at the sun or in the galaxy cannot be definitely answered on the basis of the available data; however, the following properties of these electrons are consistent with their being galactic. First, the differential energy spectrum of this 3- to 12-Mev component fits smoothly onto a spectral plot of the cosmic-ray electron intensities (References 1, 2, and 4) at much higher energies. Second, the time variations of the electrons can be compared to those of cosmic rays in that there is a strong correlation between the electron intensity increases and quiet interplanetary conditions, evidenced by K_p minima and very small sea-level cosmic-ray intensity increases. Third, there appears to be a long-term increase of electron intensity after a correction of the same order is applied for a slow, monitored drift in detector gain; if this increase is real, it is similar to the 11-year modulation of cosmic rays as solar minimum is approached. However, the fact that the differential cosmic-ray proton intensity is peaked at about 1 Bev/c rigidity and negligible below 150 Mev/c markedly contrasts with the fact that electrons of rigidity $\gtrsim 3.5$ Mev/c are more abundant than those of greater rigidity. Parker has recently pointed out (Reference 9) that particles with gyroradius close to the idealized irregularity scale of the modulating medium should be deflected more than those of either extreme; thus these electrons of low rigidity might originate in the galaxy and penetrate the solar system as easily as those of great rigidity.

In spite of the foregoing arguments for galactic origin, it is not impossible that the electrons come instead from the sun. Several possibilities present themselves. For example, relativistic electrons might be generated over most of the upper surface of the solar atmosphere, in which

*See pp.

case regions of enhanced and expanded plasma (which contain recurrent proton fluxes) would tend to contain fewer electrons while regions of quiet-time streaming would contain more, as we have observed. Further, the deceleration of the electrons in the enhanced plasma might be much greater than that in the quiet-time streaming. Alternatively, the electrons might be associated with the development of new sunspot regions, which is a characteristic of this phase of the solar cycle and appears to correlate weakly with the observed pattern of intensity increases.* We have not, however, found a correlation with any solar radio or optical activity.

The results we quote here are preliminary: an evaluation of the detector response, providing a more exact spectrum, and a detailed investigation of the time variations will be given elsewhere. We are happy to acknowledge the efforts of the many people who made the IMP 1 a success.

REFERENCES

1. Earl, J. A., *Phys. Rev. Ltrs.* 6:125, 1961.
2. Meyer, P., and Vogt, R., *Phys. Rev. Ltrs.* 6:193, 1961.
3. Meyer, P., and Vogt, R., *J. Geophys. Res.* 6:3950, 1961.
4. DeShong, J. A., Jr., Hildebrand, R. H., and Meyer, P., *Phys. Rev. Ltrs.* 12:3, 1964.
5. Bridge, H. S., Egidi, A., Lazarus, A., Lyon, E. F., and Jacobson, L., *Space Research 5*, N. Holland Publ. (COSPAR Proceedings, Florence, 1964).
6. Bryant, D. A., Ludwig, G. H., and McDonald, F. B., *I.R.E. Trans. Nuclear Science NS-9:376*, 1962.
7. Bryant, D. A., Cline, T. L., Desai, U. D., and McDonald, F. B., *Phys. Rev. Ltrs.* 11:144, 1963.
8. Fan, C. Y., Gloeckler, G., and Simpson, J. A., *Goddard IMP Symposium*, March 1964.
9. Parker, E. N., *J. Geophys. Res.* 69:1755, 1964.

*H. D. Prince and R. Hedeman, Private communication.

N65-29562

MEASUREMENT OF LOW ENERGY PRIMARY COSMIC RAY PROTONS ON IMP 1 SATELLITE

by

F. B. McDonald

G. H. Ludwig

Goddard Space Flight Center

The first precise determination of the intensity and energy spectra of primary cosmic ray protons in the 15-75 Mev interval has been made with a three element energy versus energy-loss telescope aboard the IMP 1 (Explorer XVIII) satellite. This spacecraft had an apogee of 193,000 km and only data obtained well beyond the effects of the earth's magnetosphere are considered. The measurements reported here cover the time interval 8 December 1963 to 6 May 1964 and are considered to be representative of the period just prior to solar minimum. The proton intensity in the range 15-75 Mev was observed to be 19 protons/m²-sec-ster or approximately 1 percent of the total primary cosmic ray intensity and to exhibit a steeply falling energy spectrum toward lower energies, decreasing by a factor of 5 over this interval. One point for helium was obtained in the range 65-75 Mev/nuc.

The E vs dE/dx telescope (Figure 1a) provides a means of studying this low energy component in the presence of higher energy cosmic rays (Reference 1). Because of the background and low flux in this energy interval, significant measurements cannot be obtained by balloon or rocket techniques but are dependent on satellite measurements. The principal of operation of the telescope is shown in Figure 1. For each particle which traverses the ΔE counter and stops in the E crystal (as defined by the plastic scintillator anticoincidence cup) measurements of ΔE and E - ΔE are made by 512 channel pulse height analyzers and transmitted over the satellite telemetry systems. As shown in Figure 1b, this provides

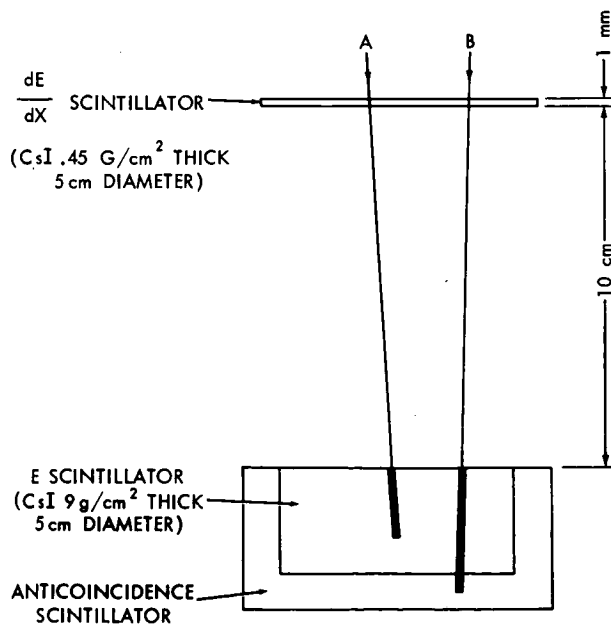


Figure 1(a)—Schematic Drawing of E vs dE/dx telescope. Particles which stop in the lower scintillator (a) are accepted for analysis while those which enter the anticoincidence cup (b) are rejected.

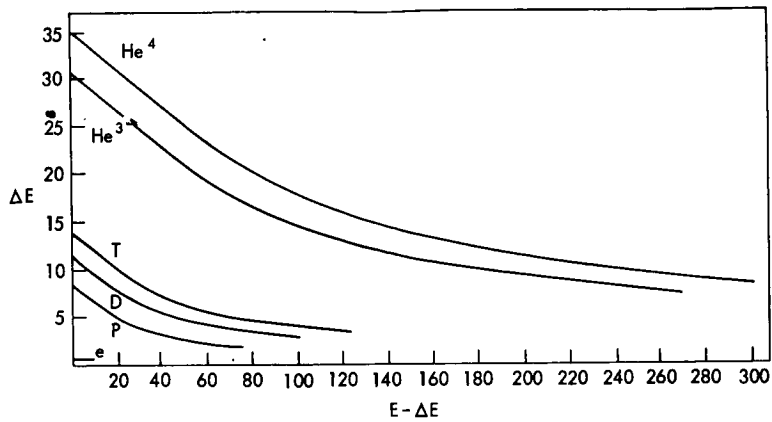


Figure 1(b)—Mass and energy response of $E [\sim(E - \Delta E)]$ and $dE/dx (\sim \Delta E)$ telescope.

a measure of mass, charge and energy resolution for $Z = 1, 2$ particles. The electron data are discussed in an accompanying paper.* Saturation effects prevented the alpha particle data from being extended to lower energies. This does not affect the H or e data. Mass histograms have been obtained in the proton region for six energy intervals of about 10 Mev each by summing the data in 11 channels constructed parallel to and centered about the proton line of Figure 1b. These six energy intervals for H are shown in Figure 2. The clean resolution of the proton distribution at all energies is striking. The background correction (illustrated by the dashed line of Figure 2) has been applied using the experimental proton distribution obtained from the small solar cosmic ray event of 16 March 1964. The rigidity and energy spectra obtained from the mass histogram data of Figure 2 along with the single α point is shown in Figure 3.

To search for long term variations, the data were divided into two intervals covering the period 8 December 1963—14 March 1964 and 22 March 1964—6 May 1964. Except at the lowest energy point, the data are consistent with a change of less than 10 percent in the proton flux in the 15-75 Mev region between these two periods. The increase on the low energy point may be due to an increase in the galactic flux or, most probably, to the small solar proton event of 16 March 1964. We cannot rule out large short time variations since the long times required to obtain meaningful statistics preclude the possibility of observing variations occurring over a shorter time scale. Proton and helium data obtained at higher energies from the balloon data of Balasubrahmanyam and McDonald, (Reference 2) and Fichtel, et al., (Reference 3) are shown for comparison. It is observed that at this period of the solar cycle just prior to solar minimum there is a sharp decrease in both spectra toward lower energies that extends to the lowest observed energy.

The flux of deuterium could not be resolved from the background and an upper limit of 8 percent of the proton flux over the corresponding energy interval was placed on its abundance.

During the last solar minimum an arctic latitude survey by Meredith, et al., (Reference 4) using a rocket borne single Geiger counter had indicated the cosmic ray intensity did not increase

*See pp.

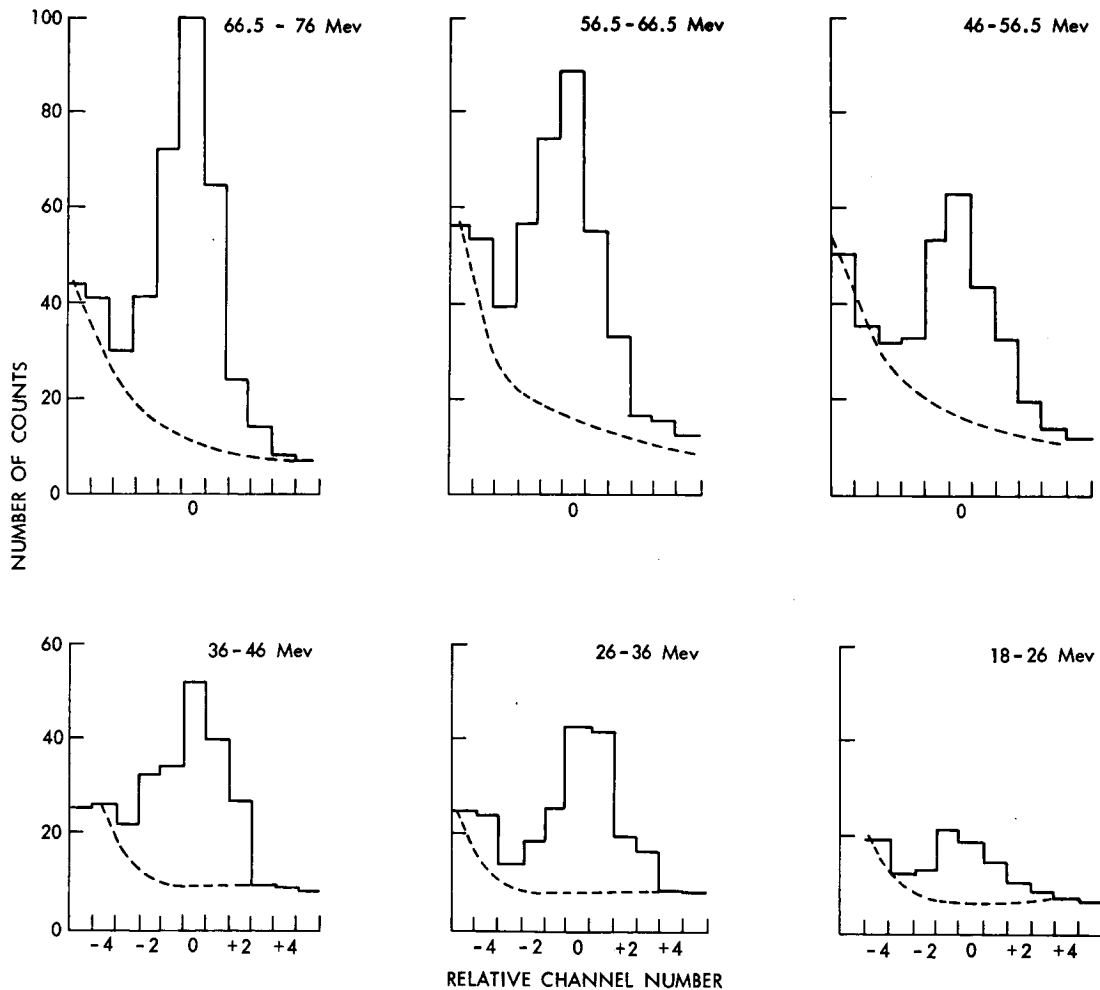


Figure 2—Mass histogram for 6 energy intervals in proton region.

strongly at low energies. The ionization chamber data of Neher (Reference 5) at balloon altitude suggested a strong variation in the low energy range >100 Mev anticorrelated with solar activity.

The only previous satellite measurements in this region were made by Stone (Reference 6) in late 1961 on a polar orbiting satellite. This study was based on 12 counts in the energy interval 11-125 Mev. They were consistent with a flat energy spectrum and served to place an upper limit of about 1 proton/ m^2 -sec-Mev on the proton flux since an active anticoincidence device was not used. The data in Figure 3 show the highest energy point of the IMP data reported here is in general agreement with the lowest energy point obtained in the June 1963 balloon flight by Balasubrahmanyam and McDonald (Reference 2) and Fichtel, et al., (Reference 3). It is also consistent with the upper limit of $dJ/dE < .49$ protons/ m^2 -sec-Mev obtained on a high latitude flight of Brunstein in 1962 (Reference 7) and with the lowest energy points obtained by Freier and Waddington (Reference 8) and Ornes and Webber (Reference 9) from 1963 balloon flights. Further confirmation of the splitting of the normalized low rigidity spectra is also obtained.

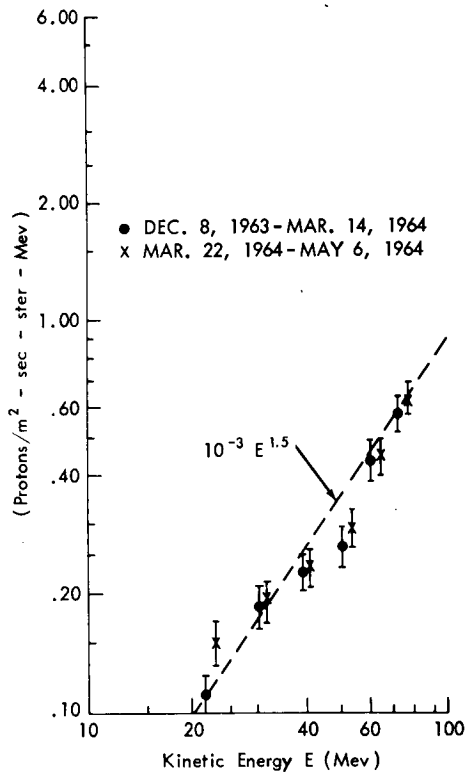


Figure 3(a)—Cosmic ray proton energy spectra for two different time periods. The dotted line indicates an empirical fit to the data of the form $10^{-3} E^{1.5}$.

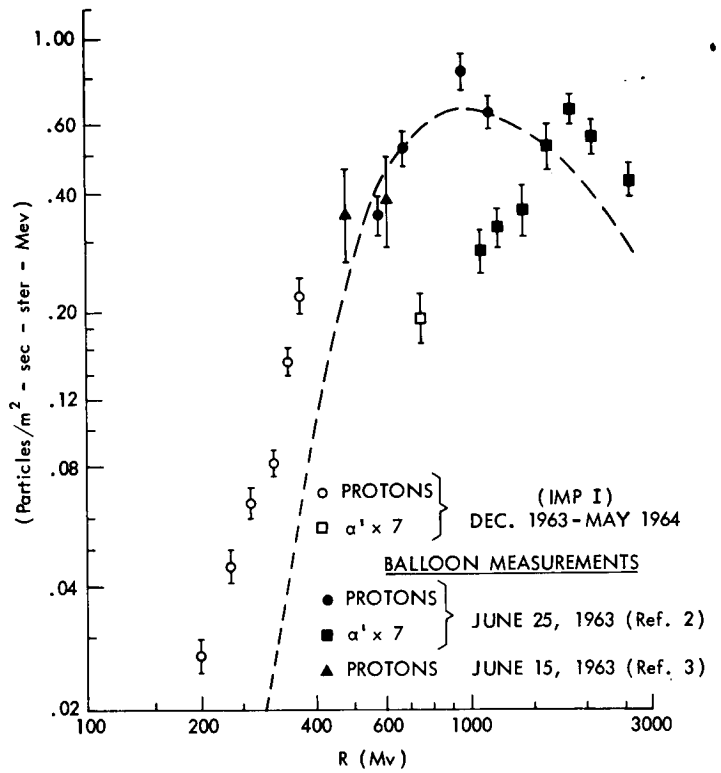


Figure 3(b)—IMP proton and α rigidity spectra. Shown for comparison is the balloon data of Fichtel, et al., (Reference 3) and Balasubrahmanyam, et al., (Reference 2).

The proton and alpha spectra as observed in interplanetary space result from a superposition of three processes—initial acceleration, diffusion through the galaxy and solar modulation. To illustrate these processes assume:

- (1) Energy spectra at injection are of the form

$$\mu(E) = \frac{10^4}{w(1+E)^{2.5}} \text{ protons/m}^3\text{-ster-bev}$$

- (2) Traversal of 2.5 gm/cm^2 of hydrogen before reaching the solar system; and
- (3) The solar modulation is of the form

$$\frac{dj}{dE} = \frac{dj_0}{dE} \exp\left(-\frac{\text{const}}{w}\right)$$

where $\mu(E)$ is the density of cosmic rays with kinetic energy E , and dj/dE is the observed differential energy spectrum while dj_0/dE is the unmodulated or stellar spectrum and w is the particle

velocity. Assumption (1) is based on an extrapolation to low energies of observations above 4 Bev (Reference 10). The 2.5 gm/cm^2 of H is implied by the relative abundance of Li, Be, and B in the primary beam (Reference 11) and the solar modulation function is a diffusion model proposed by Parker (Reference 12). In this model an equilibrium state is established between diffusion inward through irregular magnetic fields and removal by outward convection. The solar modulation effects have been obtained by normalizing at 200 Mev. These calculations are shown by the dotted curve of Figure 3b. While it can be concluded that either the injection spectra are steeper than a simple power law (as one might hypothesize from solar cosmic ray studies) or that the effects of solar modulation are not as strong at low energies (in agreement with the lack of significant long term time variations), the primary effect of these admittedly crude assumptions is to show that indeed the production of the observed steep proton energy spectrum is not unexpected on the basis of other cosmic ray observations. It is to be expected that further observations over the period of solar minimum coupled with low energy measurements of multiply charged primaries will permit more accurate determinations of the source spectra and the solar modulation mechanism.

The authors wish to thank Paull, Cancro, and Janniche of the Goddard Space Flight Center for designing and testing the spacecraft electronics for the IMP experiment, and to Flanick and Clark of Goddard for testing and calibrating the detector system. The support of Paul Butler and the IMP project team is gratefully acknowledged.

REFERENCES

1. Ludwig, G. H., and McDonald, F. B., "Proceedings of the International Symposium on Nuclear Electronics," Paris 195, 1963.
2. Balasubrahmanyan, V. K., and McDonald, F. B., *J. Geophys. Res.* 69:3289, 1964.
3. Fichtel, C. E., Guss, D. E., Kniffen, D. A., and Neelakantan, K. A., *J. Geophys. Res.* 69:3293, 1964.
4. Meredith, L. H., Van Allen, J. A., and Gottlieb, M. B., *Phys. Rev.* 99:198, 1955.
5. Neher, H. V., *Phys. Rev.* 107:588, 1957.
6. Stone, E. C., *J. Geophys. Res.* 69:3939, 1964.
7. Brunstein, K. A., *Phys. Rev.* 133:B(1520), 1964.
8. Freier, P. S., and Waddington, C. J., *Phys. Rev. Ltrs.* 13:108, 1964.
9. Ormes, J., and Webber, W. R., *Phys. Rev. Ltrs.* 13:106, 1964.
10. McDonald, F. B., *Phys. Rev.* 109:1370, 1958.
11. Badhwar, G. D., Daniel, R. R., and Vijayalakshmi, B., *Prog. Theor. Phys.* 28:607, 1962.
12. Parker, E. N., "Interplanet Dynamical Processes," (Interscience, 1963) p. 199.